Swansea University E-Theses

Near-field photocurrent characterisation of semiconductor devices.

Ackland, Mathew Paul

How to cite:

Ackland, Mathew Paul (2005) *Near-field photocurrent characterisation of semiconductor devices..* thesis, Swansea University.
http://cronfa.swan.ac.uk/Record/cronfa42382

Use policy:

This item is brought to you by Swansea University. Any person downloading material is agreeing to abide by the terms of the repository licence: copies of full text items may be used or reproduced in any format or medium, without prior permission for personal research or study, educational or non-commercial purposes only. The copyright for any work remains with the original author unless otherwise specified. The full-text must not be sold in any format or medium without the formal permission of the copyright holder. Permission for multiple reproductions should be obtained from the original author.

Authors are personally responsible for adhering to copyright and publisher restrictions when uploading content to the repository.

Please link to the metadata record in the Swansea University repository, Cronfa (link given in the citation reference above.)

http://www.swansea.ac.uk/library/researchsupport/ris-support/

Near-field photocurrent characterisation of semiconductor devices

by

Mathew Paul Ackland M.Phys.

Department of Physics
University of Wales Swansea

This thesis is submitted to the University of Wales in candidature for the degree of Doctor of Philosophy

March 2005

ProQuest Number: 10798090

All rights reserved

INFORMATION TO ALL USERS
The quality of this reproduction is dependent upon the quality of the copy submitted.

In the unlikely event that the author did not send a complete manuscript
and there are missing pages, these will be noted. Also, if material had to be removed,
a note will indicate the deletion.

ProQuest 10798090

Published by ProQuest LLC (2018). Copyright of the Dissertation is held by the Author.

All rights reserved.
This work is protected against unauthorized copying under Title 17, United States Code
Microform Edition © ProQuest LLC.

ProQuest LLC.
789 East Eisenhower Parkway
P.O. Box 1346
Ann Arbor, MI 48106 – 1346

Abstract

A near-field scanning optical microscope (NSOM) has been modified to perform near-field photocurrent imaging via the development and implementation of a two-stage amplification/detection scheme. The near-field photocurrent imaging capability has been employed along with simultaneous topographic image acquisition in the analysis of the buried Schottky interface of nickel-silicon carbide (Ni-SiC) Schottky contacts. Silicon carbide is stable at high temperatures and operating powers and thus could fulfil a wide range of potential applications, however in order to implement SiC devices in such applications stable metal contacts are a necessity and remain a field requiring optimisation. Near-field photocurrent imaging has directly imaged the buried interface properties and lateral variations in the Schottky barrier energy on the nanoscale, which have been related to the macroscopic electrical characteristics of the Schottky contact. The Schottky barrier energy has been increased by 0.155eV via annealing at 500°C, this resulted in an increase in the lateral variation in barrier properties, as reflected in the ideality factor increase of 0.3, and similarly recorded by near-field photocurrent imaging. Near-field photocurrent imaging has also been applied in the characterisation of quantum well laser devices, and powerfully combined with the complementary optical collection and topographic imaging modes. The photocurrent imaging mode probes the electronic device characteristics, whilst near-field collection imaging characterises the optical output of operating laser devices, the two independent imaging modes are correlated by the simultaneous surface topographies. GaInP / AlGaInP based quantum well lasers have been used in the study of the effectiveness of multi-quantum barrier (MQB) reflectors in enhancing the electronic carrier confinement of the quantum well active region, and thus in increasing the operational efficiency of such devices. Collection imaging has proved that the incorporation of MQB's does not impair the devices optical characteristics, whilst near-field photocurrents have sensed the location of the MQB's and detected improvements in the electronic carrier confinement. The NSOM has also been employed in the characterisation of InGaAsP / InP buried heterostructure multi-quantum well lasers, imaging the active region and surrounding current blocking structure at high resolution. Photocurrent imaging has mapped the location and extent of the *pn*-junctions that form the current blocking structure, and aided the identification of probable current leakage paths through the structure. Collection imaging has characterised the highly confined optical output of such devices and located electroluminescence external to the active region, again aiding the identification of current leakage pathways. These imaging modes are complemented by simultaneous topographic images displaying unprecedented sensitivity to the active region and sample structure.

Acknowledgements

This work was conceived and motivated by Dr Peter Dunstan who was instrumental in my embarkation upon this course of research, and to whom I am indebted to for his extremely generous time, supervision and friendship. Although performed by the author, this work was only possible by drawing upon the skills and expertise of the following; I must firstly express particular thanks to Dr Owen Guy who aided in the fabrication of the Schottky samples discussed within this thesis, and the very many that are not. Preparation of UHV Schottky samples was also aided by Ian Blackwood and Dr Vincent Teng. Laser diode samples were provided by Prof Steve Wilks and Dr Vincent Teng, who along with Prof Paul Rees I must thank for their expertise and the many discussions regarding the various devices examined within this work. Prof Tim Davies and Dr James Franks were invaluable consultants during the electronic developmental phase of this work. The implementation of these experiments would not have been possible without the technical skills of Julian Kivell, Huw Thomas, Mike Rogers and Dave Payne, and without my colleagues Dr Gareth John, Mark Holton, Richard Baylis and Omar Al Hartomy. I again wish to emphasise my thanks to Dr Peter Dunstan who was always forthcoming with his help and heavily involved throughout the course of these studies. I finally wish to express my gratitude to my family who selflessly give their support and encouragement which make anything possible.

Contents

Abstract....i
Acknowledgments....ii
Contents....iii

1. Introduction....1
- **1.1** Near-field photocurrent microscopy....2
- **1.2** Metal - Silicon carbide contacts....3
- **1.3** Quantum well laser diodes and multi-quantum barrier reflectors....3
- **1.4** Buried heterostructure multi-quantum well lasers....3
- **1.5** Outline of thesis....4
- **1.6** References....4

2. Theory: Near-field optics and scanning microscopy....6
- **2.1** Conventional microscopy and resolution....6
- **2.2** The development of NSOM....7
- **2.3** STM and the realisation of NSOM at visible wavelengths....9
- **2.4** The optical imaging process....9
  - **2.4.1** Evanescent waves....10
  - **2.4.2** Fine structure and evanescent fields....11
  - **2.4.3** Near-field resolution and Heisenberg's uncertainty principle....13
  - **2.4.4** Modelling near-field optics....14
- **2.5** The tapered optical fibre NSOM probe....15
- **2.6** Probe-sample distance regulation....16
  - **2.6.1** Quartz tuning forks and force detection....17
  - **2.6.2** Shear-force feedback for distance regulation....18
- **2.7** NSOM modes of operation....20
- **2.8** Summary....21
- **2.9** References....22

3. Theory: Metal-semiconductor contacts....24
- **3.1** Schottky barrier formation....24

3.1.1 Schottky-Mott theory....25
3.1.2 Surface/interface states and the Bardeen model....27
3.1.3 Real surfaces and interfaces....29
3.2 Ohmic contacts....30
3.3 Current transport: Thermionic emission....31
3.4 Current transport: Field emission....32
3.5 Measuring Schottky barrier heights....33
3.6 I-V technique....34
3.7 Silicon carbide....34
3.8 Metal-silicon carbide contacts....35
3.9 Summary....37
3.10 References....37

4. Theory: *pn*-junctions and laser diodes....39
4.1 *pn*-junction formation....39
4.2 Built in potential, V_B....41
4.3 Carrier transportation in *pn*-junction diodes....42
4.4 Depletion region....43
4.5 Laser diodes....46
4.6 Quantum wells and laser diodes....48
4.7 Multi-quantum well super lattices....50
4.8 Multi-quantum barrier reflectors....50
4.9 Buried heterostructure laser diodes....52
4.10 Summary....54
4.11 References....55

5. Theory: Near-field photocurrent microscopy....56
5.1 Internal photoemission....56
5.2 Fowler's theorem....57
5.3 Near-field photocurrent microscopy....58
5.4 Schottky junctions and photocurrent mechanisms....59
5.5 *pn*-junctions and photocurrent mechanisms....62
5.6 Summary....64
5.7 References....65

6. Experimental......67

6.1 Introduction......67

6.2 NSOM configurations / specifications......67

6.3 The development of near-field photocurrent microscopy – from macroscopic to nanoscopic photocurrents......71

6.4 NSOM analysis of Schottky diodes......77

6.4.1 Sample preparation: Ni-SiC Schottky diodes......77

6.4.2 Contact deposition: Edwards evaporation chamber......79

6.4.3 Contact deposition: UHV evaporation system......80

6.4.4 Schottky diode sample holder......81

6.4.5 Near-field photocurrent imaging of Schottky diodes......83

6.5 Cross-sectional NSOM analysis of laser diodes......84

6.5.1 Sample cleaving......84

6.5.2 Laser diode sample holder......85

6.5.3 Cross-sectional collection imaging......87

6.5.4 Cross-sectional photocurrent imaging......89

6.5.5 Tip approach techniques for cross-sectional imaging......90

6.6 Scanning artefacts in NSOM imaging techniques......91

6.7 Imaging artefacts in photocurrent NSOM......95

6.8 Summary......96

6.9 References......96

7. Results: Ni-SiC Schottky diodes......98

7.1 Introduction......98

7.2 Samples......99

7.3 Top contact thickness and the imaging of buried interfaces......101

7.4 Near-field photocurrent imaging of buried interfaces......102

7.5 Imaging the depletion region at the lateral contact boundary......106

7.6 Photocurrent imaging of buried interfaces through flat surfaces......108

7.7 Increasing Schottky barrier height by thermal annealing......111

7.8 Fabrication process dependence......115

7.9 Summary......117

7.10 References......118

8. Results: Planar quantum well lasers and MQB reflectors..............................120
8.1 Introduction..120
8.2 Sample details...121
8.3 Sample preparation...123
8.4 Topographic imaging...124
8.5 Collection NSOM of operating devices...128
8.6 Near-field photocurrent imaging..132
8.6.1 Correlating the photocurrent response with cross-sectional structure..134
8.6.2 Probing the effect of MQB's using near-field photocurrents....136
8.6.3 Control laser photocurrent characteristics................................138
8.6.4 MQB photocurrent characteristics...140
8.7 Summary..142
8.8 References..142

9. Results: Buried heterostructure multi-quantum well laser.............................144
9.1 Introduction..144
9.2 Sample structure...144
9.3 Sample preparation...145
9.4 BH-MQW laser surface topography...146
9.5 BH-MQW laser: Photocurrent imaging..149
9.5.1 BH-MQW laser photocurrent characteristics and excitation energy..150
9.5.2 Correlation of photocurrent and topography.............................157
9.5.3 Multi-quantum well active region..159
9.6 The effectiveness of the *pnpn* blocking structure and the implications of leakage currents in buried heterostructure lasers................................163
9.7 Optical characterisation: Collection NSOM...166
9.8 Summary..171
9.9 References..172

10. Conclusions and details of continuing studies...174

11. Appendices

11.1 SiC wafer cleaning techniques....179

11.2 Planar quantum well laser structures....180

11.3 Gaussian curve fitting - Vertical transverse optical cross-section of operating Control QW laser....182

Chapter 1
Introduction

As the technology applied in modern electronics rapidly progresses, new semiconductor materials and their application in increasingly complex devices are continually developing. In order to increase operating speeds, electronic devices are decreasing in size into the nano-regime where the overall device properties are dominated by the quantum mechanical characteristics of confined structures, instead of previously being characterised by the bulk properties of the constituent components of the device. The development of nanotechnology therefore requires the simultaneous development of characterisation techniques, particularly in respect to their resolution. Classical macroscopic characterisation techniques typically measure the overall properties of a device, whereas analysis techniques which probe devices at the micron scale are well known and heavily used. However, the characterisation and development of quantum structures ultimately requires the structural, electronic and chemical properties to be probed on the nano scale.

Different microscopy techniques have been developed in pursuit of the demands of increased resolution, leading to the advent of the first serial scanning imaging technique, the scanning tunnelling microscope (STM)[1,2], followed by a host of related proximinal probe techniques encompassed within the field of scanning probe microscopy (SPM). The various SPM techniques exploit a spectrum of different probe-sample interaction mechanisms to characterise a plethora of properties on the nano-scale. The near-field scanning optical microscope (NSOM) utilises scanning proximinal probe technology to image a sample using an optical field with nano-scale lateral resolution, thus overcoming the classical resolution limit of far-field microscopy (i.e. diffraction)[3].

The study of the interaction of a sample with light forms the oldest and most used analysis technique available. The optical properties of a sample can provide information regarding a wealth of characteristics including the surface morphology, refractive index distribution, polarization properties, and electronic structure[4]. Optical interactions are highly favoured for analytical techniques because as well as giving a

wealth of information they are inherently non-destructive, unlike many other techniques.

The high lateral resolution of NSOM is a consequence of the use of a sub-wavelength aperture within the imaging process, forcing light to interact in the highly confined near-field regime[5,6]. By interacting a sample with the evanescent field of a sub-wavelength aperture, the optical properties of a sample can be characterised on the nano-scale with similar approaches to those used in traditional far-field studies. Thus the powerful optical characterisation techniques are transposed into the sub-wavelength resolution range.

The work carried out within this thesis aims to exploit the near-field of NSOM in order to characterise a variety of semiconductor device systems, and extend specific analysis to the generation and mobility of charge carriers at the surface of structures and at buried interfaces. To do this a detailed understanding of the specific technologies and their corresponding mechanisms is required, the basic considerations are described briefly within the following sections.

1.1 Near-field photocurrent microscopy

Optical fields are also used in the analysis of the electronic properties of fabricated semiconductor devices via the optical stimulation of charge carriers within the device structure, and subsequent measurement of the intensity of the photo-generated current at the devices external electrical contacts. The photo-stimulated current is sensitive to the electronic structure of the sample under analysis, thus the local photo-generation of charge carriers probes the lateral variation in sample properties. This has traditionally been performed in the far-field regime by the technique of optical beam induced current (OBIC)[7]. To increase the lateral resolution of this imaging mechanism, the technique is transposed into the highly confined regime of the optical near-field by near-field photocurrent microscopy. This is a potentially invaluable technique that has previously received limited investigation[8] due to the inherent difficulties associated with its implementation. The theoretical foundations of near-field induced photocurrents are discussed within chapter 5 and the experimental development and implementation of this imaging mechanism are addressed in chapter 6.

1.2 Metal - Silicon carbide contacts

Silicon carbide (SiC) is a highly researched semiconductor by virtue of its high stability with temperature and operating powers, thus making it suitable for applications beyond the scope of silicon based devices. However, the implementation of SiC based devices is dependent upon the successful formation of stable metal contacts, and this is an area which requires further optimisation[9]. Nickel has been identified as a suitable candidate, and is thus researched in consideration for both ohmic and Schottky contact types. Near-field analysis techniques are applied within this investigation to the buried Ni-SiC Schottky interface, the theoretical aspects of which are discussed in chapter 3. Photocurrent imaging is sensitive to buried interface properties by optically probing directly through the thin Ni top contact by exploiting internal photoemission (IPE)[10], and detecting the photo-stimulated current of the interface at the external device contacts. The results of this investigation are the topic of chapter 7.

1.3 Quantum well laser diodes and multi-quantum barrier reflectors

GaInP / AlGaInP based quantum well lasers operating at the 630nm wavelength are highly sought for several applications, but suffer from the thermally activated loss of electrons from the active region, thus reducing the efficiency of achieving a population inversion to sustain stimulated emission[11]. The band-offset determines the active region confinement and it has been shown theoretically that these can be increased by the inclusion of a multi-quantum barrier (MQB) super lattice within the *p*-type cladding layers, adjacent to the active region[12], as discussed within chapter 4. Experimentally the band-offset enhancement is rarely successfully implemented within such devices, primarily as a consequence of inaccuracies in the growth of the MQB super-lattice and the complexity of the electronic band structure in such systems[11]. The near-field photocurrent imaging mechanism is sensitive to the electronic properties of a device, and is applied in the analysis of MQB's and their effectiveness in increasing electronic confinement to the active region, the results of which are discussed in chapter 8.

1.4 Buried heterostructure multi-quantum well lasers

The near-field imaging mechanisms are similarly applied in the investigation of buried heterostructure multi-quantum well (BH-MQW) lasers, used primarily in

telecommunications. The objective of the buried heterostructure is to channel injected charge carriers efficiently to the MQW active region for stimulated emission, and to optically emit at the fundamental mode by confining (waveguiding) the stimulated radiation[13] (chapter 4). Near-field characterisation techniques are applied to the output of the operating device, and in the analysis of the electronic properties when un-biased, the results of which are considered in detail within chapter 9.

1.5 Outline of thesis

The thesis reviews the origins and fundamental theory of NSOM that lead to its super-resolution capabilities in defeating the classical diffraction limited resolution of far-field imaging within chapter 2. In order to facilitate the interpretation of data, the fundamental principles of the Schottky diode and laser diode samples investigated are then introduced within chapters 3 and 4. This study primarily focuses upon the use of near-field photocurrent imaging as an analysis tool, and thus its theoretical treatment and application in the characterisation of such samples is considered in chapter 5. The key experimental developments and procedures are then addressed within chapter 6, particularly focussing upon the amplification/detection scheme implemented during this work to detect the sub-pico amp photocurrents. The photocurrent imaging capability was initially developed using the Ni-SiC Schottky diode sample. Specific samples were prepared and analysed simultaneously as the perfecting of the photocurrent imaging capability. Therefore the results of the investigation of Ni-SiC Schottky diodes are then addressed in detail within chapter 7. The near-field analysis techniques are subsequently applied in the characterisation of MQB and BH-MQW laser diode structures, the results of which are presented an analysed in chapters 8 and 9. The work is finally concluded within chapter 10, and the continuation of these studies is discussed.

1.6 References

[1] G. Binnig, H. Rohrer, *Helv. Phys. Actua,* **55,** 726 (1982)

[2] G. Binnig, H. Rohrer, C. Gerber, E. Weibel, *Phys. Rev. Lett.* **49,** 57 (1982)

[3] E. Abbe, *Archiv. Mikros. Anat.* **9,** 413 (1873)

[4] M.A. Paesler, P.J. Moyer, *Near-field optics*, (Wiley int., Third Ed., 1996)

[5] E.H. Synge, *Phil. Mag.* **6,** 356 (1928)

---

[6] E.H. Synge, *Phil. Mag.* **13**, 297 (1932)

[7] S.M. Lindsay, *Phys. Stat. Sol.* A **53**, 311 (1979)

[8] . Karrai, G. Kolb, G. Abstreiter, A. Schmeller, *Ultramicroscopy* **61**, 299 (1995)

[9] B. Pecz, *Appl. Surf. Sci.* **184**, 287 (2001)

[10] R. Williams, *Phys. Rev.* **140**, A569 (1965)

[11] K.S. Teng, M. Brown, A. Kestle, P. Smowton, P. Blood, S. Pinches, P.A. Mawby, S.P. Wilks, *Appl. Surf. Sci.*, **190**, 284 (2002)

[12] K. Iga, H. Uenohara, F. Koyama, *Electron. Lett.* **22**, 1008 (1986)

[13] M. Fukuda, *Optical semiconductor Devices*, (Wiley, 1999)

Chapter 2

Theory: Near-field optics and scanning microscopy

2.1 Conventional microscopy and resolution

Optical microscopy techniques have a long history of development and are widely applicable in a broad spectrum of scientific applications due to the powerful optical contrast mechanisms available. Spectroscopic capabilities, high temporal resolution, and polarization properties are enormously informative in many applications. Coupled with this is the non-destructive nature of the radiation used and the variety of environments possible. The combination of such properties makes optical microscopy a very useful technique. There is however one major drawback which is related to the ultimate spatial resolution attainable by conventional (far-field) optics. The German physicist Abbe[1] used diffraction theory to predict the existence of a theoretical resolution limit. For an objective lens of numerical aperture NA, the resolution is approximately half the wavelength λ, of the light employed. It was subsequently expressed concisely by Lord Rayleigh in the relation known as the Rayleigh criterion, equation (2.1), which states that two point objects may be resolved only if the distance r between them is greater than a quantity involving the wavelength, λ, of the light used, the refractive index, n, of the medium, and the semi-angle of aperture, θ, of the objective lens used.

$$r \geq \frac{1.22\lambda}{2n\sin(\theta)} \tag{2.1}$$

The criterion was established assuming propagating waves and intimately ties the ultimate resolution of far-field microscopes to the wavelength of light used. Improvements in resolution, i.e. decreases in r, are achieved by increasing the aperture angle of the microscope and by working in very high index materials, as in immersion microscopy, however the increase in resolution is only small. Optical resolution is further improved by using light of a shorter wavelength. However, when UV and shorter wavelength photons are used, restrictive problems arise due to the absorption of such wavelengths by atmospheric gasses, liquids, and many materials used in conventional optics. The most dramatic gain in resolution is achieved by moving away from optics, with the use of propagating electrons, as in electron

microscopy[2]; however samples must be conducting or coated with a conducting layer, and are significantly altered by the imaging process.

2.2 The development of NSOM

The need to overcome the diffraction limited resolution of optical microscopy led to the conception of near-field scanning optical microscopy, NSOM. In 1928 Synge proposed the concept of the near-field scanning optical microscope in an exchange of letters with Einstein[3,4,5]. Synge proposed an optical imaging technique that would defeat diffraction limited resolution through the use of a tiny light source formed by illuminating a sub-wavelength diameter aperture in a conducting metal screen, as represented in Figure 2.1. The light, incident from the rear of the screen, is laterally restricted by the dimensions of the aperture and a confined field exists within and near the front of the aperture, extending approximately one aperture diameter away. This is known as the near-field region.

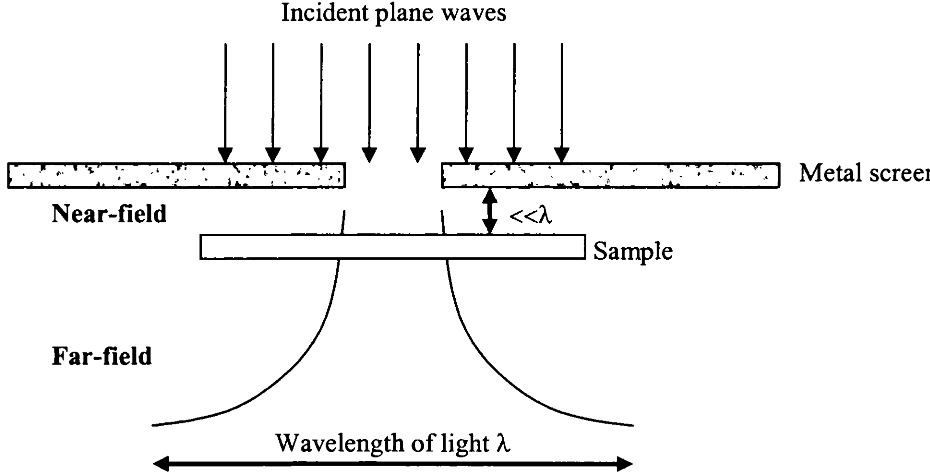

Figure 2.1 Schematic representation of Synge's proposed method of achieving sub-diffraction limited optical resolution. An optical field is confined by a sub-wavelength aperture in a metal screen. By positioning a sample in close proximity to the aperture (within the near-field region) it can be optically probed in sub-wavelength regions.

By positioning a sample in front of the aperture within this near-field region, only the area of the sample directly beneath the aperture is illuminated, allowing optical image formation by raster scanning of the sample. Thus the optical properties of the sample are probed on a sub-wavelength scale. Synge accurately described current near-field scanning optical microscopes more than fifty years before they were technologically possible. He suggested that the realization of near-field microscopes would require

nanometric position control, and sharpened glass probes with vacuum evaporated opaque coatings to confine the optical field to a sub-wavelength aperture at the apex.

The feasibility of the proposals of Synge were first confirmed theoretically by the work of Bethe[6], who addressed the passage of light through a sub-wavelength diameter hole in an infinitely thin perfectly conductive screen. Prior to the work of Bethe, the interaction of light with small holes (diameter > λ) was described using conventional diffraction methods, however this technique failed to accurately consider the boundary conditions at the aperture. This resulted in a small deficiency for large apertures, and becomes increasingly important as the aperture size is decreased. Bethe overcame this limitation by satisfying Maxwell's equations and the boundary conditions with the introduction of fictitious magnetic surface charges and currents in the aperture region[6]. However, in Bethe's original work the electric field in the aperture was not continuous due to an error in the magnetic current density expression. This was later corrected by Bouwkamp[7,8,9], satisfying the expressions for the field components just above the aperture in the near-field region.

The near-field concepts proposed by Synge were later reaffirmed many times in experiments carried out independently from 1950 onwards[10,11,12,13,14]. All corroborated Synge's original configuration and each a step closer to the realisation of near-field microscopes. Commonly the authors concluded that the ultimate resolution is determined by the effective diameter of the source and that sub-wavelength distances could be resolved with the fabrication of sufficiently small sources. It was not until 1972 that the near-field method of sub-wavelength resolved imaging was conclusively demonstrated. Ash and Nichols used microwave radiation (λ = 3cm) and a 0.5mm diameter aperture to image periodic features in a metal grating with λ/60 spatial resolution[15]. These results illustrated the feasibility of Synge's original proposal and prompted renewed interest in scanning near-field optical microscopy using visible light. However it took another decade to overcome the difficulties presented by NSOM using visible light, i.e. the restrictions imposed on aperture size and probe-sample positioning by the shorter wavelengths of visible light

2.3 STM and the realisation of NSOM at visible wavelengths

In 1981 Gerd Binnig and Heinrich Rohrer[16,17] developed the scanning tunnelling microscope STM, which utilised piezoelectric position control to probe sample surface topographic and electronic properties. The STM essentially utilises a sharp metallic tip, which is ideally a single atom sharp at the apex, to probe conducting or semiconducting samples. An electric potential is applied across the tip and sample and the tip is approached to a few angstroms from the sample surface. Electrons quantum mechanically tunnel between electron states within the sharp tip and sample beneath, and a high resolution tunnelling map can be constructed by raster scanning. It was not until the advent of the STM that it became possible to utilise technologies to control the position of an optical aperture and, via raster-scanning a sample in its near-field, construct an optical image pixel by pixel. In fact the development of the STM prompted world wide research into similar proximinal probe techniques which essentially differ only in the nature of the measurable nanoscale interaction, and hence the field of Scanning Probe Microscopy (SPM) was born.

The first near-field scanning optical microscopes at visible wavelengths were subsequently implemented almost simultaneously during 1982 at IBM Zurich (where the STM originated) and at Cornell University. D. Pohl *et al*[18,19] at Zurich clearly demonstrated sub-wavelength resolution by imaging across a step of nanometer size. Independently at Cornell University A. Lewis *et al*[20,21] reported sub-wavelength resolution and near-field imaging of a test grating at a resolution of 150nm. The almost immediate implementation of visible light NSOM upon the advent of piezoelectric positioning technology indicated that the theoretical understanding of near-field optics was ahead of the technological capabilities, as previously predicted by Synge[3,4].

2.4 The optical imaging process

Prior to the implementation of near-field scanning optical microscopy, optical imaging had been performed by projecting photons from a source, on to the sample under analysis, and capturing the reflected light using a detector. The reflection trajectory and number of photons is dependent upon the sample properties, thus information about the sample is projected onto the detector target and an image of the sample is collected. The process of imaging aims to closely measure the sample

properties however the sample is a 3-dimensional object, whereas an image is usually a 2-dimensional mapping of the intensity of some property of the sample. The imaging process is thus more accurately described by considering the light field intensity associated with the sample, and the corresponding intensity in the image plane. The light field over a sample is related to the sample structure by Maxwell equations which link the electron densities inside a sample to its external electromagnetic field[22]. Oscillating charges and currents within a sample induce electromagnetic field variations that propagate into free space, and by the principle of continuity, the spatial field distribution very close to the sample surface will reproduce the charge density and current distributions of the sample surface. This implies that the field very close to a sample objects surface can vary over extremely small distances, far less than a wavelength. This leads to the distinguishing of the two field regimes, the near-field that exists within a few nanometers of the sample surface, and the far-field which extends from the near-field region to infinity. The near-field contains both propagating components and non-homogenous wave components confined to the sample surface and exponentially damped away from the surface. The near-field properties are intimately tied to the sample material near the surface and thus the near-field cannot exist in free-space. Note, the propagating and non-propagating components are complementary and cannot exist in isolation, thus if the non-propagating components are perturbed the propagating components are similarly modified.

2.4.1 Evanescent waves

The non-propagating components of the near-field, tied to the sample surface, are known as evanescent waves and were originally observed by Newton when studying the chromatic effects of light. When attempting to frustrate the total internal reflection of an optical beam incident upon a prism surface by contacting it with a second prism of convex surface, as shown in Figure 2.2, Newton expected to observe the transmission of light at the point of contact[22]. The cross-sectional area of the transmitted beam was however greater than the contact area of the two prisms. Newton attributed this to the velocity of the light particles carrying them through the surface of the first prism, prior to their re-attraction by the matter of the second prism, a simple explanation not entirely dissimilar to the modern near-field reasoning.

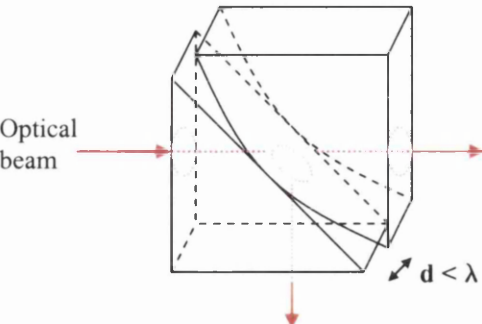

Figure 2.2 The total internal reflection of a light beam within a prism is disrupted by the interaction of a second prism when approached within a distance of less than a wavelength. The optical intensity transmitted through the second prism is an exponential function of the distance, d.

This is explained by the continuity of boundary conditions across the prism surface, the field exists inside the prism thus must also exist outside of the prism, propagating along the surface but attenuated perpendicularly away from the surface. Thus if a suitable dielectric material, such as the second prism, is immersed in an evanescent field, a conversion into a propagating field occurs in respect to the continuity conditions at the interface, this is known as the photon tunnelling effect. This discussion of Newton's original experiment demonstrates the presence and interaction of the near-field (evanescent waves) by a macroscopic experiment; however it does not describe the interactions involved in the imaging process of the nanoscale near-field probe which must incorporate diffraction into the conversion process.

2.4.2 Fine structure and evanescent fields

The simplest description of the interaction between a nanoscale diffracting object, such as an NSOM probe, and an evanescent field assumes that the probe tip behaves as a dipole, point scatterer[23]. Placing the dipole into the non-radiating evanescent field causes it to become excited, it then subsequently generates an electromagnetic field possessing both propagating and non-propagating components. The propagating components are thus transported away from the sample surface and can be detected by a remote (far-field) sensing element. This basic approach is generalised for extended objects by the theoretical work of Wolf and Nieto-Vesperinas[24] in the assumption that a light beam impinging on a limited object will be always converted into propagating and evanescent fields. This is applicable for both propagating and evanescent incident fields[22]. A limited object is one which possesses a sharp discontinuity, i.e. its

associated spatial Fourier spectrum is infinite and contains all spatial frequencies from zero to infinity. Limited objects include for example a metallic cluster, and a circular hole in an opaque screen. An example of an extended object is a metallic layer deposited upon a semiconductor substrate, which can be considered as a summation of small limited objects such as metallic grains. The Wolf-Nieto theorem is thus applicable to such a sample object characterised by fine structure with details smaller than $\lambda/2$, and a light beam impinging upon it will be converted into propagating components able to propagate through free space, and evanescent components confined at the sample surface. Propagating components are connected to the low spatial frequencies of the sample while evanescent components are characterised by the sample's high spatial frequencies[22]. Thus all sub-wavelength details of a sample are encompassed by the non-propagating evanescent modes, thus requiring the interaction of a near-field scattering source to release the sample's fine structure by conversion into propagating modes for detection by a remote sensing element.

A sample characterised by high spatial frequency will generate evanescent waves when illuminated with either an evanescent or propagating source. The resulting undetectable evanescent fields do not obey the Rayleigh criterion equation (2.1) and exhibit sub-wavelength spatial variations, which by reciprocity can be converted into propagating fields by a limited object. Note the evanescent field is converted by a limited object into evanescent and propagating components. The conversion process is linear and therefore the detectable propagating field is directly proportional to the Poynting vector at a certain point of the evanescent field. This allows the construction of a 2-dimensional image using a raster scanning mechanism to accurately reproduce the localised variations of the evanescent field.

A non-propagating field can be mathematically described by equation (2.2) which incorporates the previously discussed characteristics.

$$U(x,y,z,t) = \underbrace{A(x,y,z)}_{\substack{\text{Field}\\ \text{amplitude}\\ \text{at } (x,y,z)}} \times \underbrace{\exp[-i(k_x x + k_y y)]}_{\substack{\text{Wave propagation}\\ \text{term in the } (x,y)\\ \text{plane}}} \times \underbrace{\exp(-\alpha z)}_{\substack{\text{Attenuation}\\ \text{along the}\\ z\text{-axis}}} \times \underbrace{\exp(i\omega t)}_{\substack{\text{Time}\\ \text{dependence}\\ \text{of the field}}} \qquad \textbf{(2.2)}$$

The field propagates in the (x,y) plane i.e. along the sample surface, but is attenuated exponentially in a direction perpendicular to the surface (z), the decay coefficient α is a function of the materials properties and spatial structure. The finer the surface structure the greater the magnitude of α, and thus the greater the field attenuation and confinement to the surface.

2.4.3 Near-field resolution and Heisenberg's uncertainty principle

When considering the resolution capabilities of near-field imaging it is useful to consider the Heisenberg uncertainty principle, which can be seen as a generalisation of the Rayleigh criterion encompassing both propagating and evanescent fields[25].

The optical image of an object can be represented by a field distribution $U(x,y,z)$ at a point $P(x,y,z)$, as shown in Figure 2.3. It is characterised by its amplitude $A(x,y,z)$ and propagation vector $\boldsymbol{k}(x,y,z)$, where the magnitude of $\boldsymbol{k}$ is given by $|\boldsymbol{k}| = 2\pi n/\lambda$, when propagating within a medium of index n.

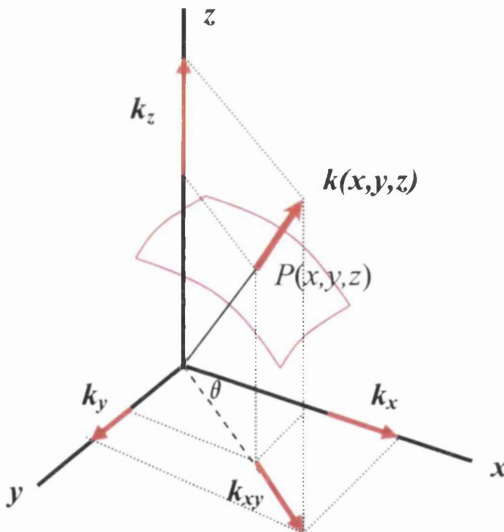

Figure 2.3 Representation of a section of an electromagnetic field, which at a point $P(x,y,z)$ is characterised by an amplitude and propagation vector $k(x,y,z)$.

The field contains the information about the sample object and thus exhibits local variations, implying the probability that two separate points will have different intensities. The ultimate resolution of an imaging system is determined by the smallest separation between two discernable points, thus it is important to consider the uncertainty in the measurement of the position of a point P, i.e. Δx, Δy, Δz, and

the uncertainty in the measurement of the propagation vector Δk_x, Δk_y, Δk_z. Applying the Heisenberg uncertainty principle in the *x*-direction (note, the same argument is applicable in the *y*-direction)[25,26]

$$\Delta x \times \Delta k_x \geq 1 \quad \textbf{(2.3)}$$

The variable range of k_x is $\Delta k_x = 2k_x^{max}$ where k_x^{max} is the largest value that k_x can take, therefore

$$\Delta x \geq 1 / (2\, k_x) \quad \textbf{(2.4)}$$

Thus for a rapidly varying field Δx is very small and the light is strongly scattered i.e. Δk_x becomes large, implying that a strongly perturbed field is strongly scattered and diffracted[25]. The smallest resolvable feature is therefore determined by the largest value that can be expected for k_x, which is the projection of the propagation vector $\boldsymbol{k}$ in the *x*-direction, as given by

$$k_x = |\boldsymbol{k}| \sin\theta \quad \textbf{(2.5)}$$

Where θ is the projection angle of $\boldsymbol{k}$ from the *x*-axis, and k_x is always smaller than the modulus of the $\boldsymbol{k}$ vector. The uncertainty relation (2.4) then becomes

$$\Delta x \geq \lambda / (2n.\sin\theta) \geq \lambda / 2n \quad \textbf{(2.6)}$$

reproducing the classical Abbe limit of resolution (equation (2.1)), however if the *k*-components can take complex values $|k_x|$ is no longer limited by $|\boldsymbol{k}|$ and must only satisfy

$$|k_x| = (\, |k|^2 - (k_z)^2 - (k_y)^2\,)^{1/2} \quad \textbf{(2.7)}$$

therefore, k_x can take large values if and only if either k_y or k_z are imaginary. Thus returning the definition of an evanescent field, given in equation (2.2), for the case of k_x and k_y real, with k_z complex. The Heisenberg uncertainty relation therefore implies that an electromagnetic field can vary over sub-wavelength dimensions, providing the propagation vector $\boldsymbol{k}$ is 2-dimensional in real-space and the field is confined to the samples surface, i.e. by its third complex component.

2.4.4 Modelling near-field optics

The modelling of near-field optics is highly complex and must account for the actual geometries of real NSOM probes and the finite conductivity of the metal cladding layer, which can affect the resolution of a particular probe. The theoretical modelling of the field of an NSOM probe must also incorporate the influence of a closely approached sample, which can strongly influence the power transmission a probe.

Ideally this requires the exact solution of Maxwell's equations, however analytical solutions are not available and approximate methods must be employed.

A very important technique in understanding the optical interactions and super-resolution of a near-field microscope has been the multiple multipole method which is based on matching boundary conditions at interfaces. This has been extensively used by Novotny *et al*[27,28] to accurately model in two and three dimensions the field distribution and radiation properties for specific geometries of metal clad, tapered dielectric probes, and nearby sample. The theoretical results have proved important in understanding and interpreting the optical images of NSOM, particularly in addressing the complex and controversial issue of the coupling of the topographic image, i.e. probe *z*-motion, and optical image, which is addressed closely in sections 6.7 and 6.8.

2.5 The tapered optical fibre NSOM probe

The primary element of any scanning probe microscope is the probe itself which determines the quality of the images obtained, this holds true for NSOM. Many NSOM probe designs have been investigated to enhance optical signal levels and optimise lateral image resolution. The most commonly utilised and successful method is the aperture probe introduced by Betzig *et al*[29,30] which consists of a tapered optical fibre probe with a sub-wavelength diameter aperture at its apex. These are discussed here in some detail as such probes have been extensively employed in this work. Probes are fabricated by the highly reproducible process of heating a single-mode optical fibre in the beam of a focussed CO_2 laser, and pulling to a fine point using a pipette puller, the cone angle and tip diameter are controlled by the temperature and the pull rate. An extensive study of how pulling parameters affect taper angle, tip size and optical throughput was conducted by Valaskovic[31].

As light propagates along the probe towards the apex the diameter of the tip reduces, and once below the mode-field cut-off of the waveguide, light escapes from the sides of the fibre probe shaft preventing the formation of a well defined optical aperture. In order to increase the optical confinement of the probe and define a sub-wavelength aperture the sides of the probe are coated with an opaque metal by thermal evaporation. The deposition of a metal by evaporation is a line-of-sight process, thus

as the metal is evaporated vertically the probe is tilted away from the horizontal by 10-20^0 to leave an uncoated aperture at the apex. The probe is also rotated during this process to ensure an even metal coverage. For the application of visible wavelengths aluminium exhibits the shortest skin depth and thus requires a minimum thickness of metal coverage in order to provide optical confinement, typically a 50-100nm thick layer is used. Ideally a perfectly smooth uniform metal coating would be applied, however aluminium forms grains and thus the layer must be suitably thick to prevent the formation of pin-hole leaks which limit the optical resolution and photo-bleach the image.

The precise properties of a probe are highly dependent upon its geometric parameters, for a 50-100nm diameter aperture when performing illumination-mode NSOM, a laser of mW power is coupled into the probe fibre tail, the power at the aperture is typically of nW order[32]. The inefficiency of the probes is a consequence of the conversion from propagating to evanescent modes as the diameter in the taper region decreases. The lost light is either reflected back up the fibre or absorbed by the Al coating. Thermal absorption results in a local heating of the probe tip which can lead to catastrophic tip damage, thus limiting the operating power of a probe[33].

The tapered optical fibre probe has proved very successful in many diverse applications. However the requirement to enhance the optical intensity levels and tailor the probe for applications such as single molecule fluorescence detection, and spectroscopic imaging has led to the investigation of alternative probe designs. These include the localised plasmon resonance probe[34], attaching a fluorescent molecule at the apex of a NSOM tip[35], and using a laser diode as a direct NSOM source[36]. Recently perhaps the most promising configuration has been the apertureless-NSOM, which involves the focussing of an external optical source onto the apex of a sharp metal probe to enhance the field directly beneath the tip[37].

2.6 Probe–sample distance regulation

In order to implement the near-field interaction of the probe aperture and sample, the probe to sample separation must be maintained at a distance much less than the diameter of the probe aperture[29]. For an aperture diameter of 50nm a probe-sample separation of only a few nanometers is necessary. For the purpose of scanning a near-

field optical image, this separation must be constant throughout the scanning process, in particular to prevent a catastrophic collision occurring to the probe.

The most practical method of controlling tip-sample separation is to monitor the force interaction between the probe and sample, as utilised in an atomic force microscope (AFM)[38]. The AFM makes use of force variations normal to the sample surface that are dominated by attractive Van der Waals forces and repulsive interatomic forces[39]. The commonly used aperture-NSOM probe is constructed from an elongated tapered optical fibre with its axis oriented normal to the sample's surface. The presence of the long flexible optical fibre tail from the NSOM probe renders AFM-type normal force detection impractical. Instead, shear-force detection is employed to manage probe-sample separation, and was originally developed with NSOM in mind. The NSOM fibre probe is oscillated laterally, parallel to the samples surface, at its resonant frequency. Upon close approach of the sample surface shear-forces interact between probe and sample resulting in mechanical damping of the oscillation of the NSOM probe. The magnitude of this damping is used as a measure of probe-sample separation and is regulated for scanning. Early configurations relied upon optical detection schemes to monitor the probe oscillation[40,41,42], where a laser was focused onto the oscillating probe and the oscillation amplitude measured by differential interferometry or by measuring the oscillation in the specularly reflected light. However, the presence of this external light source so close to the probe aperture risks contamination of the near-field interaction between probe aperture and sample, and so a non-optical detection mechanism is preferable. Tuning forks offer a non-optical piezoelectric detection mechanism for probe-sample separation[43], and are currently the most commonly utilised method in near-field microscopes and used in this study.

2.6.1 Quartz tuning forks and force detection

Quartz tuning forks offer perhaps the most practical method of shear-force sensing currently available for NSOM application. Quartz is a piezoelectric material in which mechanical stress results in electric charge displacement that is picked up by electrical contact pads. The electrical contact configuration (see Figure 2.5) is designed to optimize charge pickup at the mechanical resonance of the tuning fork, when the prongs are oscillating in opposite directions at their maximum amplitude[44]. The contact pad arrangement is such that the piezoelectric charge displacement is always

directed from one pad to the other, coupling the two prongs of the tuning fork piezoelectrically. At resonance, f_0, the bending of the prongs is maximised, generating a piezoelectric current that oscillates with the prongs and is directly proportional to the oscillation amplitude, hence it is a direct measure of the shear-force interaction between the probe and sample. Figure 2.4 is a typical piezoelectric response of an oscillated tuning fork showing a sharp resonance to occur at approximately 95KHz, and high quality factor (Q). The Q-factor is defined as $Q = f_0 / \Delta f$, where Δf is the full frequency width at the half-maximum of the tuning fork resonant amplitude[44].

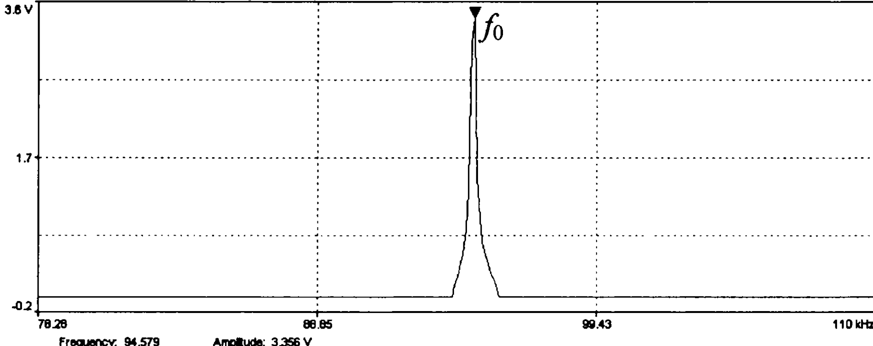

Figure 2.4 Frequency spectrum of a tuning fork–probe assembly, showing a typical oscillation response with a strong mechanical free-resonance featuring at approximately 95KHz. The tuning fork (probe) is driven at resonance (red arrow) and approached into shear-force feedback with the sample surface.

2.6.2 Shear-force feedback for distance regulation

The NSOM probe is an optical fibre that is tapered at the tip and clad in aluminium for optical confinement, to maximise throughput at the aperture. The optical fibre is then glued along the side of one prong of the tuning fork as shown in Figure 2.5. The other side of the tuning fork is mechanically oscillated by an external piezoceramic, known as a dither piezo, to excite mechanical resonance of the tuning fork-probe assembly. The oscillating probe-tuning fork generates a piezoelectric current proportional to the oscillation amplitude. The probe is approached normally to the sample and the oscillation is damped by shear-forces when the tip is within tens of nanometres of the surface. The damping is a measure of the probe–sample interaction force and is used to regulate the probe–sample distance separation. The piezoelectric current from the tuning fork is amplified by a transimpedance amplifier to an

oscillating voltage, and the amplitude or phase lag with respect to the oscillation signal is used to measure probe–sample interaction/separation using a lock-in detection scheme. The instruments utilised for the work within this thesis make use of the phase information to regulate distance.

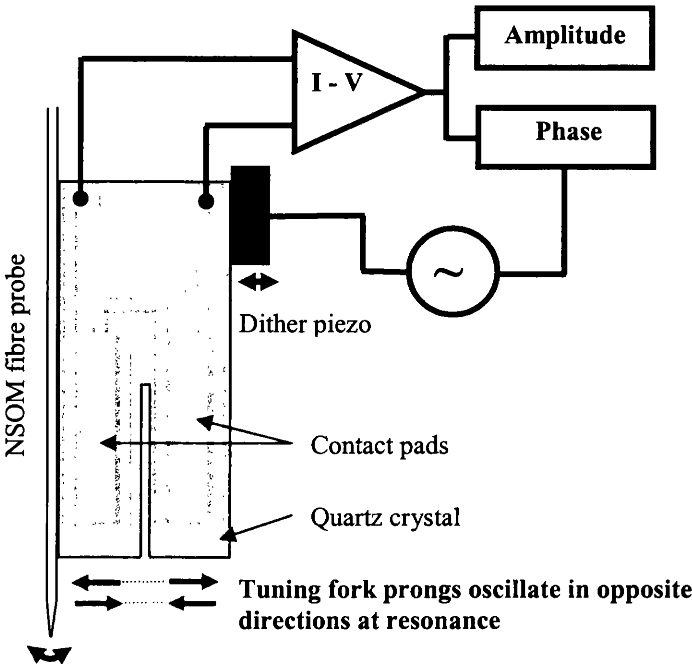

Figure 2.5 Schematic of a quartz tuning fork configured for shear-force detection, and the arrangement of the tuning fork electrical contacts. The tuning fork / NSOM probe are mechanically oscillated at resonance by an external dither piezoceramic. On close approach of a sample, shear-forces damp the oscillation, the magnitude of which is measured from the piezoelectric current of the tuning fork.

Shear-force feedback is widely used in NSOM; however the actual origin of the shear-force interaction remains an uncertainty. Viscous drag, van der Waals interactions, electrostatic and capillary forces were originally thought responsible[45]. Research has been conducted into the precise nature of the shear-force interaction, and from the very many approach experiments and combined shear-force and STM experiments, two proposed models have evolved. The first model applies strongly when NSOM is being performed under ambient conditions, a condensed fluid layer is assumed present over the sample surface and the shear-force interaction is dominated by viscous forces[46,47]. The degree and range of this interaction depend strongly on the humidity and how hydrophilic the sample[48]. When the probe is closer to the sample surface, and for large oscillation amplitudes, a second model applies. Known as the knocking model, the probe is in intermittent contact with the sample surface,

undergoing nonlinear bending, resulting in a drop in oscillation amplitude and an asymmetric resonance curve on approaching the sample. The degree of damping also depends on the tilt angle of the probe with respect to the sample, if the probe were exactly perpendicular to the surface; damping from the knocking mechanism would be minimal[49,50]. The overall shear-force interaction experienced by the NSOM probe is a combination of both mechanisms, the degree to which depend on the ambient conditions and tilt angle of the probe.

2.7 NSOM modes of operation

The super-resolution of the near-field imaging technique is achieved using a sequence of optical conversions between propagating and evanescent, non-propagating modes, as discussed earlier within this chapter. The direct proportionality of the field intensity during conversion processes allows the NSOM to be applied in a number of configurations, suited to different applications. This discussion concerns the primary operational configurations of the aperture-NSOM, as utilised for this study, which are schematically represented in Figure 2.6.

Figure 2.6(a) transmission-collection mode, shows the sample being illuminated from beneath and the transmitted light collected using the NSOM fibre probe. (b) Illumination-transmission uses the NSOM probe to locally illuminate the sample and collects the transmitted light using the transmission objective lens. (c) Illumination-reflection again uses the NSOM probe to locally illuminate the sample, but instead collects the reflected light using the reflection objective lens. Photocurrent NSOM (discussed in detail later) similarly uses the NSOM probe to locally illuminate a sample then detect the photocurrent response using external amplification. (d) Collection mode imaging of a self-radiating sample uses the NSOM probe to locally collect the light emanating from a sample, as used extensively in chapters 8 and 9 in the analysis of quantum well laser structures. (e) External illumination-collection uses the NSOM probe to locally detect reflected light from an external illumination source. Finally (f) Illumination-collection uses a beam splitter to optically pump the probe aperture with an illumination source, and simultaneously collect the light reflected from the sample.

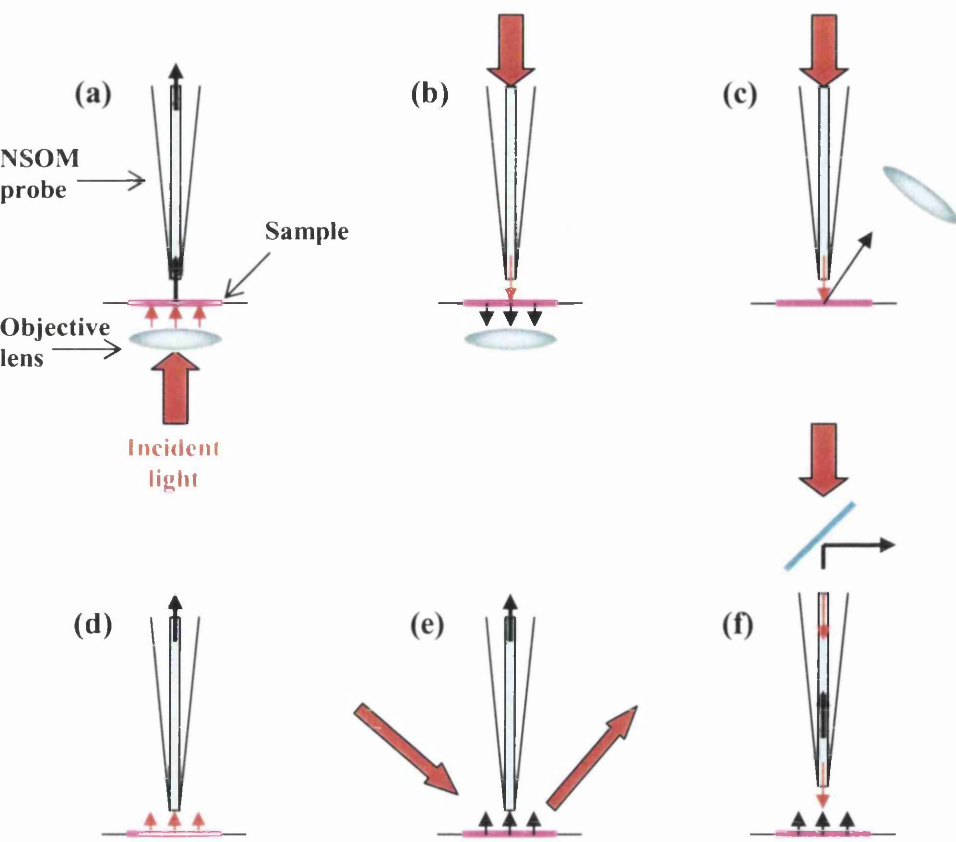

Figure 2.6 Schematic representations of the operational modes of the aperture-NSOM. **(a)** Transmission-collection, **(b)** Illumination-transmission, **(c)** Illumination-reflection, **(d)** Collection mode (self-radiating sample), **(e)** Collection (external illumination), and **(f)** Illumination-collection.

2.8 Summary

The advent of NSOM marked a major advancement in the field of microscopy and optical microscopy in particular. Sub-wavelength resolution optical imaging has an historical development of almost a century, but was only physically implemented upon the advent of the STM and accompanying technologies necessary for the serial scanning of a proximinal probe. These include piezoelectric position control, and anti-vibration technology which is essential in maintaining a probe-sample separation of nanometer order, and especially in preserving the integrity of the near-field aperture. The theoretical foundations of NSOM have been discussed, focussing on the nature of the near-field, the properties exploited by the near-field microscope, and the origins of its sub-wavelength resolution. The design and preparation of the fundamental element of the aperture-NSOM is discussed, the probe and corresponding sub-wavelength diameter aperture which determines the resolution of

the instrument and overall quality of the images obtained. Finally the implementation of shear-force microscopy has also been addressed due the importance of the simultaneously acquired topographic imaging mechanism, which is a major strength of NSOM imaging and discussed throughout the results sections presented in this thesis.

2.9 References

[1] E. Abbe, *Archiv. Mikros. Anat.* **9**, 413 (1873)

[2] L. Reimer, *Scanning electron microscopy*, (Springer, Berlin, 1985)

[3] E.H. Synge, *Phil. Mag.* **6**, 356 (1928)

[4] E.H. Synge, *Phil. Mag.* **13**, 297 (1932)

[5] D. McMullen, *Proceedings RMS* **25**, 127 (1990)

[6] H.A. Bethe, *Phys. Rev.* **66** (7,8), 163 (1944)

[7] C.J. Bouwkamp, *Philips Res. Rep.* **5**, 321 (1950)

[8] C.J. Bouwkamp, *Philips Res. Rep.* **66**, 163 (1950)

[9] C.J. Bouwkamp, *Rep, Prog. Phys.* **17**, 35 (1954)

[10] R.J. Moon, *Science* **112**, 389 (1950)

[11] F. Roberts, J.Z. Young, *Instr. Electr. Engrs.* **1348**, 382 (1952)

[12] H.H. Patee, *J. Opt. Soc. Am.* **43**, 69 (1953)

[13] J.A. O'Keefe, *J. Opt. Soc. Am.* **46**, 359 (1956)

[14] A.V.J. Baez, *J. Opt. Soc. Am.* **46**, 901 (1956)

[15] E.A. Ash, G. Nicholls, *Nature*, **237**, 510 (1972)

[16] G. Binnig, H. Rohrer, *Helv. Phys. Actua,* **55**, 726 (1982)

[17] G. Binnig, H. Rohrer, C. Gerber, E. Weibel, *Phys. Rev. Lett.* **49**, 57 (1982)

[18] D.W. Pohl, W. Denk, M. Lanz, *Appl. Phys. Lett.* **44** (7), 651 (1984)

[19] U. Durig, D.W. Pohl, F. Rohner, *J. Appl. Phys.* **59** (10), 3318 (1986)

[20] A. Lewis, M. Isaacson, A. Murray, A. Harootunian, *Biophys. J.* **41**, 405a (1983)

[21] E. Betzig, A. Lewis, A. Harootunian, M. Isaacson, E. Kratschmer, *Biophys. J.* **49**, 269 (1986)

[22] D. Courjon, C. Bainier, *Rep. Prog. Phys.* **57**, 989 (1994)

[23] M.A. Paesler, P.J. Moyer, *Near-field optics*, (Wiley int., Third Ed., 1996)

[24] E. Wolf, M. Nieto-Vesperinas, *J. Opt. Soc. Am.* **2**, 886 (1985)

[25] M. Born, E. Wolf, *Principles of Optics*, (2nd Ed., Pergamon Press, 1964)

[26] J.M. Vigoureux, D. Courjon, *Appl. Opt.*, **31**, 3170 (1992)

[27] L. Novotny, D.W. Pohl, P. Regli, *Ultramicroscopy*, **57**, 180 (1995)

[28] L. Novotny, D.W. Pohl, B. Hecht, *Ultramicroscopy*, **61**, 1 (1995)

[29] E. Betzig, J.K. Trautman, T.D. Harris, J.S. Weiner, R.L. Kostelak, *Science* **251**, 1468 (1991)

[30] E. Betzig, J.K. Trautman, *Science*, **257**, 189 (1992)

[31] G.A. Valaskovic, M. Holton, G.H. Morrison, *Appl. Opt.* **34**, 1215 (1995)

[32] R.C. Dunn, *Chem. Rev.* **99**, 2891 (1999)

[33] Ch. Lienau, A. Richter, T. Elsaesser, *Appl. Phys. Lett.* **69** (3), 325 (1996)

[34] M. Specht, J.D. Pedarnig, W.M. Heckl, T.W. Hansch, *Phys. Rev. Lett.* **68**, 467 (1992)

[35] R. Kopelman, W. Tan, *Appl. Spec. Rev.* **29**, 39 (1994)

[36] S. Heisig, O. Rudow, E. Oesterschulze, *Appl. Phys. Lett.* **77**, 1071 (2000)

[37] F. Zenhausern, Y. Martin, H.K. Wichramasinghe, *Science*, **269**, 1083 (1995)

[38] G. Binnig, C.F. Quate, Ch. Gerber, *Phys. Rev. Lett.* **56** (9), 930 (1986)

[39] D. Sarid, *Scanning force microscopy*, (Oxford University, New York 1991)

[40] R. Toledo-Crow, P.C. Yang, Y. Chen, M. Vaez-Iravani, *Appl. Phys. Lett.* **60** (24), 2957 (1992)

[41] E. Betzig, P.L. Finn, J.S. Weiner, *Appl. Phys. Lett.* **60** (20), 2484 (1992)

[42] R.D. Grober, T.D. Harris, J.K. Trautman, E. Betzig, *Rev. Sci. Instrum.* **65**, 626 (1994)

[43] K. Karrai, R.D. Grober, *Appl. Phys. Lett.* **66** (14), 1842 (1995)

[44] W.H.J. Rensen, *Tuning fork tunes*, (2002)

[45] J.W.P. Hsu, *Mat. Sci. and Eng.* **33** (2001)

[46] F.F. Froehlich, T.D. Milster, *Appl. Phys. Lett.* **70** (12), 1500 (1997)

[47] J.U. Schmidt, H. Bergander, L.M. Eng, *J. Appl. Phys.* **87** (6), 3108 (2000)

[48] T. Okajima, S. Hirotsu, *Appl. Phys. Lett.* **71** (4), 545 (1997)

[49] M.J.Gregor, P.G. Blome, J. Schofer, R.G. Ulbrich, *Appl. Phys. Lett.* **68** (3), 307 (1996)

[50] K. Hsu, L.A. Gheber, *Rev. Sci. Instrum.* **70** (9), 3609 (1999)

Chapter 3

Theory: Metal-semiconductor contacts

The contacts formed between metals and semiconductors can be characterised into two distinct classifications based on their electrical properties, i.e. their current-voltage characteristics. Contacts with linear current-voltage characteristics are called ohmic contacts and ideally possess very low contact resistance, they are necessary in forming electrical connections with semiconductor devices. Contacts displaying rectifying properties are known as Schottky contacts as a consequence of the Schottky barrier formed at the metal-semiconductor interface, and are critical in forming voltage dependent devices such as diodes and transistors. Both types of contacts are discussed within this chapter but emphasis is placed upon Schottky contacts as they can be studied by near-field photocurrent mechanisms (see chapter 5) and their investigation forms one of the major results chapters of this thesis (see chapter 7).

3.1 Schottky barrier formation

Consider the situation in Figure 3.1 where a metal of work function ϕ_m and an *n*-type semiconductor of work function ϕ_s, such that $\phi_m > \phi_s$, are electrically neutral and separated in space prior to contact formation. The Fermi levels of the metal and semiconductor are denoted E_F^m and E_F^s respectively, and in the case of the semiconductor is dependant upon the doping. The work function is the separation in energy (in electron-volts, eV) between the Fermi level and the vacuum level.

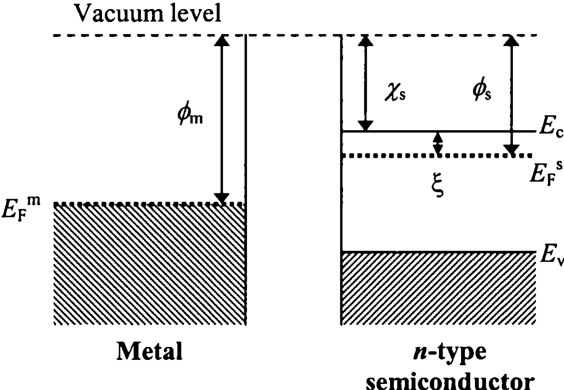

Figure 3.1 Energy-band diagram of a metal and semiconductor separated in space, prior to contact formation, with the vacuum levels aligned.

Within the semiconductor the electron affinity, denoted χ (eV), is the minimum energy required to release an electron from the semiconductor, such that $\phi_s = \chi_s + \xi$ where ξ is the position of the Fermi level E_F^s relative to the conduction band edge.

When combining a metal and semiconductor to form a contact, that contact may be described as Schottky in characteristic if a barrier exists to electron flow across the junction between the two materials. To understand this formation many theories have been developed to explain the existence and degree of barrier between the semiconductor and metal. Described here are two of the main models that have been successful in understanding the physics of these interfaces. For more detailed and extensive theories please refer to Rhoderick and Williams [1].

3.1.1 Schottky-Mott theory

The Schottky[2]-Mott theory of barrier formation assumes the flat-band condition for the *n*-type semiconductor implying that no field exists within the semiconductor. Physically this implies that the semiconductor terminates at the surface without distortion of the electronic energy levels and hence no electronic states exist at the surface[3]. In the formation of a contact the metal and semiconductor, isolated in Figure 3.1, are brought together and electrons pass from the semiconductor into the metal forcing the two Fermi levels into equilibrium, i.e. $E_F^m = E_F^s$, as shown in Figure 3.2(a). This accumulates a negative charge at the surface of the metal which is balanced by a net positive charge at the semiconductor surface establishing a dipole field that opposes further electron flow at equilibrium.

The negative charge at the surface of the metal consists of extra conduction electrons that are contained within the Thomas-Fermi screening distance (~0.5Å) of the interface, labelled as the electron accumulation region in Figure 3.2(b)[1,4]. The semiconductor is *n*-type and the positive charge near its surface is due to positive donor ions that are uncompensated by the reduction in conduction electrons within the semiconductor at the interface. The donor ion concentration in the semiconductor is many orders of magnitude less than the electron concentration of the metal, therefore the uncompensated donor ions occupy a depleted layer of substantial thickness, *w*,

similarly as the depletion layers seen in *pn*-junction formation, as shown in Figure 3.2(b).

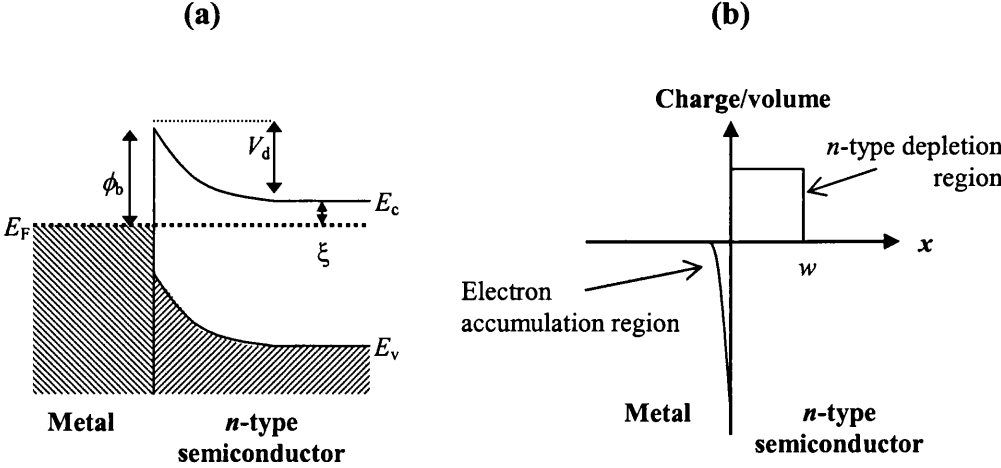

Figure 3.2 (a) An ideal Schottky contact, and **(b)** the charge distribution about a metal-semiconductor Schottky junction.

The depletion within the semiconductor and alignment of the Fermi levels leads to a parabolic band-bending of the semiconductor energy-bands at the interface and the establishment of a barrier ϕ_b, as shown in Figure 3.2(a), of height measured relative to the Fermi level:

$$\phi_b = \phi_m - \chi_s \tag{3.1}$$

this is known as the Schottky-Mott limit. The barrier, ϕ_b, must be overcome by electrons from within the metal in order to penetrate the semiconductor by acquiring ϕ_b eV of energy. Electrons within the conduction band of the semiconductor face a barrier of V_d known as the diffusion potential to overcome in order to penetrate the metal, however this barrier is bias dependant whereas ϕ_b is not, which leads to the rectifying characteristics of Schottky junctions.

The ideal situation described by Schottky and Mott is never realised in practice usually due to the presence of a thin insulating layer of oxide (~10-20Å thick) on the surface of the semiconductor, typically the interfacial oxide layer is so thin as to be transparent to electron flow[11]. Experimentally it is found that ϕ_b is a much less sensitive function of ϕ_m than implied by equation (3.1), and often completely independent of ϕ_m, suggesting serious flaws in the Schottky-Mott theory, which

assumed constancy of the surface dipole layer, no localized states on the semiconductor surface, and perfect contact between the metal and semiconductor.

3.1.2 Surface/interface states and the Bardeen model

Bardeen later suggested that the discrepancy may be due to the presence of surface states localised at the metal-semiconductor interface[5]. Surface states are a consequence of the interruption of the periodicity of the semiconductor crystal lattice and are present at the interface between the semiconductor surface and insulating layer in a continuous distribution of states, as represented in schematic Figure 3.3. The occupancy of surface states is dependant on their energy relative to the Fermi level at the surface, and they are characterised by a neutral level ϕ_0, which is the energy level measured relative to the valence band, to which the surface states are filled when the surface is neutral. In the absence of surface states the negative surface charge of the metal was balanced by uncompensated donor ions in the depletion region of the semiconductor, however with the incorporation of surface states the overall charge neutrality condition must also be satisfied for charge accumulated at the semiconductor surface.

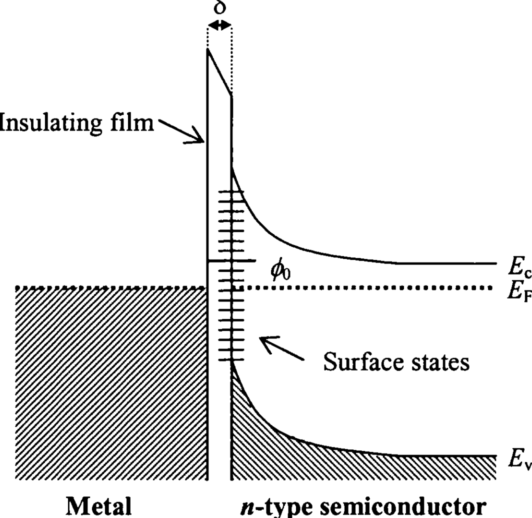

Figure 3.3 Metal-semiconductor contact with a thin insulating film at the interface and surface (or interface) states.

If the surface state neutral level ϕ_0 is above the Fermi level then the surface is positively charged requiring a reduction in the positive charge contained within the depletion region, therefore the width of the depletion region is reduced, decreasing the

amount of band-bending and consequently the barrier height ϕ_b. The lowering of ϕ_b has the knock-on effect of pushing the surface state neutral level ϕ_0 towards the Fermi level thus reducing the positive charge within the surface states. Conversely if ϕ_0 is below the Fermi level the surface is negatively charged requiring compensation by an increase in the positive charge contained within the depletion region and thus increasing the depletion width, the degree of band-bending, and barrier height ϕ_b, therefore pulling ϕ_0 towards the Fermi level. For a large number of surface states the Fermi level at the surface of the semiconductor will be at ϕ_0 resulting in the presence of band-bending and a space charge layer even in the absence of a metal contact.

Band-bending according to the Schottky-Mott model was entirely due to the difference between ϕ_s and ϕ_m, however in the presence of an interfacial layer and large density of surface states the potential difference ϕ_m-ϕ_s will act entirely across the interfacial layer as the charge in the surface states will facilitate the necessary potential difference. Therefore during metal-semiconductor contact formation there is no change to the charge density within the depletion region of the semiconductor, thus the barrier height ϕ_b is independent of metal work function ϕ_m, and the metal and semiconductor Fermi levels are constant across the interface, in which case the barrier height is given by,

$$\phi_b = E_g - \phi_0 \tag{3.2}$$

This is known as the Bardeen limit, where the barrier height is independent of ϕ_m and is said to be "pinned" or "stabilised" by the high density of surface states.

However this scenario is also rarely realised in practice and actual metal-semiconductor junctions have a barrier height ϕ_b somewhere between the Schottky-Mott limit, equation (3.1), and Bardeen limit, equation (3.2). This was expressed by Cowely and Sze[1,6] for the flat band condition (no electric field inside the semiconductor) as shown in Figure 3.3, where the interfacial layer has thickness δ, permittivity ε_i, and the surface state density is N_{ss}, as

$$\phi_b = \gamma(\phi_m - \chi_s) + (1 - \gamma)(E_g - \phi_0) \tag{3.3}$$

where the dimensionless parameter γ is given by

$$\gamma = \varepsilon_i / (\varepsilon_i + qN_{ss}\delta) \tag{3.4}$$

The parameter γ varies between 1 and 0, and is dominated by the density of surface states N_{ss}, for a low surface state density $\gamma \approx 1$ and equation (3.3) reduces to the Schottky-Mott limit, whereas for a high density of surface states $\gamma \ll 1$ and equation (3.3) tends to the Bardeen limit. This is known as the linear interface potential theory and has previously been utilised extensively and proved very useful, it is however based on a highly simplified distribution of surface states, applicable only for certain materials. Real metal-semiconductor systems follow the discussed theorems in a general manner, but are influenced by many different surface and interface mechanisms according to the materials and contact preparation technique, and thus deviate from the theoretical descriptions.

3.1.3 Real surfaces and interfaces

The growth mode and formation of metal-semiconductor contacts is a highly complex process and very difficult to encompass in a general model for all material systems, for example the deposition of the metal can perturb intrinsic electron states present on the semiconductor surface by changing the matching conditions, replacing them with metal-induced gap states MIGS[7]. The tails of conduction electron wavefunctions within the metal tunnel into the band-gap of the semiconductor at the interface, resulting in extra states within the band-gap around E_F. The extra states penetrate a few atomic layers into the semiconductor depending on the magnitude of the band-gap, the larger the band-gap the smaller the penetration depth. The occupation and penetration levels of the MIGS has direct implications on the position of the Fermi level, degree of band-bending, and consequently the barrier height ϕ_b.

During metal deposition, the impact process of the metal atom may occur in several ways involving the atom remaining upon the surface or diffusing across the boundary into the semiconductor producing an interface that is not atomically abrupt or ordered. Interdiffused metal atoms can occupy substitutional or interstitial sites within the semiconductor, doping the surface region and disrupting the previously assumed uniform doping profile. This can result in a very thin barrier profile which conduction electrons may tunnel through thus destroying the rectifying properties of the junction[3]. Similarly it is also possible for constituent atoms of the semiconductor to diffuse into the metal contact generating a point defect in the semiconductor or leaving an

accumulation of a remaining constituent. Additionally imperfections of the semiconductor surface such as vacancies or steps may lead to extra localised states energetically located within the band-gap. The departure of a surface from chemical stoichiometry can lead to the formation of electrically active sites and Fermi level pinning at the interface, thus greatly influencing the mechanism of barrier formation.

The interface of a metal-semiconductor contact is clearly a very complex region where the precise mechanism of barrier formation can vary over the area of the junction. The macroscopic resultant characteristics of Schottky junctions are easily probed and well known, however the precise mechanisms forming the barrier fluctuate over the interface on an atomic scale, causing localised pinning of the Fermi level and thus localised variations of the Schottky barrier height. In order to further understand the overall process of barrier formation, and the importance of the various localised mechanisms, it is therefore essential to probe the interface characteristics at the highest possible resolution.

3.2 Ohmic contacts

If all metal-semiconductor junctions formed Schottky barriers then semiconductor devices would be rendered useless as it would be impossible to interconnect devices with metallic conductors. This however is facilitated by junctions that obey Ohm's law which allow current to conduct in either direction, known as ohmic contacts. Ohmic contacts are formed between a metal and n-type semiconductor when their corresponding work functions are such that $\phi_m < \phi_s$ (for Schottky contacts on *n*-type semiconductors $\phi_m > \phi_s$) producing a very small potential barrier for electron flow from the metal to the semiconductor which is easily overcome by an applied bias, and presenting no barrier for conduction from the semiconductor to the metal. An ohmic characteristic can result when a metal is deposited on a highly doped semiconductor such that the depletion region is very narrow, resulting in a very thin potential barrier through which electrons can tunnel when bias is applied in either direction. This can be achieved by depositing a metal on a semiconductor with normal doping levels, as in the deposition of a Schottky contact, and subsequently alloying the contact by heating it to an elevated temperature for a certain duration in a process called annealing. The heating of the junction causes the metal and semiconductor to form a

eutectic liquid where dopants can rapidly diffuse, on cooling a thin layer of very highly doped semiconductor re-grows below the metal-film, creating the desired highly doped metal-semiconductor junction.

3.3 Current transport: Thermionic emission

Current transport across a forward biased Schottky diode is dominated by thermionic emission[8] where the majority carriers with kinetic energies greater than V_d - V are emitted from the semiconductor into the metal, as represented in Figure 3.4.

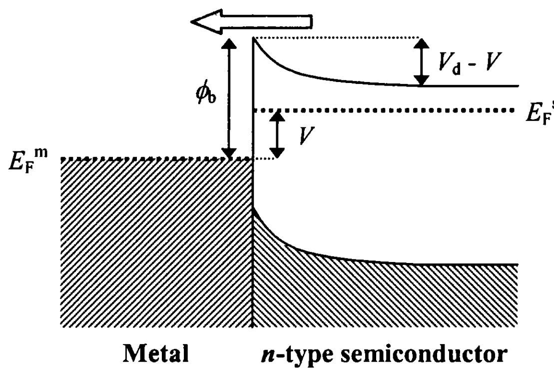

Figure 3.4 A Schottky junction under an applied forward bias of V. Electrons with a kinetic energy in excess of V_d - V are emitted over the reduced diffusion barrier and a forward bias current flows.

For an *n*-type semiconductor junction under forward bias, assuming $q\phi_b \gg k_BT$, according to thermionic emission theory the current is comprised of electrons emitted over the top of the barrier into the metal; the drift and diffusion that occur due to collisions in the depletion region are assumed negligible[3]. The emitted electrons are in equilibrium with the electron population in the semiconductor and are thus distributed in energy according to Maxwell's distribution. The current density I for an applied bias V is then[9]

$$I = A^*T^2 \exp(-q\phi_b / k_BT)[\exp(qV / k_BT) - 1] \qquad \textbf{(3.5)}$$

Where the parameter A^*, known as Richardson's constant is given by

$$A^* = 4\pi q m_e^* k_B^2 / h^3 \qquad \textbf{(3.6)}$$

The effective mass of the majority carriers (electrons) is denoted m_e^*, k_B and h are Boltzmann's and Planck's constants respectively. For m_e^* = m_0 the free electron mass, Richardson's constant A^* = 120 A/cm^{2}K^2, however the actual value of A^*

varies according to m_e*, the majority carrier effective mass, which depends on the band structure of the semiconductor, therefore actual values of A* are determined experimentally for different materials. Equation (3.5) describes the I-V characteristics frequently observed for Schottky diodes, it is however derived upon the assumption that the barrier height ϕ_b is independent of the applied bias. The actual situation is more complex than assumed in the simple models, and as a result of image-force lowering and an interfacial layer, the applied Schottky barrier energy $\phi_b^{applied}$ depends upon the electric field within the semiconductor which is induced by the applied bias. The dependence of $\phi_b^{applied}$ on V is represented in a Taylor series[9], shown in equation (3.7) retaining terms linear in V

$$\phi_b^{applied} = \phi_b + \beta V \quad \textbf{(3.7)}$$

here ϕ_b is the previously used barrier energy for zero applied bias, and β is a constant. Substituting equation (3.7) into equation (3.5) generates

$$I = A^* T^2 \exp(-q\phi_b / k_B T) \exp(qV / nk_B T) \quad \textbf{(3.8)}$$

This can be expressed in the form

$$I = I_0 \exp(qV / nk_B T) \quad \textbf{(3.9)}$$

Where I_0 is the saturation current, given by

$$I_0 = A^* T^2 \exp(-q\phi_b / k_B T) \quad \textbf{(3.10)}$$

$$n = (1 - \beta)^{-1} \quad \textbf{(3.11)}$$

n is a parameter called the ideality factor of the Schottky junction, as when the I-V characteristic of a junction is that of an ideal Schottky diode, a value of n = 1.0 is evaluated. For deviations from the ideal behaviour of a Schottky junction, ideality factor values of $n > 1$ are determined, with a greater departure from ideality being reflected by a greater magnitude of ideality factor, typical values are within the range $1 \leq n < 2$. For example the Schottky barrier energy is typically inconsistent across the entire area of the diode and this is contributes to induce an ideality factor greater than unity.

3.4 Current transport: Field emission

Quantum-mechanical tunnelling across the metal-semiconductor interface is the current transport mechanism which dominates the characteristics of an ohmic junction. An ohmic contact is defined as a metal-semiconductor contact which is characterised by a linear I-V relationship (over a useful range of V), is non-rectifying,

and demands a negligible voltage drop compared to the potential across the contacted device (i.e. posses a small resistance)[3]. Such an interface is engineered by manipulation of the doping by various means, to increase the doping at the interface and thus decrease the depletion width, narrowing the potential barrier to allow quantum-mechanical tunnelling of electrons through the barrier. For high doping levels the barrier is thin enough for field emission to dominate and electrons are emitted directly from states at the Fermi level in the semiconductor to vacant states in the metal. At moderately high doping concentrations the barrier is wider and tunnelling is only feasible to electrons with sufficient thermal energy to tunnel near the top of the barrier, in a process called thermionic-field emission[10,11].

3.5 Measuring Schottky barrier heights

The Schottky barrier height ϕ_b, or energy, can be experimentally determined by a variety of techniques, each founded on certain assumptions and possessing its own strengths and limits, which leads to variation in the determined value of ϕ_b dependent on the measurement technique implemented. The photoresponse or photocurrent method is one the most direct and commonly used techniques[12], based upon the irradiation of the Schottky diode with monochromatic photons of sub band-gap energy ($h\nu < E_g$)[13]. The photon energy is tuned across the barrier energy, exciting electrons in the metal over the barrier, for $h\nu \geq \phi_b$, into the semiconductor where they are detected as a photocurrent. The barrier energy ϕ_b is then evaluated from a plot of the photocurrent yield versus the photon energy[14], this technique is discussed in detail later. Another method is the Capacitance-Voltage, C-V, technique which measures the flat-band barrier height of the Schottky junction, i.e. there is no image-force lowering as no carriers are transported across the barrier during the capacitance measurement[1,15]. The capacitance-voltage characteristic of the Schottky barrier is plotted in the form C^{-2} versus V_r, the reverse bias voltage, which produces a straight line of gradient that is inversely proportional to the net doping and voltage intercept which is used to evaluate the barrier height. The most commonly utilised method is called the Current-Voltage, I-V, technique and uses the current-voltage characteristic of a Schottky diode to determine ϕ_b by a variety of experimental processes[1]. This technique was used to measure the Schottky barrier energy and ideality factor of

samples used within this work immediately after the preparation process and is described in detail.

3.6 I-V technique

The diode current density is measured as a function of the applied forward bias which is performed at a fixed temperature and in the absence of light; ideally the measurements are also performed within a Faraday cage enclosure to eliminate the noise influences of external sources. The data is then fitted according to equation (3.9) in the form of a log(I) versus V plot as given by

$$\ln(I) = \ln(I_0) + qV / nk_BT \qquad \textbf{(3.12)}$$

An extrapolation of the straight line portion of the ln(I) versus V plot to V=0 produces a current intercept that yields a value for I_0, the saturation current density. Substitution for I_0 into equation (3.10) evaluates the Schottky barrier energy ϕ_b by

$$\phi_b = -\,(\,k_BT / q\,).\ \ln(\,I_0 / A^*\,T^2\,) \qquad \textbf{(3.13)}$$

Whilst the gradient of the extrapolated straight line is given by $q\ /\ nk_BT$, which yields a value for the ideality factor n.

Note, this method of ϕ_b determination is typically very successful when measuring Schottky barriers with p-type semiconductors exhibiting ± 0.5% accuracy, however the process is more difficult in the case of n-type semiconductors and ϕ_b values are generally evaluated with an accuracy of ± 10.0%.

3.7 Silicon carbide

Silicon has been the primary material of the semiconductor industry for many years due to its electrical properties, high availability and low cost. It has therefore been the focus of intense research and silicon based systems are currently in a state of high optimisation. However new materials are continually sought and researched in electronics, especially for applications in which silicon based devices have never fulfilled the desired specifications, such as in extreme conditions where silicon based devices suffer catastrophic breakdown.

Several materials have been investigated for high power, high temperature, and high radiation applications, including diamond, gallium nitride, and silicon carbide.

Silicon carbide, SiC, is an extremely promising candidate to fulfil such requirements and posses the advantage over its competitors that its native oxide is SiO_2 allowing easy integration into existing silicon based fabrication methods. 4H-SiC is one of the polytypes of SiC which possesses a high band-gap of 3.2eV (c.f. E_g(Si) = 1.1eV), the highest electron mobility of the hexagonal polytypes of SiC at 1000 $cm^2V^{-1}s^{-1}$, a high saturated electron drift velocity of 2×10^5 ms^{-1}(1×10^5 ms^{-1} for Si), a high breakdown electric field of 3×10^8 Vm^{-1} (6×10^7 Vm^{-1} for Si), and high thermal conductivity of 4.9 $WK^{-1}cm^{-1}$ (1.5 $WK^{-1}cm^{-1}$ for Si)[16]. However the success of SiC depends upon its ability to form stable metal contacts of both Schottky and ohmic characteristics in order to obtain reproducible devices. SiC Schottky diodes have previously shown their potential to exceed the performance of slower Si-based *p-i-n* diodes currently used in power electronics applications, for example SiC Schottky diodes can exhibit rectification for very high voltages up to 4KV[17], and there are devices functioning up to 600 ^{0}C[18], SiC Schottky diodes also exhibit relatively low leakage currents and forward bias resistance when compared to Si-based diodes. However, a device is only as good as the properties of its substrate and SiC suffers from the fact that it is very difficult to produce with a low density of defects, the best substrates typically containing a density of micro-pipes[19] of 1cm^{-2}, thus causing difficulties in the production of good quality Schottky diodes.

3.8 Metal-silicon carbide contacts

The SiC substrate itself possesses the necessary properties for high temperature, frequency, power, and radiation applications, however its successful implementation in such scenarios is dependent on its ability to form reliable and high temperature stable, non-reactive Schottky and ohmic contacts. The suitability of many metal-SiC combinations has been explored with differing degrees of success, the following examples are some of the more promising. When an elemental metal layer is deposited on SiC at room temperature a Schottky contact is naturally formed[20], in the majority of cases, displaying a high barrier energy. Ohmic contacts are usually formed by high temperature annealing a metal contact which is Schottky on deposition, thus alloying the metal-SiC interface and destroying its rectifying characteristics by altering the chemical stoichiometry of the junction. Ohmic contacts previously investigated include WSi_2 and $MoSi_2$ [21], and TiN which forms a stable

ohmic contact that is non-reactive up to 1100^0C [22]. However the most common ohmic contact is a single Ni layer or a Ni-based contact preferred for its simple preparation[22]. The suitability of Ni has also been investigated for Schottky contact formation and demonstrated rectification up to 600^0C [18]. The metals investigated for SiC Schottky contacts include Pt and Cu which are rectifying up to 500^0C [23], W and W-based contacts which have displayed rectification up to very high temperatures of 800^0C [24], as has Mo which remained Schottky up to 900^0C[25].

Nickel has previously been implemented successfully and extensively in Si-based devices as its contacts posses a very low contact resistivity and their electrical properties are controlled during the relatively easy preparation procedures. Therefore its interaction with SiC has received considerable research interest in the pursuit of reliable and stable rectifying and ohmic contacts, with particular focus on the Ni-SiC ohmic junction. When deposited at room temperature upon *n*-type SiC, Ni naturally forms a Schottky contact which will remain rectifying up to 600^0C [18]. An ohmic junction is formed by the solid phase reactions that occur during annealing the contact at $900\text{-}1000^0C$ for 10mins[26], which produces an ohmic contact with very low specific contact resistivity of $3\times10^{-6}\Omega\,cm^2$, as determined by the transmission line method[22]. Investigations into the physical and chemical changes that occur at the junction have revealed a high Si content in the contact layer with microprobe measurements carried out in a transmission electron microscope, TEM, identifying the Ni_2Si phase[27], which is not detected for Schottky samples annealed up to 600^0C. The reaction of the Si leaves carbon which has been detected by Auger depth profiling in the contact region. TEM analysis has also revealed that after annealing there is a large number of voids formed within the contact layer, it has also been discovered that some of the excess C is accumulated over the internal surface of these voids[22]. The presence of such voids does not promise long term stability of Ni-SiC ohmic contacts. However Ni-SiC ohmic contacts do display excellent electrical characteristics, thus efforts have been made to eliminate the formation of voids by the introduction of a silicon interlayer designed to provide Si in the contact layer for the formation of Ni_2Si. This method has proved successful in eliminating void formation and retaining the electronic characteristics of the junction.

3.9 Summary

Within this chapter the physics of metal-semiconductor (n-type) contact formation are discussed beginning with the basic theories of Schottky, Mott, and Bardeen originally set out to characterise such contacts. However metal-semiconductor contacts are highly complex regions and very difficult to encompass in a single theory, therefore the different processes occurring in real metal-semiconductor contacts have also been discussed. The transportation mechanisms allowing electronic conduction are addressed including thermionic emission which applies to Schottky junctions and is implemented in the I-V technique of measuring barrier heights, utilised throughout the course of this work. Finally the development of silicon carbide electronic devices for implementation in extreme conditions is discussed, reviewing previous investigations reveals a depth of knowledge of Ni-SiC ohmic contacts but uncertainty in the origins of the electrical properties of Ni-SiC Schottky contacts. The electrical properties of a junction are a consequence of the reactions that occur at the interface during deposition; therefore it is imperative to understand the physical and chemical processes of the interface in as much detail as possible. This investigation aims to gain a further understanding of the Ni-SiC Schottky contact by analysing the nanostructure of the interface using near-field photocurrent imaging to reveal the nature of variations in the Schottky interface.

3.10 References

[1] E.H. Rhoderick, R.H. Williams, *Metal-semiconductor contacts*, (2nd Edition, 1988)

[2] W. Schottky, *Naturwissenschaften*, **26**, 843 (1938)

[3] C.W. Wilmsen, *Physics and chemistry of III-V compound semiconductor interfaces*, (Plenum, NY, 1985)

[4] M.J. Cooke, *Semiconductor devices*,(Pentrice Hall International, 1990)

[5] J. Bardeen, *Phys. Rev.* **71**, 717 (1947)

[6] A.M. Cowley, S.M. Sze, *J. Appl. Phys.* **36**,3212 (1965)

[7] V. Heine, *Phys Rev.* A. **138**, 1689 (1965)

[8] H.A. Bethe, *MIT Radiation Lab. Rep.* 43-12, (1942)

[9] S.M. Sze, *Physics of semiconductor devices,* (Wiley, NY, 1969)

[10] F.A. Padovani, R. Stratton, *Solid-state Electron.* **9**, 695 (1966)

[11] C.R. Crowell, V.L. Rideout, *Solid-state Electron.* **12**, 89 (1969)

[12] T. dell'Orto, J. Almeida, C. Coluzza, A. Baldereschi, G. Margaritondo, M. Cantile, S. Yildirim, L. Sorba, A. Franciosi, *Appl. Phys. Lett.* **64** (16), 2111 (1994)

[13] C.A. Mead, *Solid-state Electron.* **9**, 1023 (1966)

[14] R.H. Fowler, *Phys. Rev.* **38**, 45 (1931)

[15] Y.P. Song, R.L. Van Meirhaeghe, W.H. Laflere, F. Cardon, *Solid-state Electron.* **29**, 633 (1986)

[16] M. Sochacki, J. Szmidt, A. Werbowy, *J. Wide Band-gap Mat.* **9** (4), 307 (2002)

[17] H.M. McGlothlin, D.T. Morisette, J.A. Cooper, M.R. Melloch, *IEEE Device Res. Conf.* (1999)

[18] J.N. Su, A.J. Steckl, *Inst. Of Phys. Conf. Ser.*, 697, (IOP Publishing, 1996)

[19] C.H. Carter, V.F. Tsvedkov, R.C.Glass, *Mater. Sci. Eng. B*, **61**, 1 (1999)

[20] A. Itoh, O. Takemura, T. Kimoto, H. Matsunami, *Inst. Phys. Conf. Ser.* **142**, 685 (1996)

[21] J. Kriz, T. Scholz, K. Gottfried, J. Leibelt, C. Kaufmann, T. Gessner, *Mater. Sci. Forum*, **783**, 264 (1998)

[22] B. Pecz, *Appl. Surf. Sci.* **184**, 287 (2001)

[23] T. Hatayama, T. Suezaki, K. Kawahito, Y. Uaroka, T. Fuyuki, *Mater. Sci. Forum*, **615**, 353 (2001)

[24] O. Noblanc, C. Arnodo, S. Casette, C. Brylinski, A. Kakanakova-Georgieva, Ts. Marinova, L. Kassamakova, R. Kakanakov, B. Pecz, A. Sulyok, G. Radnoczi, *Mater. Sci. Forum*, **817**, 264 (1998)

[25] K. Nishikawa, M. Shimizu, B. Foster, H. Iwakuro, *Mater. Sci. Forum*, **611**, 353 (2001)

[26] A. Kestle, S.P. Wilks, P.R. Dunstan, M. Pritchard, P. Mawby, *Elec. Lett.* **36** (3), 267 (2000)

[27] B. Pecz, G. Radnoczi, S. Casette, C. Brylinski, C. Arnodo, O. Noblac, *Diam. Relat. Mater.* **6**, 1428 (1997)

Chapter 4
Theory: *pn*-junctions and laser diodes

4.1 *pn*- junction formation

A *pn*-junction forms one of the essential components of optical semiconductor devices, and the properties of the junction dominate the device characteristics. For example, radiative recombination in laser diodes and LED's is dependant on carrier injection through a *pn*-junction into the conduction and valence bands of the active region. The light sensitivity of photodiodes is dependant on the properties of a *pn*-junction, electron-hole pairs produced by illumination are separated in opposite directions at the *pn*-junction and the resultant photocurrent is utilised as an electrical output.

A *pn*-junction is formed when a *p*-type semiconductor is grown in contact with an *n*-type semiconductor. This can be a junction between two different materials and is known as a heterojunction (as shown in the following example), or between materials of the same type, known as a homojunction. The contact can be produced by impurity diffusion from the sample surface after crystal growth, or by impurity doping during crystal growth.

Figure 4.1 displays the energy band diagrams of a *p*-type semiconductor and an *n*-type semiconductor, of different material, in isolation from each other. The upper edge of the valence bands and the lower edge of the conduction bands are labelled E_v and E_c.

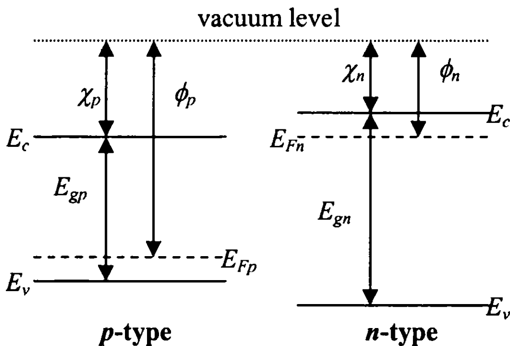

Figure 4.1 Energy band diagram of isolated *p* and *n*–type semiconductors, showing the Fermi levels, E_F, electron affinities χ, work functions ϕ, and band-gap energies E_g of both *p* and *n*-type materials.

The band gap energy of the *p* and *n*-type semiconductors are denoted E_{gp} and E_{gn} respectively, as similarly are the Fermi levels E_{Fp} and E_{Fn}. The work functions are labelled ϕ_p and ϕ_n, and represent the energy required to remove an electron from the Fermi level to the vacuum level. These work function energies are dictated by conduction type and carrier concentration of the semiconductor. The electron affinities are denoted by χ_p and χ_n, and represent the energy required to remove an electron from the conduction band edge to the vacuum level.

When a *p* and *n* -type semiconductor are formed in intimate contact with each other there is unequal doping across the interface that results in a diffusion current flowing. Electrons from the *n*-type material diffuse into the *p*-type material and vice versa due to the differing carrier concentrations. The diffusion of charge carriers about the semiconductor interface leaves static donor and acceptor ions bound within the crystal lattice in equal proportions to the diffused charge carriers. The dopant ions remain as space charge bound either side of the *pn*-boundary by electrostatic attraction as shown in Figure 4.2(a), resulting in an electric field across the junction, in a layer called the depletion or space charge region. The electric field is a maximum at the *pn*-boundary and goes to zero at the edges of the depletion region, as displayed in Figure 4.2(b).

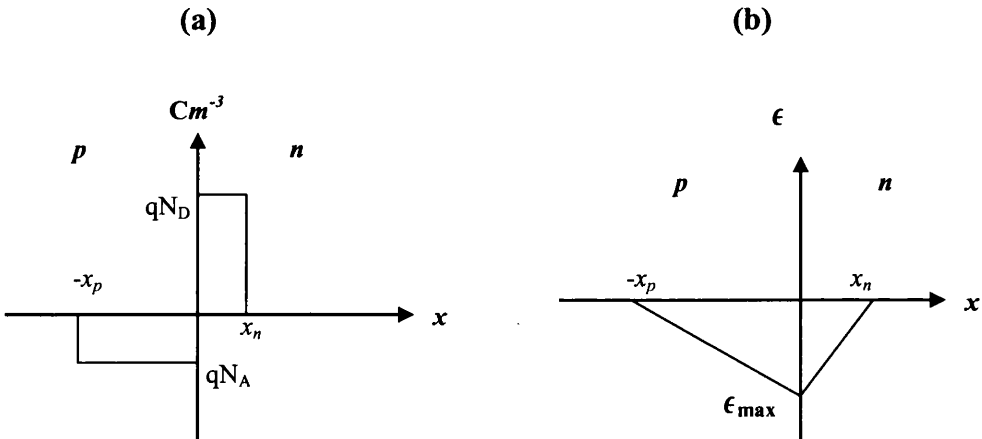

Figure 4.2 (a) Charge distribution within the depletion layer of a *pn*-junction. N_D and N_A are the donor and acceptor ion concentrations respectively, x_p and x_n are the depletion widths in the *p* and *n* –type materials. **(b)** Displays the electric field, ϵ, across the *pn*-junction, exhibiting the maximum field strength ϵ_{max} at the *pn*-interface.

The carrier diffusion ultimately results in band bending of the fully formed junction, as seen in Figure 4.3, showing upward band bending in the positively charged (*n*-

type) region and downward band bending in the negatively charged (*p*-type) region, causing a potential difference between the two sides called the built in potential, V_B. This built in potential forms a barrier that ultimately prevents further diffusion of charge carriers and a dynamic equilibrium condition is established. In the formation of a *pn*-heterojunction between two semiconductors with a large difference in band gap energy, E_g, there are additional barriers formed within the band bending region known as spikes and notches[1], as represented in the conduction band of Figure 4.3.

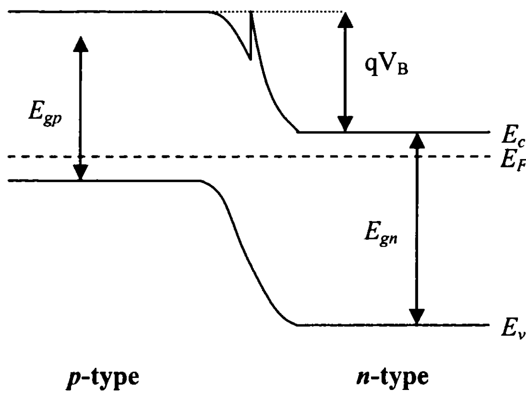

Figure 4.3 Equilibrium energy band diagram of a *pn*-junction (heterojunction). The built-in potential of the junction, or energy band discontinuity is labelled qV_B.

4.2 Built in potential, V_B

The built in potential comes from the difference in the intrinsic Fermi energies of the *n* and *p* semiconductors, that are $E_{Fn} = - q\phi_n$; and $E_{Fp} = - q\phi_p$ respectively, these are the local potentials. The total barrier potential, or built in potential, is given by[2]:

$$V_B = \phi_n - \phi_p \tag{4.1}$$

The equilibrium equations for the majority carrier densities are:

$$n_n = n_i \exp[\, q(\phi_n - \phi) \,/\, k_B T \,] \tag{4.2}$$

$$p_p = n_i \exp[\, q(\phi - \phi_p) \,/\, k_B T \,] \tag{4.3}$$

Where n_n is the electron number density in the *n*-type side, p_p is the hole number density in the *p*-type side, n_i is the intrinsic carrier number density, and ϕ is the Fermi potential. Multiplying these together:

$$n_n\, p_p = n_i^2 \exp[\, q(\phi_n - \phi_p) \,/\, k_B T \,] \tag{4.4}$$

The Fermi level is constant across the interface in equilibrium, and so is constant in equations (4.2) and (4.3). Thus substituting equation (4.1) into (4.4) for the built in potential, V_B, gives:

$$V_B = \frac{k_B T}{q} \ln\left(\frac{n_n p_n}{n_i^2}\right) \quad \textbf{(4.5)}$$

Away from the *pn*-junction region the majority carrier densities take their bulk equilibrium values of N_A and N_D, the acceptor and donor dopant densities respectively:

$$V_B = \frac{k_B T}{q} \ln\left(\frac{N_A N_D}{n_i^2}\right) \quad \textbf{(4.6)}$$

Equation (4.6) is the value for the built in potential, V_B, in volts, which acts over the depletion width and gives the magnitude of the equilibrium barrier height of the *pn*-junction.

4.3 Carrier transportation in *pn*-junction diodes

The built in potential barrier of a *pn*-junction gives it the characteristics of a diode rectifier. When the junction is forward biased by an applied potential V_A, the *p*-type material is biased positively, as seen in Figure 4.4(a). The applied potential reduces the built in potential barrier, V_B, to $V_B - V_A$ and the majority carriers conduct along the concentration gradients across the junction forming a current. Carriers leave the side in which they are the majority species and are injected across the depletion region into a material where they are minority carriers in a process called minority carrier injection. The applied potential acts almost completely across the junction, which is defined by the depletion region. This leaves only very small electric fields in the bulk material to drive drift current.

At either side of the depletion region the injected carriers, which are now in the minority, form a diffusion current. They diffuse away from the *pn*-junction and recombine with majority carriers causing the diffusion current to decay. The decay of the diffusion current must be countered by an increase in the drift current, as by Kirchoff's current law, the current into one end of the diode must also flow out of the other. In order for a drift current to flow, an electric field is necessary to drive carriers away from the depletion region to the contacts, i.e. some of the applied bias acts over the bulk areas of the diode, and not completely over the depletion region, the

magnitude of the drift current is dependant on the number and mobility of charge carriers as well as the electric field.

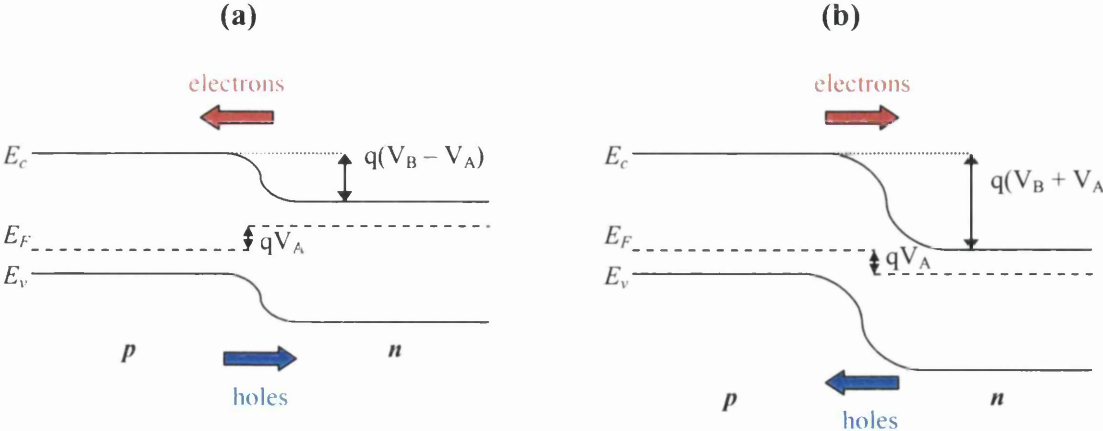

Figure 4.4 Band structure of a *pn* junction under **(a)** forward bias, and **(b)** reverse bias. The red and blue arrows denote conduction of electrons and holes respectively.

Under reverse bias it is the *n*-type side that is biased positively, increasing the potential barrier to $V_B + V_A$, shown in Figure 4.4(b). Minority carrier injection, as seen under forward bias, does not occur and a reverse or leakage current flows. Minority carriers within the depletion layer undergo the energetically favourable journey across the junction into a region where they have lower energy and are majority carriers; again a small part of the applied reverse bias drives a drift current to the device contacts. The edges of the depletion regions see a great reduction in minority carrier density which results in a diffusion of minority carriers towards the junction, thus supporting the reverse or leakage current. The I-V characteristics of a *pn*-junction are given by the equation[2]:

$$I = I_0\left(\exp\left(\frac{qV_A}{k_BT}\right) - 1\right) \tag{4.7}$$

For reverse applied bias, i.e. V_A is negative, the exponential term becomes small and the current tends to $I \approx I_0$ amps, where I_0 is the reverse leakage saturation current, and is constant for reverse applied potentials.

4.4 Depletion region

The depletion region was described previously as the layer of space charges i.e. dopant ions that remain fixed in the crystal lattice either side of the *pn*-interface after

the mobile charge carriers have diffused across the junction. The depletion zone essentially has no mobile charge carriers and a total charge distribution equivalent to that of the ionized dopants within, this is known as the depletion approximation. In reality majority carriers penetrate into the depletion region edges but are prevented from travelling further by the band bending of the built in potential barrier, and so neutralize the space charge at the edge of the depleted layer. The width of the depletion region is very important in determining the size of the *pn*-junction and the degree of band bending, which are important parameters when interpreting photocurrent images. The charge distribution, according to the depletion approximation, is illustrated in Figure 4.2(a), the *pn*-boundary is at $x = 0$ metres and the depletion region extends x_p metres into the *p*-type material and has a charge concentration of $-qN_A$ $\mathrm{Cm^{-3}}$. Similarly, the depletion region extends x_n metres into the *n*-type material and has a charge concentration of qN_D $\mathrm{Cm^{-3}}$. The determination of the extent of the depletion region requires the solution of Poisson's equation (4.8) for the potential, V, in each region of the device separately[2].

$$\frac{d^2V}{dx^2} = \frac{-\rho(x)}{\varepsilon} \tag{4.8}$$

Where ε is the permittivity. Using the charge density, $\rho(x) = qN$, where N is the dopant concentration of the region, Poisson's equation can be expressed for the *p* and *n* –type regions as:

p-type:
$$\frac{d^2V}{dx^2} = \frac{qN_A}{\varepsilon} \tag{4.9}$$

n-type:
$$\frac{d^2V}{dx^2} = \frac{-qN_D}{\varepsilon} \tag{4.10}$$

Integrating both equations (4.9) and (4.10) twice gives:

p-type:
$$\frac{dV}{dx} = \frac{qN_A}{\varepsilon}x + C_1 \tag{4.11}$$

$$V = \frac{qN_A}{2\varepsilon}x^2 + C_1x + C_2 \tag{4.12}$$

n-type:
$$\frac{dV}{dx} = \frac{-qN_D}{\varepsilon}x + C_3 \tag{4.13}$$

$$V = -\frac{qN_D}{2\varepsilon}x^2 + C_3x + C_4 \tag{4.14}$$

Where C_1, C_2, C_3, C_4 are unknown constants of integration. Equations (4.11) and (4.13) evaluate the electric field strength across the junction, as previously represented graphically in Figure 4.2(b). The following five conditions are then satisfied to solve equations (4.12) and (4.14) for the depletion widths x_p and x_n.

The formation of the junction involved charge transfer from its native areas, charge was neither created nor destroyed. Therefore, the initially neutral diode must remain neutral, thus for uniform doping on both sides:

$$q\,N_A x_p = q\,N_D x_n \qquad \textbf{(4.15)}$$

The potential at the *pn*-boundary at $x = 0$ is continuous. Therefore, arbitrarily setting the potential at $x = 0$ to 0 volts in equations (4.12) and (4.14) gives:

$$C_2 = C_4 = 0 \qquad \textbf{(4.16)}$$

The electric field, $-dV/dx$, is continuous across the *pn*-boundary, as is the dielectric constant. Applying electric field continuity at $x = 0$ to equations (4.11) and (4.13) gives:

$$C_1 = C_3 \qquad \textbf{(4.17)}$$

The depletion approximation implies that the electric field decreases to 0 Vm^{-1} at $-x_p$ and x_n, substituting for this condition into equations (4.11) and (4.13) derives:

$$C_1 = \frac{qN_A}{\varepsilon}x_p \qquad \textbf{(4.18)}$$

$$C_3 = \frac{qN_D}{\varepsilon}x_n \qquad \textbf{(4.19)}$$

Finally, the built in potential, V_B, of the junction is equal to the potential difference between the two edges of the depletion region:

$$V_B = V(x_n) - V(-x_p) \qquad \textbf{(4.20)}$$

$$V_B = \left(-\frac{qN_D}{2\varepsilon}x_n^2 + C_3 x_n\right) - \left(\frac{qN_A}{2\varepsilon}x_p^2 - C_1 x_p\right) \qquad \textbf{(4.21)}$$

Solving for the depletion widths in the *p* and *n* –type regions in terms of V_B, expressed earlier in equation (4.6), generates:

$$x_p = \left(\frac{2\varepsilon V_B}{q} \frac{N_D}{N_A(N_A + N_D)} \right)^{1/2} \quad \textbf{(4.22)}$$

$$x_n = \left(\frac{2\varepsilon V_B}{q} \frac{N_A}{N_D(N_A + N_D)} \right)^{1/2} \quad \textbf{(4.23)}$$

The equations show that the depletion width is dependant on the dopant concentrations of both sides, and the barrier potential, which is shown in equation (4.6) to be dependant on the dopant concentrations itself. The total width of the depletion region is simply the sum of these two lengths. In the case of unequal doping the majority of the depletion region occurs on the side of the junction with lighter doping, this is evident from equation (4.15).

4.5 Laser diodes

A laser diode utilises the electrical and optical properties of a *pn*-junction under forward bias operation, similar to a light emitting diode LED. However, an LED emits incoherent light via a spontaneous emission process, whereas a laser diode emits coherent radiation generated by stimulated emission, i.e. LASER: light amplification by stimulated emission of radiation. In order for a device to operate in a laser action a sufficiently high radiation density is required along with a population inversion in charge carriers. Population inversion can be achieved under forward bias in a simple *pn*-junction formed between two highly doped semiconductors. The requirement is that the doping must be degenerate so that the Fermi level does not reside within the band-gap, resulting in a very thin depletion region and a built-in potential that exceeds the band-gap energy. Under a sufficiently high forward bias a population inversion can be achieved within the depletion region resulting in a lasing action when above a high threshold current. This principal is refined for efficiency in the design of the heterostructure laser, which is a single crystal *pn*-junction formed between dissimilar semiconductors with small lattice mismatch. For example *p*-AlGaAs/GaAs/*n*-AlGaAs and *p*-InP/InGaAsP/*n*-InP are commonly used compositions, and structured as in Figure 4.5(a)[1]. When under forward bias, double injection occurs, minority carriers are injected into the intrinsically doped *active* layer, while majority carriers diffuse into the active layer restoring electrical neutrality, Figure 4.5(b). For a population inversion to be established in the active region a very

high injected carrier concentration is required as shown in Figure 4.5(c), this is achieved by using a thin intrinsic layer, typically of the order of 100nm.

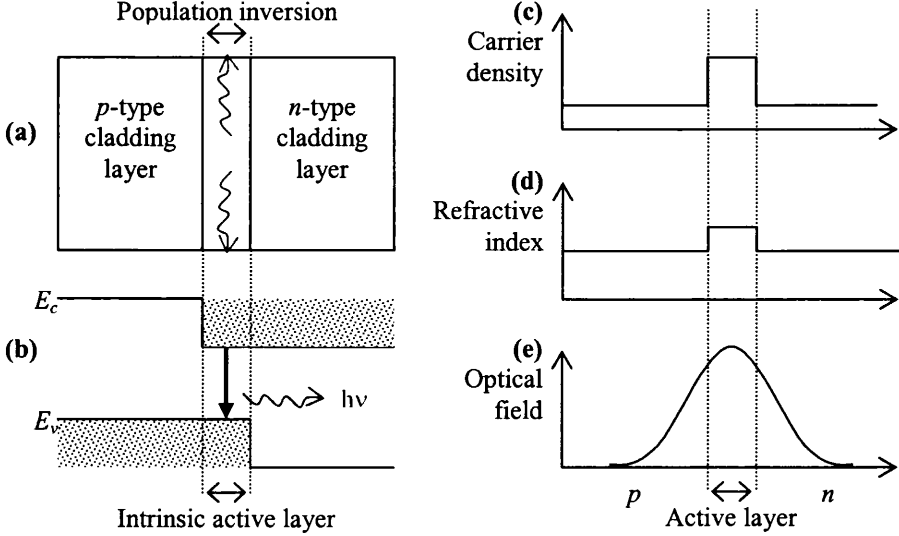

Figure 4.5 Basic heterostructure laser **(a)** structure, **(b)** band diagram, **(c)** carrier density, **(d)** refractive index, and **(e)** Optical field.

In order for stimulated emission to be sustained efficiently the radiated photons must also be confined within the active layer in a high concentration. This is done at either end of the device by two parallel mirror facets, usually (110) cleaved surfaces, oriented perpendicular to the active layer and these form a Fabry-Perot optical cavity. Lateral confinement of photons to the active layer is maintained by total internal reflection as in optical fibres. The refractive index of a material is dependant upon its composition, thus the active layer is chosen to have a higher refractive index than its neighbouring *cladding layers*, Figure 4.5(d). The design of the heterostructure laser is such that a population inversion is achieved very efficiently, and the radiated photons are heavily confined to the active layer as shown in Figure 4.5(e), thus establishing a state of stimulated emission (lasing) for less input power, i.e. a lower threshold current. This is a description of a basic heterostructure laser, there are many variations of this simple recipe as will be discussed further, each designed for a specific use, and each having its own strengths and drawbacks. However, almost always the key developmental goals include the following: operation at increased efficiency, i.e. lowering the threshold operating power, and increasing the operational lifetime of the device.

4.6 Quantum wells and laser diodes

The dominant feature of a laser diode is the active region which is typically a direct band-gap semiconductor with intrinsic doping, the band-gap being narrower than that of the adjacent cladding layers. If the thickness of this sandwiched layer is reduced, the device characteristics deteriorate, i.e. the optical confinement is reduced resulting in an increased threshold current. However, when the thickness of the central layer approaches the de Broglie wavelength ($h/m_{e,p}$ where h is Planck's constant and $m_{e,p}$ is electron or hole momentum) quantum effects become dominant. Carrier motion perpendicular to the active layer is restricted and the kinetic energy is quantized into discrete energy levels, carrier motion in the direction parallel to the well remains unrestricted and the continuum states are formed. The thickness of such a layer is typically less than 10nm and is called a *quantum well.*

The 2-dimensional confinement of a quantum well structure leads to a reduction in the density of states in the active region in contrast to the continuum of states of the conduction and valence bands of a bulk semiconductor. The density of states for a quantum well near the band edges is changed from the regular parabolic form to a step like function of discrete quantized energy states, as shown in Figure 4.6.

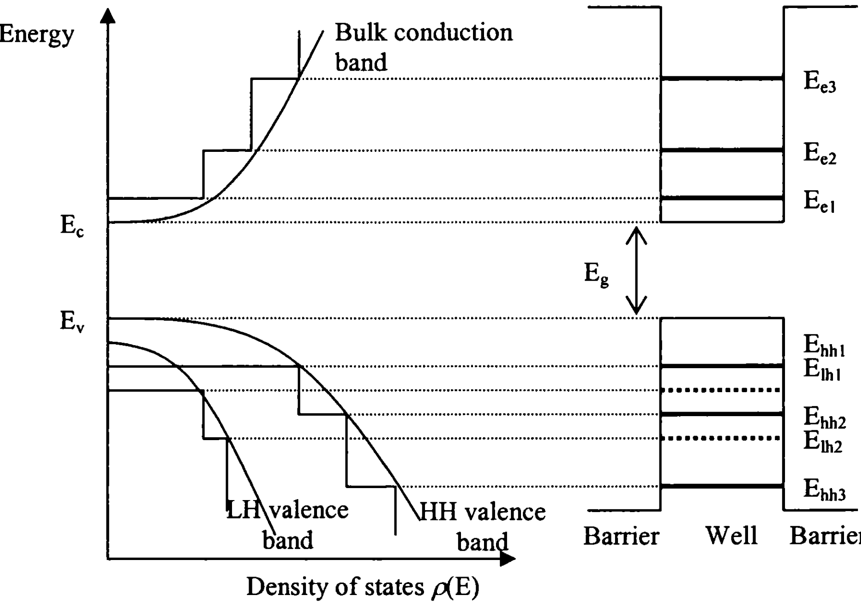

Figure 4.6 The density of states of a quantum well structure are modified from their bulk parabolic form to the step like form of quantized energy levels in the direction perpendicular to the well. Parallel to the well there is no confinement and the density of states retain their parabolic distribution.

This has direct consequences for optical transitions that occur within the quantum well, as they no longer take place between the valence and conduction bands of the bulk, but between the quantised energy sub-bands, resulting in photons of shorter wavelength. The transition mostly occurs between the lower energy conduction sub-band E_{e1} and the heavy-hole (HH) band E_{hh1}, whose density of states is larger than the light-hole (LH) band.

If the materials used in the well have a lattice mismatch of only a few percent then a *strained quantum well* is formed having slightly different properties. Lattice mismatch introduces a large number of misfit dislocations that generate interfacial states and result in the degradation of device characteristics. However, if the lattice mismatch is low and the well thickness is kept below a *critical layer thickness* then a quantum well can be formed between materials having different lattice constants without misfit dislocation formation. The compressive or tensile strain introduced by the lattice mismatch between the well and the barriers is relaxed across the well by elastic deformation of the well lattice material if kept thin enough, i.e. below the *critical layer thickness.* The deformation of the well layer causes a variation of the band-gap energy, the conduction and valence band edges are shifted and the light and heavy –hole sub-bands of the valence band also translate in energy. Consequently, the density of states and hole effective mass are lowered, thus lowering the threshold current for light amplification. Lasing transitions thus occur between the sub-bands of the conduction band and only one of the now separated valence sub-bands. The stimulated emission energy of the device can therefore be controlled by varying the strain of the quantum well, therefore wavelengths unattainable to lattice matched systems can be achieved.

The optical modes of a laser diode are dependant on the valence sub-bands. The heavy and light –hole bands are coupled to the lateral transverse TE and vertical transverse TM-modes respectively. Laser diodes that posses bulk active layers or a lattice matched quantum well emit a mixture of TE and TM-modes, whereas strained quantum wells exhibit strong mode selection. Under compressive strain of the quantum well the diode lazes predominantly in the TE-mode, under tensile strain the TM-mode is predominantly selected[1].

4.7 Multi-quantum well super lattices

The properties of quantum well laser diodes may be further enhanced by incorporating more than one quantum well, separated by wide band-gap barrier layers, in multi-quantum well super lattice structures. The laser's characteristics are controlled by tuning the multi-quantum well structure, i.e. the dimensions and number of wells and barriers. Multi-quantum well laser diodes also display excellent optical confinement perpendicular to the active region, with laser emission restricted to the active region effectively. This results in the optical gain for lasing being achieved at a lower threshold current density.

4.8 Multi-quantum barrier reflectors

The theoretical concepts of multi-quantum well super lattices can also be employed in the enhancement of electronic confinement to the active layer of quantum well laser diodes. This is particularly applicable in the case of red-emitting AlGaInP quantum well lasers that operate at the desirable 630nm wavelength, and are highly susceptible to the thermally activated loss of electrons from the active region, thus limiting the power output of the device.

The efficiency of electron confinement to the active region of a device is dependant on the magnitude of the conduction band offsets, i.e. the potential barrier U between the waveguide layer and *p*-type cladding, as shown in the schematic of Figure 4.7(a). However the choice of materials available for use in these layers is limited by the optical requirements of the laser system, i.e. by the refractive index requirements of wave-guiding, therefore an alternative method of barrier enhancement is necessary. A possible method of barrier enhancement is the multi-quantum barrier, MQB, technique initially proposed by Iga *et al*[3] in 1986, and is based on the incorporation of a multi-quantum barrier/well super-lattice into the *p*-type cladding layer close to the active region. A series of thin ($\leq$5nm) narrow band-gap quantum wells and large band-gap barrier layers are used. If the widths of the barriers are sufficiently thin, the confined states of the individual wells overlap to broaden into a series of allowed and forbidden electron energy mini-bands. By tuning the periodicity of the super-lattice, a band of forbidden energy states can be energetically aligned with the conduction band minimum of the *p*-type cladding layer resulting in an increase in the potential barrier from U to $U+dU$ (eV), as shown in Figure 4.7(b). A multi-quantum barrier, MQB, is

composed of such a super-lattice preceded by a thicker first barrier which inhibits the tunnelling of low energy electrons through the structure that can destroy the delicate mini-band effect. The composition of such MQB structures can be optimised theoretically by solving the Schrödinger equation across the structure, the transfer matrix method is applied to obtain the electron reflectivity probability as a function of the normalised incident electron energy[4].

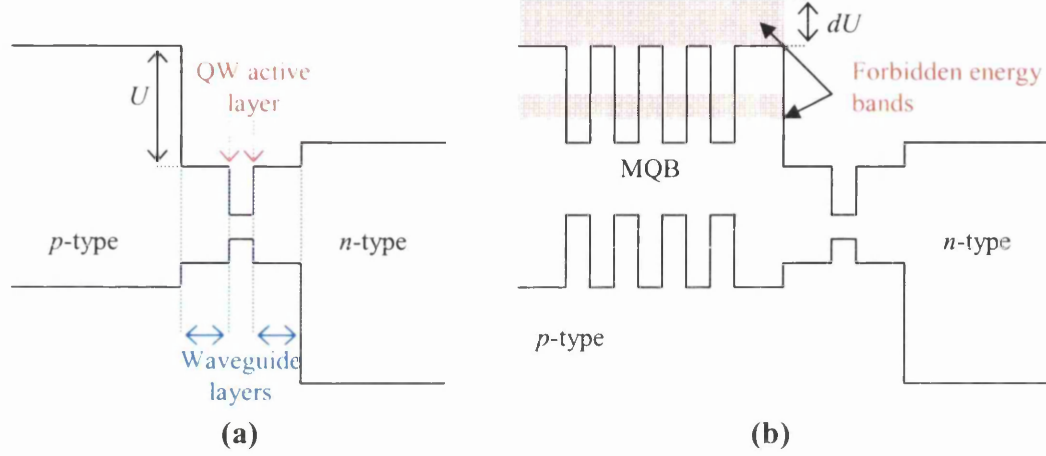

Figure 4.7 Equilibrium band diagrams of **(a)** standard quantum well laser diode, and **(b)** quantum well laser diode with a multi-quantum barrier, MQB, structure in the *p*-type cladding layer close to the active region. The schematic illustrates the theoretical enhancement dU in the band offset induced by the MQB.

The MQB technique of barrier enhancement has been successfully demonstrated for metal-semiconductor junctions, where a 40% enhancement was measured for Au-AlGaAs and Au-GaAs Schottky contacts, however when employed in AlInP/GaInP based structures the theoretically predicted enhancement is not seen[5]. Similarly when applied to AlGaInP red-emitting quantum well laser diodes a 16-20% enhancement in the conduction band discontinuity is theoretically modelled, which is not experimentally observed for fabricated devices[6,7]. This may be attributed to several possible reasons including, the ability to successfully grow abrupt and accurate super-lattices, and the accuracy of the modelling techniques. Much work remains in the optimisation of such structures.

4.9 Buried heterostructure laser diodes

Planar laser structures are very inefficient, have a high threshold current and suffer instability of the optical output. Their carrier and optical confinement, particularly of the vertical transverse TM-mode, perpendicular to the active region (Figure 4.8), are drastically improved by utilising quantum well and strained quantum well structures in the active region. However, the important lateral transverse TE-mode, parallel to the active region remains unstable.

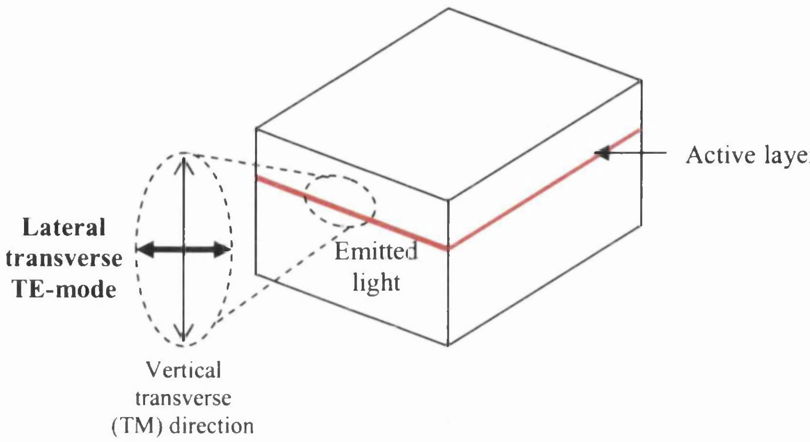

Figure 4.8 Optical emission modes of an operating laser diode.

Fortunately the TE-mode is highly sensitive to the structure of the active region. Several structures have been designed that utilise the concept of gain guiding or refractive index guiding, and the buried heterostructure, BH, is one of the more successful.

Buried heterostructure laser diodes are characterised by a low threshold current and stable mode operation. This is the result of the tight confinement of charge carriers and photons to the active region by the adjacent current blocking (thyristor) structures, as shown in Figure 4.9. The *n*-InP buffer and active layers are grown upon the substrate then the curved mesas are defined and etched, the InP blocking layers are then re-grown around the active region and the *p*-InP cladding layer is grown on top, capping the device. A multi-quantum well structure is typically used as the active region, leading to 2-dimensional carrier and optical confinement, as the refractive index distribution around the active region results in total internal reflection. The degeneracy of the TE and TM –modes are broken by the quantum confinement of the multi-quantum well structure and the dimensions of the active region (i.e. the stripe

width) are sufficiently small so that only the fundamental lateral transverse TE-mode can propagate[1,8]. Thus the multi-quantum well structure is fine tuned by the mesa structure to impose stability on the laser mode of the device. The effective refractive index of the active region is sufficiently higher than the neighbouring cladding regions that it operates as a waveguide, resulting in the single TE-mode having good enough confinement on the device for efficient coupling into optical fibres.

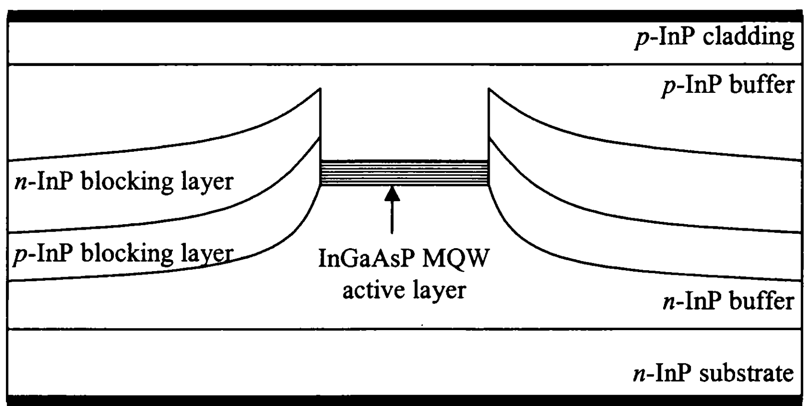

Figure 4.9 Transverse cross section of a buried heterostructure, BH, laser diode. The diagram illustrates the crucial area around the active region; the curved mesa structure is etched into the device before the subsequent re-growth of the blocking layers adjacent to the multi-quantum well active region.

The function of the current blocking layers is to funnel the injected current into the active region under forward bias, for stimulated emission to occur. When driven in the forward direction one of the *pn*-junctions of the *pnpn* blocking structure is under a reverse bias thus offering a substantial barrier to current flow across that region of the device, hence promoting the injected current to flow into the MQW active region. The crucial point of the structure is the area between the blocking layers and the MQW active region. Unfortunately, the *pn*-junction that opposes current flow around the MQW, the junction between the *p*-InP and *n*-InP blocking layers, cannot be grown right up to the edge of the active region. The presence of a low dopant buffer layer is necessary between the *n*-InP blocking layers and the MQW's to prevent dopant diffusion from the highly doped *n*-InP blocking layers into the intrinsic quantum wells. Therefore the properties of the interface between the *p*-InP blocking layer and *pn*-junction layer, i.e. the area between the *n*-InP blocking layer and the MQW's, is crucial to the efficiency of the device performance. Although the *p*-InP blocking layer and *pn*-junction layers are physically connected either side of the active region,

the current path between the two is blocked by the depletion region of the reverse biased *pn*-junction at the corners of the mesa structure[9]. The device performance is therefore very sensitive to the dimensions of the structure and extent of the depletion region at this location.

The structure gives the BH-MQW laser good characteristics, however it is in the complexity of the structure that the device weaknesses also lie. The curved mesa structure is chemically etched upon the wafer surface after the device is grown up to the active layer; blocking layers are then re-grown on top. It is the quality of the etched curved heterointerface where problems can originate. During operation there can be an increase in the defect density at the heterointerface, leading to an increase in non-radiative recombination current, consequently the threshold current increases. This problem is dependant on the physical manufacturing process of the device and as such is an aspect extensively researched.

4.10 Summary

This chapter provides an overview of quantum well laser diodes starting at the basic principles of *pn*-junctions upon which the mechanisms of more complex laser structures base their fundamental properties. The basic properties of *pn*-junctions, such as the built-in potential and depletion region, are paramount in the interpretation of photocurrent images; photocurrent imaging directly maps the distribution and characteristics of *pn*-junctions. The utilisation of *pn*-junctions in laser devices is then discussed, along with the important incorporation of quantum wells into the active layer to enhance the laser's characteristics. The principles behind two particular laser structures, the planar multi-quantum barrier QW-laser diode, and buried heterostructure multi-quantum well laser diode, are briefly outlined. In particular their application and developmental difficulties are discussed. This chapter provides the fundamentals necessary for the interpretation of near-field optical and near-field photocurrent measurements taken in the characterisation of both multi-quantum barrier lasers and buried heterostructure laser devices that are presented in chapters 8 and 9 respectively.

4.11 References

[1] M. Fukuda, *Optical semiconductor Devices*, (Wiley, 1999)

[2] M.J. Cooke, *Semiconductor devices*,(Pentrice Hall International, 1990)

[3] K. Iga, H. Uenohara, F. Koyama, *Electron. Lett.* **22**, 1008 (1986)

[4] R. Tsu, L. Esaki, *Appl. Phys. Lett.* **22**, 562 (1973)

[5] S.P. Wilks, A. Kestle, *Appl. Surf. Sci.* **117**, 334 (1997)

[6] K.S. Teng, M. Brown, A. Kestle, P. Smowton, P. Blood, S. Pinches, P.A. Mawby, S.P. Wilks, *Appl. Surf. Sci.*, **190**, 284 (2002)

[7] M.R. Brown, K.S. Teng, A. Kestle, P. Smowton, P. Blood, P.A. Mawby, S.P. Wilks, *Appl. Surf. Sci.*, **234**, 434 (2004)

[8] S.K. Buratto, J.W.P. Hsu, J.K. Trautman, E. Betzig, R.B. Bylsma, C.C. Bahr, M.J. Cardillo, *J. Appl. Phys.* **76** (12) 7720 (1994)

[9] D. Ban, E.H. Sargent, J. Dixon-Warren, G. Lethal, K. Hinzer, J.K. White, G. Knight, *IEEE J. Quantum Electronics*, **40**, No. 2 (2004)

Chapter 5
Theory: Near-field photocurrent microscopy

5.1 Internal photoemission

The technique of internal photoemission (IPE) probes the buried interfaces of semiconductor devices by irradiating them with an external photon source of a sufficient energy, $h\upsilon$, such that charge carriers are optically pumped over band-discontinuities producing a photo-excited current, called a photocurrent, which can subsequently be detected at the external device contacts[1]. The method is applicable to both Schottky diodes and semiconductor heterostructures however the precise mechanism of photocurrent generation is different for each and is thus sensitive to different features[2]. The strength of IPE lies in its ability to directly probe the characteristics of real buried interfaces as opposed to surface sensitive techniques that can only hypothesise the precise interface physics by examining the surface pre-burying. If IPE is performed with photons of a variable energy in a technique known as internal photoemission spectroscopy (IPS), then a series of features can be revealed by plotting the photocurrent with the photon energy that correspond to the energetic phenomena that are activated within the device as the photon energy is tuned.

An alternative technique is sensitive to lateral variations in such energetic processes by scanning the optical source, at fixed photon energy, over the sample and mapping the photocurrent intensity, thus producing a spatial image of photocurrent contrast in a method called photocurrent imaging. The ability of all imaging techniques is ultimately measured by their maximum resolution, and thus different excitation sources and schemes have previously been employed in efforts to perform photocurrent experiments using increasingly focussed excitation spot sizes. The technique of optical beam induced current (OBIC)[3] excites a photocurrent by focussing the plasma arc spot of a mercury lamp onto a pinhole aperture which acts as a well defined point light source, that is re-imaged onto the sample surface using a microscope with a long working distance objective. The illumination spot size achieved by this method is approximately 15μm in diameter[4]. An alternative technique is to use the high energy electron beam of a scanning electron microscope (SEM) to provide the excitation source in a method called electron beam induced

current (EBIC)[5]. The ultimate spot size achievable by a SEM is approximately 10nm; however this is implemented using highly energetic electrons (10-30KeV) which can easily damage the device under test and lead to the formation of surface states or inversion layers thus altering the electrical properties of the device, such damage is only averted by using a reduced accelerating voltage below approximately 1.5KeV, unfortunately this results in noisy images of poor resolution[6]. Clearly there is a necessity for an optical based imaging technique which does not perturb the sample and has a far superior resolution (illumination spot size) to that implemented in these previous experiments.

Note that the scenarios discussed here are for zero applied external field, internal photoemission experiments can be performed under forward and reverse bias conditions and were attempted during the course of this study. However the best results were attained for zero volts applied bias, thus all theoretical discussions are for zero applied bias. Although internal photoemission spectroscopy was not performed as part of this study it is still extremely relevant in discussing the origins of photocurrent generation and in considering the foundations of photocurrent mapping.

5.2 Fowler's theorem

Internal photoemission techniques are based upon the optical activation of charge carriers within a sample above an energetic boundary. In the case of Schottky diodes this is the Schottky barrier ϕ_b, and electrons within the metal at the junction which are excited with an energy $h\upsilon \geq \phi_b$ are transported across the junction by the built-in field producing a photocurrent signal. For semiconductor heterojunctions, such as *pn*-junctions, the energetic boundary is characterised by the band-gap energy E_g of the material, electron-hole pairs are optically generated when $h\upsilon \geq E_g$ and transported across the heterojunction by the built-in field of the interface, generating a photocurrent signal.

The theoretical foundations of internal photoemission spectroscopy are based on the classical treatment of the photoelectric effect by Fowler[7]. For the photoelectric effect, the number of electrons N emitted from the metal into the vacuum level is given by[8]

$$N = AT^2 \left[\frac{\pi}{6} + \frac{1}{2}\mu^2 - \left(e^{-\mu} - \frac{e^{-2\mu}}{4} + \frac{e^{-3\mu}}{9} - \ldots \right) \right] \quad \textbf{(5.1)}$$

and $$\mu = \frac{\hbar\omega - \phi}{k_B T} \quad \textbf{(5.2)}$$

where $\hbar\omega$ is the photon energy (= $h\nu$), T is the temperature, A is a constant, and ϕ is the barrier height (work function). The threshold energy for photoemission is $\hbar\omega \approx \phi$, and above threshold for ($\hbar\omega$ - ϕ) $\geq 6k_BT$, equation (5.1) reduces to the simplest quadratic form with an accuracy of 5%

$$N = AT^2\mu^2 \quad \textbf{(5.3)}$$

The internal photocurrent, I_P, is proportional to N, therefore equation (5.3) can be rewritten

$$I_P = (h\nu - \phi)^2 \quad \textbf{(5.4)}$$

The barrier height can thus be extracted from equation (5.4) by plotting the square root of I_P versus $h\nu$, in a graph known as a Fowler plot, and extrapolating the linear portion to $\sqrt{I_P} = 0$, the $h\nu$ intercept denotes the barrier energy[9].

Equation (5.4) for the photocurrent I_P can be employed for both Schottky junctions and semiconductor heterojunctions by replacing ϕ with ϕ_b, the Schottky barrier height, and E_g the semiconductor band-gap[10], respectively.

5.3 Near-field photocurrent microscopy

Upon the implementation of near-field microscopes operating at optical wavelengths there was a surge of research to transpose traditional far-field techniques into the newly realised geometry of the near-field, and thus enhance the capabilities of the various experiments by incorporating the nanoscale resolution of NSOM. The optically-stimulated current techniques were first implemented using the near-field probe as a localised excitation source to photo-excite currents at the surfaces of semiconductors[11,12] and laser diodes[13,14], thus performing OBIC in the near-field. Later buried interfaces were probed by implementing the more difficult technique of IPE using the highly localised excitation source of the near-field aperture[15]. The work carried out within this thesis aimed to further these early near-field induced current experiments by (a) enhancing and optimising the imaging mechanism, and (b) investigating new samples using the polished technique. Note, both near-field optical

beam induced current (at surfaces) and near-field internal photoemission (at buried interfaces) are encompassed by the term near-field photocurrents or photocurrents hereafter.

The combination of NSOM with photocurrent techniques, which were previously restricted in resolution by the illumination spot size, enables the measurement of photocurrents with high lateral resolution, and thus the investigation of variations in solid interface properties and the distribution and extent of *pn*-junctions. The employment of former space averaged, or illumination spot size limited techniques in the geometry of the near-field allows local variations in sample properties to be revealed at resolutions of the order of the near-field aperture diameter. Coupled with the simultaneously acquired information of the shear-force topographic imaging mechanism, and other complementary NSOM modes such as collection imaging (as is discussed later when analysing QW diode lasers), these mechanisms make near-field photocurrent imaging at surfaces and buried interfaces a very powerful analytical technique for semiconductors and their related interfaces and devices.

The precise photocurrent generation mechanisms for Schottky junctions and *pn*-junctions are slightly different and as a result are sensitive to different features of the relevant junction; the following sections elucidate on the stimulation of photocurrents in the structures examined in this study and discuss the resolution of imaging such devices.

5.4 Schottky junctions and photocurrent mechanisms

For a metal–semiconductor (*n*-type) Schottky junction under zero applied bias, a photocurrent signal is generated when photons of energy $h\nu \geq \phi_b$ are incident at the interface. Electrons at the metal surface are optically excited from the metal Fermi level to an energetic state above the barrier energy, as shown in Figure 5.1. In the absence of an applied field it is only those excited electrons close to the Schottky interface (within a diffusion length) that are driven over the barrier by the built-in field of the junction, that exists between the electron accumulation layer within the metal boundary and the positive uncompensated donor ions that are fixed within the depletion region of the *n*-type substrate. Once over the barrier a field is established

which is sensed as a photocurrent. The photon energy used is far less than the band gap energy ($E_g > hv \geq \phi_b$), and thus less than that required for inter-band transitions within the semiconductor. It is possible that electronic transitions may occur from states residing within the band-gap, such as MIGS or defect states, however it has been shown that photocurrents are only very weakly affected by such phenomena due to the low absorption coefficient of the semiconductor at such energies[16]. The effect of such states has previously been discussed in chapter 3, and is most likely manifested in Schottky barrier pinning (Fermi-level pinning).

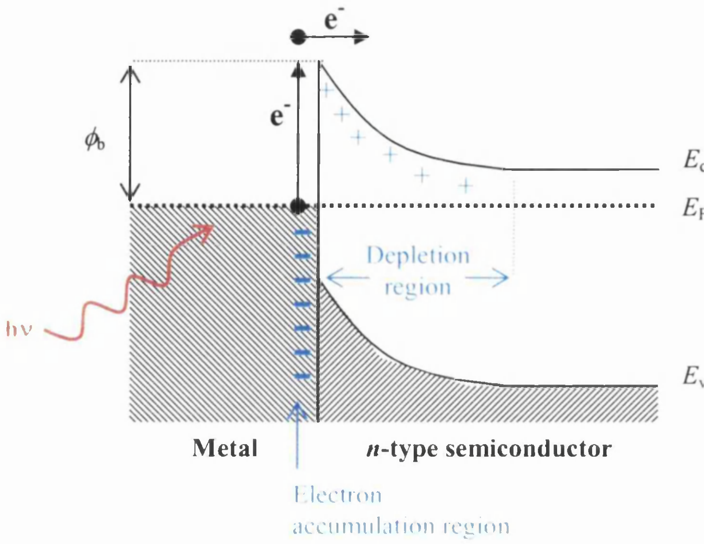

Figure 5.1 Photocurrent generation at a Schottky junction excited by photons of energy $hv \geq \phi_b$ for zero applied bias.

Near-field photocurrent imaging uses a fixed photon energy to locally excite carriers and generate a photocurrent at each pixel of the image. The photon energy is constant therefore variations in the photocurrent intensity are ideally a consequence of variations in the Schottky barrier height resulting from inhomogeneities of the interface, assuming a constant optical intensity is incident at the interface. Thus near-field photocurrent imaging directly probes the Schottky barrier and reveals fluctuations in its magnitude that can be attributed to local variations in interface stoichiometry, barrier pinning mechanisms such as metal-induced gap states, interface defects, and dopant effects.

Note the mechanism of near-field photocurrent imaging is highly sensitive to the optical intensity at the interface, which forms a primary factor that must always be considered when interpreting photocurrent images. Photocurrent imaging of Schottky

diodes is performed by illumination of the interface through the thin metal top contact, the semiconductor substrate is atomically flat, and therefore variations in the surface topography of the metal layer, detected by shear-force imaging, are due to variations in the thickness of the metal layer itself. This indicates variations in the separation of the near-field aperture and optically sensitive interface, and thus variations in the optical intensity incident at the interface. For example, an increased surface topography increases the probe-interface separation, which reduces the optical intensity at the interface. The surface topography of a rough sample can therefore influence the photocurrent imaging mechanism, inducing a topographic artefact in the optically generated signal[12], as discussed fully in chapter 6, sections 6.6 and 6.7. Precautions are taken to avoid such processes contaminating photocurrent data, such as the engineering of flat samples to minimise or eliminate any topographic component of the photocurrent signal.

The resolution of near-field photocurrent imaging is a complex issue and is highly dependent upon the nature of the sample and the imaging configuration. The resolution and contrast of near-field photocurrent imaging of dislocation defects on semiconductors has been investigated by Xu *et al*[17] using a numerical simulation based on a two-dimensional carrier diffusion model with a localised generation term. Comparison with experimental images revealed good agreement in lateral resolution, contrast, and sharpness, where lateral resolution was found to be limited by either the aperture diameter or the defect diameter, whichever is larger. The situation in the photocurrent imaging of Schottky junctions is more complex however as the photosensitive interface is buried beneath the metal top contact. The light incident at the interface therefore passes through the intermediate metal contact layer and is dispersed from the highly confined near-field aperture by diffraction and scattering in the metal. This is limited by using a metal layer that is of minimum thickness, typical Ni thicknesses used in this study of Ni-SiC diodes were 20-40nm, note it is favourable to illuminate the interface via the metal top contact as illumination via the thick (~340μm) substrate would further optical dispersion. The near-field photocurrent imaging of Schottky junctions has received very limited previous investigation, a similar study carried out by J. Almeida *et al*[20] on the Pt-GaP Schottky junction estimated a lateral resolution of 100-200nm, which is approximately a factor of 20

times improvement over the similar far-field OBIC technique. This compares closely with that measured for the near-field photocurrent imaging of stretch-oriented polymer films at ~150nm lateral resolution[18], and studies of solar cells that estimated ~250nm lateral resolution[19]. The resolution observed for these studies of the Ni-SiC Schottky interface was within the range 100-200nm, although the diameter of the near-field source used was ideally 50nm (50-100nm), resolution was limited for the Schottky diodes by optical scattering during transmission to the buried photo-sensitive interface.

The photocurrent imaging of buried Schottky interfaces performed at zero applied bias conditions maximises the sensitivity to the barrier properties, under forward bias the signal to noise ratio is improved however the photocurrent sensitivity to the barrier is diminished[20]. Under reverse bias the photocurrent is enhanced by the higher junction field strength which decreases the probability of recombination, however it also decreases the barrier thickness which allows tunnelling mechanisms to contribute to the photocurrent signal.

5.5 *pn*-junctions and photocurrent mechanisms

When a semiconductor in equilibrium (zero applied bias) is illuminated by photons of energy $h\nu$, greater than the band-gap energy, E_g, of the semiconductor then optical absorption occurs and an electron is excited to the conduction band leaving a vacated hole in the valence band, thus forming an electron-hole pair. The electron only remains in its excited state for a short period, known as the carrier lifetime, τ (order ~10pS), during which period carriers can diffuse up to the carrier diffusion length, L ($L^{electrons}$ ~100nm, and L^{holes} ~10nm), before the electron relaxes to recombine with a valance band hole. If the photo-excitation occurs within the depletion region or within a diffusion length from it, an electron-hole pair is created and the charge carriers are quickly separated by the built-in field of the depletion regions of the *pn*-junction, establishing an electric field in the sample that propagates a photocurrent, as shown in Figure 5.2. If the charge separation occurs within the *p*-type depletion layer the photo-excited electron is quickly swept across the *pn*-junction by the built-in field into the *n*-type semiconductor, thus lowering its energy, while the hole is trapped in the *p*-type material by the barrier. Conversely, when an electron-hole pair is

generated within the *n*-type depletion layer it is the hole that undergoes the energetically favourable transition across the junction into the *p*-type semiconductor. Thus the excitation of electron-hole pairs within the depletion region of a *pn*-junction results in the transport of the minority carrier across the junction, inducing a "photocurrent" that flows in the reverse direction.

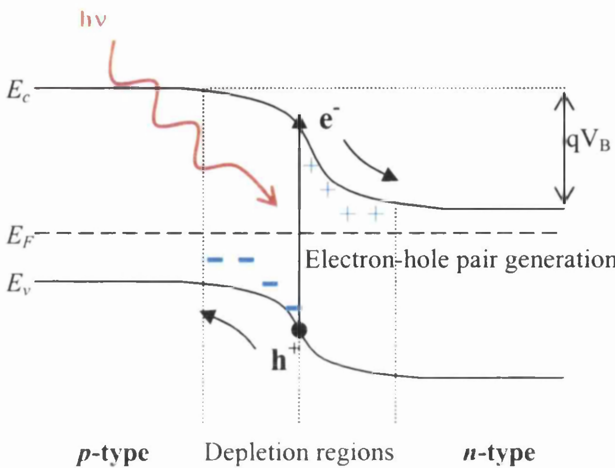

Figure 5.2 Photo-excited electron-hole pairs within the depletion region of a *pn*-junction are quickly separated by the built-in field inducing a reverse direction (or leakage) "photocurrent".

Unlike the photocurrent imaging of Schottky diodes, semiconductor heterostructure devices consisting of *pn*-junctions are imaged in these studies with the NSOM probe oriented parallel to the growth plane of the device i.e. in the cross-sectional configuration (see section 6.5). Within the bulk regions of the device there are no fields and thus a photocurrent does not propagate when the NSOM probe is scanned there, however when the probe scans across the interface of a *pn*-junction charge carriers are separated and a photocurrent is sensed. Therefore near-field photocurrent imaging is extremely useful in accurately locating the precise position of *pn*-junctions and determining the extent of their associated depletion regions. The near-field photocurrent imaging technique directly images the electronic device structure of fabricated devices, which can be correlated with the simultaneously acquired surface topography, and collection imaging modes. Photocurrent imaging effectively maps the minority carrier transport properties of the device, and is sensitive to growth uniformity and non-radiative defects, properties that are very important to device physics.

The resolution of cross-sectional near-field photocurrent imaging of semiconductor heterostructures is determined by a combination of the excitation volume (near-field aperture area × absorption length) and the minority carrier diffusion length, L. The minority carrier type and diffusion length depends upon the doping of the different layers in the device; therefore the photocurrent resolution will vary across the device structure according to the material properties. The near-field aperture area is of the order r^2, where r is the aperture radius, the evanescent waves of the near-field aperture decay exponentially away from the probe within approximately r, thus the excitation volume is of the order r^3. Photocurrent is thus generated from a total source volume of a combination of the excitation volume and the carrier diffusion, the spatial dependence of the photocurrent I_{photo} is given by[21,22]

$$I_{\mathrm{photo}} = I_0 \exp(-x/L) \qquad \textbf{(5.5)}$$

where

$$L = (D\tau)^{1/2} \qquad \textbf{(5.6)}$$

and D is the diffusion constant and has the value

$$D = k_B T\mu/q \qquad \textbf{(5.7)}$$

μ is the carrier mobility, and I_0 is the current observed from the centre of the depletion region. By estimating the quantum efficiency of evanescent modes to be 8% and the carrier lifetime from far-field excitation experiments, Buratto *et al*[13] conducted photocurrent imaging on InP based devices and estimated resolutions of 430nm and 150nm in the p and n type materials respectively. However the observed resolution was approximately 250nm in the n-type material, still indicating an asymmetric photocurrent response of pn-junctions. Similar investigations of photocurrent capabilities on heterostructures were conducted by Unlu *et al*[14] who reported an average resolution of ~350nm, which is in agreement with the results of Buratto *et al*[13]. The studies of multi-quantum barrier and buried-heterostructure laser devices conducted here demonstrated average lateral resolution in the range 100-200nm, similar to that observed in the analysis of Schottky diodes.

5.6 Summary

Near-field photocurrent microscopy is a very powerful imaging mechanism, especially when coupled with other simultaneous NSOM modes such as shear-force topography or collection NSOM. The photocurrent generation mechanism is

dependent upon the material system being examined, which must be considered when interpreting photocurrent images. Another factor that must be considered is the influence of topographic artefacts on the near-field photocurrent signal response; however this is only a factor when imaging samples of rough surface topography and non-uniform metal top-contact layer thickness.

Within this chapter the theoretical origins of photo-excitation measurement techniques is discussed, along with the far-field predecessors to near-field photocurrent imaging. The mechanism of photocurrent generation at the buried Schottky interface is discussed along with the possible causes of photocurrent contrast that allow Schottky barrier properties to be mapped at high resolution, providing insight into the sub-micron distribution of interface properties previously characterised by large scale averaging techniques. Such interface phenomenon includes interface states, defects, voids, and carbon segregation, that all may cause variations in the Schottky barrier height.

The corresponding mechanisms responsible for photocurrents in *pn*-junction based laser structures are similarly discussed. These allow the accurate imaging of *pn*-junctions, and the distribution and extent of the associated depletion regions. Coupling knowledge of the device operational mechanisms with this can reveal probable conduction pathways throughout the device structure, and assess the functionality of a device and quality of its fabrication.

5.7 References

[1] R. Williams, *Phys. Rev.* **140**, A569 (1965)

[2] C. Coluzza, G. Margaritondo, A. Neglia, R. Carluccio, *J. Vac. Sci. Technol. A* **10** (4), 744 (1992)

[3] S.M. Lindsay, *Phys. Stat. Sol.* A **53**, 311 (1979)

[4] M. Frischholz, K. Rottner, A. Schoner, T. Dalibor, G. Pensl, *Diam. Relat. Mater.* **6**, 1396 (1997)

[5] L. Reimer, *Scanning electron microscopy*, (Springer, Berlin, 1985)

[6] T. Wilson, E.M. McCabe, *J. Appl. Phys.* **61** (1), 191 (1987)

[7] R. Fowler, *Phys. Rev.* **38**, 45 (1931)

[8] G. Gigli, M. Lomascolo, M. De Vittorio, R. Cingolani, A. Cola, F. Quaranta, L. Sorba, B. Mueller, A. Franciosi, *Appl. Phys. Lett.* **73** (2), 259 (1998)

[9] D.K. Schroder, *Semiconductor material and device characterisation 2nd Ed.*, (J. Wiley and sons, NY, 1988)

[10] T. dell'Orto, J. Almeida, C. Coluzza, A. Baldereschi, G. Margaritondo, M. Cantile, S. Yildirim, L. Sorba, A. Franciosi, *Appl. Phys. Lett.* **64** (16), 2111 (1994)

[11] J.W.P. Hsu, E.A. Fitzgerald, Y.H. Xie, P.J. Silverman, *Appl. Phys. Lett.* **65**, 344 (1994)

[12] K. Karrai, G. Kolb, G. Abstreiter, A. Schmeller, *Ultramicroscopy* **61**, 299 (1995)

[13] S.K. Buratto, J.W.P. Hsu, J.K. Trautman, E. Betzig, R.B. Bylsma, C.C. Bahr, M.J. Cardillo, *Appl. Phys. Lett.* **65** (21), 2654 (1994)

[14] M.S. Unlu, B.B. Goldberg, W.D.Herzog, D. Sun, E. Towe, *Appl. Phys. Lett.* **67**, 1862 (1995)

[15] J. Almeida, T. dell'Orto, C. Coluzza, G. Margaritondo, O. Bergossi, M. Spajer, D. Courjon, *Appl. Phys. Lett.* **69** (16), 2361 (1996)

[16] C.R. Wronski, B. Abeles, G.D. Cody, T. Tiedje, *Appl. Phys. Lett.* **37**, 96 (1980)

[17] Q. Xu, M.H. Gray, J.W.P. Hsu, *J. Appl. Phys.* **82** (2), 748 (1997)

[18] J.A. DeAro, D. Moses, S.K. Buratto, *Appl. Phys. Lett.* **75** (24), 3814 (1999)

[19] A.A. McDaniel, J.W.P. Hsu, A.M. Gabor, *Appl. Phys. Lett.* **70** (26), 3555 (1997)

[20] J. Almeida, G. Margaritondo, C. Coluzza, S. Davy, M. Spajer, D. Courjon, *Appl. Surf. Sci.* **125**, 6 (1998)

[21] T. Fuyuki, *J. Phys. D* **13**, 1503 (1980)

[22] H.J. Leamy, *J. Appl. Phys.* **53**, R51 (1982)

Chapter 6
Experimental

6.1 Introduction

Within this chapter the key experimental developments are discussed including the device specific procedures implemented in making electrical contact with samples to enable their subsequent imaging. The chapter begins with the standard configurations and specifications of the two NSOM's used and progresses to discuss the development of near-field photocurrent imaging, focussing on the amplification of small signals and the implications of electrical noise to such measurements. The implementation of near-field imaging mechanisms with respect to Schottky diodes and laser diodes is then addressed, including the vital formation of electrical contacts and imaging procedures. Finally the problem of scanning artefacts is addressed with a theoretical discussion and experimental precautions taken to minimise such pollution of data.

6.2 NSOM configurations / specifications

During this work two commercial near-field scanning optical microscopes have been utilised, the Veeco Aurora-2 and Aurora-3 NSOM's. The example of the Aurora-2 is first used to demonstrate the implementation of NSOM, the differences and modifications of the Aurora-3 are subsequently described.

The fundamental element used in both NSOM systems is identical and is the fibre optic aperture probe; probes consist of a single-mode optical fibre tapered to a sharp end with an aperture produced of typically 50nm in diameter. The fibre taper is also coated with aluminium approximately 100nm in thickness to increase optical confinement and realise resolutions dictated by the size of the aperture. Note that during the course of these studies NSOM probes with larger aperture diameters of 100nm were also employed to increase signal throughput in cases of collecting extremely low optical intensities and low quantum yield efficiency.

As discussed previously in chapter 2, it is not only the aperture dimensions that make near-field experiments possible, the sample must also be scanned within the near-field

zone of the aperture which requires a tip-sample separation of usually less than 10nm. The Aurora instruments operate in a non-contact, shear-force mode and they use a quartz tuning fork mechanism to control probe-sample separation, as described fully in chapter 2. The NSOM probe is attached to the side of one prong of the tuning fork with the tip slightly proud of the end (figure 2.5, section 2.6.2) [1]. The vibrating piezoelectric tuning fork produces a small voltage which is used to measure the probe vibration amplitude by amplification and detection using a lock-in amplifier. The phase difference between the tuning fork signal and the drive signal is measured and utilised in the feedback circuit, as illustrated in Figure 6.1.

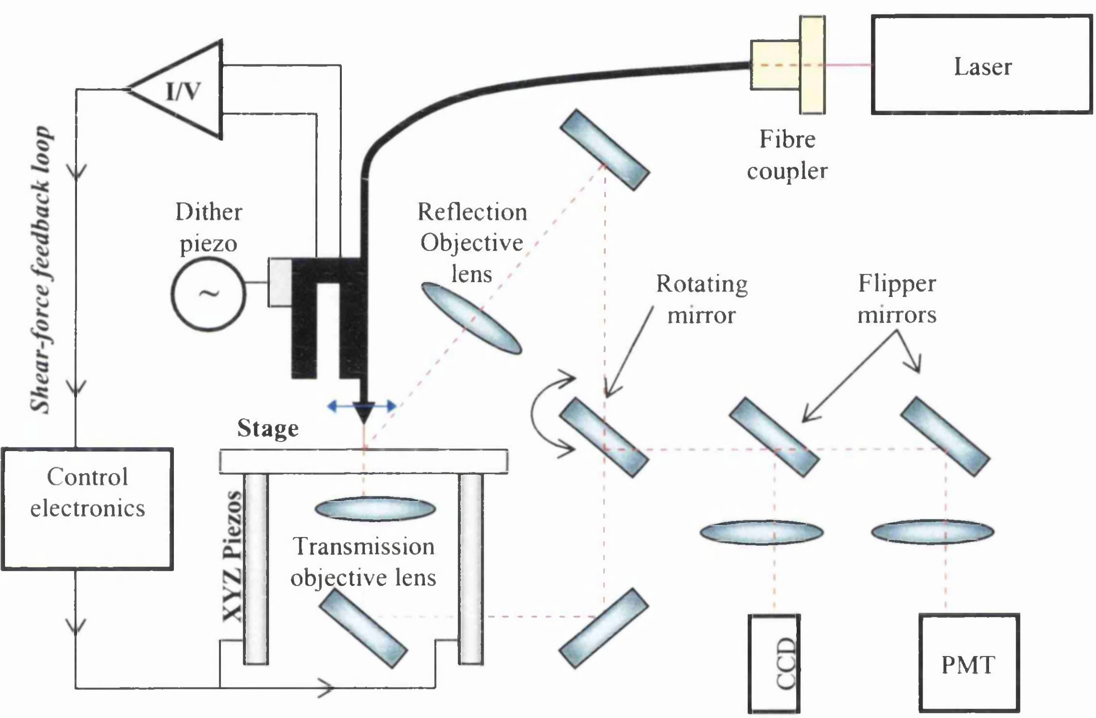

Figure 6.1 Schematic representation of the Aurora-2 near-field scanning optical microscope.

Both Aurora systems use identical probe / tuning fork systems that are mounted on machined PCB (printed circuit board) plates which are interchangeable in the microscope heads, these are installed under three sprung contact pins that make electrical connection to the tuning fork and serve to mechanically locate the PCB mounting plate.

Crude probe positioning is performed using a tripod combination of finely threaded posts, two are manually adjusted and one motorized for fine control. The sample is

mounted directly upon the scanning stage which is controlled by a three piezo scanner arrangement, which is itself mounted upon a precision *xy* table driven by DC motors that facilitate accurate alignment of the probe and sample to the desired location.

The schematic of Figure 6.1 also illustrates the various optical paths of the Aurora-2 NSOM and some of the standard optical components used in recording data, focussing the optical elements, and monitoring the probe-sample approach. Both the reflection and transmission optical paths are illustrated, and are selected between using the rotating mirror, located in the optical tower. The reflection objective lens is located just above the sample fixed at an angle, while the transmission objective lens is positioned directly beneath the sample stage; both lenses are positioned with *xyz* translators for focussing.

When approaching the tip and sample, the reflected path is used and directed to the CCD camera by the flipper mirrors, the highly magnified view of the probe and sample is then displayed on an external monitor and used for the final positioning and approach. The probe and sample are illuminated by a light source located within the microscope head controlled externally.

When using the NSOM aperture to illuminate the sample as a near-field optical source, the fibre tail of the NSOM probe is coupled to an external laser source. A 633nm, 1.96eV HeNe laser, and a 488nm, 2.55eV Ar^+ laser were available for these investigations, both producing ~25mW for coupling into the probe fibre tail. The instrument can then be setup for reflection or transmission-NSOM by using the rotating and flipper mirrors to guide the desired optical path to the photomultiplier detector PMT. The NSOM probe is also used as an illumination source when performing near-field photocurrent microscopy, in this configuration only the reflection path and CCD are used in approaching the probe and sample. Photocurrent measurements are performed by system modifications which are discussed in detail in section 6.3.

Light emitting samples can be imaged by using the NSOM aperture to collect light at the sample surface using the instrument in the collection-imaging configuration (see chapter 2, figure 2.6(d)). The probe samples and collects the light emitted at the

aperture location on the sample surface, which then propagates through the fibre. The local optical intensity is then measured by focussing the end of the fibre tail onto the PMT detector; however intensities typical of this configuration are very low and require a more sensitive optical detector, such as an avalanche photo-diode, APD. The detector used was a Perkin Elmer photon counting module, which is highly sensitive and in theory can detect individual photons; however its sensitivity requires careful attention to prevent destructive saturation of the device which can measure a maximum count rate of 13 MHz, which implies a maximum count rate of 65 KHz at a typical integration time of 10ms. The APD is ideally suited to performing collection NSOM and may also by utilised in performing low intensity reflection or transmission-imaging by replacing the PMT by the APD in apparatus arrangement set out in Figure 6.1. When using the APD in any measurement configuration the APD detection time, i.e. integration time, becomes the rate determining step of the imaging process by virtue of its comparatively long duration, and thus the time spent by the probe at each image pixel is dictated by the APD integration time instead of the scan rate parameter in the device software.

The Aurora-3 NSOM is essentially a very similar instrument to the Aurora-2 with some additional improvements. The most apparent difference is that the reflection and transmission optical paths are independent and have their own CCD cameras. The benefit of separating the optical pathways is that reflection and transmission-imaging mechanisms can be performed simultaneously, requiring two optical detectors. The most significant improvement of the Aurora-3 is that it uses a real-time, closed-loop linearised scanner, which is extremely accurate and eliminates all piezo-drift, this was a typical problem encountered when using the Aurora-2 instrument for prolonged periods. The closed-loop scanner also allows for the NSOM probe to be accurately manipulated to a location and held at a point for a period enabling localised point spectroscopy to be performed.

Both NSOM systems are mounted upon extremely heavy vibration isolation tables which are suspended by pressurised air-leg pistons to mechanically isolate the microscopes. Optically they are both isolated by highly efficient optical enclosures, removing all external background light, which also prevents disruption of the sensitive shear-force scanning condition by unwanted noise vibration. To ensure

background optical levels are minimised imaging is performed in a dark room with non-essential instrument panels blackened and monitors dimmed, this is crucial in enabling the alignment of the very sensitive APD detector.

6.3 The development of near-field photocurrent microscopy – from macroscopic to nanoscopic photocurrents

Far-field photocurrent experiments using micron scale illumination sources have been successfully utilised for a number of years, these include optical beam induced currents, OBIC[2,3,4], and the higher resolution electron beam induced conductivity measurements, EBIC[5]. Both methods rely on far-field focussing techniques and use a modulated illumination source allowing the implementation of lock-in amplification detection. Although both of these methods have been successfully implemented they also have a common weakness, the ultimate resolution attainable is of micron order magnitude, whereas it is desirable to examine interfaces with much smaller nanoscale sensitivity. This is achieved by combining the nanoscale illumination properties of a near-field scanning optical microscope with photocurrent imaging experiments and has previously been performed to a limited extent for semiconductor devices including Schottky diodes[6,7], semiconductor heterostructures[8,9], and solar cells[10]. All of these previous near-field photocurrent experiments on varying samples used a common photocurrent measurement configuration, relying solely on a lock-in amplification detection scheme as in the far-field scenarios.

Near-field photocurrent microscopy modifications to the NSOM, in the case of the work presented here, were developed using Ni-SiC Schottky diodes as the sample, thus the preparation of suitable samples was refined in parallel with the development of the photocurrent detection technique. The preparation and improvement of suitable Ni-SiC samples is discussed in detail later, this section focuses on the measurement of near-field induced photocurrents. Photocurrent generation and near-field induced photocurrents are discussed in chapter 5.

Ni Schottky contacts are deposited on the SiC wafer surface through a mask in the form of 600μm diameter circular dots. Far-field photocurrent measurements are performed by focussing the output of a cleaved fibre optic coupled to a 25mW laser onto the entire Ni dot surface. The dot has an external electrical connection upon the

Ni surface which is connected to a Keithley 2400 Source-meter and 6485 Pico-ammeter, the circuit is completed with a connection to the SiC back contact. Note making electrical connections to Ni-SiC diodes is discussed in detail in the following sections. Such far-field photocurrent measurements were performed frequently as a crude test of the Schottky nature of a sample, i.e. testing the quality of the Schottky junction, if a sample is a poor Schottky junction or in the extreme case an ohmic interface then no photocurrent is observed. The quality of the electrical connections made with the sample can also be assessed in this way, if the top contact has pierced through the Ni and is in direct contact with the substrate then again no photocurrent response is observed.

Typically far-field illumination of entire Ni Schottky dots on SiC excited a photocurrent intensity measured by the pico-ammeter to be in the range 10^{-9} to 10^{-8} Amps. This is a very small photocurrent signal for entire dot illumination and indicates the difficulties presented by near-field induced photocurrent measurements especially upon such samples displaying very low optical interaction. A simple estimate can be made from these far-field photocurrent intensities of the expected orders of near-field induced photocurrent to be measured by assuming that both illumination regimes exhibit the same intensity per unit area. Far-field illumination covered a circular dot of 600μm diameter whereas the near-field excitation field is restricted by the circular aperture of 50nm diameter this implies a near-field photocurrent intensity of 10^{-17} to 10^{-16} Amps, which is negligible. However, fortunately the interaction of the evanescent waves of the near-field aperture with the sample surface is more efficient than the assumption made by this estimation and so the near-field intensity is much greater than the simple far-field equivalent over the 50nm diameter area, consequently the near-field photocurrent intensity will also be greater.

As demonstrated by previous near-field experiments modulation of the illumination source and lock-in detection is necessary, and was confirmed as essential by a near-field photocurrent imaging experiment using the Keithley 6485 Pico-ammeter as a detector and coupling its varying analogue voltage output to an external input of the NSOM ECU (electronic control unit) for mapping. This was performed using an opened-aperture NSOM probe that delivered a large but broad optical intensity and

induced a detectable level of photocurrent. However the signal measured by the pico-ammeter and mapped by the NSOM ECU was a replica of that plotted by the shear-force topographic image, indicating that the varying potential applied to the scanner piezos in following the sample surface induced a current within the closely mounted sample or connection wires, which dominated the small photocurrent signal. Screening of this interference using earthed metal shielding dramatically improved the response but still highlighted the necessity for source modulation and lock-in detection to fully remove noise from the signal.

Near-field induced photocurrent signals are inherently tiny and thus require careful precautions to reduce the influence of noise within the photocurrent detection system. The most efficient method of noise rejection is the use of a lock-in detection technique whereby the optical excitation field is modulated at a tuned frequency that is referenced to the lock-in amplifier, LIA. The sample is illuminated by the oscillating optical field thus exciting an oscillating photocurrent within the sample. The photocurrent signal, plus noise, is input into the LIA which detects signals that oscillate as the reference frequency, amplifying them to specified parameters, and rejecting all other signals i.e. noise influences. The strength of the technique relies upon the tuning of the optical field modulation, i.e. reference frequency, to a frequency that is dissimilar to the oscillation of any unwanted noise signals. The available frequency range however is limited by the photocurrent response time of the sample and the scan rate of the photocurrent imaging process, the excitation field cannot be modulated faster than the sample response while it must also be faster than period of the data collection time per imaging pixel. These considerations were taken into account and the optimum optical modulation rate estimated and finely tuned experimentally.

Lock-in detection is a very effective technique, however further noise reduction steps are required in accurately measuring and mapping such small currents. During the photocurrent imaging process the sample is acting as a current source and has a very high impedance, thus it is highly susceptible to the pick-up of noise. In order to reduce the influence of unwanted signals it is necessary to convert the varying photocurrent signal to a varying voltage which is a low impedance signal less susceptible to noise, this must be done as physically close as possible to the sample

and is performed using a I-to-V preamplifier. The circuit used for the I-to-V photocurrent preamplifier is displayed in Figure 6.2, and is based on the Analog Devices AD549 ultra-low input bias current operational amplifier, which is a monolithic electrometer op-amp with very low input bias current and input offset voltage drift[11]

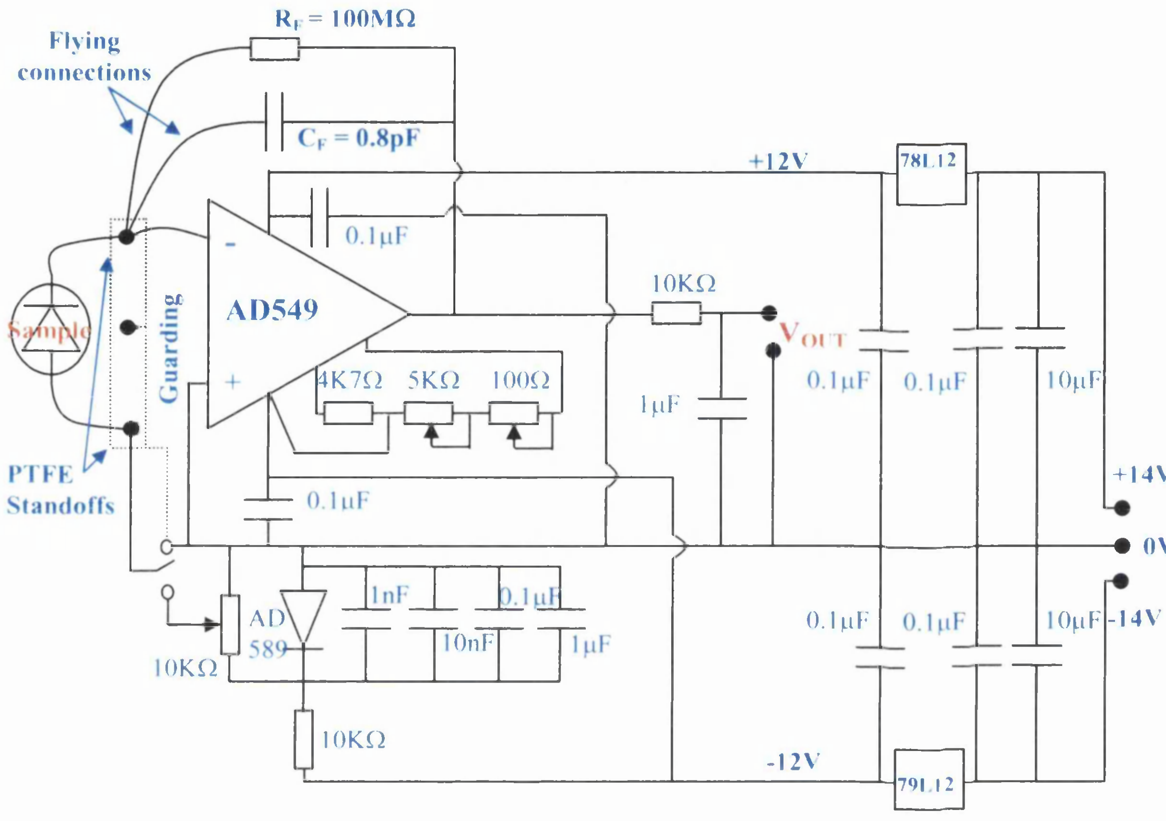

Figure 6.2 I-to-V photocurrent preamplifier based on the AD549 ultra-low input bias current operational amplifier.

The preamplifier is connected to the sample by single-core shielded cables which are of the minimum required length and connect to the op-amp via PTFE standoffs that are isolated by an earthed guarding loop, to prevent surface leakage on the printed circuit board, PCB. The AD549 op-amp is mounted in a PTFE socket and the photocurrent signal is connected from the standoff to the inverting input pin of the amplifier by a flying connection. The remaining sample terminal is connected from its standoff to either the earth rail or a stable variable potential between 0V and -1.0V determined by the 10KΩ potentiometer connected across AD589 reference diode and smoothing capacitors. The feedback resistance R_F and capacitance C_F are connected

from the op-amp output back to the inverting input using flying leads to eliminate surface leakage of the PCB, the voltage output is also screened before the output terminal by a low-pass filter.

The AD549 op-amp is an extremely sensitive device, therefore a stable power source is essential to its accurate operation, requiring the stability of a battery supply over the possible fluctuations of a mains driven power source. The op-amp is driven by two banks of three nickel metal hydride (4.8V, 150mAh) rechargeable PCB batteries, connected in series thus delivering ± 14.4V to the positive and negative rails, the 0V rail is a floating earth referenced at the centre point between the two 14.4V banks of cells. The two banks of cells are trickle charged through a 210Ω resistor and (4002) diode in series at 18V. The batteries are connected to the op-amp circuit by positive (78L12) and negative (79L12) voltage regulators and smoothing capacitors, which control the driving voltage to a stable ±12V. The driving voltage is finally smoothed one last time by the 0.1μF capacitors located very close to the AD549's power input pins. The circuit is constructed to be as compact as possible minimising PCB connection lengths, and free space is covered with earthed copper providing additional shielding from noise, particularly surrounding the op-amp.

The I-to-V photocurrent preamplifier circuit and power source is housed within an earthed die-cast enclosure for additional screening as shown in Figure 6.3. The preamplifier inputs are carried by single-core screened cables, however the last 5cm of the connections are very thin, bent, insulated but unscreened wire, this was necessary to allow the sample scanning stage free movement, and apart from the sample is the only unscreened element in the photocurrent detection scheme. The varying voltage output of the preamplifier is input directly into the LIA, where the photocurrent signal is extracted and amplified via lock-in with the reference signal from the optical chopper, used to modulate the laser source prior to launching into the NSOM fibre probe. The optimum chopper frequency for signal detection and noise rejection was estimated and experimentally determined as 169Hz. The LIA is a Stanford Research Systems SR850 DSP, and has a maximum sensitivity of 2nV. The preamplifier exhibits a gain of 10^8 adequately increasing the near-field photocurrent

signal to a detectable level. The output from the LIA is input into the NSOM ECU for mapping via an external data channel with 0-10V limits.

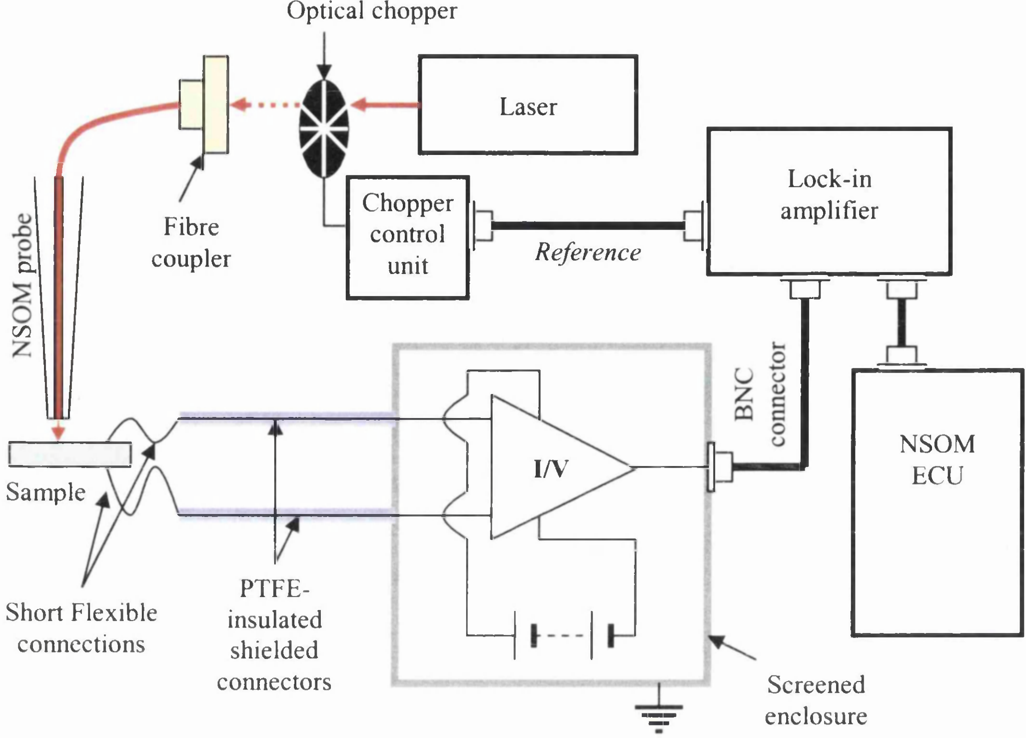

Figure 6.3 Near-field photocurrent imaging configuration. The laser output is modulated by an optical chopper prior to launching into the NSOM probe fibre tail, the frequency of which is referenced to the LIA. The sample is connected directly to the I-to-V photocurrent preamplifier (Figure 6.2) which is housed within an earthed die-cast enclosure along with the battery power source, the output of which is input into the LIA, and subsequently mapped by the NSOM ECU.

The voltage offset of the amplifier is an important factor when imaging different device samples, the I-V characteristics of devices can vary considerably and this is reflected in the dark current measured induced by a tiny offset voltage. The various stages of the photocurrent detection scheme have their own input limits which are easily saturated preventing photocurrent detection, therefore it is important to minimise the offset measured in dark conditions. This is implemented by the 4K7Ω resistor and two multi-turn potentiometers connected in series, crude offset balancing is done by the 5KΩ potentiometer while fine trimming is performed by the 100Ω potentiometer.

6.4 NSOM analysis of Schottky diodes

The near-field scanning optical microscope was employed in the study of nickel Schottky contacts with silicon carbide using shear-force topographic imaging simultaneously with reflection and primarily photocurrent imaging mechanisms. The NSOM probe was approached onto the Ni surface oriented perpendicular to the surface plane and thus also to the Ni-SiC interface. When performing near-field photocurrent imaging in this configuration the shear-force topographic image follows the Ni surface contours, whereas the near-field photocurrent is sensitive to the buried Ni-SiC interface, i.e. photocurrent imaging aims to map nanoscale spatial variations in the buried Schottky barrier by optically probing through the thin Ni top contact. The success of photocurrent imaging of Schottky diodes is therefore dependant upon the thickness of the Ni top contact, too thick and the probing optical field will not penetrate to the Schottky interface. However there is also a minimum Ni thickness as electrical contact must be made to the Ni top contact without piercing directly through to the SiC substrate beneath. As discussed, there are several difficulties in the successful implementation of near-field photocurrent imaging of Schottky diodes and the thickness of the Ni layer is fundamental to this, therefore much effort was focussed into the preparation of suitable samples. Sample preparation techniques are discussed briefly as it is the implementation of near-field photocurrent imaging that formed the primary focus of the work.

6.4.1 Sample preparation: Ni-SiC Schottky diodes

The near-field photocurrent investigation of Schottky diodes focussed on nickel contacts with silicon carbide, a material system which has been implemented successfully but requires optimisation and remains the topic of investigations[12,13]. Schottky diodes were fabricated specifically for near-field photocurrent imaging with particular focus on the accurate deposition of uniform thin Ni top contacts, i.e. thin Ni Schottky contacts.

The basic sample structure (Figure 6.4) consisted of a silicon carbide substrate of 340.36μm total thickness including a 10μm thick *n*-type epilayer doped with Nitrogen at a concentration of 10^{16}cm^{-3}. The Ni back contact is deposited using an Edwards evaporator, and subsequently the back Ni-SiC interface is manufactured to be ohmic in nature by annealing at a temperature of 900 to 1000°C for 10 minutes, this is

necessary as Ni-SiC interfaces are naturally Schottky in character when deposited[14,15]. The Schottky Ni top contacts are deposited through a tantalum mask to produce circular contacts of 600 or 800μm in diameter (depending on the tantalum mask used), this is necessary as the SiC surface is not perfect and contains a certain density of surface defects that, when incorporated in a Ni-SiC interface provide a current leakage path dominating the device characteristics, resulting in ohmic behaviour of the junction. By producing finite circular contacts as opposed to blanket coverage of the SiC surface, the probability of a Ni-SiC contact containing such a defect is reduced. The critical top contacts were deposited using either a high vacuum Edwards evaporation chamber or an ultra-high vacuum evaporation system, however for both the back contact was deposited first using the HV Edwards system and subsequently annealed to ohmic in the same system.

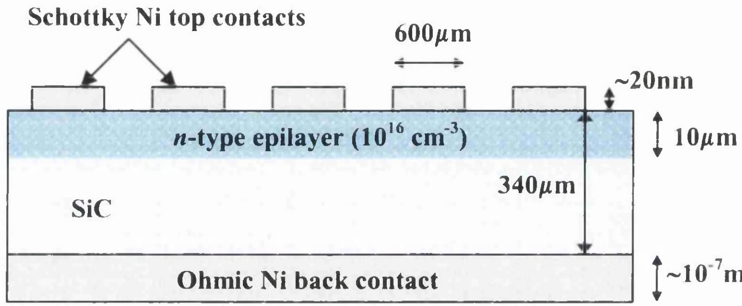

Figure 6.4 Basic structure of a Ni-SiC Schottky diode fabricated for analysis by near-field photocurrent imaging.

Prior to contact deposition by either the HV Edwards evaporator or UHV evaporation system the SiC wafer surface was processed by a sequence of ex-situ cleaning and etching steps to produce an atomically clean surface suitable for the growth of accurate electrical contacts. The cleaning process comprised of a solvent clean, a piranha clean, and an RCA clean, the full routine is described in appendix 11.1. The solvent clean uses trichloroethylene, acetone and isopropanol to gently remove oil based contaminants and dust from the wafer surface. The piranha clean uses sulphuric acid and hydrogen peroxide to further remove organic substances. The RCA cleaning step is harsher and chemically removes ionic contaminants, organic substances and strips surface oxides by etching the SiO_2, leaving the SiC surface atomically clean and flat[16].

6.4.2 Contact deposition: Edwards evaporation chamber

Ni deposition was primarily performed using an Edwards E306A thermal evaporator which operated at high vacuum in the 10^{-6} to 10^{-7} mbar range, achieved with a rotary and a diffusion pump. Working in a HV environment has the advantage of a drastically reduced pumping time over UHV techniques, resulting in much shorter sample preparation time, also deposition in an Edwards evaporator is comparable to industrial manufacturing processes.

The Edwards system achieves metal evaporation by e-beam bombardment using a tungsten coil filament to irradiate small pieces of pure nickel within a graphite crucible, typically the filament current is 20mA and the crucible is at a potential of 4.2kV. The sample is located approximately 30cm directly above the Ni source oriented with the side to accept Ni deposition facing downwards, with the SiC face perpendicular to a line intersecting the crucible. For back contact deposition the sample is fixed by two small clips at opposite corners leaving the SiC face open to Ni deposition. Top contacts are deposited through a tantalum mask perforated with a mesh of either 600 or 800μm diameter holes that is fitted tightly to the SiC wafer surface, thus the mask also serves to locate the sample wafer during deposition. A translatable shield is inserted between the crucible and sample which, when in position, shadows the sample from the evaporating Ni flux, and is translated out of the flux path to control the Ni deposition time. The metal evaporation rate, or Ni flux, is measured by an in-situ crystal monitor, and once the desired constant flux is achieved the shield is translated away to commence deposition. The deposition rate is controlled by the filament current and crucible potential, and measured using the crystal monitor, thus the deposited layer thickness is subsequently controlled by the deposition time.

Metal evaporation by this method is suited to the rapid deposition of thick layers ($\geq 10^{-7}$m), however near-field photocurrent imaging of Schottky interfaces requires uniform thin layers of the order 10^{-8}m. Thin layer deposition was achieved by establishing a very low steady flux rate, only possible after the initial melting of the small Ni pieces within the crucible, once a stable flux was achieved the sample shield was removed for very short deposition times typically 20sec to 1min. However this process was dependant on the accuracy of the crystal monitor in measuring the Ni

flux, which proved to be a very unreliable technique, resulting in a hit or miss nature to thin layer deposition using the Edwards evaporation system.

The Edwards evaporation system was used in the preparation of the majority of Schottky top contacts examined primarily due to equipment availability, and also as samples manufactured by this technique were prepared in approximately half the duration required when using UHV deposition.

6.4.3 Contact deposition: UHV evaporation system

Samples with the top contact deposited in the UHV evaporation system were cleaned as previously discussed, and the thick back contact deposited in the Edwards evaporation system, without annealing. In the UHV system, as in the Edwards evaporator, the top contact was deposited through a tightly fitted tantalum mask which mounted the sample onto a sample holder stub top-plate. When working under UHV conditions cleanliness is paramount, thus the stub top-plate and tantalum mask were cleaned via an Aqua Regea etch consisting of a 3:1 mixture of nitric acid to sulphuric acid for a duration of 2mins. Subsequently the mask and top plate were admitted to UHV (without sample) and degassed by e-beam bombardment using a previously degassed filament at 2.7A and an accelerating potential of 1kV. The sample mounting stub was then removed from vacuum and the re-cleaned sample (solvent clean and HF dip) clamped beneath the tantalum mask, and subsequently installed into vacuum. Prior to UHV deposition the sample was heat treated in vacuum by e-beam bombardment to a temperature of 1000°C, this removed oxygen from the sample surface and simultaneously annealed the previously deposited back contact to an ohmic nature. Ni contact deposition was performed with the sample oriented as in the Edwards system and similarly using a shield system to control the deposition time, metal was evaporated using an Oxford Research EGN4 mini e-beam UHV evaporator. Nickel of 99.99% purity was deposited at a rate of 1Å in 7sec, thus a 20nm thick top contact was deposited in 23mins. The benefit of depositing metal contacts in such is a system, apart from the high level of cleanliness, is the fine control of the evaporation procedure and the accuracy in depositing specifically thin layers, a result of accurate source calibration. However, the obvious drawback is the duration of the procedure which can take over seven days.

6.4.4 Schottky diode sample holder

The imaging of Schottky diodes is performed with the NSOM probe oriented perpendicular to the Ni top contact surface and approached from above. The photocurrent imaging mechanism requires external electrical connections to be made with the samples ohmic back contact and circular Schottky top contact in order to implement the photocurrent amplification / detection system. Therefore an electrical contact must be made with the 600 or 800μm diameter Schottky dot that does not physically interfere with the NSOM probe or tuning fork.

The thickness of the Schottky top contacts was optimised to be as thin as possible, in order to maximise optical penetration to the Schottky interface, whilst maintaining an adequate thickness to physically make electrical contact to, without penetrating directly through the Ni layer to the SiC substrate beneath. The coupling of these three requirements makes the formation of electrical connections with thin Schottky top contacts a formidable task, however this was achieved using the Schottky diode sample holder specified in Figure 6.5.

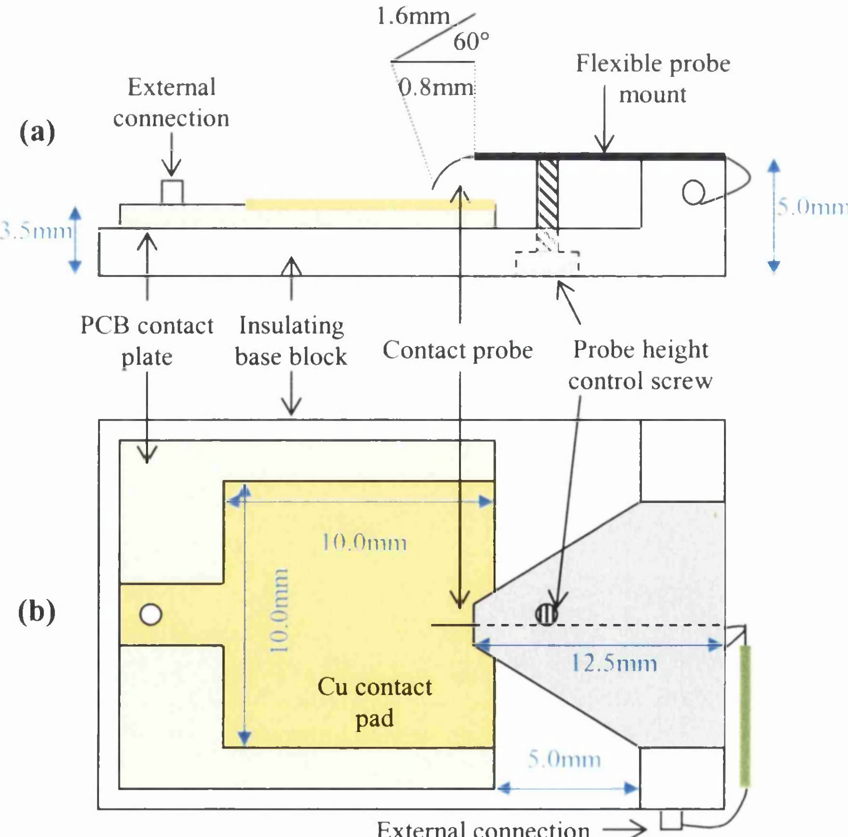

Figure 6.5 Schottky diode sample holder **(a)** side view, and **(b)** top view.

The Schottky diode sample holder was designed to mount directly onto the NSOM scanner stage and fit within the confinement of the NSOM scan head. The sample holder is constructed upon an insulating base block incorporating an elevated platform from where the flexible probe mount is located above the sample. The flexible probe mount is constructed from a composite of two insulating sheets, sandwiching the tail of the contact probe, and is designed to fit within a vertical opening within the NSOM scan head footprint. The contact probe is fine tungsten wire, bent into the desired form with a tip flattened parallel to the sample surface in order to reduce the probability of piercing through the thin Ni top contact to the SiC substrate beneath. The sample is positioned upon a copper contact pad, which makes electrical contact with the samples ohmic back contact, the copper (Cu) contact pad is etched onto a printed circuit board (PCB) incorporating a Cu track connecting to a short external connection pin, as displayed in the photo of Figure 6.6.

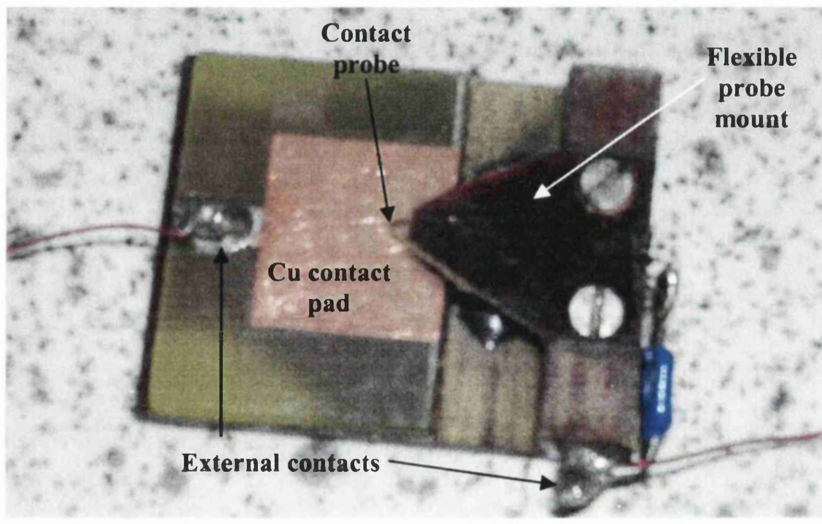

Figure 6.6 Photograph of the Schottky diode sample holder.

The height of the top contact probe is controlled by a small screw countersunk into the insulating base block, which exerts an upward force on the flexible contact probe mount. The tail of the top contact probe is finally led via an insulated wire to a fixed external connection pin mounted on the side of the base block, and both external connections are made using short lengths (~8cm) of thin flexible insulated wires to allow free movement of the NSOM scanner stage.

When establishing an electrical connection to the thin Ni Schottky layer the sample holder is connected to the Keithley 2400 Source-meter and 6485 Pico-ammeter and a 1V forward bias is applied. The sample is placed upon the copper contact pad of the sample holder and positioned beneath the tungsten top contact probe such that the tip of the probe is located slightly within the boundary of the Ni Schottky dot, leaving the maximum possible surface area accessible to the NSOM probe. The contact probe is then gently lowered using the finite adjustment of the countersunk control screw while monitoring the reading of the Keithley 6485 Pico-ammeter. When electrical contact with the Ni Schottky layer is established the external circuit is complete, and a current flows driven by the 1V bias, this is displayed by the pico-ammeter and signals the correct position of the top contact probe; further lower will result in the undesirable penetration to the SiC substrate. Once an electrical connection has been achieved I-V data is recorded prior to installation within the NSOM, using the described configuration of meters in order to establish the Schottky barrier height and ideality factor of the junction.

6.4.5 Near-field photocurrent imaging of Schottky diodes

Near-field photocurrent imaging is performed using the experimental configuration represented in Figure 6.7.

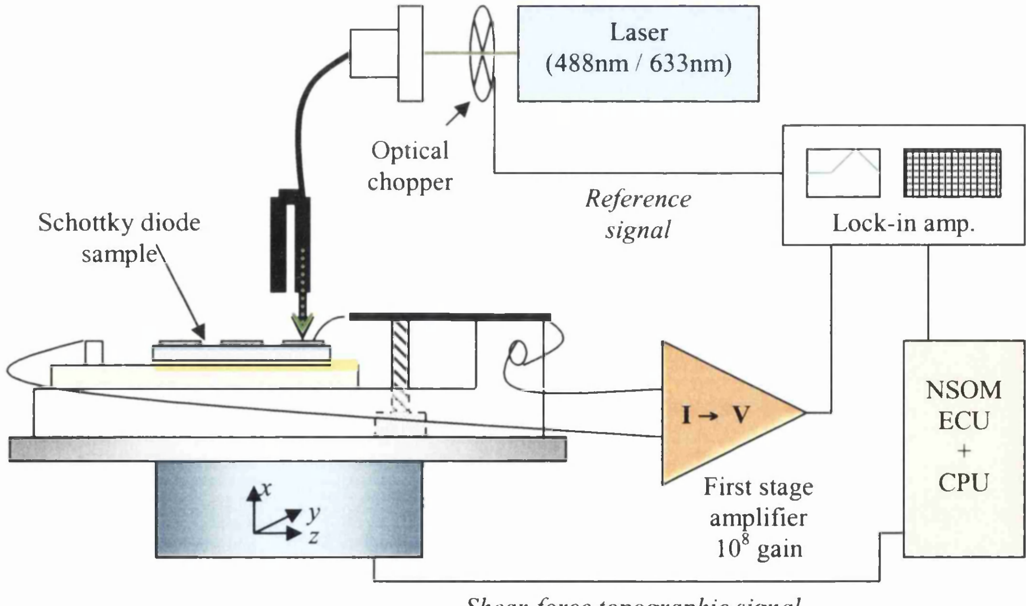

Figure 6.7 Schematic of the experimental configuration for the near-field photocurrent imaging of Schottky diodes.

The detection scheme has been described in detail previously. The NSOM probe and electrical contact probe are approached to the same Schottky dot oriented such that the tuning fork is on the opposite side of the NSOM probe to the contact probe, thus preventing interference of the large tuning fork with the equally large flexible contact probe mount. Note, it is also possible to perform collection NSOM with the sample mounted in the sample holder as the top contact probe does not interfere with the optical path of the reflection objective lens.

6.5 Cross-sectional NSOM analysis of laser diodes

The NSOM was utilised in the study of two specific laser structures, planar single quantum well lasers incorporating multi-quantum barrier reflectors, and buried heterostructure multi-quantum well lasers. The following configurations and procedures apply to both. In order to probe the device characteristics of laser diodes it is necessary to approach the NSOM probe in the cross-sectional orientation, i.e. in a perpendicular orientation directly onto the edge of the semiconductor wafer, this must be performed with the *p* and *n*-type electrodes in electrical contact with external devices.

6.5.1 Sample cleaving

The most important step in the successful imaging of laser devices is the cleaving of the sample, the semiconductor lasers examined develop a surface oxide in air which can grow to be tens of nanometers thick and have a detrimental effect on NSOM imaging techniques. The evanescent field at the NSOM aperture decays exponentially away from the aperture surface within approximately one aperture diameter length[17,18], therefore the presence of an intermediate oxide layer between the probe and sample will greatly reduce the intensity of the optical interaction between the aperture and the optically active surface of the sample. The reduction in optical intensity is highly undesirable considering NSOM imaging mechanisms rely on the detection of signals already at tiny magnitudes, also the surface oxide scatters the localised near-field optical source causing a spreading in the achieved resolution. Therefore it is essential to cleave a fresh sample surface immediately prior to imaging in order to reduce the impact of surface oxides.

Cleaving is performed by scoring the sample using a blade and straight edge (within a fume cupboard) and applying pressure to one end of the score mark. Ideally the sample breaks in a clean fashion exposing a perfectly flat clean surface to examine, however in reality this occurred for approximately 40% of cleaves. The problem with cleaving lies in the metal contact layers deposited on the samples surface which do shear in a clean fashion and can affect the uniformity of the cleave at the edge of the semiconductor wafer. Unfortunately the active region of interest of all the laser samples is located within microns of the metal contact layer. The only method of detecting if the required layers cleaved perfectly intact is to actually perform the near-field imaging experiments, which are time consuming to setup and perform, therefore the success determining step in the whole procedure is the most uncontrollable. When a good sample cleave is achieved freshly exposing a perfectly flat surface, the next step is to clamp the sample making good electrical contacts to the external electrodes of the sample device, ready for installation in the NSOM scanner.

6.5.2 Laser diode sample holder

The imaging of semiconductor diode lasers is performed by approaching the probe onto a freshly cleaved side edge from directly above. However clamping and making electrical contacts to diode lasers is inherently difficult due to the fragile nature of the wafers, which have a tendency to shear on the application of any localised force. Therefore the clamping surfaces have to be parallel, and are maintained so by the translation of the contact block on two tightly fitting translation rails. The sample is delicately clamped in the vice-like mechanism of the sample holder as in Figure 6.8, making electrical contact with the p and n contact layers. Gold leaf is used for the contact pads, due to its soft malleable nature, making it ideal for forming good electrical contacts with fragile samples, and can be seen in Figure 6.9.

The sample wafer is positioned between the two gold pads which are then slowly approached using the translation control screw. The contact is delicately approached until a tiny resistive force is experienced, immediately this is the contact point, any further approach typically results in sample fracture.

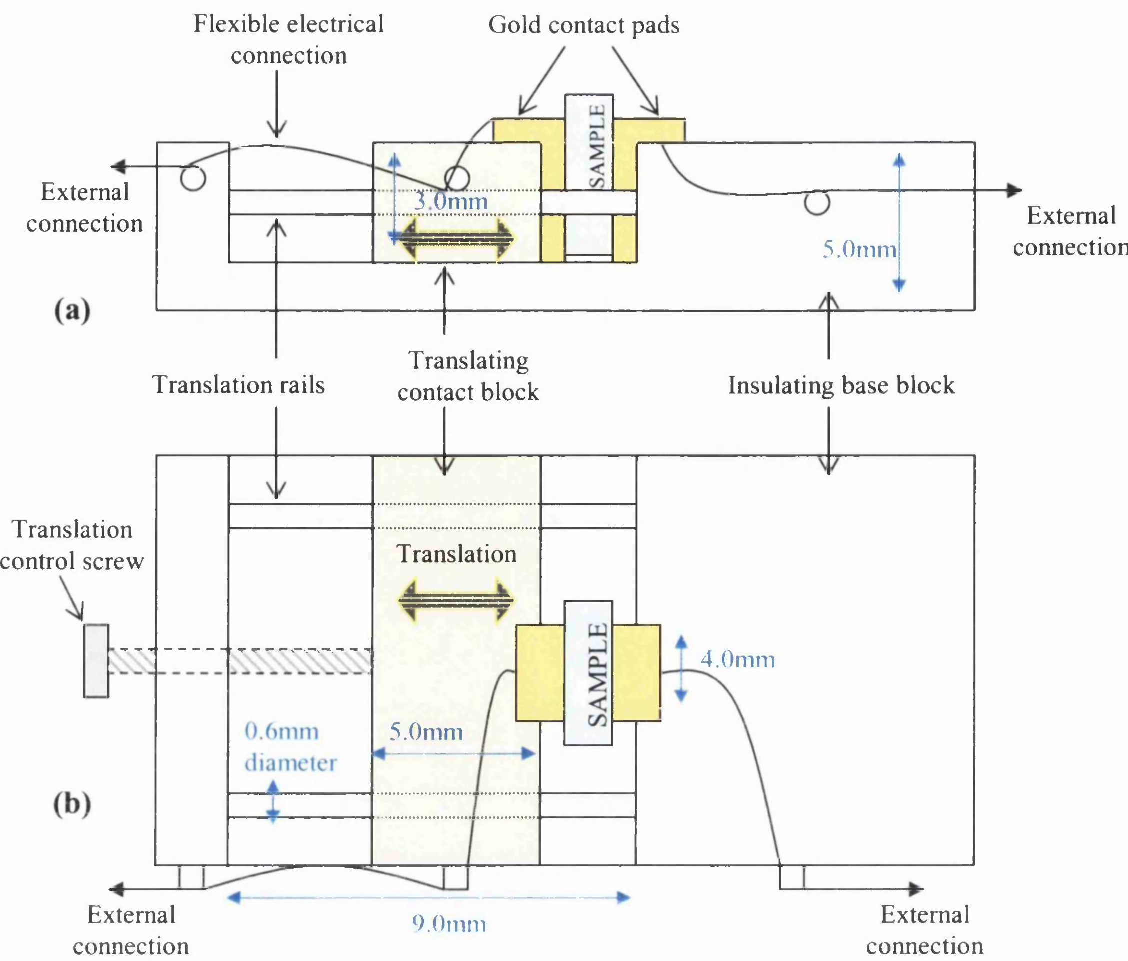

Figure 6.8 (a) side view, and **(b)** top view, of the sample holder used in the cross-sectional imaging of semiconductor diode lasers. The footprint area is $(25\text{mm})^2$.

The sample holder was designed to be as thin as possible, in order to fit within the NSOM system, while providing a large enough surface area to make contact to the sample wafer, and importantly electrical contact as close to the top cleaved edge as possible. The main block of the holder is insulating, thus isolating the gold contact pads from each other, and the sample from the NSOM scanner stage upon which it is mounted. Electrical contact leads are fed from the gold pads to the edges of the holder for connection to the external amplifier through the narrow gap (<10mm) between the NSOM scanner stage and tuning fork head. The electrical contact wire between the translating contact block and the anchor point for external electrical contact is made by very thin flexible insulated wire, which is slightly excessive in length and bent to ensure minimal resistance to the translation of the contact block that could result in asymmetric approach.

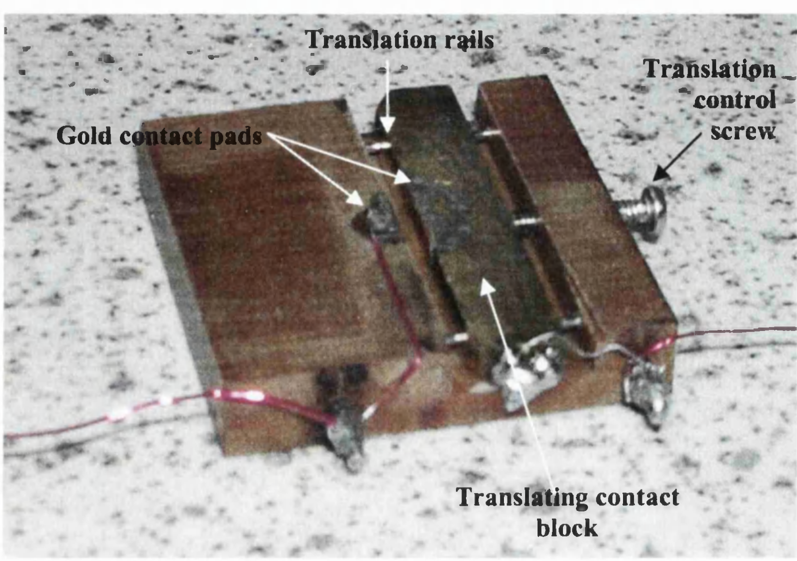

Figure 6.9 Photograph of the laser diode sample holder.

The sample holder is fixed to the NSOM scanner stage using highly adhesive thin double sided tape, and thin flexible insulated connection wires are passed between the NSOM tuning fork head and scanner stage to either a power source or external amplifiers, for collection NSOM or photocurrent imaging.

6.5.3 Cross-sectional collection imaging

Collection NSOM is performed upon an operating laser diode as displayed in the schematic configuration of Figure 6.10. The NSOM probe is approached and scanned by shear-force feedback as previously described, allowing the simultaneous measurement of the surface topographical profile. The external electrical connections of the sample holder (Figure 6.8) are connected to a power source, and the laser is biased in the forward direction. Light evolving from the sample is locally collected by the NSOM aperture and propagates up the probe and fibre tail, the loose end of which is clamped horizontally for focussing onto the detector.

An avalanche photo diode, APD, detector is employed to measure the very low optical intensities collected, which itself has a very small aperture approximately 1mm in diameter. Therefore, precise focussing of the collected light from the fibre tail onto the APD aperture is required; this is performed using two focussing lenses, the second of which is mounted upon micro-adjustable translators for final alignment onto the APD. The APD is a highly sensitive detector and the intensities measured

are typically very low, requiring 10ms or more APD integration time. Therefore, to increase the signal to noise of the measurement the optical focussing path of the APD is enclosed, restricting the incident light on the detector to the desired signal. Imaging is performed within a light-tight enclosure, however light emitted from the powered sample radiates within the enclosure producing background noise that is eliminated by enclosing the optical path.

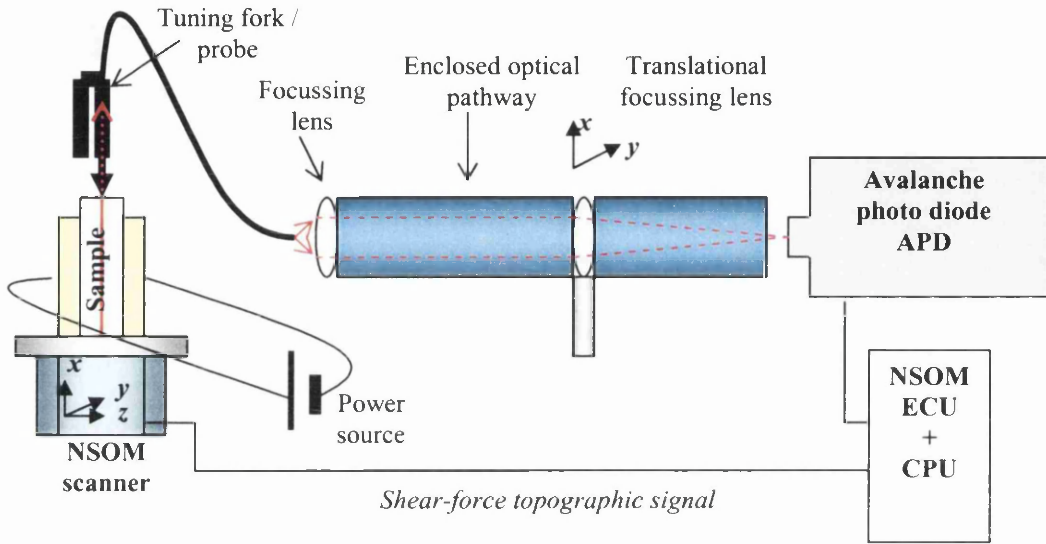

Figure 6.10 Collection mode NSOM performed in the cross-sectional orientation on an operating laser diode. The schematic displays the key elements of the configuration including the enclosed optical path focussing the probe fibre tail onto the APD detector.

The precise focussing of the collection signal onto the APD element is very difficult as the optical intensity is obviously too low to be detected by eye. Crude alignment is performed by replacing the probe fibre tail by a standard fibre optic with an attenuated laser focussed at its other end; the optical signal can then be visually aligned upon the APD aperture. Final optimisation is performed with the NSOM probe in feedback over the active sample and the laboratory in total darkness. The optical signal is then delicately fine-tuned onto the operating APD (using a very short integration time) prior to imaging.

During imaging the NSOM probe is scanned in the usual manner however the rate is now determined by the integration time setting of the APD, which applies to each pixel of the image. The sample laser can be driven at any power however there is a maximum at which the shear-force feedback condition maintaining the probe-sample

separation becomes unstable and the probe tends to retract. This is a consequence of the sample heating and expending and also thermal modification of the probes mechanical properties via heating by the intense localised laser output.

6.5.4 Cross-sectional photocurrent imaging

The sample is mounted in the laser sample holder displayed in Figure 6.8, and mounted directly onto the NSOM scanner stage, again the NSOM probe is oriented perpendicular to the freshly cleaved sample edge for scanning in the cross-sectional orientation. The external connection points of the sample holder are connected directly to the first stage I-to-V amplifier and the equipment is setup using two-stage amplification lock-in photocurrent sensing, configured as schematically displayed in Figure 6.11, similarly as in the photocurrent imaging of Schottky diodes.

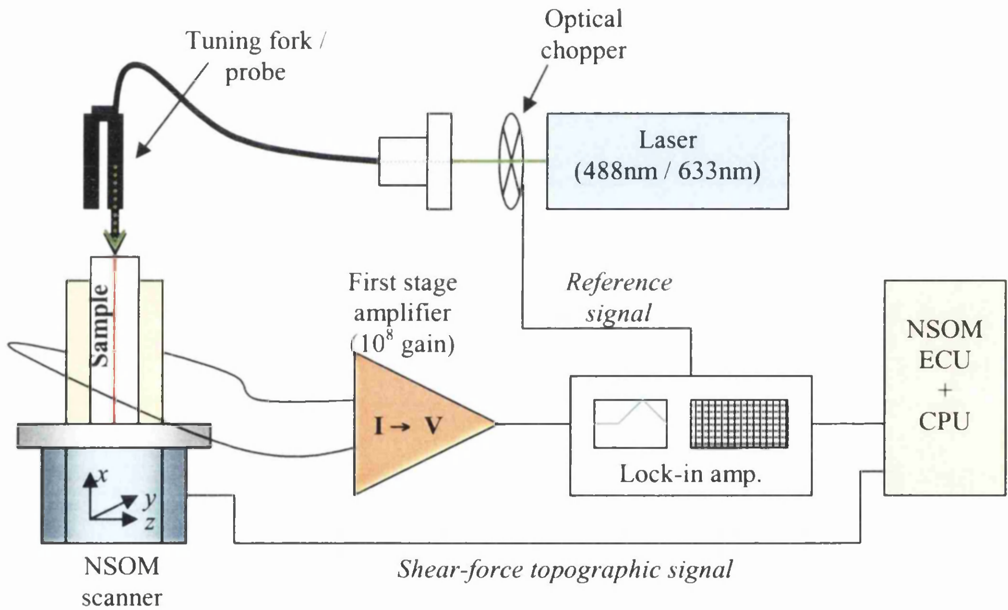

Figure 6.11 Schematic configuration of cross-sectional near-field photocurrent imaging displaying the primary elements of the setup.

Both 633nm and 488nm laser sources are used and modulated by the optical chopper at a frequency of 169Hz, which was again established as the optimum rate for noise rejection by considering the period of acquisition per imaging pixel, and fine tuning by trial and error. The first stage amplifier is set at a gain of 10^8, however the laser samples displayed a considerably higher photo-response than the Schottky diodes, thus requiring lower second stage amplification by the lock-in amplifier in order for

the photocurrent signal to be within the 10V limit for input into the NSOM electronic control unit, ECU. The high photo-response of the laser samples (when compared to the low photocurrent activity of the Schottky diode samples) required careful fine tuning of the voltage offset-null of the I to V first stage amplifier in order to prevent saturation of the output, this was not a requirement for the photocurrent imaging of Schottky diodes.

6.5.5 Tip approach techniques for cross-sectional imaging

Locating the active region of quantum well laser devices can be very difficult as the active layer is typically of the order $1\mu m$ from the cleaved wafer edge. Once the sample device is cleaved, fixed in the sample holder (Figure 6.8), and mounted on the NSOM scanner stage, it is connected to the amplification scheme shown in Figure 6.11 for photocurrent detection. The NSOM probe is approached in the cross sectional orientation to the centre of the sample wafer edge, where the risk of catastrophic probe damage occurring is minimised. This is a consequence of parallax in the image viewed via the NSOM CCD camera which is mounted at an angle ($\sim 45^0$) to the sample surface and probe axis. When the probe is in feedback at the centre of the sample wafer surface $5\mu m$ line scans are performed perpendicular to the active layer as shown in Figure 6.12(a) and the probe is translated in small steps towards the active edge.

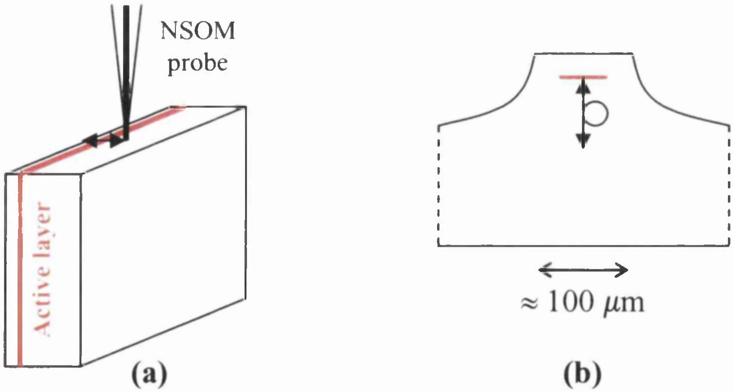

Figure 6.12 (a) Approaching the active edge of laser diodes from the wafer interior using photocurrent imaging, and **(b)** approaching the short ~1500nm active region of buried heterostructure multi-quantum well lasers using the CCD camera for crude positioning then photocurrent detection for final locating of the active region.

The system is setup for photocurrent detection, and the photocurrent response is monitored as the probe is translated, and thus the active layer is identified and located using its strong photocurrent signal. This photocurrent location method is also used when setting up to perform collection imaging. Locating the active region of buried heterostructure multi-quantum well lasers is achieved via the same technique however it is slightly more difficult to perform on such a device due to the 1.5μm length of the active region. The NSOM tip is approached by aligning the probe centrally with the notch profile at the wafer edge, as shown in Figure 6.12(b), the active region is located at the centre of the notch positioned a few microns from the *p*-type contact edge. As the probe is translated in steps towards the active region the photocurrent signal is monitored, a high photocurrent is observed when over the active region. Fortunately the *pn*-junctions adjacent to the highly confined active region also exhibit a high photocurrent signal which enables identification of the lateral plane containing the active region. Line scans are then performed along the length of the *pn*-boundary and the active region identified by its larger photocurrent response and offset position with respect to the adjacent *pn*-junctions.

When the active region has been located, photocurrent imaging can be performed immediately, or the NSOM is configured for collection imaging. This is performed with the NSOM probe in position at the active region, but retracted out of shear-force feedback with the sample surface using the scanner piezo, thus preventing any possible contact between the tip and sample when manipulating the sample holder flying connections, but allowing the probe to be directly re-approached to the active region. The short, flexible flying connections from the sample holder are then disconnected from the first stage amplifier and re-soldered to a power source immediately at their exit from the NSOM scanner.

6.6 Scanning artefacts in NSOM imaging techniques

It is well known that the images generated by the various optical imaging mechanisms of NSOM are susceptible to influence from the surface topography, and thus can represent a convolution of the sample's optical and topographic properties. As has become customary for any NSOM investigation, the credibility of images of near-field optical origin must be evaluated and the susceptibility to topographic contamination assessed.

Near-field microscopes typically operate in constant-gap mode to scan the near-field aperture along the sample surface at a very small separation. As already indicated, this is performed using shear-force detection for the instruments utilised within this work. The regulation of the probe-sample separation during imaging leads to motion of the probe normal to the sample surface (*z*-motion) which often induces undesired cross-talk in the near-field optical image, known as topographic artefacts. The *z*-motion artefact induces features in the optically generated image that are highly correlated with the structures in the topographic image. Thus the presence of this artefact is not obvious as the sample topography is part of its optical structure, i.e. the topographic structure is expected to be visible in the near-field optical microscope similarly as it is in a conventional microscope.

A near-field optical image strongly showing topographic features can be a genuine near-field image, display only purely *z*-motion artefacts, or comprise a superposition of both[19]. Without any prior knowledge of a sample it can be very difficult to interpret a NSOM image and distinguish true optical information from topographic influence[20]. For example, a sample with a topographic elevation can produce the same image as a sample where the elevation is replaced by a buried region with a higher refractive index.

The super-resolution capability of NSOM is achieved by the optical confinement of the sub-wavelength aperture, allowing features of the order of the aperture radius to be resolved[21]. Therefore, lateral resolution is increased by decreasing the dimensions of the circular aperture, increasing the lateral field confinement. However, the higher the field confinement, the faster it decays perpendicularly away from the aperture, thus the probe-sample coupling is increased and the NSOM probe must be scanned in closer proximity to the sample surface. High resolution NSOM images are therefore strongly influenced by topographical variations of the sample as an unwanted consequence of the enhanced probe-sample coupling. Novotny *et al*[20] demonstrated theoretically that the sensitivity of the optical field to *z*-motion artefacts is inversely proportional to the field confinement, i.e. the aperture diameter.

The occurrence of a strong *z*-motion artefact is typically signified by a one-to-one correspondence between optical and topographic images, and is characterised by

features in the optical image correlating very closely in terms of resolution with the same feature in the topography. The two simultaneous images are generated by different interaction and detection mechanisms and thus it is very unlikely that both will exhibit identical resolution. Also the near-field optical and shear-force interaction sites of aperture probes do not usually coincide, resulting in a physical translation in the correlation of images as demonstrated in the schematic Figure 6.13.

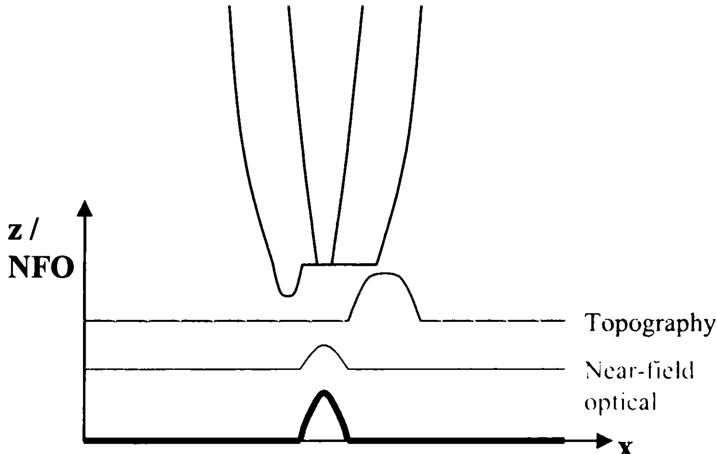

Figure 6.13 Resultant near-field optical (reflection-mode) and topographic contours plotted as the NSOM probe scans across a surface feature.

The near-field optical imaging process is dependent upon the near-field circular aperture dimensions, and its geometric centre. Whereas the shear-force distance regulation and imaging mechanism interacts with the sample at the site of the furthest protrusion of the tip apex, this is usually the grain of aluminium in the metal film surrounding the aperture that protrudes furthest. The topographic contour plotted by the shear-force imaging mechanism is therefore a convolution of the sample surface and NSOM probe geometry[19].

The origins of topographic imaging artefacts have been discussed however the probability of their occurrence is highly dependent upon the sample being imaged. Artefacts are a consequence of the *z*-motion of the NSOM probe during the scanning operation and thus are an inherent problem when imaging rough samples exhibiting fine structure. Conversely the influence of topographic imaging artefacts when analysing highly flat samples is negligible.

The presence of topographic imaging artefacts is illustrated in Figure 6.14 using the example of reflection NSOM imaging of a Ni-SiC surface. The surface is very rough exhibiting a maximum height variation of 90nm, and a rapidly varying surface topography. Imaging has been performed using un-optimised shear-force and/or scan parameters, thus the force detection mechanism is struggling to maintain a constant tip-sample separation during the scan procedure. This is typical when imaging rough surfaces and often signifies an excessively high scan speed[19,22]. As the probe is scanned across regions of rapidly varying topography, the probe-sample distance regulation mechanism cannot maintain the prescribed gap-width fast enough, resulting in variation in the probe-sample coupling and thus the presence of an imaging artefact in the optical response, as marked with white arrows in Figure 6.14.

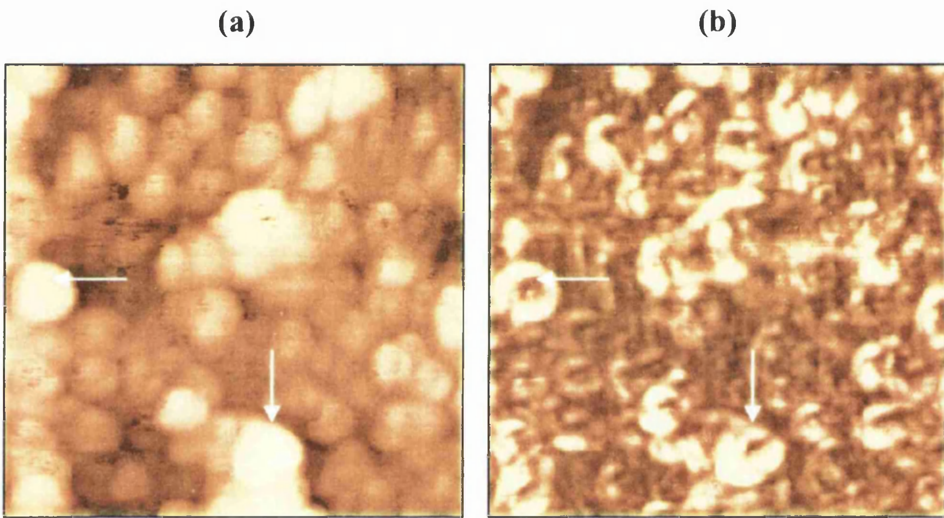

Figure 6.14 $(8.5\mu m)^2$ **(a)** topography (90.0nm maximum height), and **(b)** reflection NSOM images (PMT voltage intensity). Images are collected using un-optimised shear-force and scan parameters, thus the probe struggles to accurately scan the surface, resulting in artefacts as marked with white arrows.

The lateral boundary of a Ni-SiC contact is similarly imaged using reflection-mode NSOM in Figure 6.15, however here the imaging parameters are suitable (i.e. slower scan speed and stable feedback parameters) for such a sample surface and topographic imaging artefacts are not evident in the reflection NSOM image. The surface topography is due to the presence of Ni, therefore is evident in the reflection NSOM image as a consequence of the refractive index difference of Ni and SiC. However, the two images do not display a one-to-one correspondence and the reflection NSOM

image particularly displays a far superior lateral resolution over the simultaneous topographic image. Such features characterise a true near-field optical response.

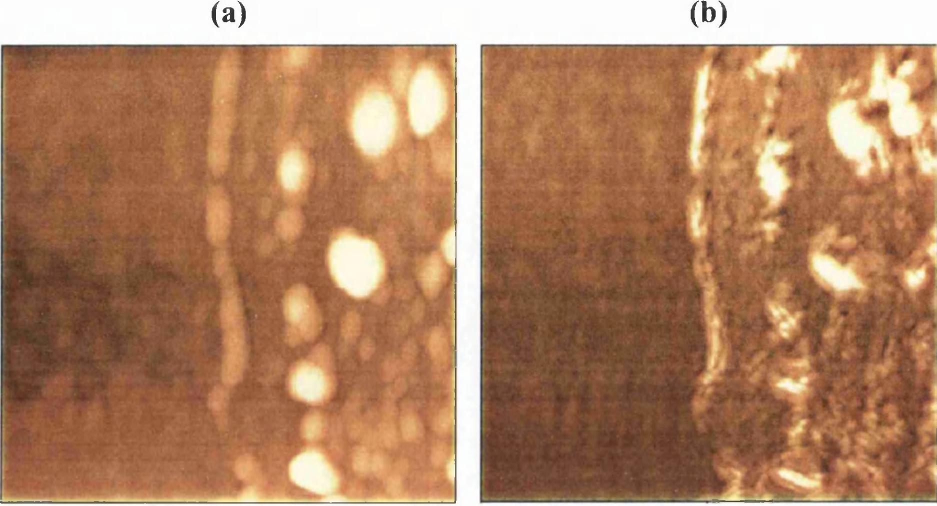

Figure 6.15 $(15\mu m)^2$ **(a)** topography (114.0nm maximum height), and **(b)** reflection NSOM images (PMT voltage intensity), recorded at the Ni-SiC contact boundary. Topographic imaging artefacts are not evident in the reflection NSOM image, which displays superior resolution to simultaneous topography.

6.7 Imaging artefacts in photocurrent NSOM

The risk of topographic imaging artefacts applies to all near-field optical imaging mechanisms, including near-field photocurrent imaging. As previously mentioned this is only a concern when imaging samples with rough surfaces, and is thus not applicable to cross-sectional imaging of freshly cleaved flat laser structures. Near-field photocurrent imaging of buried Ni-SiC Schottky interfaces is however highly sensitive to the surface topography[21], which must be considered carefully in analysing such images. As the NSOM tip is scanned across the sample surface it follows the surface contours of the Ni top contact layer, not the very flat SiC substrate buried beneath. If the Ni contact layer is not similarly flat, then as the tip-sample gap is maintained constant, the tip-interface gap will fluctuate with the Ni layer thickness. The optical field of the NSOM aperture decays exponentially, thus the optical intensity impinging on the photosensitive Ni-SiC interface also varies as the Ni layer thickness. Therefore the near-field photocurrent image of a buried Schottky interface is highly sensitive to the sample surface and will always represent a convolution of the Ni layer thickness (surface topography) and the Schottky interface properties. When imaging such a sample the topographic component cannot be ignored, however it may be minimised with careful selection of scan parameters or by imaging through

highly flat and uniform, thin metal top contact layers. This results in a near-field photocurrent image with the contrast optimised for sensitivity towards the interface properties.

6.8 Summary

This chapter has addressed the key features of the experimental techniques employed in the various near-field imaging experiments used within this study. The general features and geometry of the NSOM microscopes utilised in this study are first described, prior to the development and implementation of the near-field photocurrent imaging capability. The detection of photocurrents is implemented using a two stage amplification/detection scheme consisting of a first stage I-V amplifier (10^8 gain) and second stage lock-in amplifier. The development and implementation of the femto-amp sensitive detection scheme is addressed fully, reflecting its successful implementation as a key milestone in the development of this study. The chapter then focuses on the experimental setups employed in the imaging experiments performed upon the Schottky diode, multi-quantum barrier QW laser, and buried heterostructure laser diode, samples. Particular focus is given to the experimental procedures key to the success of this analysis. Finally the near-field imaging problem of topographically induced imaging artefacts is addressed, including its origins, nature, and highlighting situations susceptible to such artefacts. Note, within this work topographic imaging artefacts are only a concern in the case of near-field imaging of Schottky diodes, however samples were designed and prepared to minimise the susceptibility to artefacts, and steps were taken to similarly reduce such a risk via scan parameters.

6.9 References

[1] Veeco Aurora-2 and Aurora-3 instrument user manuals.

[2] J.R. Tuttle, D.S. Albin, A. Tennant, A.M. Gabor, M. Contreras, R. Noufi, *Sol. Energy Mater. Sol. Cells* **35**, 193 (1994)

[3] J.R. Tuttle, M. Contreras, M.H. Bode, D. Niles, D.S. Albin, R. Matson, A.M. Gabor, A. Tennant, A. Duda, R. Noufi, *J. Appl. Phys.* **77**, 153 (1995)

[4] T. Negami, N. Kohara, M. Nishitani, T. Wada, T. Hirao, *Appl. Phys. Lett.* **67**, 825 (1995)

---

[5] B.M. Basol, V.K. Kapur, A. Halani, C.R. Leidholm, J. Sharp, J.R. Sites, A. Swartzlander, R. Matson, H. Ullal, J. *Vac. Sci. Technol. A* **14**, 2251 (1996)

[6] J. Almeida, G. Margaritondo, C. Coluzza, S. Davy, M. Spajer, D. Courjon, *Appl. Surf. Sci.* **125**, 6 (1998)

[7] C. Coluzza, G. DiClaudio, S. Davy, M. Spajer, D. Courjon, A. Cricenti, R. Generosi, G. Faini, J. Almeida, E. Conforto, G. Margaritondo, *J. Micros.* **194**, 2/3, 401 (1999)

[8] S.K. Buratto, J.W.P. Hsu, E. Betzig, J.K. Trautman, R.B. Bylsma, C.C. Bahr, *Appl. Phys. Lett.* **65** (21), 2654 (1994)

[9] M.S. Unlu, B.B. Goldberg, W.D. Herzog, D. Sun, E. Towe, *Appl. Phys. Lett.* **67** (13), 1862 (1995)

[10] A.A. McDaniel, J.W.P. Hsu, A.M. Gabor, *Appl. Phys. Lett.* **70** (26), 3555 (1997)

[11] Analog Devices, AD549-product reference sheet.

[12] M. Badila, G. Brezeanu, J. Millan, P. Godignon, V. Banu, *Diam. Rel. Mater.* **11**, 1258 (2002)

[13] M. Sochacki, J. Szmidt, M. Bakowski, A. Werbowy, *Diam. Rel. Mater.* **11**, 1263 (2002)

[14] B. Pecz, *Appl. Surf. Sci.* **184**, 287 (2001)

[15] J.N. Su, A.J. Steckl, *Inst. Phys. Conf. Ser.* **142**, 697 (1996)

[16] W. Kern, D.A. Puotinen, *RCA Rev.* **31**,187 (1970)

[17] U. Durig, D.W. Pohl, F Rohner, *J. Appl. Phys.* **59**, 3318 (1986)

[18] E. Betzig, A. Harootunian, A. Lewis, M. Isaacson, *Appl. Opt.* **25**, 1890 (1986)

[19] B. Hecht, H. Bielefeldt, Y. Inouye, D.W. Pohl, L. Novotny, *J. Appl. Phys.* **81** (6), 2492 (1997)

[20] L. Novotny, B. Hecht. D.W. Pohl, *Ultramicroscopy*, **71**, 341 (1998)

[21] K. Karrai, G. Kolb, G. Abstreiter, A. Schmeller, *Ultramicroscopy*, **61**, 299 (1995)

[22] R.L. Williamson, L.J. Brereton, M. Antognozzi, M.J. Miles, *Ultramicroscopy*, **71**, 165 (1998)

Chapter 7
Results: Ni-SiC Schottky diodes

7.1 Introduction

Schottky junctions are conventionally characterised using the macroscopic I-V technique which measures the average barrier properties of the entire diode[1]. Electrical analysis derives an average barrier height, ϕ_b, for the entire Schottky junction, the quality of which is described by the corresponding ideality factor, n, which is unity for an ideal diode, and greater than unity for deviations from ideality. Variations in the Schottky barrier height across the diode interface represent deviations from ideality, thus the more varied the barrier energy across the interface, the greater the value of n.

Near-field photocurrent imaging reveals the lateral distribution of Schottky interface properties at the sub-micron scale. Therefore it is possible to measure the distribution and extent of the local fluctuations in the barrier height that combine to give a Schottky contact its overall properties.

Nickel-silicon carbide Schottky diodes were investigated simultaneously with the development of the near-field photocurrent imaging capability. Consequently the control of the Ni-SiC Schottky top contact deposition, and the Ni thickness formed the primary focus in sample preparation. This proved critical to the success of photocurrent imaging using the high lateral resolution and low intensity regime of the near-field optical geometry.

The ideal scenario for the photocurrent analysis of buried interfaces is to scan the near-field probe over a highly flat surface, optically probing the buried interface through a thin uniform metal layer. As discussed in chapters 5 and 6, the flat surface eliminates the possibility of topographically induced artefacts in optically derived images which are caused by variations in tip-sample separation that can occur when following the fluctuating contours of a rough surface. A highly flat surface also indicates an extremely uniform Ni layer thickness, which in turn indicates lateral uniformity in the optical transmission to the buried interface. Thus the risk of

imaging artefacts is minimised, and the photocurrent contrast is optimised to sense fluctuations in interface properties, i.e. lateral variations in Schottky barrier characteristics. Schottky contacts with flat Ni surfaces were manufactured by different processes and probed using standard I-V analysis and near-field photocurrent imaging, the findings of which are discussed.

The contrast mechanism in the photocurrent imaging of Schottky interfaces is dependent on the magnitude of the Schottky barrier and the energy of the probing excitation source (chapter 5). It is optimised when the probing excitation is very close in energy to the Schottky barrier height, ϕ_b, which in the ideal situation is tuneable across an energy range centred at ϕ_b. Excitation sources of wavelengths 633nm (1.96eV) and 488nm (2.55eV) were applied to this investigation, which are both energetically in excess of the barrier heights measured for as-deposited Ni-SiC Schottky contacts. Therefore in order to enhance the photocurrent contrast when imaging at the lower available probing energy 1.96eV (633nm), barrier heights could be enhanced via sample annealing to reduce the energy difference between the probe and barrier, and increase the sensitivity of the imaging mechanism to the buried interface.

7.2 Samples

The wafers were all prepared prior to deposition by *ex-situ* solvent, piranha, and RCA cleaning steps which are detailed in Appendix 11.1. Thick (~1μm) Ni ohmic back contacts were all deposited and annealed at 1000^{0}C using the rapid Edwards evaporation system. The requirements for a thin Ni Schottky top contact layer were explored via a variety of complex procedures based on the metal-deposition systems of the Edwards evaporation chamber and UHV deposition system and are described fully in chapter 6. The results presented within this section are acquired from samples with top contacts suitable for these measurements. The samples highlighted in this section focus on the affect of annealing the top contact, and UHV versus Edwards preparations. Note, each Ni-SiC sample produced possesses on average 20 individual, 600μm diameter circular diodes, the I-V data presented is averaged over many diodes.

Sample type 1: The top contact was deposited via a rapid deposition, using the Edwards evaporator for a deposition time of 29sec. Shear-force topographic imaging at the diode edge revealed the Ni layer thickness to be 30-40nm. I-V analysis measured the Schottky barrier height to be ϕ_b = 1.425eV with an ideality factor n = 1.557.

Sample type 1 was subsequently annealed at 500^{0}C for 600sec in order to increase the Schottky barrier energy, the mechanisms are discussed later within this chapter, section 7.7. The barrier was found to have increased by 0.155eV to ϕ_b = 1.58eV and n = 1.86. The I-V characteristics of sample type 1 are presented in Figure 7.1.

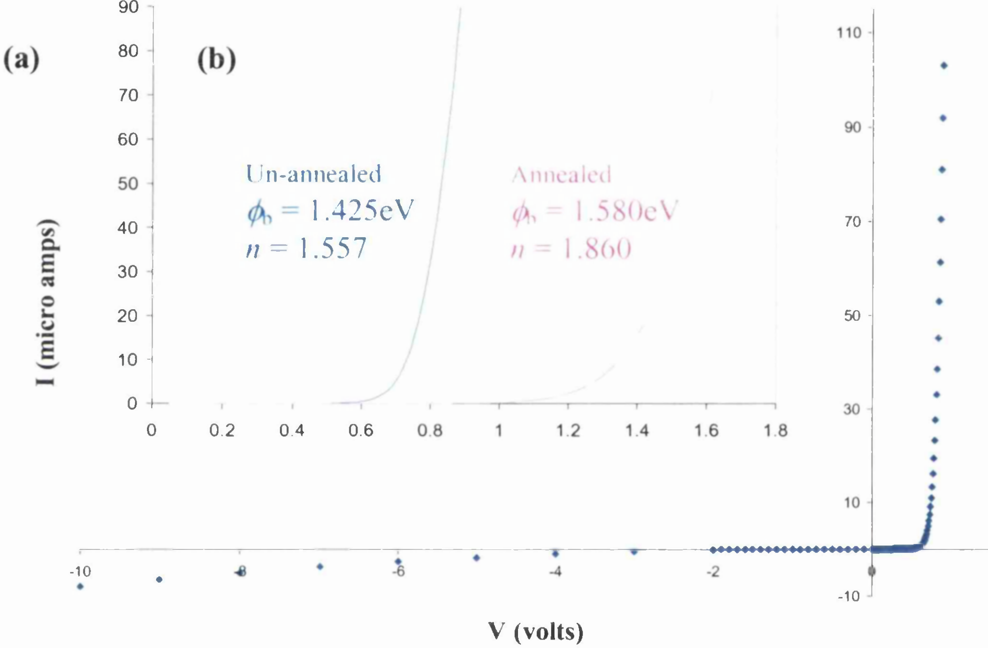

Figure 7.1 I-V characteristics for sample1, **(a)** displays the full I-V characteristic typical of the diodes on sample 1 immediately after fabrication, the inset **(b)** displays the forward bias switch-on characteristics before and after sample annealing.

Sample type 2: The top contact was again deposited in the Edwards evaporator, however at a much slower and more controlled rate for a deposition time of 510sec. Shear-force microscopy measured the typical Ni layer thickness to be 20-40nm. The Schottky barrier height was determined to be ϕ_b = 1.657eV with an ideality factor of n = 1.252.

Sample type 3: The top contact was deposited using the UHV evaporation system which deposited Ni at a slower rate and via a highly controlled evaporation process. Ni was deposited at a rate of 1Å in 7sec for 1380 sec, producing a 20nm layer thickness, according to the system calibration. The Ni Schottky dots produced via this method possessed diffuse non-abrupt edges, as a consequence of deposition through a mask, and it was thus impossible to fully evaluate the Ni layer thickness using shear-force imaging. The Schottky barrier height was measured at ϕ_b = 1.60eV with an ideality factor n = 1.534.

		Sample 1	**Sample 1 (annealed)**	**Sample 2**	**Sample 3**
ϕ_b **(eV)**	(± 0.05eV)	1.425	1.580	1.657	1.600
n	(± 0.1)	1.557	1.860	1.252	1.534

Table 7.1 Summary of the average barrier heights ϕ_b and ideality factors n evaluated from the I-V characteristics of the Schottky diode samples, including the experimental standard errors.

Sample types 2 and 3 produced highly rectifying I-V characteristics similar to that demonstrated in Figure 7.1 for sample 1, the barrier energies and ideality factors evaluated for all samples are summarised in Table 7.1. The barrier height ϕ_b, and ideality factor n, values quoted are average values for multiple (8-12) functioning devices produced by the same deposition on the same SiC wafer. Differences in electronic properties between samples are discussed later with respect to the different preparation procedures and considering near-field photocurrent findings.

7.3 Top contact thickness and the imaging of buried interfaces

The buried Ni-SiC Schottky interface is probed using near-field photocurrent imaging by illuminating through the Ni top contact, this must also physically be contacted by electrical connections in order to detect the photo-excited current. If the Ni top contact is too thick the nanoscopic illumination of the near-field probe will be scattered and attenuated prior to interaction at the photo-sensitive interface, too thin and the electrical contact probe will penetrate through to the SiC substrate preventing photocurrent detection. Thus the critical Ni top contact thickness is a compromise of these two factors.

UNIVERSITY OF WALES SWANSEA LIBRARY

Near-field imaging increases lateral resolution by utilising a sub-wavelength aperture, the resulting optical intensities are very low (order ~nW at aperture) and this is extremely apparent in the imaging of buried interfaces which is only feasible through suitably thin Ni layers, and only then using a modulated excitation source and a two stage photocurrent amplification/detection scheme (chapter 6). The success of near-field induced photocurrent imaging at buried interfaces is entirely dependent upon the transmission of a sufficient intensity of the probing illumination source to the optically responsive interface region where a photocurrent is generated. This is determined by the skin effect of the metallic top contact layer which describes the rapid attenuation of electromagnetic fields with depth inside a good conductor. The skin depth, δ, is dependent on the type of metal in the conductor and the frequency of the applied field, it defines the point at which the field is reduced by a factor of 1/e, and is given by

$$\delta = \frac{c}{\sqrt{2\pi\sigma\omega\mu}} \tag{7.1}$$

where σ is the metal conductivity, μ is its magnetic permeability, $\omega = 2\pi f$ where f is the frequency of the electromagnetic field, and c is the speed of light. The skin depth of Ni for both the 633nm and 488nm wavelength fields used for photocurrent imaging here is evaluated to be approximately 10nm. The penetrating field is generally completely attenuated within $5\times\delta$, the actual value is 5/e of the original intensity which is 0.674%. Therefore the 633nm and 488nm probing fields used for near-field photocurrent imaging are attenuated at a depth of approximately 50nm of Ni, thus the Ni top contact layers of the previously described samples are suitably within this limit.

7.4 Near-field photocurrent imaging of buried interfaces

Near-field photocurrent imaging was successfully performed[2] using both 633nm and 488nm excitation wavelengths, that are greater in energy than the average Schottky barrier height, ϕ_b, of all three samples. The excitation source was modulated at a frequency of 69Hz which provided a balance between sufficient noise elimination, by the lock-in amplifier (LIA), whilst transmitting a great enough optical intensity to the near-field aperture for photocurrent stimulation and detection. The photocurrent intensity was plotted by the NSOM electronic control unit (ECU) at each pixel

(typically 300-500 pixels per line) to generate a map of lateral variations in the properties of the buried interface, i.e. local fluctuations in the Schottky barrier characteristics. A stable and reproducible photocurrent signal required a slow scan rate, typically up to 60sec per line, thus for a 300 pixel image, acquisition times can be up to 5 hours, therefore stability of the photocurrent generation/detection mechanism with time is essential to the imaging process.

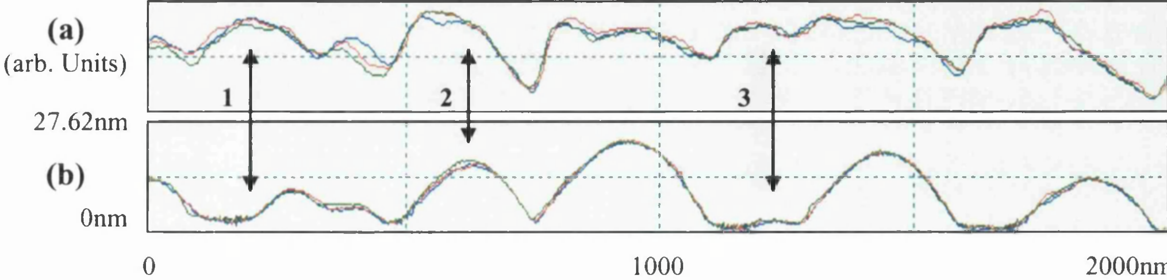

Figure 7.2 Simultaneously acquired $2\mu m$ long **(a)** photocurrent, and **(b)** topography linescans. The line is imaged three times consecutively and the profiles overlaid to reference reproducibility. The image was acquired from sample 2 using the 633nm excitation source at 0V applied bias.

This was achieved for the described parameters as demonstrated by the three consecutively acquired and overlaid linescans displayed in Figure 7.2 for sample type 2, which exhibit accurate reproducibility. The photocurrent linescans are represented as an arbitrary current scale due to dependence of the lock-in amplifier voltage output, the pre-amp, and intensity throughput of the near-field aperture stimulating the photocurrent. The photocurrent cross-sections displayed in Figure 7.2(a) are expanded to maximise the plot area, thus the minimum photocurrent level displayed is not a zero level. There are similarities between the photocurrent and topographic linescans which may suggest that the photocurrent signal is a function of the surface topography[3], i.e. directly influenced by topographically induced scanning artefacts[4]. The topographic image reveals variations in the Ni layer thickness, as the buried substrate is atomically flat, which implies variations in the transmission of the probing light to the photo-active interface. However if this was the only mechanism at work the photocurrent would be low at locations of high topography, and high at locations of low topography where optical transmission is maximised. The latter can be seen at location 1, marked clearly in Figure 7.2. The simultaneous imaging modes represented in Figure 7.2 indicate that this clearly is not always the case as although there does appear to be some topographic influence in the photocurrent signal

(location 2) there are locations where the photocurrent varies independently of the topography (location 3). This indicates that the photocurrent imaging mechanism can function independently of surface structure and exhibits sensitivity to the buried interface.

The example illustrated in Figure 7.2 is acquired from sample 2 after some considerable surface oxidisation has occurred, the sample therefore exhibits considerable surface roughness as indicated by the maximum height scale of 27.62nm, and thus surface oxides upon the Ni layer are approximately 15-20nm thick. Fluctuations in Ni thickness of this order would have an appreciable impact on optical transmission to the Ni-SiC interface. The fact that the photocurrent signal fluctuates almost independently of topography for such a rough surface morphology is indicative of the sensitivity of the photocurrent imaging mechanism to probe the buried Schottky interface. Note that variations in surface morphology are not necessarily independent of the buried Ni-SiC interface and may actually be seeded by aggregations in the chemical stoichiometry of the interface[5], which could give rise to features where the topography and photocurrent are both high such as location 2 in Figure 7.2. However, clearly the ideal scenario for the near-field photocurrent analysis of buried interfaces is for a highly uniform Ni top contact layer with an extremely flat surface, thus eliminating any possible topographic influence on optically derived data from a varying thickness of Ni between the sample surface and buried interface. Consequently the risk of topographic imaging artefacts (sections 6.7 and 6.8) from variations in probe-sample (surface) separation, resulting from an un-optimised shear-force feedback loop straining to follow a rapidly varying surface and/or inappropriate scan parameters[6], is also greatly reduced or eliminated entirely.

The sensitivity of near-field photocurrent imaging to the buried Schottky interface and the intimate relationship of the photocurrent and surface structure are further illustrated in Figure 7.3. The images are simultaneously acquired from sample 1, produced by rapid Edwards deposition, using the 633nm excitation source and a -1V applied bias to produce the photocurrent. The image was acquired soon after sample fabrication, allowing minimal time for surface oxide growth, and thus the Ni surface is predominantly flat. The topographic image (a) clearly shows high points marked

by white arrows that are believed to be a left over residue, from solvent rinsing of the sample, deposited upon the Ni surface.

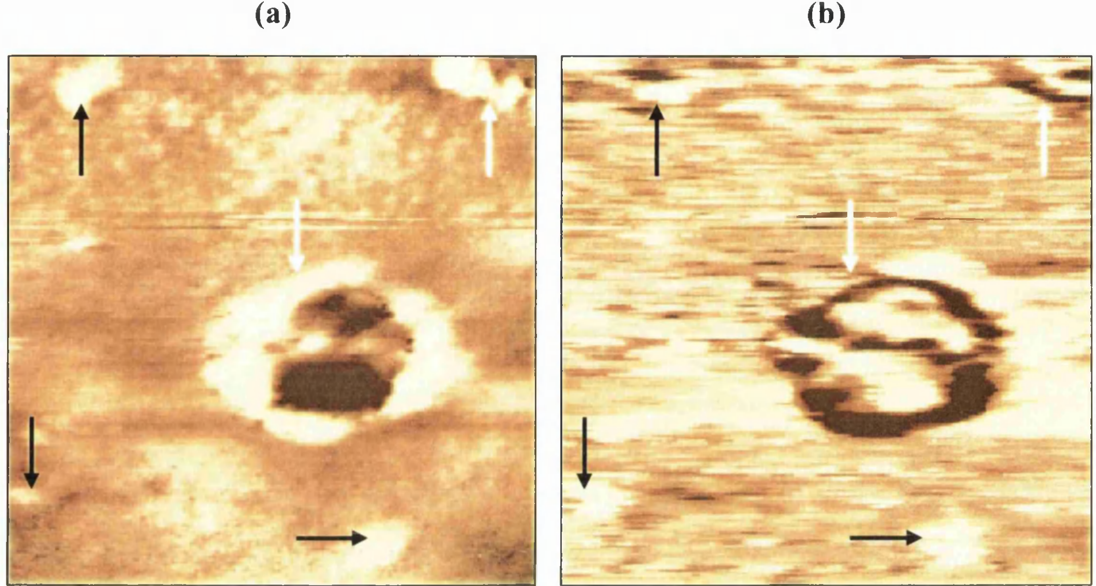

Figure 7.3 $(5.25\mu m)^2$ **(a)** topography image with maximum height 8.32nm, and **(b)** photocurrent image acquired using 633nm excitation and -1V applied bias for sample 1 (pre-annealing). Black arrows label sites of raised topography and high photocurrent intensity; white arrows label surface residues that cause a minimum in photocurrent intensity.

The corresponding photocurrent signal for such features is very low and follows the contours of the residues. This is a consequence of the attenuation of the excitation field of the near-field probe by the residue, thus preventing optical transmission to the interface for photocurrent generation to occur. The lack of photocurrent stimulation beneath such residues indicates the successful implementation of photocurrent imaging and supports the theoretical basis of current stimulation at the buried interface. The residues were later removed by further solvent rinsing and careful drying under a flow of nitrogen, confirming the above features as an external contaminant and not part of the Ni layer surface morphology.

In contrast to the absence of photocurrent beneath the residues, the locations marked with black arrows in Figure 7.3 correspond to sites of raised Ni surface topography which exhibit a greatly increased photocurrent intensity. The surface topography at these locations could be raised as a consequence of phenomenon occurring at the interface, buried by the Ni top contact layer, such as structural or point defects, or possibly the presence of impurities, which result in the formation of gap-states

allowing a large photocurrent to flow[10]. Similar results are observed by J. Almeida *et al*[5,7] when investigating the buried Pt-GaP Schottky interface, and were attributed to the presence of a local segregation of metallic gallium, revealed by photoemission electron microscopy measurements, which results in a localised difference in barrier height causing enhancement in the photocurrent contrast. In a similar chemical process, the transformation of a Ni-SiC interface from Schottky to ohmic nature, when annealed, is characterised by the formation of Ni_2Si at the interface leaving C which segregates into graphite regions often localised at voids formed at the interface[8]. The formation of Ni_2Si and C segregation is also reported at Schottky interfaces by Roccaforte *et al*[9] and is possibly occurring in sample 1 inducing local minima in Schottky barrier height and consequently local enhancement in photocurrent transmission across the barrier.

7.5 Imaging the depletion region at the lateral contact boundary

Photocurrents at Schottky interfaces originate from the photo-excitation of electrons within the metal by an external source, which these cases are 633nm (1.96eV) and 488nm (2.55eV), the photo-excited electrons are subsequently transported across the Ni-SiC interface by the built-in field of the junction. The excitation sources are energetically lower than the band-gap energy of the SiC substrate (3.2eV), therefore photo-stimulation of current should be confined to the Ni region of the Schottky interface for a perfect semiconductor. However real semiconductors and in particular metal-semiconductor junctions, posses electron states that reside within the semiconductor band-gap at the interface region, these include metal-induced gap states and defect levels (refer to chapter 3). Photo-excitation from such intermediate energy levels by a sub band-gap energy source can result in excitation of electrons into the conduction band, and the subsequent propagation of a photocurrent by the built-in field of the depletion region. Therefore photocurrent imaging can detect the extent of the semiconductor depletion region, d_{SiC}, as determined by Poisson's equation,

$$d_{SiC} = \left(\frac{2\varepsilon_{SiC}\phi_b}{qN_d} \right)^{1/2} \qquad \textbf{(7.2)}$$

where ϕ_b is the Schottky barrier height, ε_{SiC} is the dielectric constant of SiC, q is the electronic charge, and N_d is the doping concentration of the *n*-type SiC. For sample

type 1 that exhibited an average barrier height of 1.425eV (from I-V measurements), a depletion width of approximately 390nm is evaluated.

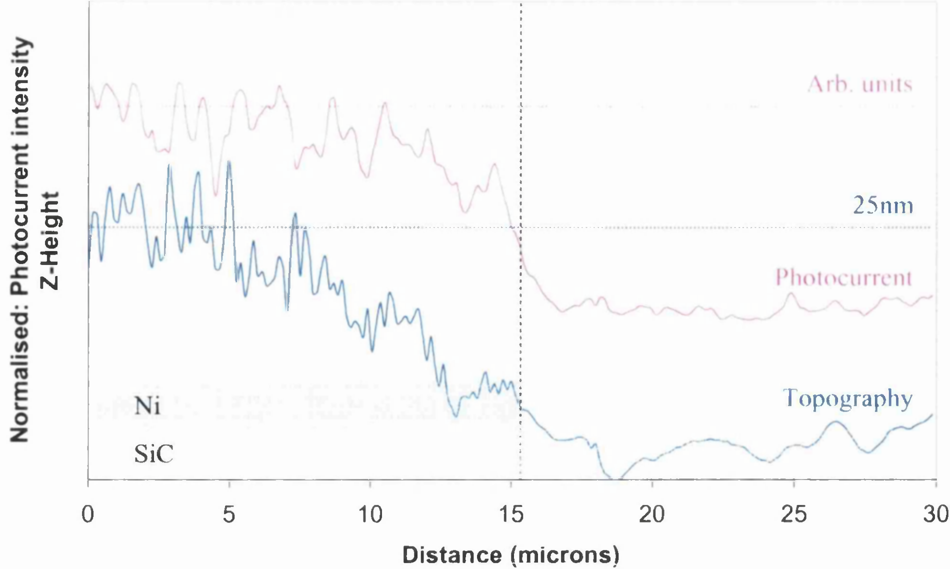

Figure 7.4 Simultaneous photocurrent and topography cross-sections of the Ni Schottky contact edge acquired for sample type 1 using the 633nm excitation source and 0V applied bias.

Simultaneously acquired topography and photocurrent cross-sections measured at the lateral boundary of a Ni contact of sample type 1 are displayed in Figure 7.4. The topography profile indicates that the Ni contact is reasonably abrupt at its edge, and reaches a maximum thickness of approximately 25nm (note, the contact edges were often very diffuse due to the fabrication process of evaporation through a mask). The photocurrent profile of Figure 7.4 is seen to plateau at a zero level (i.e. LIA did not detect a photocurrent) away from the Ni contact when the probe is scanned over the bare SiC substrate. The dashed vertical line denotes the approximate contact boundary, and the photocurrent is seen to switch on very rapidly into the Ni contact region. The rapid switch on of the photocurrent when the 50nm near-field aperture is located over the contact is more accurate than the shear-force mechanism in detecting the contact boundary at a diffuse edge. When scanning the near-field probe from the SiC onto the Ni contact region the photocurrent is seen to go from zero to maximum within distances of the order 500nm. Given that the NSOM aperture diameter is typically 50-100nm this indicates that the photocurrent transition from zero to maximum level occurs within 300-400nm. These observations correlate very closely with the depletion width of approximately 390nm evaluated using Poisson's equation.

Therefore the near-field photocurrent imaging mechanism has proved sensitive to the Schottky interface depletion region, and accurately determined its lateral extent.

This is an extremely useful application of near-field photocurrent imaging at a fixed wavelength (i.e. fixed excitation energy) as the depletion width of the semiconductor at a Schottky interface is directly proportional to the square root of the Schottky barrier height. Therefore the ability to measure the semiconductor depletion width also facilitates the measurement of the Schottky barrier magnitude, and any lateral variation it may posses at a contact boundary.

7.6 Photocurrent imaging of buried interfaces through flat surfaces

As discussed, the near-field photocurrent imaging mechanism is optimised towards interface properties when imaging through uniform Ni layers with very flat surfaces, and this formed the primary concern of the fabrication processes considered.

The simultaneous topography and photocurrent images of Figure 7.5 are recorded from sample 2, where the Ni over layer was produced by a slower Edwards deposition. The photocurrent image is generated using the 633nm excitation source and 0V applied bias. The topography image (a) indicates the Ni surface is extremely flat, exhibiting a maximum height of 1.22nm, this is a result of the sample being recently removed from vacuum thus allowing a minimal time for oxide growth, which leads to surface roughening. The sample is therefore optimised for the photocurrent investigation of the buried interface, and this is reflected in the photocurrent image (b). Upon close inspection the photocurrent image displays small fluctuations in the photocurrent intensity over a scale of approximately 100nm, which is independent of the surface morphology, for example the bright feature (high photocurrent intensity) at location 1 does not correspond to variation in the surface topography, similarly as does the dark feature (low photocurrent intensity) at location 2. The Schottky interface on average therefore possesses uniform properties, which is implied by the low ideality factor (n = 1.252 ± 0.1) as displayed in Table 7.1. The ideality factor describes the average device characteristics, whereas the near-field photocurrent image (Figure 7.5(b)) reveals the fine structure in barrier properties which may be due to small variations in the precise chemical stoichiometry of the junction region across the lateral area of the interface, or a function of the distribution of SiC surface states[10].

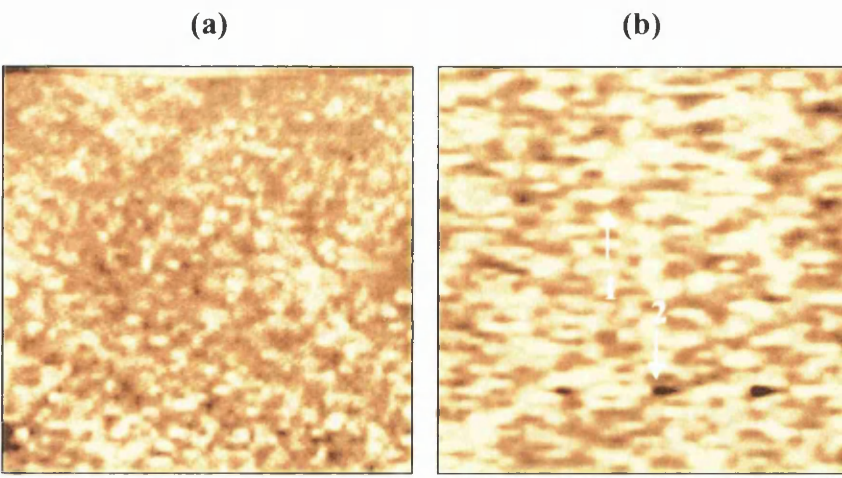

Figure 7.5 $(2.92\mu m)^2$ **(a)** Topography with maximum height 1.22nm, and **(b)** photocurrent images acquired for sample 2 using the 633nm excitation source and 0V applied bias.

The photocurrent contrast is optimised for the interface in this image as there are no topographic surface features to contaminate the photo-generated image, as exhibited in Figure 7.3 with its large residues upon the flat Ni surface of sample type 1. Although both sets of contacts were deposited in the Edwards HV deposition system, the diodes of sample type 2 were manufactured in a more precise and controlled manner, by a slower deposition rate than those of sample type 1. This is reflected in the corresponding photocurrent responses which are notably different, neglecting the residues present upon sample type 1 (Figure 7.3). As described, sample type 2 displays a highly uniform photocurrent response with short range fine structure, whereas sample type 1 exhibited localised sites of high photocurrent greater than 200nm in diameter, and this is reflected in the poorer ideality factors, *n*, of diodes sample type 1, measured by I-V measurements.

Sample type 3 was similarly imaged immediately after fabrication and removal from the UHV deposition system, but exhibited very different characteristics from those described for sample type 2, produced via a slow Edwards deposition. The topography image of Figure 7.6(a) has a maximum height variation of 7.93nm, which is considerably greater than the previous Edwards prepared sample that exhibited a maximum topographic variation of 1.22nm. The photocurrent image (b) was again generated using the 633nm excitation source and 0V applied bias. The surface displays two sizes of features in the topographic image, large features (denoted by

dashed circles) between 60-100nm in width and up to 7nm in height, and small features (black arrows) up to 35nm wide and approximately 4nm high. Note that the features in this image are variations in the Ni surface and not external contaminants residing upon the Ni layer surface (such as the residues seen on sample type 1 in Figure 7.3).

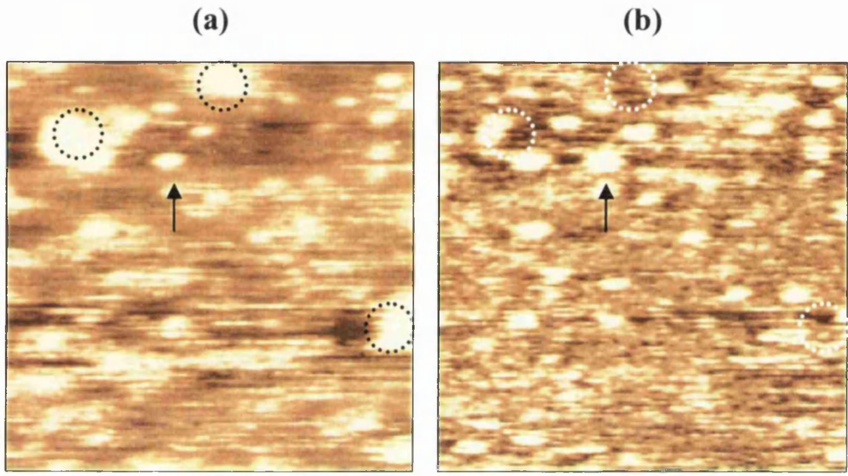

Figure 7.6 $(500nm)^2$ **(a)** Topography with maximum height 7.93nm, and **(b)** photocurrent images acquired for sample 3 using the 633nm excitation source and 0V applied bias.

The two sizes of surface features exhibit very different responses to light even though similar in height, which is seen in the photocurrent image (b) and implies differing characteristics and origins. The large features (dashed circles) are unresponsive to light and do not provide any enhancement to the photocurrent, which appears to fluctuate independently of the large features, and is of a slightly lower intensity at such locations. This implies that the large features do not originate from phenomenon occurring at the interface, i.e. their growth at such locations is not seeded by the presence of chemical species or dislocations at the SiC surface. The small reduction in the corresponding photocurrent intensity indicates that the large features are due to uneven Ni deposition, reducing the optical penetration to the interface at such locations.

The small features (black arrows) are highly photo-responsive displaying localised sites of high photocurrent intensity of similar lateral extent as the corresponding increase in surface topography, i.e. up to 35nm wide. This is very similar to that previously discussed for sample type 1 (rapid Edwards deposition) as displayed in

Figure 7.3 for the raised Ni sites. However, the extent of the features on sample type 1 was much greater, exhibiting features over 200nm in width and up to 10nm in height. Although the features are different sizes on the two samples they display the same characteristics of very high localised photocurrent intensity with respect to the average levels seen over both sample surfaces, even though the Ni surface topography is raised at such locations. This is indicative that the raised surface topography is a consequence of interface phenomenon, as instead of optical attenuation by the raised Ni there is localised photocurrent enhancement. This may be due to the location of structural or point defects in the SiC, or the presence of impurities, which result in the formation of gap-states providing a lower energy pathway for large photocurrents to flow[10]. Alternatively such features may be due to local segregations of species at the interface i.e. clusters of C or Ni_2Si which could result in a lower Schottky barrier at such a location, thus responding to sufficiently energetic light with an increased photocurrent[5,7].

Sample type 3 was manufactured using the UHV deposition system which maximises the cleanliness of the formed interface as a result of the superior vacuum conditions. The deposition was performed at a slow and controlled rate similarly as sample type 2, which would infer a similar metal layer growth mechanism. However the photocurrent characteristics imply interface properties comparable to sample type 1, which was grown rapidly in the HV Edwards system. The metal layers of sample types 1 and 3 were thus grown under highly contrasting conditions, indicating that photocurrent similarities are probably a consequence of SiC wafer quality and possibly defects, which are renowned problems of SiC based devices[8].

7.7 Increasing Schottky barrier height by thermal annealing

In order to enhance the contrast mechanism of the near-field photocurrent imaging process, the energy difference between the Schottky barrier height, ϕ_b, and lower excitation source (633nm; 1.96eV), was minimised by increasing ϕ_b. It has previously been reported that the Schottky barrier magnitude of Ni contacts with 4H-SiC is enhanced by modifying the interface via a post-deposition anneal at 500^0C for a duration of 600sec [10,11,12]. Barriers have been reported to experience a maximum increase of up to 0.25eV by such a process[11]. X-ray photoelectron spectroscopy

(XPS) performed on similar samples revealed a silicide component on the lower binding energy side of the Si core level peak, and a large graphite peak on the carbon spectra[11], also SiC has previously been seen to react with Ni at 500^{0}C forming the compound Ni_2Si [13]. This results in a peak shift to a lower binding energy and an increase in Schottky barrier height. Further annealing to higher temperatures of 1000^{0}C has been seen to change the silicide phase formation and reverse the binding energy peak shift to a higher binding energy, corresponding to a lower barrier height, resulting in a transition in electrical characteristics from Schottky to ohmic[14].

Annealing sample type 1 at 500^{0}C for 600 seconds resulted in a barrier height increase of 0.155eV, unfortunately the as-deposited barrier height was low at 1.425eV, and thus the resultant barrier energy was 1.58eV, which was significantly less than the excitation field (1.96eV; 633nm) by 0.38eV. Although the annealing of sample type 1 was successful in increasing the barrier energy, it was not to such an extent that the barrier and excitation energies were close enough to provide significant enhancement to the photocurrent contrast.

However, the annealing process did modify the Ni-SiC interface considerably, which was mirrored at the surface and provided dramatically different photocurrent characteristics, as displayed in Figure 7.7. The topographic image (a) shows how the Ni surface has been altered by the annealing process. The as-deposited Ni surface is relatively flat, with 8nm maximum topographic variations (as seen beneath the residues in Figure 7.3). Whereas the post-anneal surface is extremely roughened displaying Ni clusters of diameters between 150-200nm with maximum vertical displacement of ~20nm as shown in Figure 7.7(a). The top half of the clusters appears spherical in shape, with constantly changing surface topographies (i.e. no flat regions). At the centre of the image is a large impurity which was possibly present upon the SiC surface prior to Ni deposition, preventing the formation of an intimate contact beneath. Without a Schottky contact existing under the impurity there can be no photocurrent generated, alternatively the large impurity could attenuate the probing optical field completely prior to the underlying interface. A total absence of photocurrent is seen below the feature at the centre of photocurrent image Figure 7.7(b), which is a very different response to that of the surrounding smaller Ni clusters.

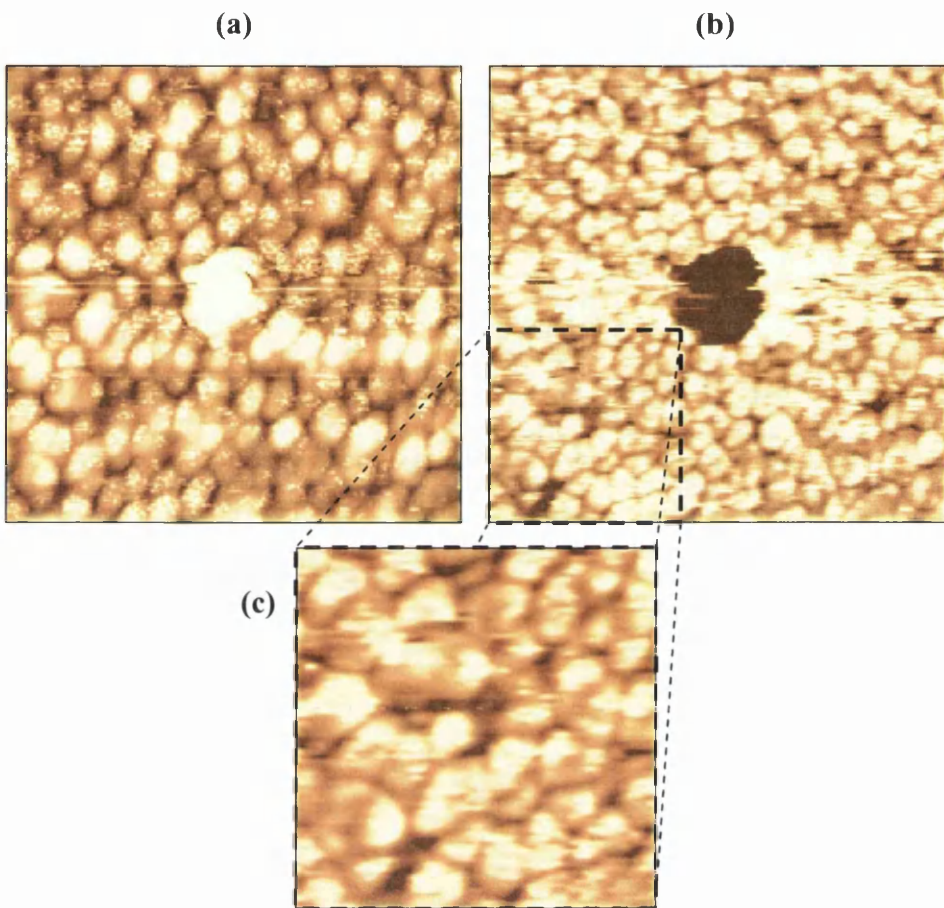

Figure 7.7 Sample 1 after annealing for 600sec at 500^0C. $(3175.2\text{nm})^2$ **(a)** shear-force topography of maximum height 19.61nm, and **(b)** photocurrent image using 488nm excitation and 0V applied bias. Image **(c)** displays a $(1333.58\text{nm})^2$ photocurrent zoom of the area marked in (b).

It is immediately apparent that the features seen in the topography (a) are mirrored in the photocurrent (b). The resolutions are also very similar, with the photocurrent responding very rapidly across features, switching on/off abruptly at Ni cluster boundaries, as shown in the zoomed photocurrent image (c). The regions between clusters display very low photocurrent levels, actually falling to zero between some clusters, as seen in the cross-sectional Figure 7.8. This may be caused by voids generated in the thin layer during annealing, and may be locations absent of Ni. Imaging the same region using the higher energy (2.55eV; 488nm) excitation source and a different probe generated an identical photocurrent image, indicating that the lack of photocurrent between clusters is not due to an increase in the barrier height to an energy between 1.9eV and 2.55eV. The photocurrent image mirrors closely the cluster boundaries as in the topographic image, however the response over the clusters i.e. the cluster interiors, is very different. The topography changes constantly over the

surface of individual clusters, whilst in contrast the photocurrent remains at a reasonably uniform level over the entire cluster, once switched on at the cluster boundary, as displayed in Figure 7.7(b) and (c) and highlighted by the cross-section of Figure 7.8. Moreover, although the clusters exhibited a variety of maximum topographic heights the photocurrent response level on Ni clusters remained uniform across the entire image area. This indicates that once the NSOM tip is over a particular Ni cluster the photocurrent response is determined by the interface properties and is independent of the Ni surface variations. Implying that beneath the clusters the Ni-SiC interface is highly uniform, displaying uniform barrier properties, whereas between clusters the Schottky barrier is very different displaying an increase in magnitude. These observations correlate well with macroscopic I-V measurements (Table 7.1) that evaluated an ideality factor increase during the annealing process from 1.557 to 1.860. This indicates that as the average total barrier is increased by annealing, the uniformity of the barrier decreases, resulting in localised sites of barrier enhancement, as seen between clusters.

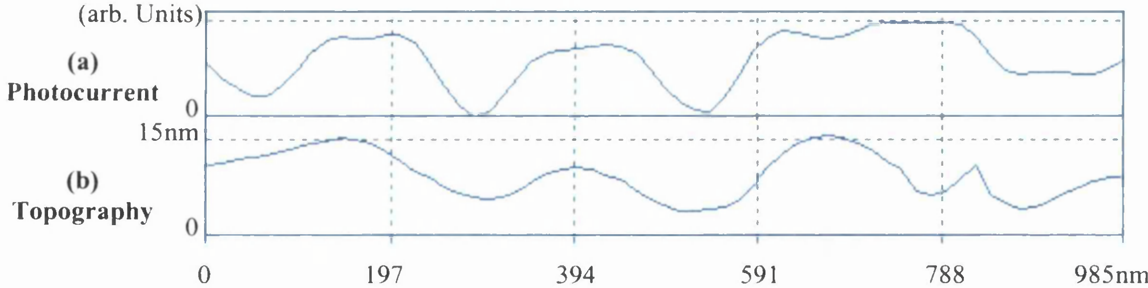

Figure 7.8 Cross-sectional line profiles taken from the image of Figure 7.7(b) displaying, **(a)** the photocurrent level which is reasonably constant in magnitude once switched-on at the cluster boundary, and **(b)** the corresponding surface topography.

Between clusters the photocurrent response is however very susceptible to topographic influence. It is probable that the tip-sample separation will vary slightly as the probe follows the rapidly changing contours at the edge of individual clusters, passing from one Ni cluster to the next, thus altering the near-field coupling to the sample surface, in a topographically induced optical image artefact[3,4]. Thus the very low, or absent, photocurrent between clusters could result from a reduction in the near-field interaction with the sample as the probe-sample separation is increased

between clusters due to the rapidly changing topography, and the relatively large diameter probe tip cannot penetrate between closely packed clusters.

The near-field photocurrent image plotted in Figure 7.7 represents a convolution of both arguments, neither of which can be neglected. The topographic influence of the rough surface is certainly contributing to the photocurrent signal at the cluster boundaries; however an increased Schottky barrier height is also exhibited at the boundaries, which is corroborated by the macroscopic I-V analysis that measured an increased average barrier height over an increasingly non-uniform interface (larger n).

7.8 Fabrication process dependence

The characteristics of a Schottky junction are a direct consequence of the original substrate properties, substrate cleanliness, and metal contact deposition procedure. However, when device preparation procedures are optimised the quality of any device is ultimately determined by the properties of its substrate, and the drawback of SiC based devices is that SiC is very difficult to produce with a low defect density (micro-pipe density $\sim 1\text{cm}^{-2}$)[15].

The three sample types examined were produced by contrasting deposition procedures, whilst controlling the wafer (i.e. epilayer doping), and pre-deposition substrate preparation (i.e. wafer cleaning). All sample preparations resulted in uniform Ni coverage. Sample type 1 was produced via the crudest method, using the Edwards high vacuum system to rapidly deposit the Ni contact layer. Sample type 2 was prepared in the same Edwards HV system by a much slower controlled Ni deposition. Finally sample type 3 was prepared using the most refined procedure of metal deposition under ultra-high vacuum conditions, using a slow and highly controlled deposition rate.

Similarities in Schottky contact characteristics may be expected between the two Edwards HV prepared device sets, or the two sets prepared using a slow and controlled contact deposition, as a result of common preparation characteristics. However, the greatest similarity between sample types occurred between types 1 and 3, the rapid Edwards deposition and UHV prepared sample. Both sample types displayed localised sites of high photocurrent response, which were also correlated

with a slightly increased Ni surface topography (4-10nm). Sample type 1 displayed sites of high photocurrent up to 200nm in diameter, whereas sample type 3 had smaller regions of photocurrent enhancement up to 35nm in diameter. The presence of such features may be attributed to one of the following, surface defects of the SiC substrate, interface defects such as voids, Ni_2Si or C segregation. The presence of such phenomena would cause Schottky barrier pinning and provide a localised low energy pathway for an increased photocurrent to cross the Ni-SiC interface. The presence of such localised sites of below average Schottky barrier height is reflected in the corresponding ideality factors as determined by I-V measurements (Table 7.1). Sample types 1 and 3 both exhibited a reasonably high ideality factor for the as-deposited Ni-SiC Schottky contacts ($n^{\text{Sample type 1}} = 1.557$; $n^{\text{Sample type 3}} = 1.534$), inferring a non-uniform Schottky interface as visualised by photocurrent imaging.

Note it is improbable that these features of enhanced photocurrent resulted from the presence of contaminant species at the interface as they were not present on all three sample types, which were cleaned via an identical procedure. This is supported by the occurrence of the features upon the UHV prepared sample which theoretically possessed the purest interface.

Sample type 2 measured the largest as-deposited barrier (1.657eV) and the lowest ideality factor (n = 1.252), corresponding well with the highly uniform photocurrent response imaged. Photocurrent imaging recorded a highly uniform Schottky interface that displayed no large deviations from the average barrier height, but a very short range fine structure. Sample type 2 displayed a very different photocurrent response to sample types 1 and 3, and this is again confirmed by the macroscopic I-V measurements which displayed corresponding differences.

7.9 Summary

Within this chapter the following points have been addressed:

- Near-field photocurrent imaging has been successfully developed and demonstrated.
- Near-field photocurrent imaging of buried Schottky interfaces has been performed using suitable signal amplification/detection, and by specifically engineering samples with uniformly- thin Ni top contacts.
- Interface defects have been successfully detected and imaged, allowing their distribution and lateral extent to be determined.
- The semiconductor depletion width has been measured, allowing evaluation of the Schottky barrier height.
- Schottky barrier heights have been enhanced by annealing post-deposition at 500^0C for 600sec, the resultant interface and surface modifications have been subsequently characterised by photocurrent and topographic NSOM-modes.
- Sub-micron interface characteristics have been correlated with conventional macroscopic I-V measurements.

The capability of near-field photocurrent imaging in the analysis of buried interfaces has been demonstrated, however the intimate coupling of the near-field photocurrent signal and surface topography has also proved apparent, which directly imposes requirements upon the suitability of the technique to examine certain samples i.e. uniform metal contact layers with flat surfaces.

Different mechanisms to enhance the photocurrent contrast have been attempted, including the minimisation of the energy separation between the probing optical source and barrier energy, the use of different excitation energies, and photocurrent imaging under the application of an applied sample bias. The primary factor in photocurrent imaging contrast enhancement proved to be the energy separation between the probing excitation source and Schottky barrier under investigation, and unfortunately the energy difference between Ni-SiC barriers and the excitation sources available to this investigation was suitably large to dominate the other methods attempted. The energy difference between the two sources used (633nm; 1.96ev and 488nm; 2.55eV) was large at 0.59eV, however both were significantly

greater in energy than the Schottky barriers examined, and this was reflected by the identical photocurrent images measured for both excitation sources. Imaging under the application of a sample bias was also attempted to enhance the photocurrent contrast, however imaging at different bias levels also produced identical photocurrent images due to the superiority of the source energy over the barriers.

The capability and strengths of the difficult technique of near-field photocurrent imaging and its application to buried Schottky interfaces has been proven, and the necessity to correlate the probing optical energy with the barrier height highlighted. Near-field photocurrent imaging is a valuable technique to device physics at the sub-micron scale, and can be tailored, using a tuneable optical source, for a particular material system to provide a powerful non-destructive imaging capability.

7.10 References

[1] E.H. Rhoderick, R.H. Williams, *Metal-semiconductor contacts*, (2nd Edition, 1988)

[2] P.R. Dunstan, T.G.G. Maffeis, M.P. Ackland, G.T. Owen, S.P. Wilks, *J. Phys.: Condens. Matter* **15**, 3095 (2003)

[3] K. Karrai, G. Kolb, G. Abstreiter, A. Schmeller, *Ultramicroscopy*, **61**, 299 (1995)

[4] B. Hecht, H. Bielefeldt, Y. Inouye, D.W. Pohl, L. Novotny, *J. Appl. Phys.* **81** (6), 2492 (1997)

[5] C. Coluzza, G. Di Claudio, S. Davy, M. Spajer, D. Courjon, A. Cricenti, R. Generosi, G. Faini, J. Almeida, E. Conforto, G. Margaritondo, *J. Microscopy*, **194** (2/3), 401 (1999)

[6] R.L. Williams, L.J. Brereton, M. Antognozzi, M.J. Miles, *Ultramicroscopy*, **71**, 165 (1998)

[7] J. Almeida, T. Dell'Orto, C. Coluzza, G. Margaritondo, O. Bergossi, M. Spajer, D. Courjon, *Appl. Phys. Lett.* **69** (16), 2361 (1996)

[8] B. Pecz, *Appl. Surf. Sci.* **184**, 287 (2001)

[9] F. Roccaforte, L. Calgano, P. Musumeci, F. La Via, *Mater. Sci. Forum*, **255**, 353 (2001)

[10] M. Sochacki, J. Szmidt, M. Bakowski, A. Werbowy, *Diam. Rel. Mater.* **11**, 1263 (2002)

---

[11] A. Kestle, S.P. Wilks, P.R. Dunstan, M. Pritchard, P.A. Mawby, *Electron. Lett.* **36** (3), 267 (2000)

[12] M. Badila, G. Brezeanu, J. Millan, P. Godignon, V. Banu, *Diam. Rel. Mater.* **11**, 1258 (2002)

[13] L.D. Madsen, E.B. Svedberg, H.H. Radamson, *Mater. Sci. Forum.* **264-268**, 799 (1998)

[14] U. Starke, M. Franke, J. Bernhardt, J. Schardt, *Mater. Sci. Forum.* **264-268**, 321 (1998)

[15] C.H. Carter, V.F. Tsvedkov, R.C.Glass, *Mater. Sci. Eng. B*, **61**, 1 (1999)

Chapter 8
Results: Planar quantum well lasers and MQB reflectors

8.1 Introduction

Red-emitting quantum well laser diodes operating at a wavelength of 630nm are required to fulfil a range of applications including data storage, printing, medicinal purposes, and metrology[1]. The generation and waveguiding of photons of such energy imposes strict requirements upon the materials used in the construction of these laser systems, which are achieved by the AlGaInP quantum well material system. However the performance and power output of such lasers is limited by the thermally activated loss of electrons from the active region, thus reducing the efficiency in achieving a population inversion.

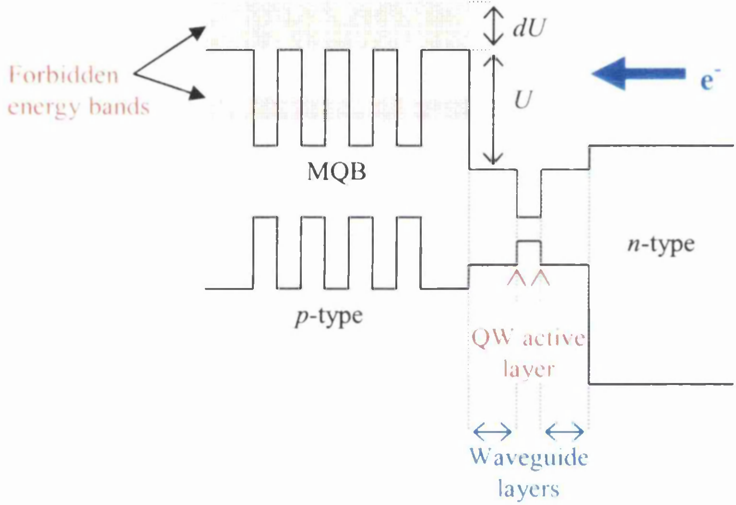

Figure 8.1 The fundamental structure of a quantum-well laser diode incorporating a multi-quantum barrier structure within the *p*-type cladding region. The MQB super-lattice is designed to enhance the conduction band discontinuity by alignment with forbidden energy mini-bands.

The efficiency of electron confinement to the active region is dependant upon the magnitude of the conduction band offsets, i.e. the potential barrier U between the waveguide layer and *p*-type cladding. In order to enhance the potential barrier and thus confinement, a multi-quantum barrier (MQB) super-lattice is introduced into the *p*-type cladding region[2], as shown in Figure 8.1. The MQB structure is engineered to align a forbidden energy mini-band of the MQB super-lattice with the conduction band minimum in order to enhance the conduction band discontinuity by dU, as described in chapter 4. The MQB structure is intended to optimise the electronic

properties of the laser device without altering its optical characteristics. This results chapter considers three samples and their characteristics by NSOM. Collection mode and photocurrent measurements are presented simultaneously with topographic images and modifications in electron transport due to the introduction of MQB's are discussed in depth.

8.2 Sample details

Three GaInP / $(Al_xGa_{1-x})_{0.52}In_{0.48}P$ based QW lasers were studied in the analysis of multi-quantum barriers and their effectiveness in barrier enhancement. Two samples contained MQB super-lattices, and a third **control laser** substitutes the MQB structure with a single layer, facilitating the evaluation of the impact of the MQB's upon the electronic and optical properties of the device. The basic structure of all three samples is represented in the schematic of Figure 8.1, showing the common quantum well laser structure. Test structures (i.e. MQB's and the control layer) were grown in the three samples within the *p*-type cladding region, adjacent to the active layer and waveguide region, as described fully in Appendix 11.2.

The samples were prepared by metal organic chemical vapour deposition, MOCVD, grown at a temperature of 690^0C. Two MQB structures were examined, **MQB 1** and **MQB 2**, containing seven and six MQB well/barrier pairs respectively. The MQB structures were theoretically optimised by solving the Schrödinger equation across the structures and maximising the electron reflectivity as a function of the incident energy[1]. The layer thickness and material compositions were varied until a reflectivity curve displaying a clear barrier enhancement and no low energy electron tunnelling was achieved. Conduction band discontinuity (barrier) enhancements of 16-20% were theoretically modelled[1,3].

The compositional structure of the three lasers examined is listed in tables 1 to 3 of Appendix 11.2, and schematics of the test structures examined are shown in Figure 8.2. The test structures are represented as a function of the aluminium concentration of the different layers as the band-gap energy of AlGaInP varies according to Al composition, thus providing a suitable representation for comparison between structures[4].

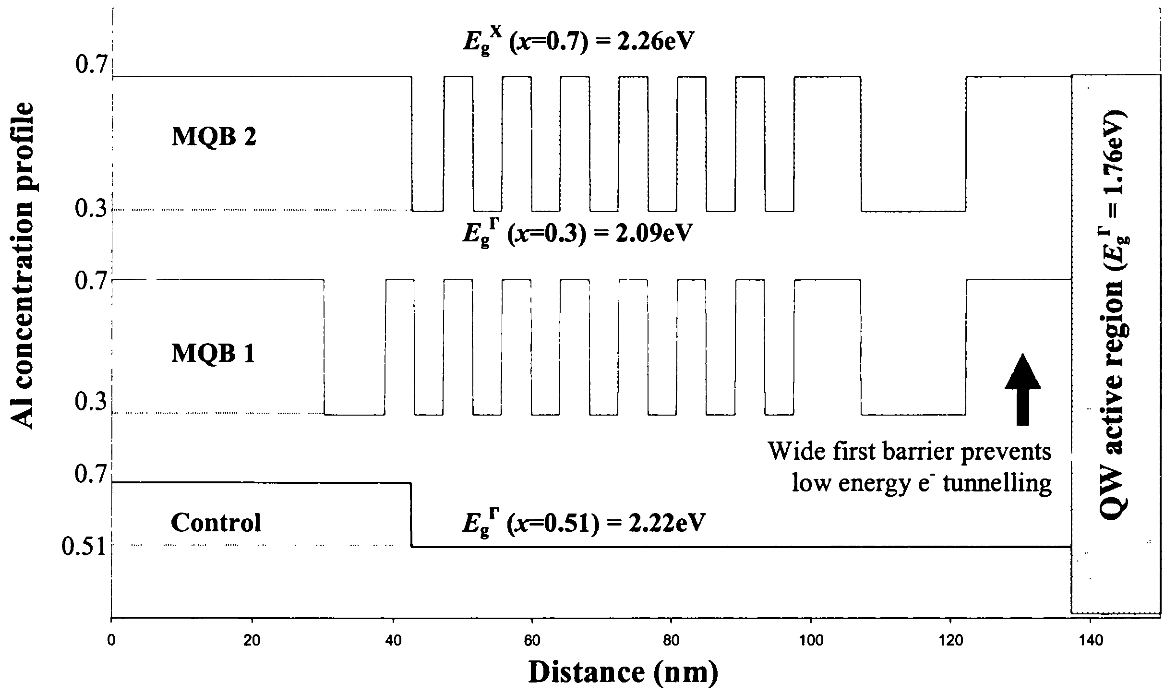

Figure 8.2 Schematic representation of the three test structures displayed in terms of the Al concentration of the different layers in the device. The location of the QW active region including waveguides is shown, and the test structures displayed in respect to that. The test structures are located within the *p*-type material of the device.

The band gap energy (E_g) of $(Al_xGa_{1-x})_{0.52}In_{0.48}P$ varies with the aluminium concentration (x) as follows for the Γ and X band transitions,

$$E_g^\Gamma = 1.91 + 0.61x \tag{8.1}$$

$$E_g^X = 2.242 + 0.022x \tag{8.2}$$

The structures are optimised for a single Γ-band model; however some electron leakage from the active region has been attributed to possible inter-valley transfer to the lower energy X-band minima and thus must also be considered[3].

The **control laser** substitutes the MQB structure with a comparable thickness of $(Al_{0.51}Ga_{0.49})_{0.52}In_{0.48}P$ composed of an intermediate composition of Al (i.e. 0.51). Note the composition of the control layer is intermediate in Al concentration between that of the MQB well (0.3) and barrier (0.7) layers.

All test structures are located adjacent to the waveguide layer of the active region, within the *p*-type material of the laser *pn*-junction. All other aspects of the laser designs are constant across the sample set. The MQB technique of barrier

enhancement has been successfully demonstrated previously for Schottky junctions, however the theoretical barrier enhancement has not been achieved in heterojunction devices[2,5,6,7]. The possible causes of this have been suggested to be inaccuracy in growing a controlled abrupt super-lattice, which has been reported in the STM study of such devices by K.S. Teng *et al*[1], and weaknesses in the theoretical modelling technique when applied to the more complex AlGaInP heterostructure devices.

8.3 Sample preparation

The samples were cleaved prior to imaging and clamped in the cross-sectional orientation using the electrical contacts of the laser diode sample holder, (see section 6.6.2). The success of the imaging technique was entirely dependant on the quality of the surface cleave and was only possible when a perfectly flat cleave was achieved, enabling the perpendicular approach of the NSOM probe and thus the maximum interaction between the sample and the near-field volume of the probe aperture. The planar quantum well laser diodes displayed a strong photocurrent response when using a far-field optical source to illuminate the entire cleaved edge of the wafer. However, upon the utilisation of a 50nm near-field optical source the photocurrent response was not detectable, even to the lock-in amplification system preceded by the pre-amplifier of 10^8 gain. This is a direct result of the similarity between the excitation energies (1.96eV, 2.55eV) and the band-gap energy of the active region (1.76eV), but primarily a consequence of the narrow width (6.8nm) of the single quantum well active region. Although very photo-reactive, as displayed under far-field illumination, the extremely small surface area ($\approx$ 6.8nm $\times$ 50nm) of the active layer illuminated by the near-field probe did not generate a detectable photocurrent intensity.

When operating the laser devices and performing collection NSOM imaging (using a 50nm aperture probe), the intensity of light coupled from the laser samples into the NSOM probe was also extremely low and inhibited accurate detection even when using the avalanche photo detector, APD. Therefore it was necessary to use larger aperture 100nm diameter probes to facilitate the NSOM analysis by both photocurrent and collection mechanisms.

8.4 Topographic imaging

Although the samples were cleaved prior to imaging, there is considerable oxide growth apparent in all topographic images collected. Imaging was commenced within twenty four hours of sample cleaving and remained possible for approximately seven days. The oxide growth clustered on the surface as it progressed and formed very different growth patterns depending upon the underlying layers. The oxides of the different layers developed at differing rates and formed clusters of various diameter and number density, again depending upon the location. The varying oxidisation characteristics are a direct indication of the variation in composition of the underlying layers, or an indicator of the variation in the average composition, as layers in the MQB structure are theoretically 4.2nm thick which is smaller than most clusters seen. As time progressed (approaching seven days) the oxides developed either side of the active region and eventually closed in covering the active region with a layer substantial enough to scatter and attenuate the near-field illumination of the NSOM probe when performing photocurrent imaging. This also sufficiently scattered the laser light when powering the device and performing collection imaging, rendering detection impossible in both cases. However, during the early stages of development the oxides proved very informative in locating the different layers via shear-force topographic imaging.

The surface topographies of the three lasers are seen in Figure 8.4, imaged at approximately similar durations after sample cleaving. The quantum well, waveguide, and multi-quantum barrier layers are labelled in the following diagrams using an overlaying coloured schematic to demonstrate their location and extent. The composition of the different layers is labelled in the colour key of Figure 8.3.

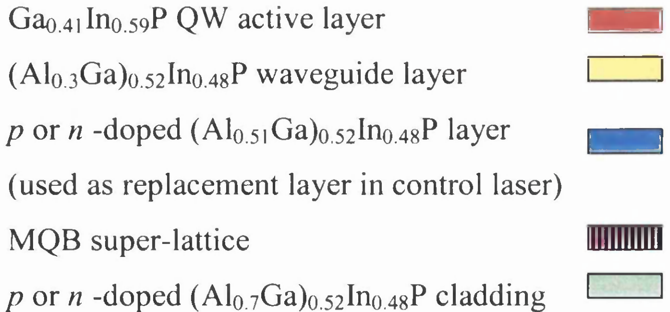

Figure 8.3 Colour key for the overlaying schematic labelling of the following topographic images displayed in Figure 8.4. Full sample structures are detailed in

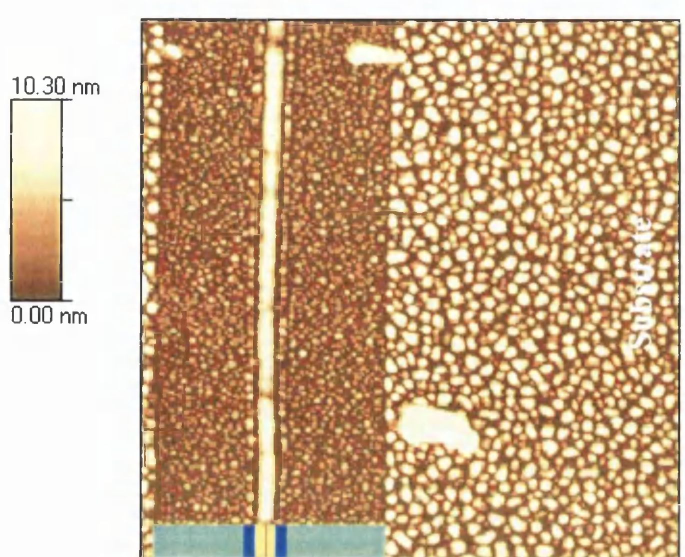

(a) Control laser

$(5000nm)^2$ image acquired during the early stages of oxide growth. The image was processed by background levelling to reduce the influence of the large feature which is possibly some debris from cleaving.

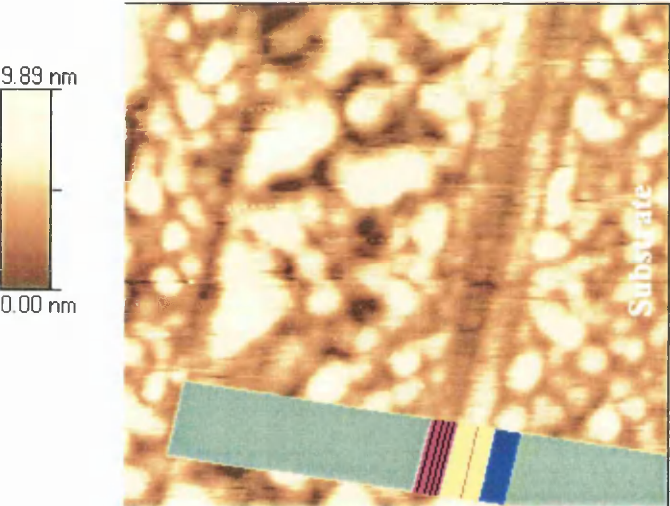

(b) MQB 1

$(2000nm)^2$ image showing a greater degree of oxide development. Note the MQB super-lattice is seen to the left of the active region (and waveguides) as the dark, i.e. lower surface stripe.

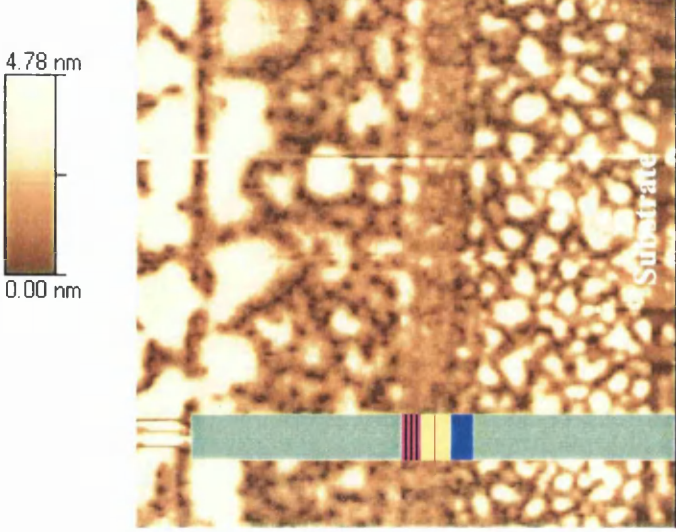

(c) MQB 2

$(2500nm)^2$ image acquired after a considerable level of oxide has developed. Note this image displays noise as it was acquired simultaneously with a collection NSOM image when the device was powered up and lasing.

Figure 8.4 Shear-force topographic images of the lasers active regions and adjacent layers. The corresponding colour key identifying the layer compositions is displayed previously in Figure 8.3.

The topographic images of all three lasers demonstrate that the actual manufactured structure is accurate with the designed parameters, as set out in Appendix 11.2, at least for the overall structure and layers that are of great enough thickness to be revealed by the oxide growth and shear-force detection. Clearly the presence of surface oxides is useful in visualising the location of the different layers in the structures, the distribution and dimensions of which can be correlated with the theoretical structures (Appendix 11.2) and attributed to the corresponding layer composition.

The multi-quantum barrier super-lattices are comprised of 4.2nm wide layers alternating in aluminium content between 0.3 and 0.7. The MQB appears in the topographic images as a single layer, as the individual wells and barrier are too narrow to be separately resolved, i.e. the oxide growth clusters are larger than 4.2nm diameter and the oxide reveals the MQB as a single layer, possibly the oxide growth distribution displayed here is a function of the average layer composition of the MQB region. This could indicate Al and Ga interdiffusion between well and barrier layers which is detrimental to the properties of the MQB that requires well defined material properties and abrupt interfaces, as previously observed by Teng *et al*[1]. However, it may have been possible to visualise the individual layers of the MQB using their surface oxides for a short period very soon after cleaving, i.e. when there is very limited oxide developed. Note that it is also not possible to separately resolve the 6.8nm thick QW active layer, which is seen for all lasers as a single layer of oxide comprising the QW and adjacent $(Al_{0.3}Ga)_{0.52}In_{0.48}P$ waveguiding layers, the width of this oxide stripe corresponds to the sum of the QW and waveguide layers.

The QW active layer is located by correlating topographic images with their simultaneously acquired photocurrent or collection NSOM images. However, throughout the course of imaging these devices several NSOM probes were used. Theoretically the NSOM probes are manufactured for consistency of the aperture diameter, however, the location of the furthest protruding point of the probe tip can vary between probes as illustrated in Figure 8.5. This does not affect the imaging properties of the probes or resolution of the topographic images; however it does have direct implications on the correlation between topographic and simultaneously acquired images. The greatest protrusion on the probe tip is the location of the shear-

force interaction site, i.e. it is the centre of shear-force imaging. However, the centre of both photocurrent and collection NSOM imaging is the centre of the probe aperture, ideally the two would coincide, as is the case for apertureless NSOM[8]. This is physically impossible for aperture NSOM therefore there is always an offset between topographies and their simultaneous images derived via an optical mechanism. This makes it difficult in the case of precisely locating a thin QW active layer.

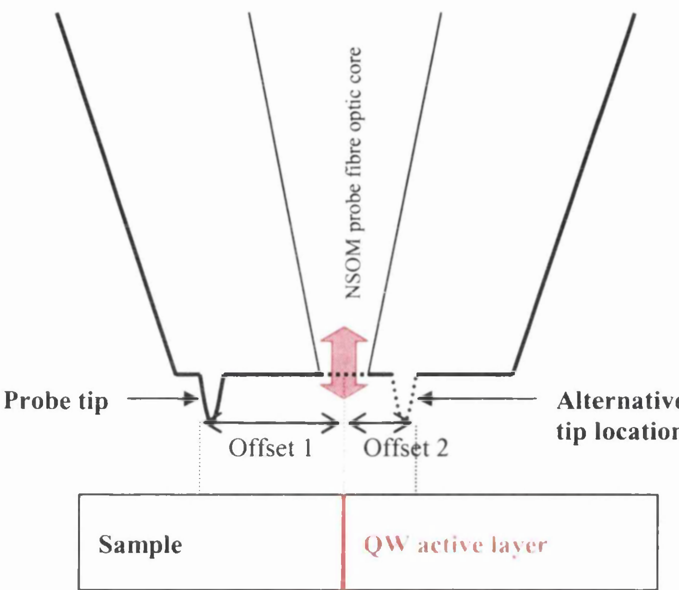

Figure 8.5 The location of the shear-force interaction site (furthest protruding point of the NSOM probe), overemphasised in this illustration, can vary between probes, resulting in a translation between simultaneously acquired images.

When the protrusion point of two differing probes are located on directly opposite sides of the aperture then the minimum offset between their corresponding images will be approximately 100nm. Thus when imaging a device such as a planar quantum well laser, the use of a number of different probes with different shear-force interaction sites provides greater insight in precisely locating the active region in respect to correlation with topographic data. This was the situation when imaging the MQB and control lasers and aided the correlation of images in locating the active QW layer at the centre of the bright stripe as labelled in Figure 8.4(a), (b), and (c).

The simultaneous shear-force topographic data, although not providing direct information about the fine structure of the MQB's, has provided an interesting reference to the photocurrent and collection NSOM images. Perhaps most

importantly it has confirmed the manufactured sample's structure and dimensions were as intended by their design and consistent throughout the sample set.

8.5 Collection NSOM of operating devices

The optical output of the operating devices was analysed by collection NSOM, which was performed as described in chapter 6, collecting near-field light at the sample surface using the nano-aperture of the probe and measuring the intensity by focussing the probe's fibre tail onto an avalanche photo diode (APD). This was initially attempted using a photomultiplier tube detector (PMT) however its sensitivity proved inadequate as a result of the low optical intensities typical of collection NSOM. As previously mentioned, in order to collect a detectable optical intensity from these single QW devices it was necessary to use 100nm diameter aperture probes, instead of the optimal 50nm aperture probes, thus increasing the optical throughput. However the drawback of this is that the ultimate optical resolution of the system is increased to 100nm, as the resolution of collection imaging is determined by the dimensions of the aperture used to sample the optical field[9,10].

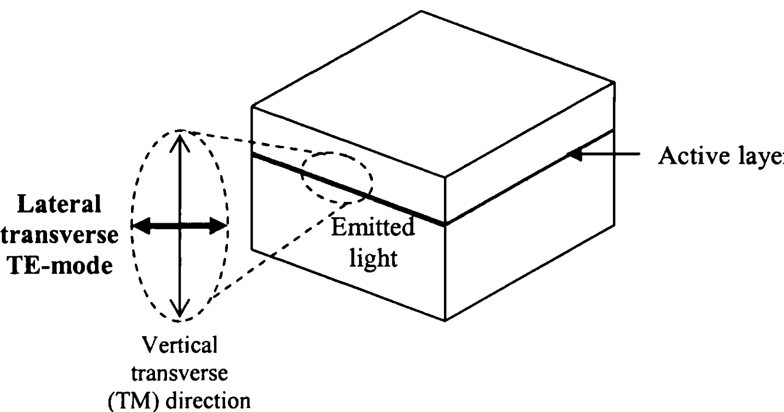

Figure 8.6 Optical emission modes of an operating laser diode.

The optical output characteristics of the three test samples were very similar, as is suggested by the device structures that posses a common active layer and waveguide region, as detailed in Appendix 11.2. The samples differ only in the structure within the *p*-type layers adjacent to the active region, all other device parameters remain constant throughout the sample set. The optical characteristics, or more precisely the spatial characteristics of the optical output, are determined by the geometry of the active layer and adjacent waveguide layers, which are identical for all samples. The

waveguiding properties of a device are also dominated by the refractive index distribution of the active layer and adjacent cladding layers; however this remains identical for the samples examined in this work. The various test structures located at the *p*-type region boundary are designed to influence the electronic confinement of the active region and theoretically should not disrupt the optical confinement of the cavity. Therefore analysing the distribution of the optical output is a direct experimental investigation to ensure the waveguide nature of the devices is not disrupted by the presence of the MQB's.

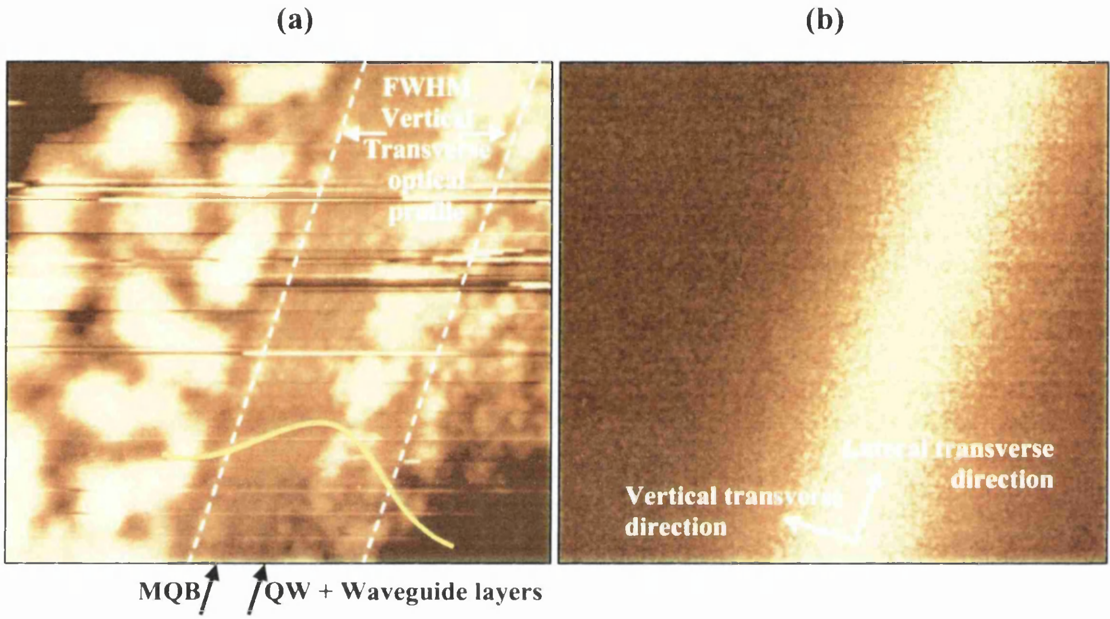

Figure 8.7 Simultaneous (1602nm)^2 **(a)** Topography, and **(b)** Collection NSOM images of laser MQB 1 operating at 2.06V; 80mA. The FWHM of the vertical transverse optical profile is correlated on the topographic image by dashed white lines, and the location of the maximum optical output is labelled by the yellow curve. The optical image (b) was acquired using an APD detector at an integration time of 10mS, the maximum intensity is 58counts.

The images of Figure 8.7 display simultaneous (a) topography, and (b) collection NSOM, of MQB 1, which demonstrates an optical response typical of what is observed for all three test samples examined. The optical output is confined to a bright "stripe" at the sample surface, parallel to the layer structure of the device in the direction known as the lateral transverse direction, as labelled in Figure 8.6 and Figure 8.7(b). The measured optical intensity is uniform along the length of this plane, as the external electrical contacts are uniformly distributed across the entire *p* and *n* –type electrodes, electrically pumping the active region along its complete length, unlike the finite electrodes used in gain guided laser devices[11].

Perpendicular to the lateral transverse direction, and growth plain of the device, is the vertical transverse direction, as labelled in Figure 8.7(b). This is oriented perpendicular to the waveguides and QW active layer and is the direction in which the waveguides are intended to provide optical confinement. The degree of optical confinement can clearly be seen in Figure 8.7 by the narrow bright output stripe which is efficiently attenuated away from the active region on either side. The simultaneous image acquisition allows for the correlation of surface topography and optical characteristics, the bright optical output stripe maxima is seen to coincide with the location of the quantum well active layer, i.e. the centre of the waveguide region, as expected.

The difficulties in physically locating the active layer by correlating topographies with optically generated images have previously been discussed. However a substantial quantity of data was collected for these planar laser devices using a number of NSOM probes, and the average location of the optical output maxima coincided with the centre of the waveguide layers, i.e. the QW active layer. The vertical transverse optical profile is correlated with the surface topographic characteristics in Figure 8.7(a) and its location is represented symbolically by the yellow curve. The positions of the full width at half maximum, FWHM, points of the vertical transverse profile are accurately denoted by the dashed white lines and can thus be visualised in respect to the active layer and waveguide geometry.

The vertical transverse optical profile of Figure 8.7(b) is displayed in the cross-section of Figure 8.8, along with the location and dimensions of the waveguide region with the quantum well residing at its centre. Reasonably good optical confinement characteristics are displayed by the device in this direction which is a consequence of the refractive index engineering of the region. The use of a quantum well as the active layer in a laser increases the electronic confinement and introduces the quantization of energy levels involved in the optical emission process. However quantum well active layers are very thin (< 10nm) resulting in a decrease in optical confinement in the vertical transverse direction.

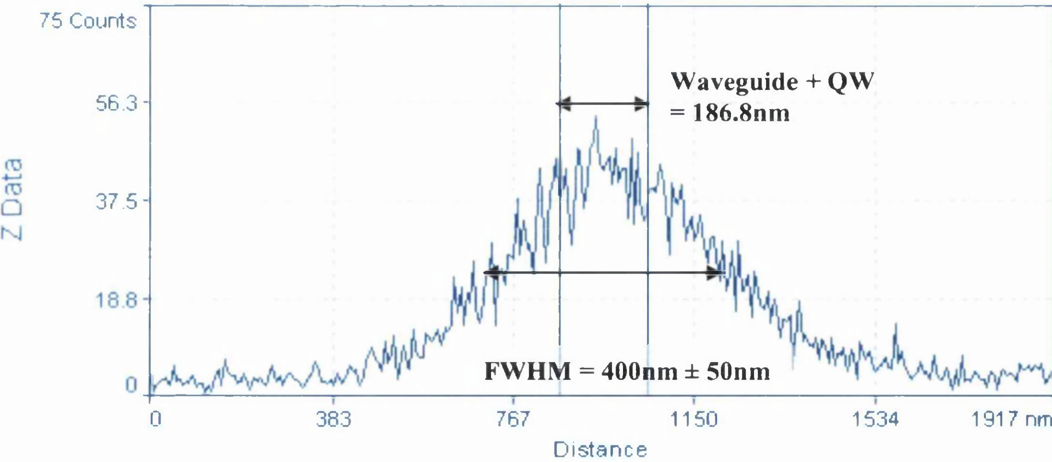

Figure 8.8 Vertical transverse cross-section of the collection NSOM image displayed in Figure 8.7(b) showing the device MQB1 powered at 2.06V; 80mA. The dimensions of the active layer and waveguides are inserted.

The FWHM of the optical distribution of Figure 8.8 is typical of that exhibited by all the test devices and the value of 400nm ± 50nm is the average value and range encompassing many collection images over the three test samples using several NSOM probes. The cross-sectional profile is correlated with the 6.8nm thick $Ga_{0.41}In_{0.59}P$ active layer, located at the apex of the distribution, and the adjacent 90nm thick $(Al_{0.3}Ga)_{0.52}In_{0.48}P$ waveguide layers as indicated in Figure 8.8. The FWHM of the optical distribution corresponds to a transverse confinement of 47.45% ± 5.95%, this is very close to previous near-field measurements of Lu *et al*[12] who measured 46% on similarly structured planar quantum well laser devices. However it must be noted that the FWHM measured here is a convolution of the laser guided mode and NSOM aperture geometry, thus by deconvolving NSOM aperture characteristics a higher degree of confinement will be detected for the device.

Figure 8.9 indicates two curves showing the vertical transverse optical profiles acquired from the control device at different operational powers, 1.78V at 27mA and 2.06V at 92mA, which are below and above the laser threshold respectively. The transverse cross-sectional profile is highly Gaussian in distribution, as shown by the very close curve fitting of Figure 8.9, indicating that the laser devices are operating predominantly at the fundamental mode. The Gaussian curves display a 96% accurate fit for electroluminescence (i.e. below threshold, 1.78V; 27mA), and a 99% accurate fit for stimulated emission of the active layer (i.e. above the laser threshold, 2.06V;

92mA). The curve fitting equation and parameters are displayed in Appendix 11.3. The degree of optical confinement varies slightly with the operational power, spreading with increasing optical intensity. Below threshold (1.78V; 27mA) the FWHM is 350nm ± 40nm, and above threshold (2.06V; 92mA) the optical spreading is greater at a FWHM of 400 ± 30nm.

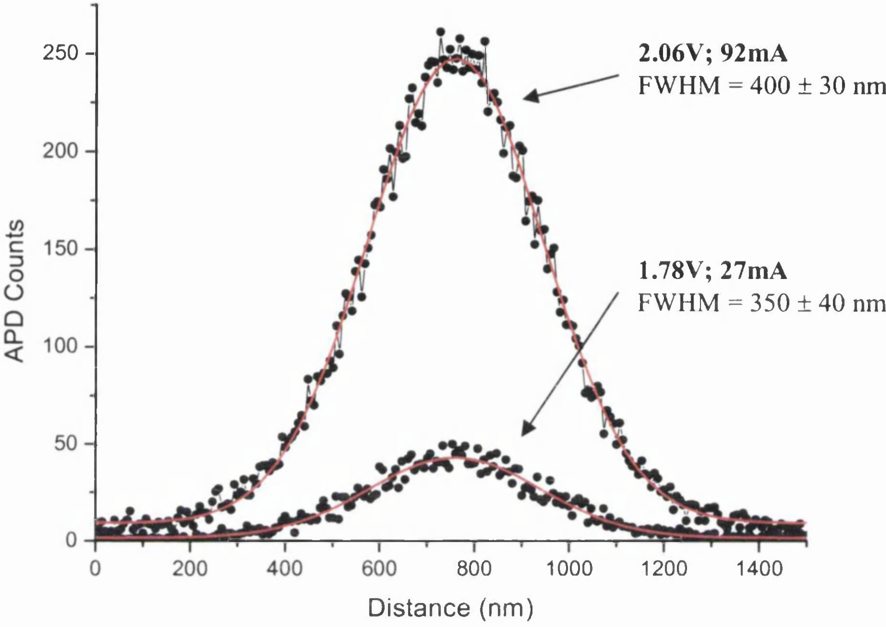

Figure 8.9 Vertical transverse profile at 1.78V; 27mA, and 2.06V; 92mA, recorded for the control device. The cross-sections are mathematically fitted by Gaussian curves (red) which display very high correlation.

Collection NSOM imaging of operational devices has mapped (at 100nm resolution) the optical intensity distribution at the emitting facet of the device allowing correlation with the surface topography, acquired simultaneously. The imaging has provided insight into the functionality of the devices, confirming the waveguide structure is constructed with the designed parameters (Appendix 11.2) and its effectiveness is not affected by the MQB structures grown within the edge of the *p*-type region. Collection NSOM has not probed the MQB structures directly, although it has confirmed that there is no electroluminescence occurring there, i.e. there is no carrier leakage past the QW active layer which results in radiative recombination when the device is operating, as proved by the closely matching widths of the vertical transverse distributions for all three test devices.

8.6 Near-field photocurrent imaging

Near-field photocurrent imaging of the three planar quantum well samples was performed in the cross-sectional orientation as described in chapter 6.6. The sample was connected directly to the first stage 10^8 gain amplifier, and photocurrent detection was performed under 0 volts applied sample bias. Imaging was performed using 100nm diameter NSOM apertures, as similarly with the collection NSOM, 50nm diameter apertures did not generate a signal level detectable to the lock-in amplifier.

The NSOM probe is employed as an optical source to locally photo-excite electron-hole pairs in the sample within the near-field volume of the sub-wavelength aperture when the excitation energy is greater than the samples band-gap energy. A photocurrent signal is detected in the external measuring circuit when electron-hole pairs are generated in the presence of an electric field, which acts to separate the opposite charge carriers before recombination occurs, and thus induces an electric field in the sample that drives the photo-generated reverse current. Therefore photocurrent imaging directly maps *pn*-junctions and is sensitive to the band-gap energy and barriers or band offsets in the conduction and valence bands.

The resolution of near-field photocurrent imaging is independent of the excitation wavelength used for small apertures (i.e. aperture diameters $< \lambda/2$)[13], and is actually a function of the near-field excitation volume, the absorption length, and is ultimately limited by the carrier diffusion length[14]. However, as determined by topographic imaging, the build up of surface oxides is rapid and several nanometers thick therefore cannot be ignored when considering the resolution of photocurrent imaging on such samples. The nanometer order thickness of surface oxide introduces a physical separation between the near-field aperture and the optically active surface of the cleaved sample, the evanescent field decays exponentially away from the aperture surface thus the probe-sample interaction is greatly reduced. This may explain the necessity for larger probe apertures of 100nm diameter in order to increase the photocurrent intensity to a detectable level. The intermediate oxide layer also scatters the localised near-field optical source, resulting in a spreading of the excitation volume and therefore decreases the resolution actually achieved by photocurrent imaging[13,15]. Therefore the experimental photocurrent resolution will be poorer than

theoretically possible. The optimum resolution observed for this study of planar quantum well laser devices was within the range 100-200nm, note this applies for the case of limited surface oxide growth which was pursued in these experiments.

8.6.1 Correlating the photocurrent response with cross-sectional structure

Photocurrent imaging is conducted simultaneously with shear-force topographic imaging, thus allowing the correlation of a sample's photocurrent response with the cross-sectional structure of the device, as measured at the cleaved surface. Although there are variations in the precise photocurrent response of each sample, the general characteristics and correlation with the surface topography is similar for all samples, therefore correlation characteristics are discussed using the single example of MQB 1. The precise differences in the photocurrent responses of the three test samples are subsequently discussed in the next section.

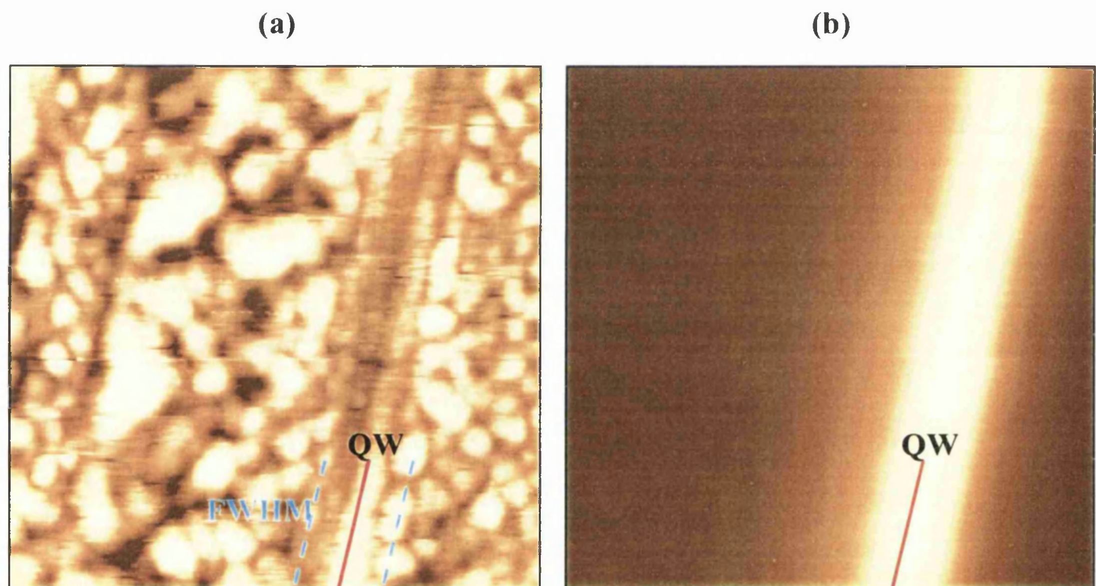

Figure 8.10 $(2000.83\text{nm})^2$ images of MQB 1 showing the **(a) Topography** (maximum height = 8.73nm), and simultaneous **(b) Photocurrent** (maximum intensity = 5.12V) variations using the 488nm (2.55eV) excitation source. The location of the active QW layer is labelled, and the FWHM distribution of the vertical transverse component of the photocurrent is correlated onto the topography.

The images displayed in Figure 8.10 were recorded for the sample MQB1 and demonstrate the correlation between (a) surface topography, and (b) photocurrent variations. The topography reveals a moderate level of surface oxide growth which is useful in distinguishing the different regions of the device structure. The location of the active QW layer and adjacent waveguides was previously determined by

measurements of the sample structure and is revealed here to coincide accurately with the maxima in the photocurrent distribution, confirming the accuracy of the previous measurements; the location is labelled for both images. The photocurrent intensity is constant in the lateral direction parallel along the length of the active layer, demonstrating continuity in the integrity of the device structure. However in the direction perpendicular to the active layer, i.e. across the device structure in the vertical transverse direction, there is a clear variation in the photocurrent response of the different compositional layers. The variation in photocurrent perpendicular to the active layer is correlated with surface topography in the cross-sectional diagram of Figure 8.11, the magnitudes of both the topographic height and photocurrent intensity are normalised for ease of comparison.

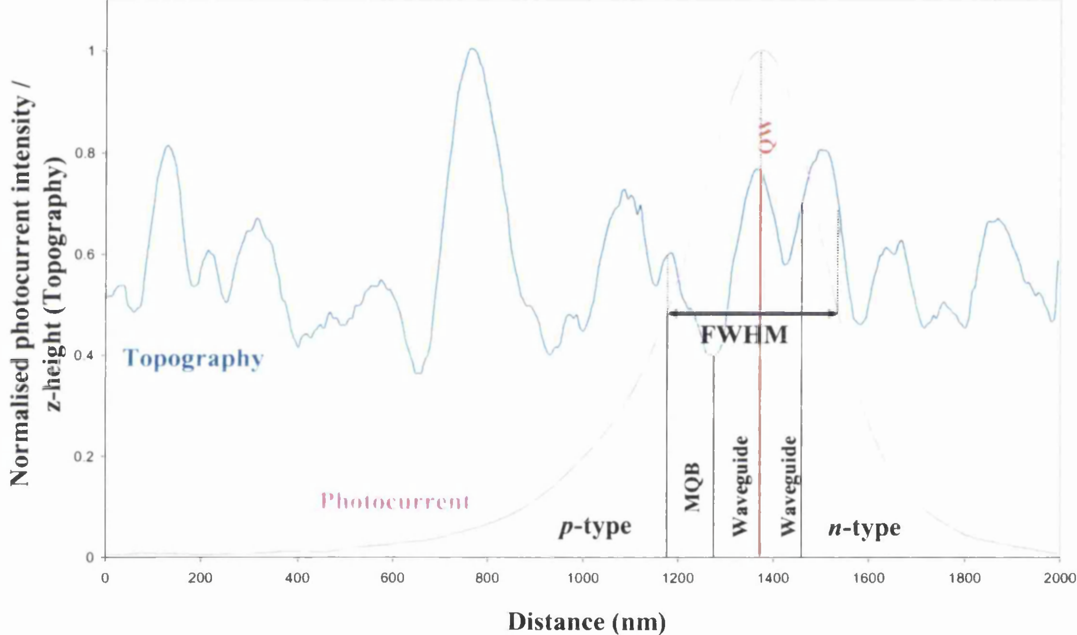

Figure 8.11 Correlation of cross-sectional profiles of the topographic and photocurrent images displayed in Figure 8.10, acquired from MQB 1 using the 488nm (2.55eV) excitation source. The cross-sections are taken perpendicular to the active layer and the magnitudes are normalised for comparison.

The photocurrent was stimulated using the higher energy 488nm (2.55eV) excitation source and displays clear asymmetry about the quantum well. The accurate alignment of the QW active layer and photocurrent maximum intensity is emphasised by the cross-sectional profiles, as however is the full width at half maximum (FWHM) of the optically activated photocurrent which measures 352nm. The origins and mechanisms responsible for the vertical transverse photocurrent distributions exhibited by the three sample devices are discussed in detail in the following section.

8.6.2 Probing the effect of MQB's using near-field photocurrents

Photocurrent generation is sensitive to the electronic properties of a device via the band-gap energy and the band profile (i.e. band discontinuities), which vary across the MQB structure as represented in Figure 8.12, but requires the presence of a field to facilitate its propagation and separate the photo-generated electron-hole pair. Thus the photocurrent images the built-in fields and diffusion characteristics of an unbiased device via minority carrier transport. By selecting different excitation sources that vary in energy about the band-gaps of the different layers in the three sample devices it is possible to probe the characteristics of the MQB devices.

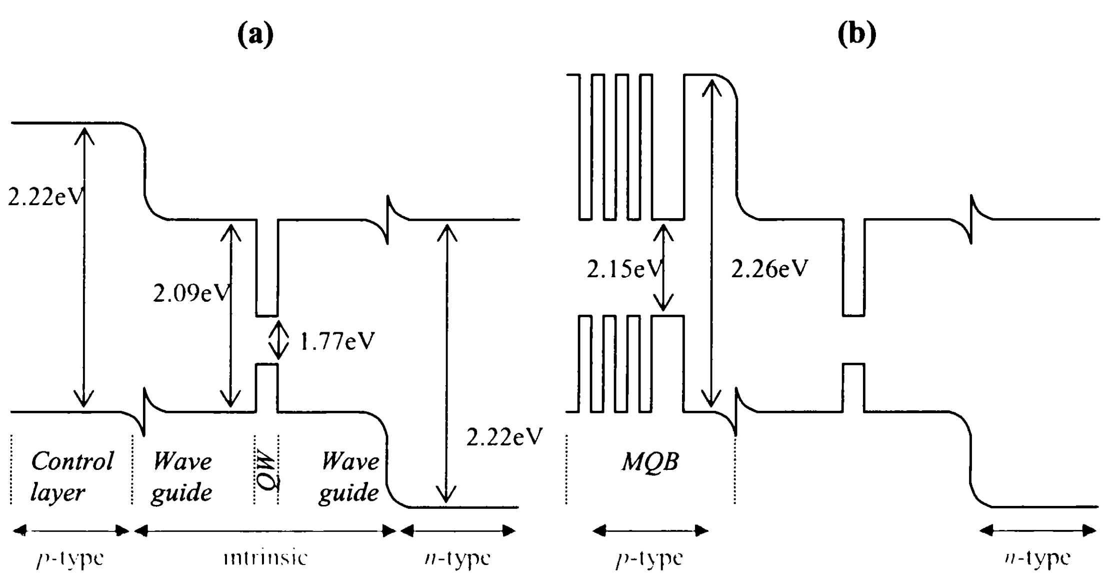

Figure 8.12 Simplified band profiles of **(a)** the **control laser**, and **(b)** the general **MQB structure**, incorporating the band-gap energies of the constituent materials. The *n*-type and waveguide regions including the QW are consistent for all samples.

Photocurrent cross-sectional profiles, perpendicular to the active layer, are displayed in Figure 8.13 for the (a) Control laser, (b) MQB 1, and (c) MQB 2 samples. Displayed for each sample are the photocurrent profiles obtained at the two excitation energies of 1.96eV (633nm) and 2.55eV (488nm). The cross-sections are normalised for comparison and the relative positions of the active region and MQB (or control layer) are labelled. The average FWHM measurements of the photocurrent cross-sections are displayed in Table 8.1, incorporating the experimental standard error values.

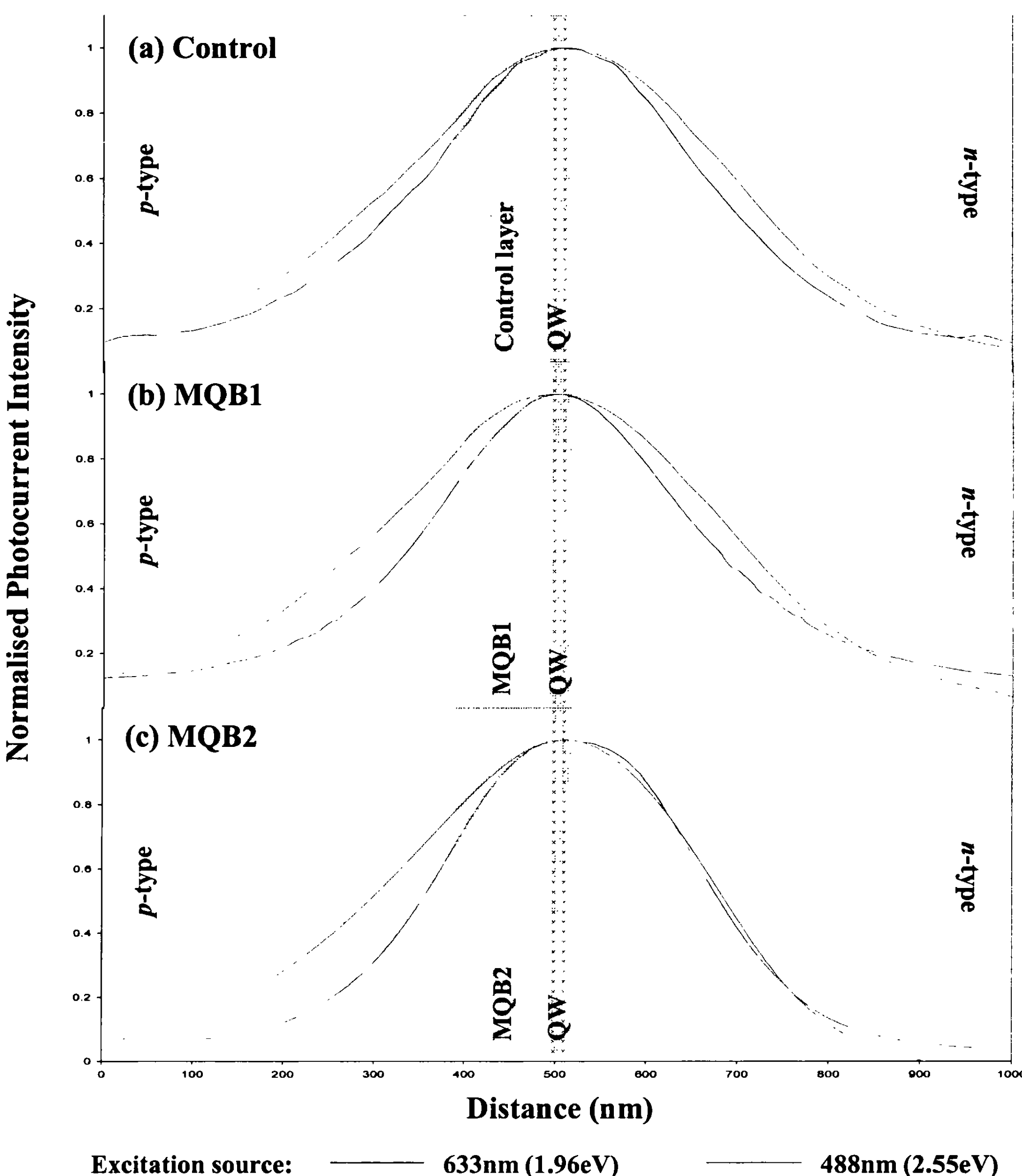

Figure 8.13 Normalised photocurrent cross-sections of the **(a) Control**, **(b) MQB1**, and **(c) MQB2** samples. The cross-sections are taken from images showing a similar level of oxide development and using new 100nm NSOM probes. The cross-sectional profiles are oriented in the direction perpendicular to the active layer.

	Control	MQB1	MQB2
633nm (1.96eV)	380 ± 30 nm	350 ± 20 nm	360 ± 20 nm
488nm (2.55eV)	450 ± 30 nm	360 ± 30 nm	385 ± 20 nm

Table 8.1 Full width at half maximum parameters for the photocurrent cross-sectional profiles displayed in Figure 8.13.

In general, for all samples the photocurrent characteristics are broader when stimulated by the more energetic source, however the width and shape of the photocurrent profiles is different for each device and this was found to be repeatable with fresh sample cleaves (i.e. not oxide dependent).

Consider the structure of the QW active layer and waveguides common to all three devices. The QW layer is 6.8nm thick and has a band-gap energy of 1.77eV, therefore electron-hole pair (*e-h*) generation occurs when excited by both energy sources [1.96eV (633nm) and 2.55eV (488nm)]. Sandwiching the QW is the two 90nm thick waveguide layers which posses a band-gap energy of 2.09eV, thus electron-hole pair stimulation only occurs for the sufficiently energetic 2.55eV (488nm) excitation source and *e-h* pair excitation is restricted to the QW for the lower energy 1.96eV (633nm) source. The band-gap separation of the remaining $(Al_xGa_{1-x})_{0.52}In_{0.48}P$ layers varies with the aluminium concentration as discussed in section 8.2 [3,16,17]. The production of a photocurrent also depends upon the presence of an electric field to separate the stimulated charge carriers, the field within the sample structure presides over the intrinsic region, predominantly at its boundaries with the *p* and *n*-type regions, however it is at the central, low band-gap, quantum well that carrier excitation is greatest.

8.6.3 Control laser photocurrent characteristics

The control sample displays photocurrent cross-sections that are reasonably symmetric in shape for both excitation energies, however the FWHM is greatly different and is on average 70nm ± 30nm wider at the higher excitation energy. The control sample contains a 94.5nm thick *p*-$(Al_{0.51}Ga)_{0.52}In_{0.48}P$ control layer (substituting the MQB structures of the other samples), which is composed of an aluminium concentration that is an average of that in the wells and barriers of the MQB structures. As mentioned, the band-gap energy varies with the aluminium concentration and for the control layer is 2.22eV, and therefore experiences electron-hole pair production only when illuminated by the higher energy 2.55eV (488nm) source, and a subsequent photocurrent in the presence of, or within the minority carrier diffusion length of an electric field. The first layer within the *n*-type side of the junction is an *n*-$(Al_{0.51}Ga)_{0.52}In_{0.48}P$ layer which also has a band-gap energy of

2.22eV (this layer is present in all three sample structures) and experiences electron-hole pair production when excited by the 2.55eV (488nm) source.

As discussed the built-in field of the device resides over the intrinsic region that is 186.8nm wide with the strongest field acting at the *p* and *n*-boundaries. A photocurrent is not only generated when excitation occurs at the location where a field acts, but also within a minority carrier diffusion length of such a location. The minority carrier diffusion lengths within the *p* and *n*-type $(Al_{0.51}Ga)_{0.52}In_{0.48}P$ layers adjacent to the intrinsic region are calculated using minority electron and hole mobility's of $\mu_e = 160\ cm^2V^{-1}S^{-1}$ and $\mu_h = 10\ cm^2V^{-1}S^{-1}$ respectively and a minority carrier lifetime of the order 100 pS, as according to theoretical and experimental investigations on such materials[18,19]. The diffusion lengths were calculated using $L_{e,h} = (D_{e,h}\ \tau)^{1/2}$,where $D_{e,h}$ is the diffusion coefficient, to be L_h = 50.87nm, and L_e = 203.47nm [14,20]. Therefore when the control sample is illuminated by the higher energy 2.55eV (488nm) excitation, a photocurrent is expected to act over a region 441.14nm in width (intrinsic region + diffusion lengths) plus the *p* and *n* region depletion lengths of approximately a few nanometers. This value corresponds very closely to the measured FWHM of the perpendicular photocurrent profile at 2.55eV (488nm) displayed in Figure 8.13(a) of 450 ± 30nm.

In the case of 1.96eV (633nm) illumination (Figure 8.13(a)), when electron-hole excitation is confined to the QW active layer alone, the photocurrent profile measured was 380 ± 30nm wide. The broad photocurrent signal measured indicates that near-field light, coupled into the waveguide layers by the NSOM probe, propagates into the QW layer (where the band-gap energy is 1.77eV) and promotes carrier separation and subsequent photocurrent propagation. The width of the waveguide region incorporating the QW active layer is 186.8nm, by accounting for the lateral resolution of the 100nm diameter aperture NSOM probes this produces a photocurrent width of the order 387nm which compares favourably with the measurement listed in Table 8.1 of 380 ± 30nm. Note, charge carrier separation can occur within the *p* and *n*-type $(Al_{0.51}Ga)_{0.52}In_{0.48}P$, and waveguide layers when exciting with the 2.55eV (488nm) source, and thus local photocurrent generation via minority carrier diffusion can

dominate in this case, as opposed to optical propagation of the excitation light throughout the waveguiding structure.

8.6.4 MQB photocurrent characteristics

The photocurrent cross-sections perpendicular to the active layer (Figure 8.13(b) and (c)) are very different for the two multi-quantum barrier samples MQB 1 and MQB 2 than the control sample. Both exhibit symmetric photocurrent profiles at 1.96eV (633nm) excitation, and broader asymmetric profiles at the more energetic 2.55eV (488nm) excitation, however the widths of each differ between the two MQB samples.

The perpendicular photocurrent width at both excitation energies is smaller for both MQB devices than for the control device, as listed in Table 8.1. This is because the MQB samples have replaced the lower band-gap 2.22eV p-$(Al_{0.51}Ga)_{0.52}In_{0.48}P$ control layer with the multi-quantum barrier structures beginning with a wide 2.26eV $(Al_{0.7}Ga)_{0.52}In_{0.48}P$ barrier layer, see Figure 8.12 and Appendix 11.2. The reduction in photocurrent widths, especially at the higher excitation energy, indicates the sensitivity of near-field photocurrent microscopy to the MQB structures. The difference in FWHM measurements and profile shape between MQB samples also indicates that the imaging mechanism is exhibiting sensitivity to the exact compositions of the multi-quantum barrier structures. The MQB sample structures posses the same intrinsic and n-type regions as the control sample, however the 94.5nm thick p-type cladding layer that proved to be active in photocurrent imaging of the control sample is replaced by apparently considerably less active MQB structures, thus reducing the photocurrent widths by approximately 94.5nm for 2.55eV (488nm) excitation, indicating the higher electronic confinement of the MQB. However this is not fully exhibited for MQB 2 where the photocurrent extends slightly into the MQB region, as indicated by the highly asymmetric cross-section in Figure 8.13(c).

The photocurrent cross-sections are very similar in profile and width at 1.96eV (633nm) excitation for both MQB samples measuring 350±20nm and 360±20 nm. The FWHM displayed by the MQB samples at 1.96eV (633nm) is also very similar to that of the control laser measured at 380±30nm, and thus the photocurrent FWHM of

all three samples, at 1.96eV (633nm) excitation, are within the experimental limitations of each other. This indicates that photocurrent imaging at such a low energy only exhibits sensitivity to the smaller band-gap active region and is not sensitive to probe the MQB. Although 380nm for the control sample is slightly larger than the MQB samples the resolution limits the analysis.

The photocurrent response of the three samples to 2.55eV (488nm) excitation is greatly contrasting, as seen in Table 8.1. The MQB samples exhibited much narrower photocurrent profiles than the control laser due to the presence of the MQB super-lattices. The excitation energy of 2.55eV is greater than the band-gap energies of both the wells (2.15eV) and barriers (2.26eV), as seen in Figure 8.12. However, the narrower photocurrent profiles (compared to the control laser) indicate the presence of barrier enhancement within the MQB super-lattice, where forbidden electron energy states extend above the conduction band edge, and appear effective for both samples.

For the 2.55eV (488nm) excitation, the photocurrent profiles of the MQB samples themselves differed considerably, at 360±30nm for MQB 1, and 385±20nm for MQB 2. This is highly indicative of the degree of barrier enhancement achieved by the differing MQB super-lattices of the two samples. The narrower photocurrent profile of MQB 1 (Table 8.1) indicates that a greater barrier enhancement is realised by the MQB super-lattice of sample MQB 1, than that achieved by MQB 2. However, MQB 2 does exhibit barrier enhancement, indicated by its narrower photocurrent profile than the control laser, but appears not as effective as MQB 1. The barrier enhancement observed for the MQB's increased the total energy required for photo-excitation above that of the basic band-gap energy of the well and barrier regions of the MQB. The absence of photo-excitation across the MQB region using the 2.55eV (488nm) excitation indicates that the barrier enhancement, particularly for MQB 1, increased the inter-band energy gap to approximately greater than the original band-gap energy of the MQB barrier layers of 2.26eV. Thus, the presence of a forbidden energy mini-band, elevated in energy above the conduction band edge, prevented the potential diffusion of photo-excited charge carriers into the built-in field of the device, forming a barrier to inhibit local photocurrent generation.

8.7 Summary

The cross-sectional NSOM study of planar quantum well lasers has proved an exciting alternative to standard characterisation methods and can add great insight into many nanoscale properties within these devices. The following conclusions can be drawn from this NSOM investigation of MQB laser devices:

- Shear-force topographic imaging has visualised the sample structure allowing the accuracy of the deposition techniques to be examined via oxide growth effects.
- Collection mode NSOM has probed the optical characteristics of operating devices and proven that, in this case, MQB's do not affect the optical confinement of the laser structure.
- Near-field photocurrent imaging has detected the presence of the MQB structures due to modification of the charge confinement.
- Results presented here clearly indicate a positive response to electron confinement in MQB structures when probed with the NSOM and compared to the control sample.
- By utilising different excitation energies near-field photocurrent imaging has proved sensitive to the different MQB structures.

An in-depth study of MQB effectiveness in quantum well lasers would require further alternative samples and possibly the use of smaller aperture (50nm) NSOM probes. The latter development would be facilitated by the elimination of the nanometer order thick surface oxide by imaging with the samples under a vacuum or inert gas. The removal of the intermediate oxide layer would be detrimental to the information in the topographic images; however the improvement in the optical efficiency of photocurrent imaging would be considerable, increasing photocurrent levels and thus allowing an improvement in resolution.

8.8 References

[1] K.S. Teng, M. Brown, A. Kestle, P. Smowton, P. Blood, S. Pinches, P.A. Mawby, S.P. Wilks, *Appl. Surf. Sci.* **190**, 284 (2002)

[2] K. Iga, H. Uenohara, F. Koyama, *Electron. Lett.* **22**, 1008 (1986)

[3] M.R. Brown, K.S. Teng, A. Kestle, P. Smowton, P. Blood, P.A. Mawby, S.P. Wilks, *Appl. Surf. Sci.*, **234**, 434 (2004)

---

[4] D.P. Bour, in: P.S. Zory Jr. (Ed.), *Quantum Well Lasers*, (Academic Press, New York, Chapter 9, 1993)

[5] S.P. Wilks, A. Kestle, *Appl. Surf. Sci.* **117/118**, 334 (1997)

[6] T. Takagi, F. Koyama, K. Iga, *Jpn. J. Appl. Phys.* **31**, 197 (1992)

[7] T. Takagi, F. Koyama, *IEEE J. Quant. Electron.* **27** (6), 1511 (1991)

[8] R. Bachelot, P. Gleyzes, A.C. Boccara, *Ultramicroscopy*, **61** (1-4), 111 (1995)

[9] U. Durig, D.W. Pohl, F. Rohner, *J. Appl. Phys.* **59**, 3318 (1986)

[10] M. Isaacson, J.A. Cline, H. Barshatzky, *J. Vac. Sci. Technol. B* **9** (6), 3103 (1991)

[11] M. Fukuda, *Reliability and Degredation of Semiconductor Lasers and LEDs*, (Artech House, Boston,1991)

[12] N.H. Lu, D.P. Tsai, C.S. Chang, T.T. Tsong, *Appl. Phys. Lett.* **74** (19), 2746 (1999)

[13] M.S. Unlu, B.B. Goldberg, W.D. Herzog, D. Sun, E. Towe, *Appl. Phys. Lett.* **67** (13), 1862 (1995)

[14] S.K. Buratto, J.W.P. Hsu, E. Betzig, J.K. Trautman, R.B. Bylsma, C.C. Bahr, M.J. Cardillo, *Appl. Phys. Lett.* **65** (21), 2654 (1994)

[15] K. Karrai, R.D. Grober, *Appl. Phys. Lett.* **66** (14), 1842 (1995)

[16] X.H. Zhang, S.J. Chua, W.J. Fan, *Appl. Phys. Lett.* **73** (8), 1098 (1998)

[17] M.P.C.M. Krijn, *Semicond. Sci. Technol.* **6**, 27 (1991)

[18] S.A. Wood, C.H. Molloy, P.M. Smowton, P. Blood, D.J. Somerford, C.C. Button, *Appl. Phys. Lett.* **75** (12), 1748 (1999)

[19] S.A. Wood, P.M. Smowton, C.H. Molloy, P. Blood, D.J. Somerford, C.C. Button, *Appl. Phys. Lett.* **74** (17), 2540 (1999)

[20] M.J. Cooke, *Semiconductor devices*, (Pentrice Hall International, 1990)

Chapter 9

Results: Buried heterostructure multi-quantum well laser

9.1 Introduction

As discussed in chapter 4 buried heterostructure (BH) laser diodes have excellent operational characteristics displaying low threshold current densities and stable modal operation. The fundamental weakness of BH lasers is in the fabrication of the curved mesa structure and subsequently deposited curved *pnpn* thyristor structure. The harshest or crudest step in the manufacture process is definitely the etching of the mesa structure, which results in a curved stepped surface (see Figure 9.1). Semiconductor growth on such a surface can lead to an interface with a large density of defects, or non-uniform distribution of dopants. Therefore it is the curved structures, *pn*-junctions that are focussed on in an effort to optimise device efficiency further. The ideal BH-MQW laser will have all of the injected carriers recombining in the MQW resulting in stimulated emission. However in reality there is a strong possibility of leakage currents bypassing the MQW and recombining in non-radiative recombination processes and electroluminescence outside of the MQW. The three possible leakage paths are:

(1) directly across the *pnpn* blocking structure,
(2) around the *n*-InP blocking layer via the *p*-InP cladding layer, *p*-InP blocking layer and *n*-InP cladding layer,
(3) directly through the active region, dopant diffusion into the active region can provide a path directly past the MQW.

The possibilities of these occurring are investigated and discussed with respect to the collection NSOM and photocurrent data.

9.2 Sample structure

The multi-quantum well active region consists of 9 InGaAsP quantum wells and 10 InGaAsP barrier layers, all of which are undoped. The wells have a width of 6nm and the barriers a width of 10nm. Adjacent to the multi-quantum well structure, above and below, are separate confinement layers, as shown in Figure 9.1, these are also undoped InGaAsP and are approximately 500nm thick perpendicular to the QW's. The *n*-type InP materials are doped with Si in the concentration range

$4\times10^{18}>N_D>2\times10^{18}$ cm^{-3}. While the *p*-doped InP materials are Zn doped and have weaker dopant concentrations in the range $2\times10^{18}>N_A>4\times10^{17}$ cm^{-3}. The device is grown upon an *n*-InP substrate and there are contact layers on the top and bottom. Due to the commercial sensitivity regarding the precise fabrication of these lasers only general specifications can be given.

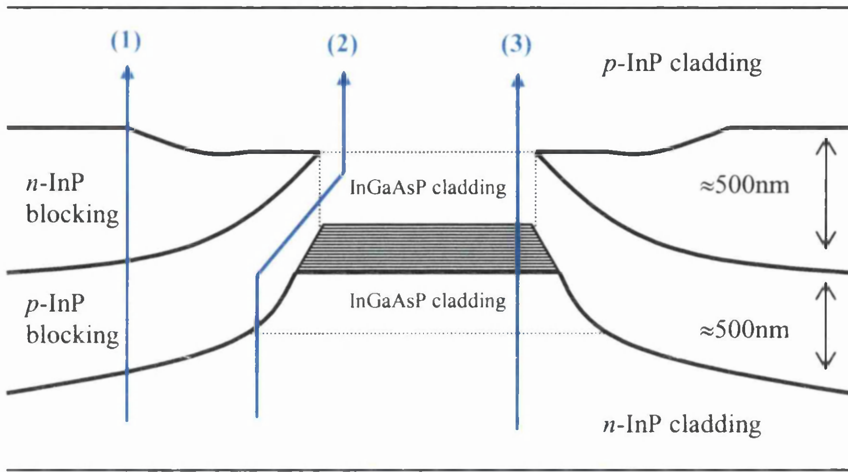

Figure 9.1 Cross-sectional schematic of the buried heterostructure multi-quantum well laser studied. Note the diagram only shows the MQW active region and surrounding *pn*-junctions that are important in addressing the following results, the three possible leakage pathways are also labelled.

9.3 Sample preparation

The sample was always freshly cleaved (in air) prior to scanning, thus allowing the minimum possible time for the growth of surface oxides. Oxide layers can be detrimental to the ultimate resolution of NSOM experiments, especially photocurrent imaging of samples displaying a low optical response, or samples with a very small active region, as discussed in chapter 8. This is because the typical penetration length of near-field light into a sample is of the order of the probe aperture diameter, which in this case is 50nm. The intensity of the evanescent modes of the near-field aperture decays exponentially away perpendicular from the aperture[1], thus the growth of an oxide between the aperture and sample will reduce the intensity at the sample surface exponentially, plus additional losses due to scattering. Therefore it is favourable when using a small aperture diameter (50nm) to avoid heavy growth of surface oxides.

Note, a probe of 50nm aperture diameter was utilised in the acquisition of all the images (collection NSOM and photocurrent) presented within this chapter for the BH-MQW laser as these devices proved more photo-active than the MQB lasers of the previous chapter.

9.4 BH-MQW laser surface topography

As discussed in section 2.6 the topographic data is acquired using the shear-force imaging mechanism of the NSOM, with resolution of approximately 0.5nm in the *z*-direction perpendicular to the sample surface and a few nanometres in the *x*-and *y*-directions. All of the topographic images displayed were recorded pixel by pixel simultaneously with photocurrent or collection NSOM images, the best resolution being observed when simultaneously performing photocurrent imaging i.e. when the device was at room temperature and not subjected to heating as when in operation.

The topographic image displayed in Figure 9.2 shows a cross section of a device, as in the schematic Figure 9.1, with extremely high resolution, the image was recorded at 500×500 pixels at a moderate rate and feedback conditions. The active region is clearly resolved, which appears never to have previously been reported using a force imaging technique. The active region forms a depressed trapezoidal shape on the cleaved surface and has the dimensions 1500nm×1100nm×240nm. The depressed trapezoid is uniform in shape and has an approximate depth of 0.5nm (see inset image of Figure 9.2); this is very close to the resolvable limit of shear-force imaging. The whole image is also very flat, with a maximum height contrast of 1.73nm. Curved contours on the sample surface are visible, suggesting the shape of the mesa structure, however this is not itself clearly resolved. Although the sample was cleaved as close as possible prior to imaging, there are definitely surface oxides present. However, unlike the topographic imaging of the planar quantum well lasers of the previous chapter, the surface oxides do not appear to be responsible for the physical contrast seen here, due to the magnitude of the surface depression (~0.5nm). A more appropriate mechanism would be the relaxation of strain, accumulated in the MQW super-lattice during growth, upon cleaving. The action of cleaving allows the new surface layers more freedom to relax under strain. This may result in the approximately 0.5nm deep surface depression in the topography of the active region as seen in the shear-force image, which is consistent with strain induced perturbations

in surface morphology of a few angstroms as measured using cross-sectional STM by Chen *et al*[2]. The shear-force mechanism of the NSOM microscope is working near the limit of its resolution capabilities here, therefore in order to seek the resolution of more features the only possibility is a mechanical zoom i.e. a smaller scan range.

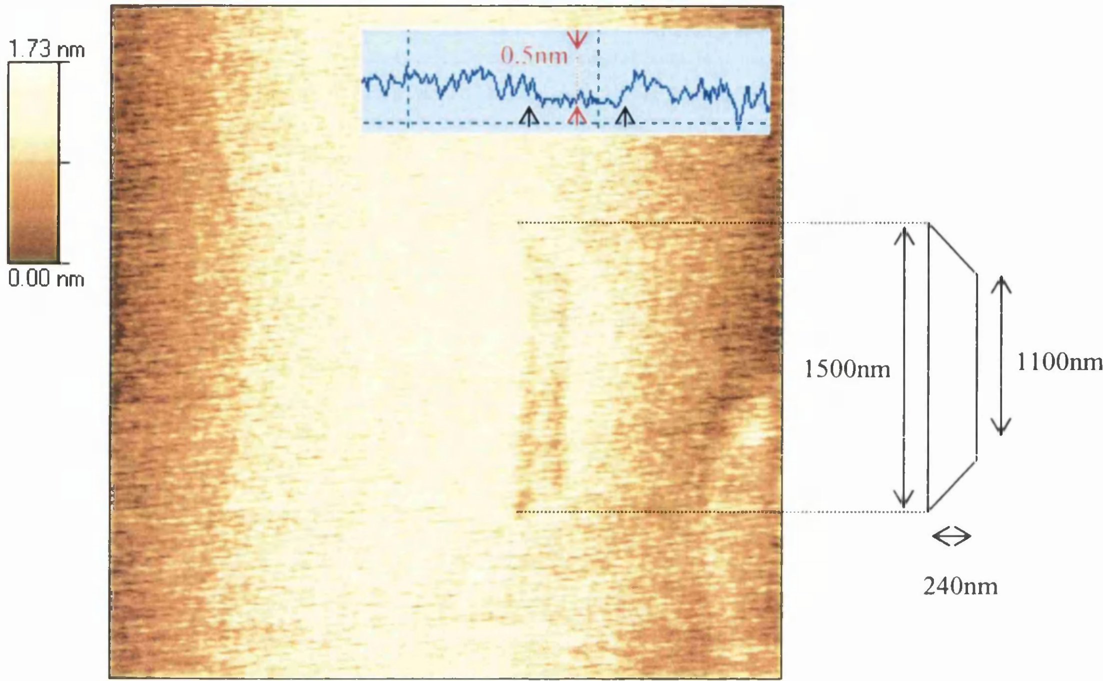

Figure 9.2 $(3500\text{nm})^2$ topographic image of a recently cleaved BH-MQW laser cross section. The image clearly resolves the active region as a uniformly defined trapezoid and the dimensions are labelled in the illustration. The inset image shows a cross-sectional line profile of the MQW active region.

The topographic image of Figure 9.3 shows the active region and one side of the mesa structure in a $(2570\text{nm})^2$ scan range. The image is very flat displaying a maximum contrast of 1.32nm, and the active region is clearly resolved. The smaller scan range of this image has allowed the shear-force sensor to become sensitive to the tiny variation in surface topography due to the curved blocking layers. The shape of the etched curvature of the mesa structure is now visible, although very faint, and is highlighted by the dashed white line labelled **A**. The curved edge of the mesa is seen to originate at the top corner of the of the active region labelled **B**, which is consistent with the fabrication process, where the active region was masked and the mesa etched on either side. The next step of fabrication process was the re-growth of the blocking layers (thyristor structure) on top of the curved surface, and this is also reflected in the surface topography in Figure 9.3. A very faint curved region is just visible and is

outlined in the image by the dashed lines; the region is slightly depressed along its edges with greatest curvature, but is most prominent by the curved surface morphology of its interior. Again this does not appear to be due to oxide growth, but a result of strain on the crystal lattice. The very small depression is only evident at the boundary locations between the different semiconductor crystals showing greatest curvature, and not on the interior of the region, this may be due to the surface relaxation at these locations of greatest strain. The curved pattern visible on the surface of the interior of the region, especially near the MQW is again likely to be a consequence of strain of the crystal lattice which is grown on the heavily curved mesa. This has not resulted in an overall depression of the region, but has led to a rougher surface in this area after cleaving that is suggestive of a heavily strained crystal lattice[2].

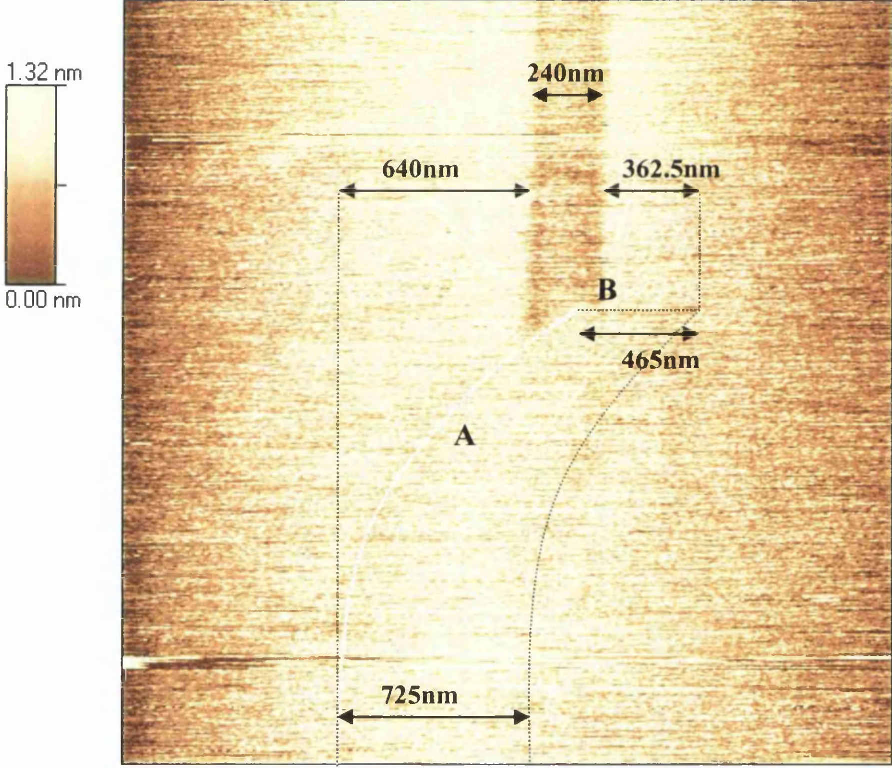

Figure 9.3 $(2570\text{nm})^2$ topographic image of the BH-MQW active region and mesa structure. The curved mesa structure is visible in this image, highlighted by dashed white line **A**. The entire curved region is outlined by the dashed lines and dimensions and position relative to the active region are labelled.

When compared to the surface topographies due to oxide growth seen on the planar quantum well lasers, it is evident that a different mechanism is responsible for the

surface morphologies observed for the BH-MQW laser. The argument given above for strain induced surface relaxation is also supported by the oxide growth pattern that is observed at the same location after a greater time has elapsed since cleaving, as seen in Figure 9.4. The oxide growth seen is heavy as indicated by the maximum height contrast of 22.99nm, compared to 1.32nm in the previous image. The location of the active region is denoted by the red trapezoid, and is not reflected by the surface oxide growth at all, none of the features previously discussed are apparent in the form of the oxide growth pattern. If the previously observed features were a result of the early stages of oxide growth then they would still be apparent after further oxide growth, thus supporting the surface relaxation mechanism.

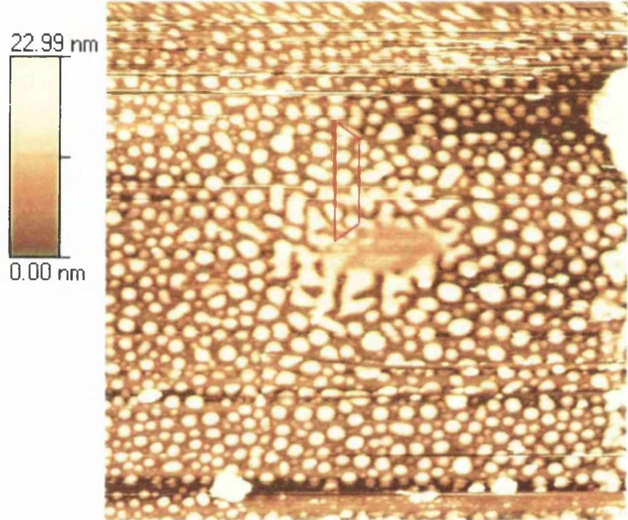

Figure 9.4 Topographic image $(5000\text{nm})^2$ of the active region and mesa structure. The location of the active region is represented by red trapezoid, and is obscured by the heavily built up oxide.

9.5 BH-MQW laser: Photocurrent imaging

Photocurrent imaging utilises the NSOM probe to optically excite charge carriers in the device within a nanometer scale excitation volume directly beneath the probe aperture. If the carriers are sufficiently separated, by an electric field, then they in turn induce an internal electric field that results in the flow of a current, which is measured and mapped via the external amplifiers. Thus the contrast mechanism of near-field photocurrent imaging is a direct measure of the local electric field within the device. Hence the larger the intensity of the photocurrent signal the stronger the

local electric field at the point of carrier excitation. However, the intensity of the photocurrent signal is also dependant upon the separated charge carriers conducting to the external circuit, therefore the actual measured intensity is a convolution of the local built-in electric field strength and efficiency of the carrier conduction path. Note that when performed at 0 Volts applied bias a photocurrent is only induced at locations where there exists a built-in field, i.e. at *pn*-junctions. Within the bulk regions of the device there exists charge neutrality and thus no field to separate excited electron–hole pairs which quickly recombine, therefore not generating a photocurrent signal at such locations. The photocurrent imaging technique is therefore extremely powerful in directly visualizing and mapping *pn*-junctions and assessing the efficiency of the conduction path to the external electrical contacts of the device.

The photocurrent images displayed in this chapter were acquired within a twelve hour period immediately after device cleaving, thus minimizing the negative effects of surface oxide growth on the photocurrent intensity and resolution. All images were recorded after optimizing the shear-force and lock-in amplifier parameters, which were kept consistent throughout. Imaging was performed with the sample in equilibrium, i.e. 0 volts applied bias. An NSOM probe of 50nm diameter aperture (stated manufactured diameter) was used; fortunately a single probe was used in the acquisition of all images, reinforcing the consistency of the experimental technique. Again photocurrent images were recorded for two excitation sources, 1.96eV and 2.55eV, the results of which are discussed in depth. For full details of the experimental configuration, procedure and parameters refer to chapter 6.

9.5.1 BH-MQW laser photocurrent characteristics and excitation energy

The photocurrent signal is the result of electron–hole separation and subsequent minority carrier transport across a *pn*-junction, thus the photocurrent can be used to effectively image *pn*-interface distribution and properties. The buried heterostructure multi-quantum well laser consists of three *pn*-junctions arranged in a *pnpn* thyristor structure, designed to channel injected charge carriers into the enclosed MQW active region to combine via stimulated emission. Therefore the technique of near-field photocurrent imaging is highly applicable to BH-MQW lasers, as is demonstrated in

Figure 9.5. The curved mesa structure and current blocking layers are clearly visible in both images either side of the central bright MQW active region.

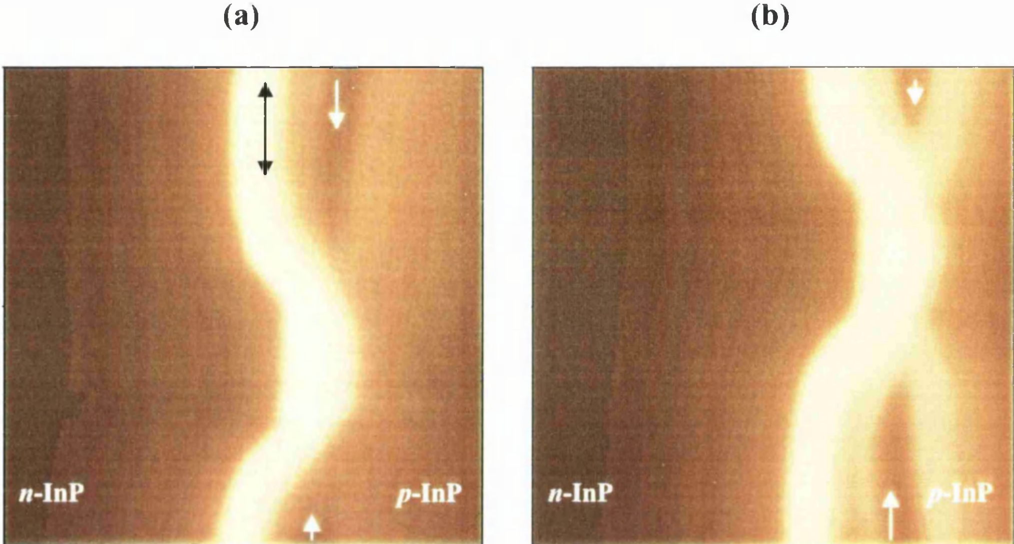

Figure 9.5 $(5000\text{nm})^2$ photocurrent images using **(a)** 488nm (2.55eV), and **(b)** 633nm (1.96eV) excitation sources, all other measurement parameters remained constant. The photocurrent imaging technique clearly identifies the MQW active region and adjacent curvature of the mesa structure. The black arrow parallel to the *pn*-junction interface is used for explanation within the text, whereas the white arrows denote the location of the *n*-InP blocking layers.

The interface of the curved mesa structure is very clear, sharply defined at the top of the *n*-InP substrate, sandwiching the MQW region. The MQW active region is not clearly distinguishable, in the direction parallel to the black arrow in Figure 9.5(a), from the bright photocurrent band excited at the *n*-InP substrate and *p*-InP blocking layer interface (refer to Figure 9.1), as it adjoins the two curved sides of the mesa structure. However, the MQW active region is resolvable via the photocurrent intensity as will be discussed in detail later. The photocurrent levels rapidly decay into the bulk region of the *n*-InP substrate in the absence of an electric field to facilitate carrier separation, as the bulk substrate contains no built-in field and the experiment is performed at 0 volts applied bias.

Dark regions are clearly resolved either side of the active region, labelled with white arrows in Figure 9.5(a) and (b), these can be attributed to the *n*-InP blocking layers exhibiting good carrier confinement, as previously reported by Buratto *et al*[3]. The *n*-InP blocking layer displays low photocurrent intensity as it is contained within two oppositely directed *pn*-junctions (refer to Figure 9.1). The resolution of the structure

appears in these images to be higher on the left, i.e. the *n*-InP cladding side, than on the right, *p*-InP cladding layer, for both the current blocking structure and active region. This is due to the nature of the near-field photocurrent imaging technique and will be fully discussed later.

The images of Figure 9.5 were acquired using identical measurement parameters, the only difference being the excitation sources used, (a) 488nm (2.55eV), and (b) 633nm (1.96eV), which are sufficiently energetic to excite electrons across the band-gap of the various InP layers that is 1.35eV (at 300K). Both images show excellent resolution capabilities on the BH-MQW laser and very similar features. The photocurrents attained at both wavelengths are extremely uniform parallel along the *pn*-junction interfaces within the structure (i.e. parallel to the black arrow in Figure 9.5(a)), indicating uniform doping along the interfaces. This characteristic infers uniform crystal growth upon the re-growing of the thyristor structure on the curved mesa after etching. This is contrary to observations made by Buratto *et al*[3] who reported highly undefined *pn*-junctions formed upon re-growth of the blocking layers, causing weak irregular photocurrent signals.

The photocurrent response of the MQW active region in the direction parallel to the growth direction (i.e. parallel to the black arrow in Figure 9.5(a)) is highly uniform for both excitation energies displayed in Figure 9.5. This again is highly contrasting to measurements made by Buratto *et al*[3], who report an asymmetrical photocurrent response of the MQW active layer in the direction parallel to the active layer. Buratto *et al*[3] attributed this to dopant diffusion into the active region, opening up recombination centres and leakage paths directly through the MQW.

The intensity of the bright *n*-InP substrate / *p*-InP blocking junction is almost exactly 85% of the uniform intensity of the MQW active region, for both excitation sources. However, there are subtle differences that are not extremely apparent from the images of Figure 9.5, but are revealed in the three-dimensional plots of Figure 9.6 for 488nm (2.55eV) excitation, and Figure 9.7 for 633nm (1.96eV) excitation, and shall be discussed further.

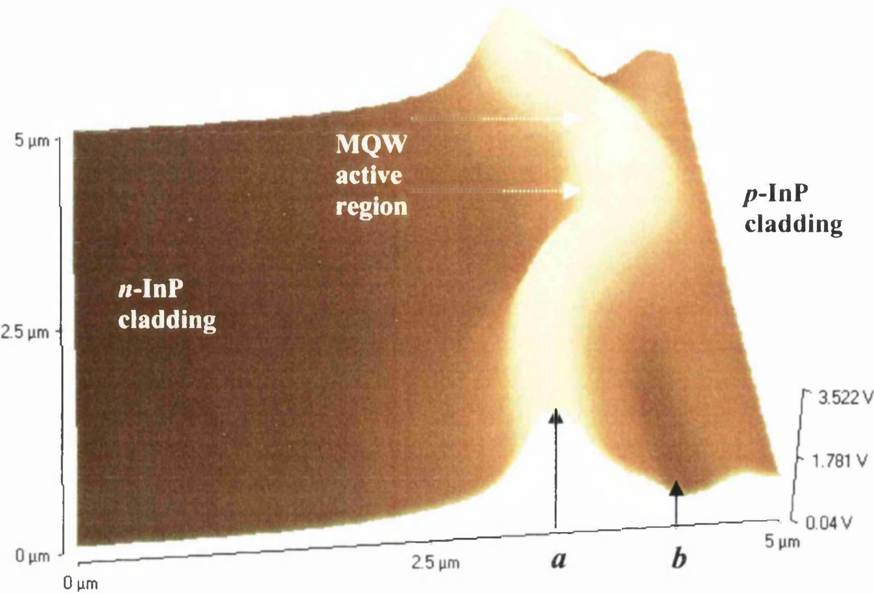

Figure 9.6 $(5000\text{nm})^2$ 3D-photocurrent image using an excitation source of 488nm (2.55eV). The image clearly shows the curved mesa shape of the *n*-InP cladding / *p*-InP blocking *pn*-junction, and MQW active region, as the single bright ridge labelled *a*. The *n*-InP blocking layer is also visible, labelled *b*, and appears as a dark trough.

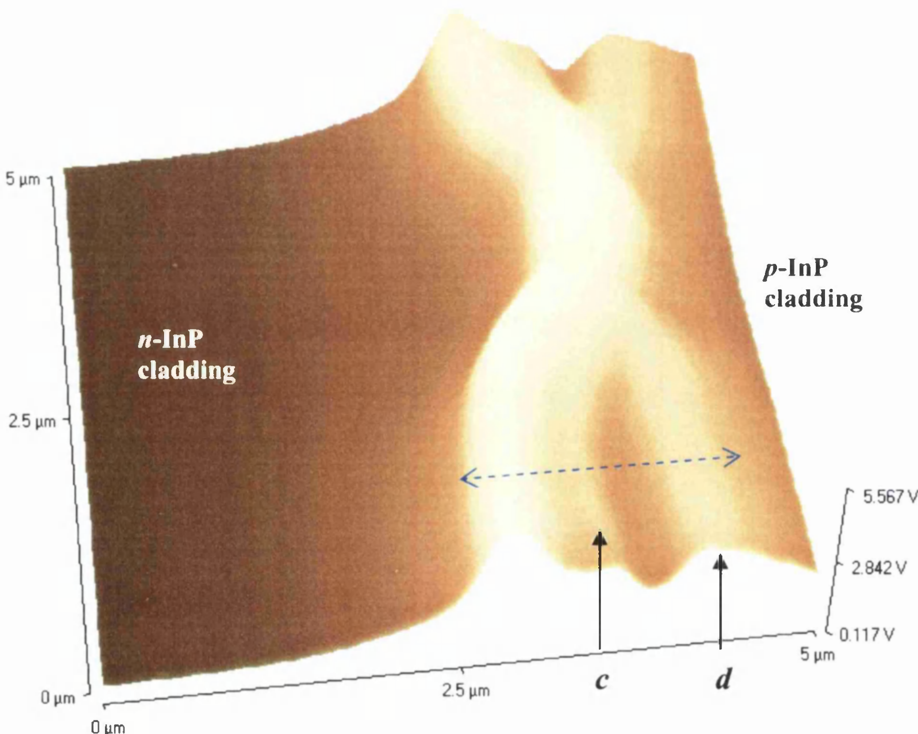

Figure 9.7 $(5000\text{nm})^2$ 3D-photocurrent image using an excitation source of 633nm (1.96eV). Photocurrent imaging at the lower excitation energy displays a greater sensitivity to the band structure of the device. The prominent features of Figure 9.6 remain equally as intense; however the *pn*-junctions of the *n*-InP blocking layer are considerably more pronounced, as highlighted by *c* and *d*.

The strongest photocurrent response is similarly seen for both wavelengths to be occurring within the MQW active region (as labelled in Figure 9.6). However, the photocurrent characteristics of the remaining *pn*-junctions of the buried heterostructure vary according to the excitation energy used. Figure 9.6 was acquired at the higher excitation energy of 2.55eV (488nm), and shows a very strong photocurrent response at the *pn*-junction of the *n*-InP cladding layer and *p*-InP blocking layer, labelled ***a*** in Figure 9.6. The location of the *n*-InP blocking layer is also prominent, revealed as a 'trough' of low photocurrent response adjacent to the MQW, labelled ***b*** in Figure 9.6.

These features are also apparent when imaging at the lower excitation energy of 1.96eV (633nm), as in Figure 9.7. However, at this excitation low intensity photocurrent peaks are also clearly apparent, and are attributed to the *pn*-junctions enclosing the *n*-InP blocking layer, i.e. the *p*-InP blocking / *n*-InP blocking junction (labelled ***c*** in Figure 9.7), and the *n*-InP blocking / *p*-InP cladding junction (labelled ***d*** in Figure 9.7).

Upon close inspection of Figure 9.6 acquired at the high excitation energy 2.55eV (488nm), it is apparent that the low intensity photocurrent peaks (labelled ***c*** and ***d*** in Figure 9.7) are also present, however not as prominently. Note the photocurrent features discussed are present for both excitation sources, albeit at differing intensities, however, importantly the locations (i.e. physical separation) of these features are constant and independent of the excitation source. Also the separation of the photocurrent peaks corresponds with the geometry of the buried heterostructure MQW device, therefore the photocurrent peaks may be attributed to the physical locations of the various *pn*-junctions of the device. This is further illustrated by the cross-sections of Figure 9.8 which are taken directly through the *pnpn* thyristor blocking structure, as illustrated by the blue arrow in Figure 9.7 (and *cross-section 2* in Figure 9.9). Cross-sections are represented for both excitation energies and are normalised for the maximum amplitude of the *n*-InP cladding / *p*-InP blocking junction labelled ***a***, and overlaid for correlation. The locations of the photocurrent peaks ***a***, ***c***, and ***d***, and the low photocurrent trough ***b***, are similarly labelled as in the previous 3-dimensional Figure 9.6 and Figure 9.7. It is apparent that the spacing of these features is identical for both excitations, and their positions relative to the

largest n-InP cladding / p-InP blocking junction peak are denoted within the Figure 9.8.

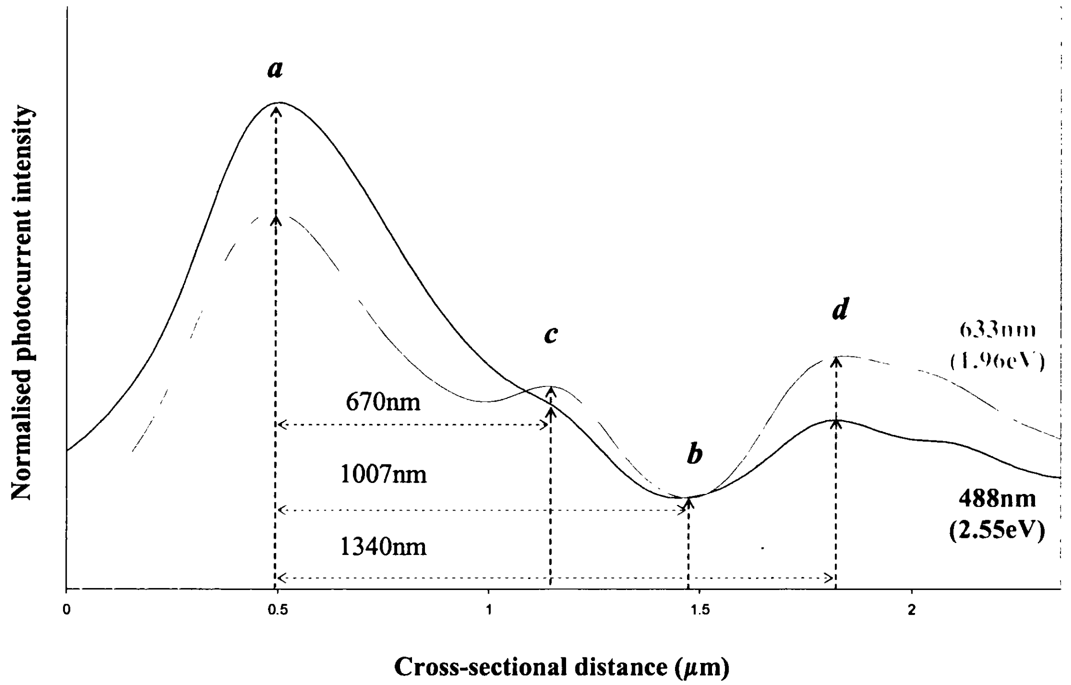

Figure 9.8 Normalised photocurrent cross-sections perpendicular through the *pnpn* current blocking thyristor structure. The cross-sections are normalised and aligned for comparison. The left hand side starts in the n-InP cladding layer bisects the blocking structure and ends on the right in the p-InP cladding layer.

The cross-sections highlight the differing photocurrent response of the device to the two excitation sources and highlight the lateral correlation of features, indicating that it is differences within the photocurrent intensity response of the features to the different excitations that is resulting in an apparent enhancement in resolution at the lower 1.96eV (633nm) excitation.

In order to interpret the differences in photocurrent according to the excitation energy, consider the origins of the generated photocurrent. The NSOM probe locally excites electron-hole pairs within the illumination volume of its aperture (approximately the diameter[3]) providing the wavelength is sufficiently short, i.e. the excitation energy is greater than the band-gap energy. When this occurs within the presence of an electric field i.e. at a *pn*-junction, the photo-excited minority carrier is swept across the *pn*-interface by the built-in field, and a photocurrent propagates. The spatial resolution of near-field photocurrent imaging is thus a function of the NSOM aperture diameter, the absorption length, and the minority carrier diffusion length, as discussed fully in

chapter 5[3,4,5,6,7]. The minority carrier diffusion length is a function of the carrier mobility, which is independent of the excitation energy, and the minority carrier lifetime. The minority carrier lifetime describes the time interval between the original carrier excitation and its final recombination across the band-gap with an opposite carrier, i.e. the transition for electrons from the conduction band edge, across the band-gap to recombine with a valence band vacancy. However, in order for an electron to undergo recombination it must have energy equivalent to the conduction band edge. In this case, electron-hole pairs are photo-excited in the photocurrent imaging process using energies greater than the band-gap energy, and therefore photo-stimulated electrons are elevated in energy above the conduction band edge by an amount corresponding to the energetic difference between the excitation energy and band-gap. Therefore for different excitation sources, the photo-excited electrons will posses different energies within the conduction band. Prior to recombination, the excited electrons undergo intraband relaxation[21] to the conduction band edge by electron-electron scattering, electron-phonon scattering, and electron-impurity scattering, for a duration called the relaxation time of the order 10^{-12}sec [8,21]. Thus electrons photo-excited at different energies will undergo a different amount of intraband relaxation to reach the conduction band edge, and thus experience different relaxation times, i.e. the higher the excitation energy, the longer the relaxation time, and thus the greater the minority carrier lifetime.

A minority carrier with a greater lifetime will be influenced by the built-in field of a *pn*-junction for a longer duration, and thus the photocurrent stimulated by a higher energy source will be increased in intensity for a given *pn*-junction. Also an increased minority carrier lifetime implies an increased minority carrier diffusion length, and thus a *pn*-junction will appear broader to a higher excitation source. This is apparent for the cross-sections displayed in Figure 9.8, where the photocurrent response at 2.55eV (488nm) excitation appears increased in intensity and broader at the *pn*-junctions. The increased photocurrent response at 2.55eV (488nm) of the closely spaced peaks at ***a*** and ***c*** reduces their resolution, compared to 1.96eV (633nm), and although still present the peak at ***c*** is not as apparent.

The band-gap of the InP layers is 1.35eV, which is inferior to both the excitation sources utilised for this study. However it is apparent that the photocurrent imaging

contrast is optimised when the probing excitation energy is closer to (but greater than) the band-gap energies of the structure under analysis. This is similar to the photocurrent imaging of Schottky diodes, in which the contrast is optimised when the excitation energy is close to (but greater than) the Schottky barrier energy[9]. Therefore further discussions presented hereafter will be based on images generated using the 1.96eV (633nm) excitation source.

9.5.2 Correlation of photocurrent and topography

Buried heterostructure multi-quantum well laser diodes are inherently extremely flat in the cleaved plane used for cross-sectional imaging. Near-field photocurrent imaging has previously been performed on a number of structures including laser heterostructures[4,6,10,11,12], and particularly work by Buratto *et al*[3,5] on buried heterostructure multi-quantum well laser devices who saw no topographical features related to the device structure. This is in contrast to the topographical data already presented and discussed within this chapter that display the finely defined profile of the MQW active region, and even the faint profile of the curved mesa and one or both of the re-grown InP current blocking layers (see Figure 9.3). These images (Figure 9.2 and Figure 9.3) were acquired simultaneously with photocurrent images generated using the favourable 633nm (1.96eV) excitation source. Correlation between the device physical structure and electronic photocurrent response is thus feasible and is discussed in this section.

The correlation of photocurrent with topographical device geometry, made possible by their simultaneous acquisition, is extremely useful in the interpretation of the photocurrent data with respect to the electronic properties of the device. The photocurrent image of Figure 9.9 is overlaid with the black dotted outline of the corresponding topographic features, as recorded in Figure 9.3. When displayed in this format it is clear that the curved region seen in the topography is due to the *p*-InP blocking layer. The two curved edges of this region coincide with intensity maxima in the photocurrent signal, indicating the presence of *pn*-junctions at its boundaries, whereas there are none within the region, indicating that the curved structure seen in the topographic image is solely due to the *p*-InP blocking layer, not both *p* and *n* – type blocking layers. If the curved topography did contain both *p* and *n* –type

blocking layers the photocurrent would peak at both edges and at some point within the boundary due to the additional *pn*-junction.

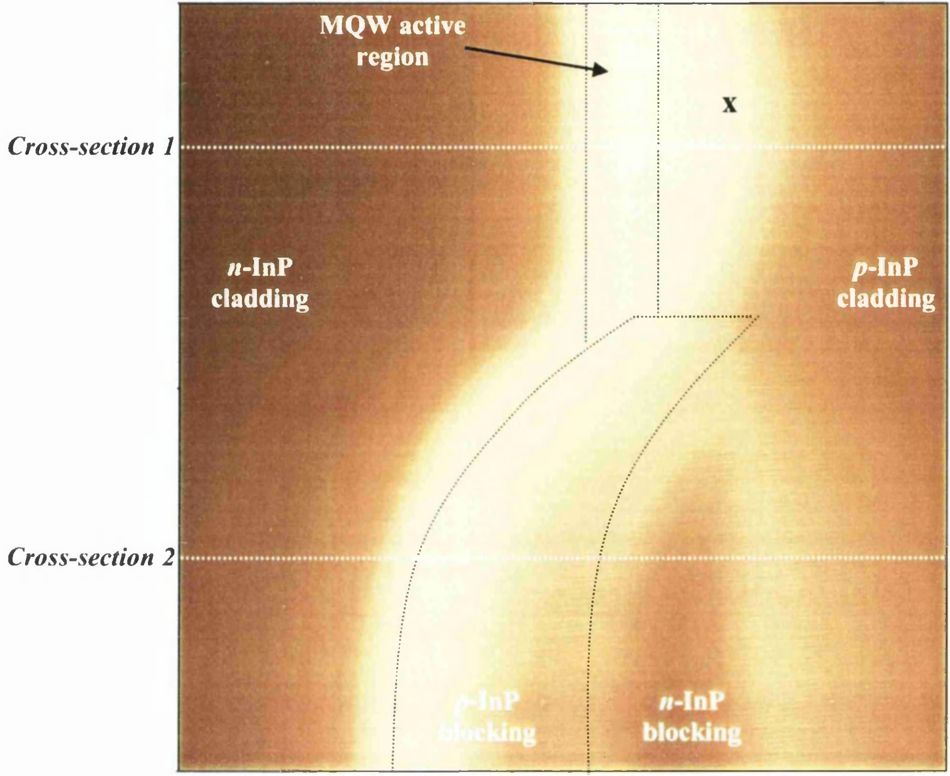

Figure 9.9 (2570nm)^2 Photocurrent image using the 1.96eV (633nm) excitation. The black lines outline the simultaneously recorded topographical features of Figure 9.3, coordinating the photocurrent with the physical geometry.

The location of the *p*-InP blocking layer confirms that the dark trough in the photocurrent signal is due to the *n*-InP blocking layer. The photocurrent level is low in this material as the *n*-InP blocking layer is contained within oppositely directed *pn*-junctions, resulting in increased confinement of charge carriers. This will be discussed further when addressing the band profile across the *pnpn* blocking structure.

The correlated image of Figure 9.9 also marks the location of the MQW active region, located very close to the left hand edge, i.e. the *n*-InP cladding layer side, of the central bright photocurrent region. This is clearly emphasised in the 3-dimensional representation of the arithmetic superposition of simultaneous topographic and photocurrent data shown in Figure 9.10. There is a large photocurrent signal seen towards the *p*-InP cladding edge of the active region which persists away from the active region, labelled **x** in Figure 9.9 and Figure 9.10, and this is addressed within the

next section. This is contrasting to the photocurrent signal on the *n*-InP side of the active region which decays sharply away from the active region within a much smaller distance. The location of the active region in respect to the large photocurrent signals of the neighbouring *pn*-junctions is also very clear from this image, and shows excellent agreement with the designed structure of the device as shown in Figure 9.1. Note the separation, labelled with a blue arrow in Figure 9.10, between the highly confined *n*-InP blocking layer (seen as a dark trough) and the MQW. The physical separation of these layers within the structure is essential in preventing dopant diffusion from the blocking layer into the MQW that can result in the formation of non-radiative recombination centres or leakage paths directly through the active region, as seen by Buratto *et al*[3].

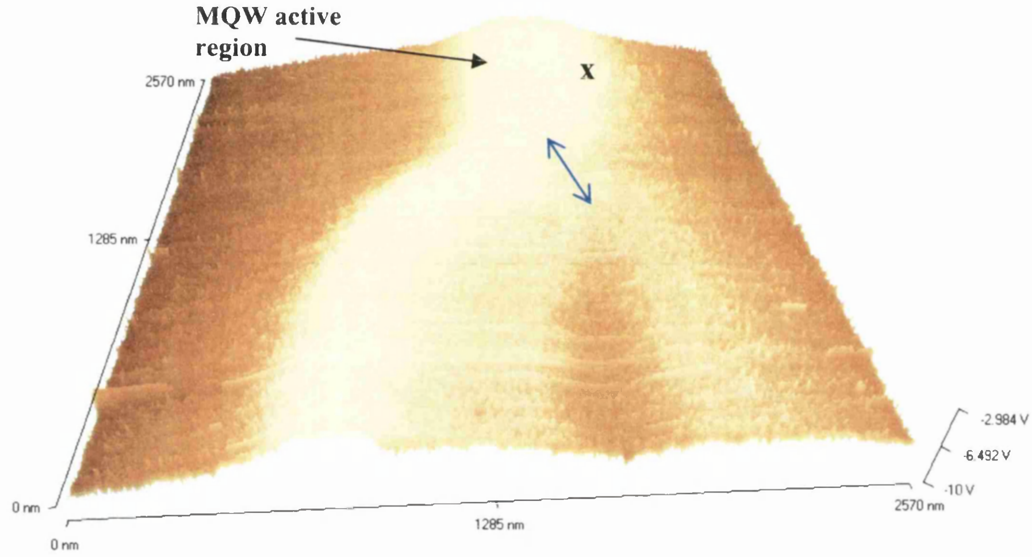

Figure 9.10 3-D Arithmetic superposition of a $(2570\text{nm})^2$ topographic image and simultaneous photocurrent image at 1.96eV (633nm) excitation. The exact location of the MQW active region is displayed in respect to the photocurrent response of the device. The MQW is positioned toward the left edge of the bright central photocurrent peak.

9.5.3 Multi-quantum well active region

The maximum photocurrent intensity was measured when the near-field probe was over the MQW active region, where the band-gap energy of the quantum wells is $E_g^{QW} = 0.84\text{eV}$; and the barriers $E_g^{Barrier} = 1.04\text{eV}$. This is substantially lower than 1.35eV for the InP blocking layers and substrate, and thus may explain the superior photocurrent stimulation detected for the active region. The second largest photocurrent response was the *n*-InP cladding / *p*-InP blocking junction which was

85% of the intensity of the active layer. This observation is contrasting with measurements made by Buratto *et al*[3], who recorded slightly lower photocurrent intensity in the active region than seen in neighbouring *pn*-junctions. This was attributed to the loss of excess momentum by excited carriers which subsequently become trapped within the MQW, thus inhibiting the photocurrent formation, although it must be noted that a sizable photocurrent was still observed.

The MQW active layer is undoped and designed to be 134nm total thickness. It is grown between two 500nm thick undoped InGaAsP cladding layers (Figure 9.1), which are designed to prevent dopant diffusion from the adjacent blocking structures into the MQW. Therefore, the theoretical total width of the intrinsic layer of the *p-i-n* device is 1134nm. This correlates well with the full width at half maximum of the photocurrent intensity distribution perpendicular across the active region, as shown in Figure 9.11, where the FWHM is approximately 1000nm. However, although the band-gap is smaller within this region, aiding the photo-separation of charge carriers, theoretically there should be a weak field acting to facilitate the separation of these excited electron-hole pairs and induce the transportation of a photocurrent. This suggests that dopant diffusion to within the active region, i.e. the 500nm InGaAsP cladding layers, has occurred establishing an increased built-in field, however this does not imply diffusion into the MQW super-lattice as the photocurrent response parallel to the active layer is highly uniform.

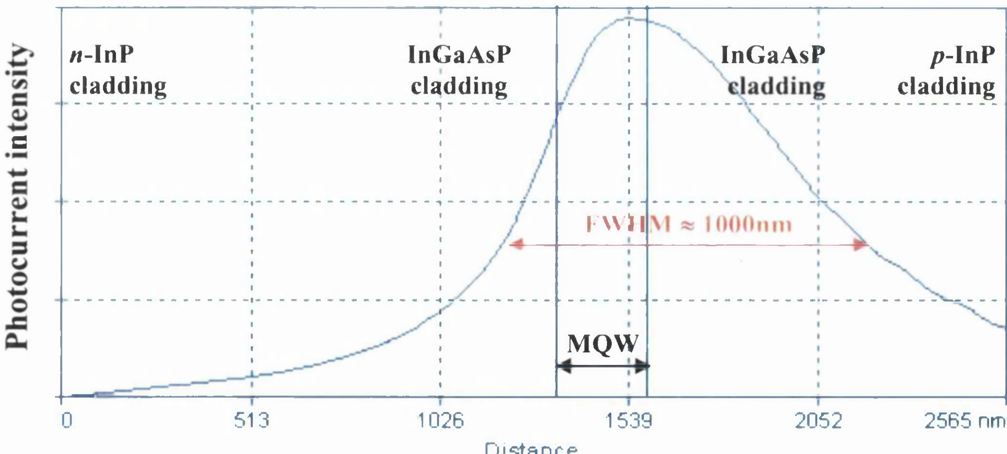

Figure 9.11 Cross-sectional profile of the photocurrent response in a perpendicular direction through the centre of the MQW active region, *cross-section 1* in Figure 9.9. The location of the MQW as correlated with topographic data is labelled and highlights the asymmetry of the photocurrent signal about the active region.

The cross-sectional photocurrent distribution shown in Figure 9.11 corresponds to the location marked *Cross-section 1* in Figure 9.9, which perpendicularly bisects the active region. The maximum photocurrent intensity occurs within the MQW however the response of the MQW is asymmetric in this direction (i.e. perpendicular to growth), with the maximum level occurring at the *p*-type boundary. The photocurrent response at this location is characteristic of a *pn*-junction existing there, where the *p*-sided InGaAsP cladding layer forms the *p*-type material and the MQW acts as the *n*-type material. *n*-type-like behaviour of a MQW in a buried heterostructure has previously been reported using scanning capacitance microscopy, SCM[13]. This response is reflected throughout the whole of the central intrinsic region of the device, InGaAsP/MQW/InGaAsP, seen as the high degree of asymmetry in the aforementioned cross-section. The photocurrent intensity decays rapidly away from the MQW towards the *n*-InP material on the left, whereas the photocurrent intensity towards the *p*-InP material on the right remains high over a much greater distance. This indicates that excited carriers are being separated by a field and leaking past the MQW without becoming trapped within the wells and undergoing recombination.

The "smearing" of the photocurrent on the *p*-type side of junctions is not isolated to the active region, although emphasised here due to the broad intrinsic region, and is a characteristic seen at all the *pn*-junctions of the buried-heterostructure. The depletion region of the *pn*-junctions of the device is typically four or more times wider within the *p*-type material than in the *n*-type, this is a direct consequence of the diffusion lengths of the minority carriers. When an electron-hole pair is photo-excited within the *p*-type depletion region the electron is the minority carrier and is transported across the *pn*-junction by the built-in field thus inducing a photocurrent to flow, the opposite case occurs for the *n*-type depletion region. However, electrons have a much greater mobility than holes (μ_e = 4600 cm^2/V s and μ_h = 150 cm^2/V s at 300K)[14] resulting in a much greater electron diffusion length and hence a photocurrent can act further into the *p*-type material. Therefore the photocurrent always appears "smeared" into the *p*-type material. Similar observations have been reported by several groups who all found the minority carrier diffusion length to dominate the resolution of photocurrent imaging[3,4,6,7].

The photocurrent intensity in the MQW was at a maximum and uniform, parallel to the MQW, over the active region. Therefore, by optimising the image contrast it is possible to profile the MQW active region by its photocurrent response. Figure 9.12 shows the contrast optimised photocurrent profile of the MQW to be very suggestive of the trapezoidal form seen in the topographic image of Figure 9.2. Although this is a rather crude measurement the approximate dimensions of the photocurrent profile of 1000nm × 250nm are comparable to the topographic dimensions of 1300nm (average length) × 240nm, which can only infer the similar proportions of the side lengths.

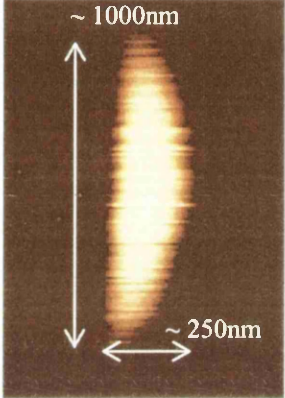

Figure 9.12 Photocurrent profile of the MQW active region. Photocurrent image with the contrast optimised to display only the maximum intensity zone of the active region.

The similarity between both topographic and photocurrent profiles is testament to the nanoscale illumination volume of the NSOM probe. The probe used in this experiment had an aperture diameter of 50nm, also the near-field optical penetration depth in the semiconductor is of the same order[4], and therefore photocurrents are generated within this volume at the sample surface. This enables the photocurrent measurements to follow closely the sample structure with high resolution, as is reflected in the profile of the MQW active region.

9.6 The effectiveness of the *pnpn* blocking structure and the implications of leakage currents in buried heterostructure lasers

The buried-heterostructure MQW laser aims to tightly confine both charge carriers and photons to the active region. The *pnpn* current blocking layers are designed to channel charge carriers into the active region for recombination via stimulated emission, however the efficiency that they perform this task is the fundamental weakness in BH-MQW laser devices.

The *pnpn* blocking structure consists of three *pn*-junctions with the middle junction in the reverse direction to the outer pair, as illustrated in the energy band diagram of Figure 9.13. The *n*-type blocking layer is enclosed within oppositely directed *pn*-junctions causing the increased carrier confinement which results in the low photocurrent intensity seen in the *n*-InP blocking layer. The high carrier confinement of the *n*-InP blocking layer suggests the *pnpn* structure prevents direct conduction of charge carriers across this region and thus channels them towards the active region.

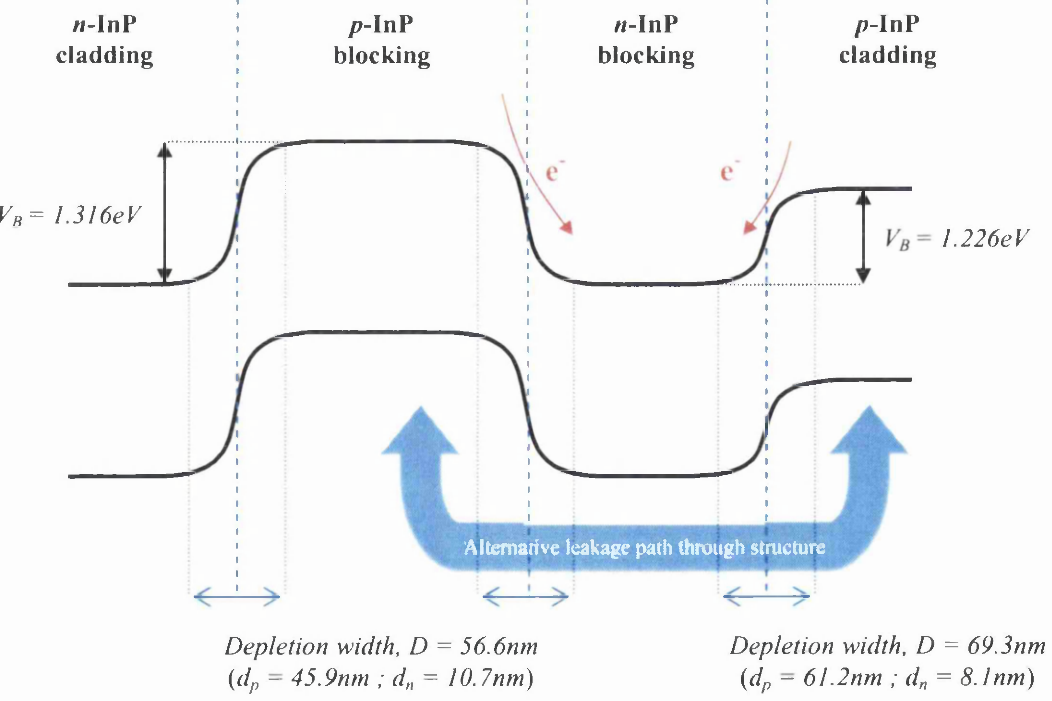

Figure 9.13 Schematic of the electronic band structure in a transverse direction through the *pnpn* current blocking structure. The barrier energies and depletion widths labelled were evaluated from the theoretical doping concentrations.

However the weakness lies in the coupling of the blocking structure to the active region, as discussed previously, in the ideal scenario the highly confined *n*-type blocking layer would be grown to the edge of the MQW. In reality this is not possible as an intrinsic buffer layer is necessary to prevent dopant diffusion directly into the MQW, as displayed in the schematic of Figure 9.14. A physical conduction path around the MQW therefore exists, passing directly from the *p*-InP cladding layer, via the intrinsic InGaAsP cladding, and *p*-InP blocking layer, to the *n*-InP cladding layer, as illustrated by the blue arrow in the schematic Figure 9.14 and electronic band diagram Figure 9.13.

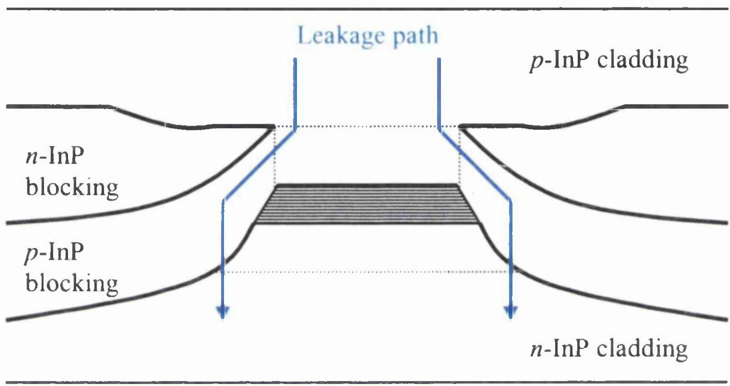

Figure 9.14 Schematic of the buried heterostructure MQW laser, the blue arrows mark the primary leakage path transporting charge carriers past the MQW active region. Conduction via this route occurs when photocurrent imaging, and is responsible for electroluminescence external to the MQW.

Although a physical conduction path exists, theoretically the passage of charge carriers via this route is electrically blocked by the depletion regions at the corner of the mesa structure[15]. By enhancing the depletion width in this area the possible conduction path width is minimised and ideally blocked. However this does not appear to occur very efficiently within the actual device, and is the most probable conduction path responsible for photocurrent conduction. For example the large photocurrent intensity generated at the *n*-InP cladding / *p*-InP blocking junction needs transport to the external circuit contacts, directly across the *pnpn* structure is energetically unfavourable, directly through the MQW would lead to carrier confinement and recombination, therefore the remaining and most probable path is between the two structures. This was the finding of Ban *et al*[13,15,16] who studied BH-

MQW lasers using a variety of techniques including scanning capacitance (SCM), voltage (SVM), and spreading resistance (SSRM) microscopy's.

The fact that such strong photocurrent signals were measured across both *p* and *n* sides of the structure indicates that a leakage path was open facilitating the conduction of the photo-stimulated current to the external device contacts. Although near-field photocurrent imaging cannot directly locate leakage paths it does highlight their presence, and using the capability to directly image *pn*-junctions throughout the device and the degree of minority carrier transport occurring at each, it is feasible to locate probable leakage pathways.

The transverse band profile of the *pnpn* region, as shown schematically in Figure 9.13, was calculated as described in chapter 4, using the theoretical dopant concentrations used in manufacturing the device. The band profile is fitted to the measured widths of the topographic data and plotted along with normalised photocurrent cross-sectional profiles in Figure 9.15.

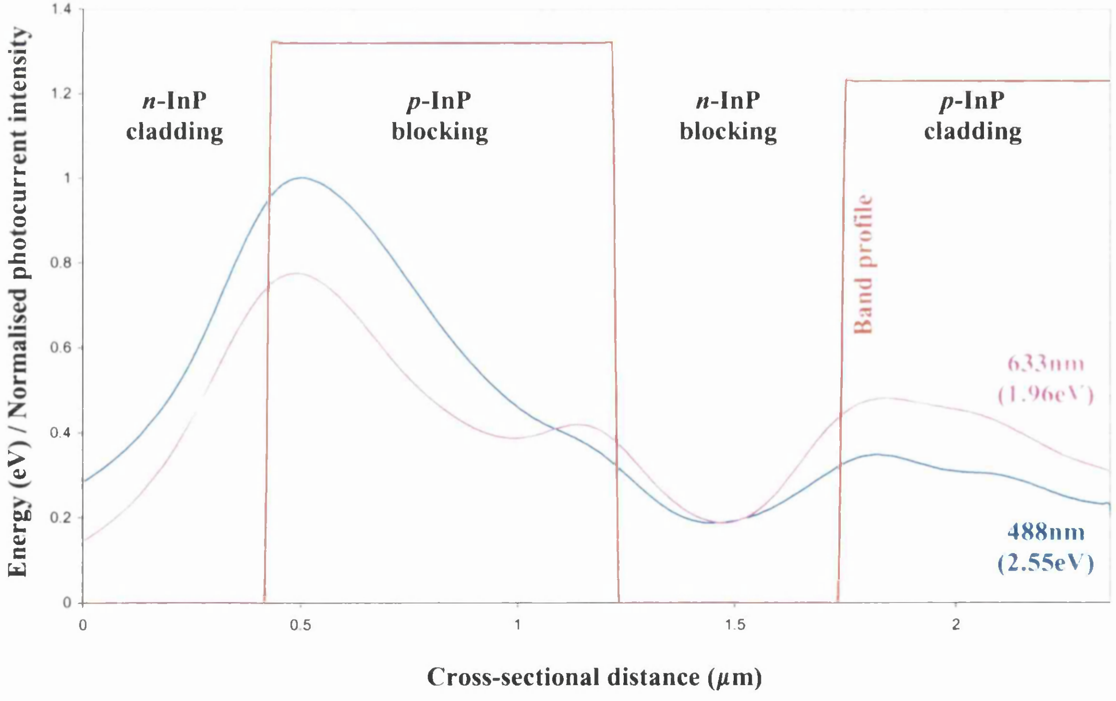

Figure 9.15 Transverse cross-sections of *pnpn* structure photocurrent response at 2.55eV and 1.96eV excitation energies. The band profile calculated from theoretical dopant concentrations and measured dimensions is plotted on the same axis.

When plotted in this format it is easy to see the correlation between the topographic measurements and the photocurrent response. The *pn*-boundaries all display peaks in the photocurrent irrespective of direction, just inside the *p*-type depletion region, and the intensity decreases into the bulk regions away from the junctions. The greatest response is as mentioned previously at the *n*-InP cladding / *p*-InP blocking interface, the remaining two *pn*-junctions at the *n*-InP blocking layer display a lower photocurrent response that are similar in intensity. The *n*-InP blocking layer displays increased carrier confinement, and this is responsible for the lower photocurrent seen at its *pn*-junctions. However it must be noted that whilst increased carrier confinement is displayed, it is not total confinement and a current does flow, as shown by the photocurrent not decreasing to zero in this region. This is indicative of carrier leakage from within the *n*-InP blocking layer, although on a much smaller scale than the previous leakage path discussed. The photocurrent at the *pn*-junctions of the *n*-InP blocking layer is reduced in amplitude as photo-excited electrons in the *p*-type depletion region are driven across the junction into the *n*-type material, as illustrated in Figure 9.13, where they are spatially restricted and the passage of a photocurrent is highly inhibited. The passage of a restricted photocurrent to the external device contacts indicates the presence of a leakage path and this may possibly be occurring at the apex of the *n*-InP material.

9.7 Optical characterisation: Collection NSOM

The device was powered and the active region and surrounding mesa scanned using the nanoscale aperture of the NSOM probe to collect light at the sample surface, as described fully in chapter 6. The resolution of collection NSOM is determined by the dimensions of the near-field aperture used to sample the optical field[1,10]. The near-field volume of the aperture is assumed to be the same in collection as it is in illumination i.e. of the order of the aperture diameter cubed. Thus light generated within or passing into the near-field volume of the aperture is coupled into the NSOM probe at each pixel of the image, therefore the resolution is determined solely by the aperture diameter which in this case is 50nm (quoting the manufacturer). Light passing up the NSOM probe and fibre tail is measured by focussing directly onto an avalanche photodiode APD, the integration time of which determines the scan rate. When using a 50nm diameter aperture the intensities of light coupled into the NSOM probe are very low and require a long APD integration time, resulting in an image

acquisition time of approximately 5hours. This has direct implications on the maximum power at which the device can be driven during imaging, as not only does the sample heat and expand; it also affects the mechanical interaction of the NSOM probe. As the probe passes through the intense optical field of the active region, illumination by the device induces thermal modifications of the physical properties of the probe as a function of position, causing the shear-force feedback condition regulating probe-sample separation to become very unstable[17,18,19,20]. Therefore the operating power of the device must be sufficiently low so as not to affect the stability of the shear-force condition during the long acquisition time of collection NSOM using an APD.

(a)

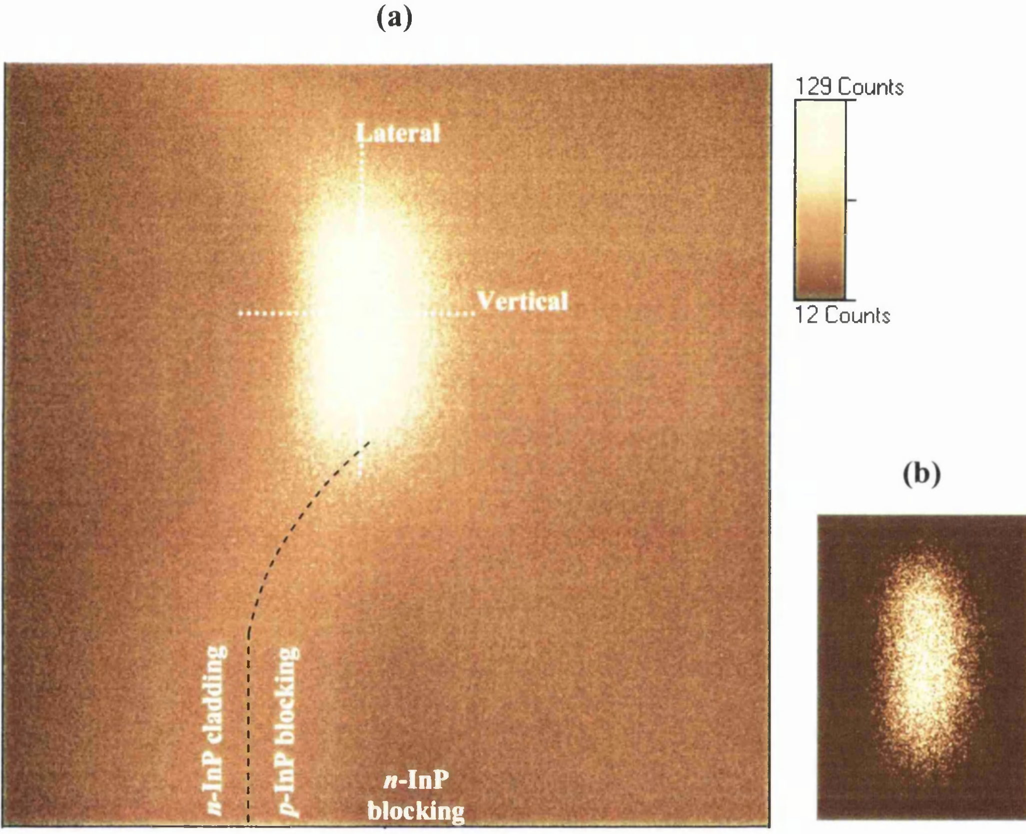

Figure 9.16 **(a)** Collection NSOM image of the BH-MQW laser powered at 1.13V; 98mA, which is above the laser threshold. The image was acquired using an APD at 10ms integration time per pixel and shows the bright optical output of the active region and surrounding electroluminescence. The modal pattern of the active region is emphasised in **(b)** by optimising the contrast to show only the higher intensities.

The buried heterostructure multi-quantum well laser not only influences electrical conduction pathways as discussed, but also serves as a waveguide confining

stimulated light to propagate along the active layer, and is reflected in the optical field measured at the emitting surface, as seen in Figure 9.16. The intensity of light measured is tightly localised to the active layer and shows over 100 counts greater APD signal than any background scattered light or electroluminescence. This is a consequence of the device structure (Figure 9.1) and shows that it is functioning as designed. The waveguide properties of the device centre on the multi-quantum well active layer which has a much greater effective refractive index than any of the surrounding InP blocking layers and InGaAsP cladding layers, thus confining propagating light to the active layer by a refractive index distribution much like an optical fibre.

The dimensions of the MQW active layer are designed to allow the laser to stably operate only in a single transverse optical mode; the length parallel to the MQW is so small that only the fundamental lateral transverse TE mode can propagate, as it has the lowest laser threshold[21]. The distribution of the laser mode in the lateral and vertical directions is displayed in the cross-sections of Figure 9.17. In the direction parallel to the active layer, the lateral transverse direction, there is very high optical confinement of over 90%. The full width at half maximum, FWHM, measures 1400nm, whereas the active MQW region was trapezoidal in structure with side lengths of 1100nm and 1500nm (average length 1300nm) in this direction. In the direction perpendicular to the active layer, the vertical transverse direction, the optical confinement is low, with a confinement factor of approximately 20% resulting from the small width of the active layer[3,21]. This is apparent from the FWHM of the vertical distribution which measures 655nm, when compared to the theoretical MQW width of 134nm, or the active region width measured from the topographic data of 240nm.

The optical distribution measured in the near-field collection image indicates that collection NSOM not only detects light generated within the near-field volume of the probe aperture, but is also highly sensitive to waveguide modes consisting of light generated within the bulk material and guided to the surface of the active region, and hence into the near-field collection volume of the probe. This is primarily indicated by the elliptical profile collected over the active region, as seen in Figure 9.16(b), which demonstrates the modal distribution of the laser. This is in contrast to the

trapezoidal form of the MQW active region, as seen in the topographic image Figure 9.2 and photocurrent image Figure 9.12. If collection NSOM was only sensitive to, or dominated by light generated within the near-field volume of the aperture then this would be indicated by a trapezoidal form in the collection profile. This is in agreement with earlier collection NSOM results of Buratto *et al*[5] and Herzog *et al*[22]. The collection NSOM image probably consists of a combination of waveguide and near-field modes, however the intensity of light generated within the near-field of the probe will be a tiny fraction of the waveguide intensity, and thus the collection image is dominated by the waveguide. Buratto *et al*[5] also conducted a study of the dependence of the near-field distribution on the drive current of the device, finding the optical output to be much smaller than the active region surface area profile for drive currents below the laser threshold, and becoming elliptical at and above the threshold for lasing. This confirms that the collection NSOM image of Figure 9.16 was conducted with the device operating above the laser threshold.

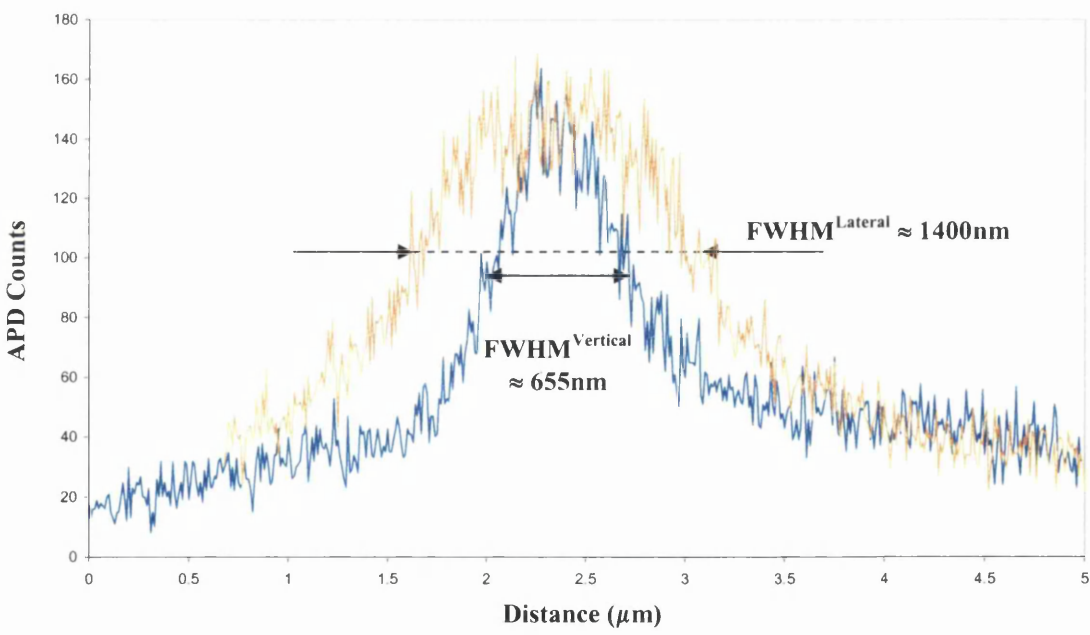

Figure 9.17 Cross-sections of the laser mode in the vertical and lateral directions. The cross-sections are labelled in Figure 9.16(a).

The collection NSOM image of Figure 9.16(a) displays the optical output of the BH-MQW device operating above its laser threshold at 50nm resolution, it is clear that the device displays high optical confinement to the high refractive index MQW active region. However there is also light emitting external to the active region, the highest

intensity of which occurs at the adjacent *pn*-junction between the *n*-InP cladding / *p*-InP blocking layers, as marked by the dashed black line in Figure 9.16(a), and is approximately 30% of the intensity of the active region (45 counts). The position of this bright fringe correlates perfectly with the location of the *n*-InP cladding / *p*-InP blocking junction in the photocurrent images. The level of light measured along this *pn*-junction is indicative of electroluminescence due to recombination of injected carriers. This is in agreement with the photocurrent imaging that found photo-excited carriers were leaking past the MQW and conducting to the external device contacts, probably conducting between the *n*-InP blocking layer and the MQW. The reverse situation is being measured in the collection NSOM image where the powered device displays injected carriers leaking past the blocking structure and MQW active region and recombining at the *n*-InP cladding / *p*-InP blocking junction resulting in electroluminescence. Or more accurately, holes injected at *p*-InP contact are leaking past the blocking structure and active region to recombine with electrons injected from the *n*-InP contact at the *n*-InP cladding / *p*-InP blocking junction. The intensity of electroluminescence is greatest over the curved mesa region of the *pn*-junction, and is a slightly lower constant intensity along the straight interface region, indicating a significant degree of carrier recombination external to the active region. This results in lowered operational efficiency, the main consequence of which is an increased lasing threshold for the device, as predicted by photocurrent imaging. The use of a multi-quantum well active region serves to increase carrier confinement once within the active region and optically confine photons, both increasing efficiency and reducing the threshold current. However the main weakness of the device is in optimising the manipulation of the conduction of injected carriers to the active layer. The *n*-InP blocking layer is dark displaying no electroluminescence and again a high degree of carrier confinement, confirming the probable leakage pathway running between the blocking structure and active region, and effectively eliminating the possibility of leakage directly across the blocking structure.

Note there are very low intensities of light detected at other locations, most notably over the InGaAsP cladding layer on the *p*-type side of the active layer, clearly visualized as an asymmetry in the residual tails of the vertical cross-section in Figure 9.17. This could possibly be the result of low levels of electroluminescence due to injected electrons leaking directly through the active region, thus correlating with

comparably high photocurrent levels seen at this location. However it is most probable to be background light leaked from within the bulk of the active layer and scattered to the surface of the device. This scenario is supported by the low background intensity level measured across the surface of the device, particularly in the *p*-type and intrinsic materials, and in comparison to the stronger *n*-InP cladding / *p*-InP blocking junction electroluminescence.

9.8 Summary

The combination of shear-force topographic imaging, near-field photocurrent imaging, and collection NSOM has proved very powerful in analysing the operational efficiency of buried heterostructure multi-quantum well lasers, and successfully demonstrated the following.

- Unprecedented sensitivity to the surface topography, detecting the location of the active region and surrounding mesa structure, thus allowing accurate correlation with simultaneous photocurrent measurements.
- Photocurrent imaging has directly mapped the location of the active region in relation to the surrounding *pnpn* blocking structure.
- The distribution of the *pn*-junctions of the *pnpn* blocking structure has been imaged, including the extent of the corresponding depletion layers.
- The location and electronic confinement of the current blocking layers has been measured, allowing the success of the buried heterostructure in charge confinement to the active layer to be evaluated and potential leakage paths to be identified.
- The optical characteristics of the operating device have been directly imaged with (approximately) 50nm lateral resolution, thus assessing the optical confinement characteristics of the device, and identifying unwanted electroluminescence external to the active region.

Buried heterostructure multi-quantum well lasers are highly complex devices in both their operation and fabrication. The various imaging modes of NSOM utilised within this work have proved very informative in the analysis of the structural quality of such devices, and their operational characteristics. The photocurrent response to different excitation energies proved to vary the contrast and resolution of such images, and thus may be exploited further with the application of different excitation sources. The

value of NSOM in analysing such devices has been demonstrated, and would prove complementary to other analysis techniques, encompassing different interaction mechanisms such as STM, for an in-depth analysis of buried heterostructure devices.

9.9 References

[1] U. Durig, D.W. Pohl, F. Rohner, *J. Appl. Phys.* **59**, 3318 (1986)

[2] H. Chen, R.M. Feenstra, R.S. Goldman, C. Silfvenius, G. Landgren, *Appl. Phys. Lett.* **72** (14), 1727 (1998)

[3] S.K. Buratto, J.W.P. Hsu, E. Betzig, J.K. Trautman, R.B. Bylsma, C.C. Bahr, *Appl. Phys. Lett.* **65,** (21) 2654, (1994)

[4] G. Kolb, K. Karraai, G. Abstreiter, *Appl. Phys. Lett.* **65**, 24 (1994)

[5] S.K. Buratto, J.W.P. Hsu, J.K. Trautman, E. Betzig, R.B. Bylsma, C.C. Bahr, M.J. Cardillo, *J. Appl. Phys.* **76**, 7720 (1994)

[6] M.S. Unlu, B.B. Goldberg, W.D. Herzog, D. Sun, E. Towe, *Appl. Phys. Lett.* **67**, 1862 (1995)

[7] B.B. Goldberg, M.S. Unlu, W.D. Herzog, H.F. Ghaemi, E. Towe, *IEEE J. selected topics in Quantum Elec.* **1**, 1073 (1995)

[8] P.S. Weiss, P.L. Trevor, M.J. Cardillo, *J. Chem. Phys.* **90**, 5146 (1989)

[9] C. Coluzza, G. Di Claudio, S. Davy, M. Spajer, D. Courjon, A. Cricenti, R. Generosi, G. Fanini, J. Almeida, E. Conforto, G. Margaritondo, *J. Microscopy*, **194**, 401 (1999)

[10] M. Isaacson, J.A. Cline, H. Barshatzky, *J. Vac. Sci. Technol. B,* **9** (6), 3103 (1991)

[11] N.H. Lu, D.P. Tsai, C.S. Chang, T.T. Tsong, *Appl. Phys. Lett.* **74**, 2746 (1999)

[12] Ch. Lienau, A. Richter, J.W. Tomm, *Appl. Phys. A* **64**, 341 (1997)

[13] D. Ban, E.H. Sargent, St. J. Dixon-Warren, T. Grevatt, G. Knight, G. Pakulski, A.J. SpringThorpe, R. Streater, J.K. White, *J. Vac. Sci. Technol. B* **20** (5), 2126 (2002)

[14] S.M. Sze, *Physics of semiconductor devices,* (Wiley, New york, 1981)

[15] D. Ban, E.H. Sargent, St. J. Dixon-Warren, G. Letal, K. Hinzer, J.K. White, G. Knight, *IEEE J. Quantum Elec.* **40** (2), 1 (2004)

[16] D. Ban, E.H. Sargent, St.J. Dixon-Warren, I. Calder, T. Grevatt, G. Knight, J.K. White, *J. Vac. Sci. Technol. B* **20** (6), 1 (2002)

[17] G. Wurtz, R. Bachelot, P. Royer, *Eur. Phys. J. AP* **5**, 269 (1999)

[18] S. Grafstrom, O. Schuller, J. Kowalski, R. Neumann, *J. Appl. Phys.* **83**, 3453 (1998)

---

[19] U. Ben-Ami, N. Tessler, N. Ben-Ami, R. Nagar, G. Fish, K. Lieberman, G. Eisenstein, A. Lewis, J.M. Nielsen, A. Moeller-Larsen, *Appl. Phys. Lett.* **68**, 2337 (1996)

[20] Ch. Lienau, A. Richter, T. Elsaesser, *Appl. Phys. Lett.* **69**, 325 (1996)

[21] M. Fukuda, *Optical semiconductor devices*, (Wiley, 1999)

[22] W.D. Herzog, M.S. Unlu, B.B. Goldberg, G.H. Rhodes, C. Harder, *Appl. Phys. Lett.* **70**, 688 (1997)

Chapter 10

Conclusions and details of continuing studies

Near-field photocurrent imaging with a current sensitivity of the order 10^{-14} Amps has been successfully developed using pre-amp / lock-in amplifier stages together with an aperture near-field scanning optical microscope. This development was critical in enabling photocurrent characterisation of electronic and optoelectronic devices with sub-micron scale lateral resolution, and these are summarised in turn below.

Schottky samples

The capability of near-field photocurrent imaging in the analysis of the sub-surface, buried Schottky interface has been successfully demonstrated, imaging lateral variations in the Schottky barrier properties and locating interface defects. The sub-micron barrier characteristics, as measured by the photocurrent, correlated closely with macroscopic I-V measurements which determine the Schottky barrier height of the contact, and its corresponding ideality factor which reflects the uniformity of the interface. Near-field photocurrent imaging has been found to be particularly applicable for the case of flat metal contacts of uniform thickness, where the risk of topographic imaging artefacts in the optically generated photocurrent signal are minimised. Imaging artefacts are always a risk when photocurrent imaging a buried interface, however it has been shown that by using appropriate sample configurations (i.e. uniform metal contact layers) and scanning at a low rate, the topographic contamination of photocurrent images can be minimised.

Imaging within this study was performed using two fixed wavelength sources, thus it was not possible to measure precisely the barrier energy using the classical optical technique of tuning the photon energy across the excitation edge of the sample, and plotting the photocurrent yield with the photon energy in a Fowler plot[12]. However the variation of the barrier height was demonstrated using fixed excitation energy. Moreover, the extent of the depletion region enabled an evaluation of the barrier energy, as determined by Poisson's equation[3]. Photocurrent imaging at zero applied bias is directly sensitive to the built-in field of the depletion region, thus by imaging at the Schottky contact perimeter it is possible to directly image the extent of the

semiconductor depletion region, and thus determine an approximate Schottky barrier height.

The Schottky barrier height was increased by 0.155eV via annealing the sample at 500°C for 600 sec. This also enhanced the lateral variations of the Schottky interface, which were reflected by an increase in the ideality factor of the contact, and in the variation of the photocurrent response[4]. Demonstrating the value of the near-field photocurrent analysis of buried Schottky interfaces.

Further Schottky investigations

Since these studies on Ni-SiC Schottky contacts by near-field photocurrent generation, work by O. Al Hartomy[5] has concentrated on using the analysis technique of ballistic electron emission microscopy (BEEM)[6], which is based upon the scanning tunnelling microscope (STM). This requires Ni-SiC Schottky contacts of a similar thickness to those used within photocurrent investigations, and the system is configured such that electrons tunnel from the STM tip to the Ni contact layer, allowing conventional STM images to be acquired from the contact layer. Injected electrons tunnel ballistically through the Ni layer to the interface, provided the metal layer thickness is comparable to the mean free path of the electrons. If the electrons have sufficient energy, determined by the tip-metal bias voltage, they can cross the interface into the semiconductor, establishing a BEEM current. Thus the barrier energy can be determined by tuning the tip-sample bias, and lateral interface properties can be measured by imaging the BEEM current across the sample at a fixed bias. This technique is complementary to that carried out in near-field photocurrent studies, and has measured the Schottky barrier height to vary between 1.5-2.3eV over a similar lateral extent as that recorded using near-field photocurrents.

MQB lasers

The capabilities of the NSOM imaging modes have been further demonstrated by powerfully combining shear-force topography, near-field photocurrent, and near-field collection modes, in the characterisation of semiconductor diode lasers. Investigations were conducted with laser samples oriented in the cross-sectional configuration, thus the particular laser structures were imaged directly (i.e. not buried as in the case of Schottky contacts) upon the highly flat, freshly cleaved surface, and

the risk of topographic imaging artefacts was negligible, if not eliminated entirely. Shear-force topographic imaging detected the device structure simultaneous to near-field photocurrent or collection imaging. Therefore the physical device structure can be correlated with the electronic characteristics determined by photocurrent imaging, and the near field optical output of the operating device detected by collection imaging.

GaInP / AlGaInP based quantum well lasers were studied in the investigation of the effectiveness of multi-quantum barriers (MQB's) in enhancing the electronic confinement of the active region. Near-field photocurrent imaging detected the presence of MQB super-lattices within the laser structures, when compared with similar devices that did not contain MQB's, by virtue of a modification to the charge confinement. By using different optical excitation energies it was possible to analyse the relative effectiveness of the two different MQB structures investigated, one of which clearly displayed superior charge confinement. The electronic properties were correlated with the device structure that was imaged via oxide growth effects. However, the presence of a surface oxide was detrimental to the photocurrent intensity and lateral resolution, as large (100nm) diameter aperture NSOM probes were required. This investigation could therefore be improved by imaging under vacuum, thus eliminating surface oxides and allowing the use of small (50nm) diameter NSOM probes. The photocurrent imaging contrast may also be optimised by using different excitation photon energies, similarly as in the case of Schottky diodes.

The optical output of the operating devices was characterised in the near-field by collection imaging, which detected high optical confinement perpendicular to the active region (i.e. the vertical transverse direction) for all devices. This confirmed that the incorporation of MQB super lattices into the *p*-type cladding layers did not affect the optical confinement of the waveguide region.

BH-MQW lasers

The NSOM has similarly been applied in the investigation of buried heterostructure multi-quantum well (BH-MQW) lasers. The shear-force topographic imaging mode displayed excellent sensitivity to detect surface relaxation of the active region and

surrounding mesa structure of order 10^{-10}m. Near-field photocurrent imaging directly mapped the location and distribution of the MQW active region and surrounding *pn*-junctions of the buried heterostructure, including the lateral extent of the depletion regions. This allowed the effectiveness of the buried heterostructure in channelling injected charge carriers into the MQW active region to be assessed, and probable leakage paths between the *n*-InP blocking layer and MQW's to be identified. The photocurrent findings were confirmed by collection mode imaging which identified electroluminescence occurring external to the active region along the *n*-InP cladding layer / *p*-InP blocking layer interface, supporting the probability of current leakage past the MQW active region, around the edge of the *n*-InP blocking layer. Collection imaging also determined the optical output profile of the active region, inferring that the device was operating at its fundamental mode.

Further laser investigations

These studies have since motivated further NSOM investigations of semiconductor laser devices, primarily focussing upon the incorporation of a spectrometer with a highly sensitive CCD detector (peltier cooled to -70°C) to facilitate localised spectroscopy of operating devices using the NSOM probe as a collector. The coupling of the NSOM probe fibre tail to a spectrometer with dual detectors permits the mapping of the laser output at single wavelengths, by coupling the very low intensity, single wavelength output of the spectrometer onto a highly sensitive avalanche photodiode detector (APD). The spectroscopic characteristics and lateral distribution of the spectroscopic output of operating BH-MQW and vertical cavity surface emitting lasers (VCSEL) are currently under investigation[7]. Note near-field photocurrent imaging is utilised within the further investigation of BH-MQW lasers to facilitate the locating of the active region.

Summary

It is clear that the NSOM developments have significantly contributed to understanding various semiconductor devices, and the enhanced near-field photocurrent capabilities are contributing to continued studies within the field. The powerful ability to analyse buried interfaces simultaneously with surface properties has been successfully demonstrated. Similarly as the capabilities of the NSOM techniques in the surface analysis of the cleaved cross-sections of complex

semiconductor structures. The samples studied highlight the versatility of the NSOM techniques to investigate a broad spectrum of devices, under a variety of configurations and operating conditions. The ability of the NSOM to examine and correlate topographic, electronic, and optical properties is extremely powerful and provides a valuable tool towards the complete characterisation of devices when coupled with complementary techniques.

References

[1] R. Fowler, *Phys. Rev.* **38**, 45 (1931)

[2] D.K. Schroder, *Semiconductor material and device characterisation 2nd Ed.*, (J. Wiley and sons, NY, 1988)

[3] M.J. Cooke, *Semiconductor devices*,(Pentrice Hall International, 1990)

[4] P.R. Dunstan, T.G.G. Maffeis, M.P. Ackland, G.T. Owen, S.P. Wilks, *J. Phys.: Condens. Matter* **15**, 3095 (2003)

[5] O. Al-Hartomy, University of Wales Swansea, *M.Phil. Thesis in preparation* (Expected submission April 2005)

[6] A.E. Fowell, R.H. Williams, B.E. Richardson, A.A. Cafolla, D.I. Westwood, D.A. Woolf, *J. Vac. Sci. Technol. B,* **9** (2), 581 (1991)

[7] M. Holton, University of Wales Swansea, *PhD studies*, *Spectroscopy studies using a near-field optical microscope.*

Appendix 11.1: Ex-situ SiC wafer cleaning techniques

The following procedures are used to clean SiC wafers prior to deposition of Ni electrical contacts for both the high vacuum Edwards evaporator and ultra-high vacuum deposition techniques. The process removes dust, oil based contaminants, organic substances, ionic contaminants, and etches SiO_2 surface oxides without modifying SiC, leaving an atomically clean surface. Note the sample is washed with de-ionised water between every chemical step of the cleaning process.

Solvent clean

This stage is carried out with beaker containing the sample and cleaning reagents within a sonic bath.

1. Trichloroethylene - 10mins.
2. Acetone – 10mins.
3. Isopropanol – 10mins.

Piranha clean

The reagents and sample are heated to 75°C using a hotplate.

Cleaning reagents: 5ml H_2SO_4 + 1ml H_2O_2

Add 1ml of H_2O_2 every 5mins.

Total time = 15mins

RCA clean

1. 1ml NH_4OH + 1ml H_2O_2 + 5ml H_2O (de-ionised) for 10mins at 75°C.
2. HF dip for 2mins.
3. 1ml HCl + 1ml H_2O_2 + 1ml H_2O (de-ionised) for 10mins at 75°C.
4. HF dip for 2mins.

Appendix 11.2: Planar quantum well laser structures

Note, red writing denotes the quantum well active layer, green writing represents the MQB replacement control layer, and blue writing denotes the MQB layers which are repeated at the frequency of the accompanying multiplier.

Table 1: Control laser

Layer	Thickness (nm)	x	Doping
GaAs	400		*p*-2E19 (Zn)
$Ga_xIn_{1-x}P$	10	0.52	*p*-2E18 (Zn)
$(Al_xGa_{1-x})_{0.52}In_{0.48}P$	500	0.70	*p*-5E17 (Zn)
$(Al_xGa_{1-x})_{0.52}In_{0.48}P$	500	0.40	*p*-5E17 (Zn)
$(Al_xGa_{1-x})_{0.52}In_{0.48}P$	900	0.70	*p*-5E17 (Zn)
$(Al_xGa_{1-x})_{0.52}In_{0.48}P$	94.5	0.51	*p*-5E17 (Zn)
$(Al_xGa_{1-x})_{0.52}In_{0.48}P$	90	0.30	Wave guide
$Ga_xIn_{1-x}P$	6.8	≈0.41	Quantum well
$(Al_xGa_{1-x})_{0.52}In_{0.48}P$	90	0.30	Wave guide
$(Al_xGa_{1-x})_{0.52}In_{0.48}P$	94.5	0.51	*n*-5E17 (Si)
$(Al_xGa_{1-x})_{0.52}In_{0.48}P$	1000	0.70	*n*-5E17 (Si)
$Ga_xIn_{1-x}P$	10	0.52	*n*-5E17 (Si)
GaAs	332.5		*n*-2E18 (Si)
GaAs substrate			

Table 2: MQB1

Layer	Thickness (nm)	x	Doping
GaAs	400		*p*-2E19 (Zn)
$Ga_xIn_{1-x}P$	10	0.52	*p*-2E18 (Zn)
$(Al_xGa_{1-x})_{0.52}In_{0.48}P$	500	0.70	*p*-5E17 (Zn)
$(Al_xGa_{1-x})_{0.52}In_{0.48}P$	500	0.40	*p*-5E17 (Zn)
$(Al_xGa_{1-x})_{0.52}In_{0.48}P$	900	0.70	*p*-5E17 (Zn)
$(Al_xGa_{1-x})_{0.52}In_{0.48}P$	8.7	0.30	*p*-5E17 (Zn)
$(Al_xGa_{1-x})_{0.52}In_{0.48}P$ } ×7	4.2 } ×7	0.70 } ×7	*p*-5E17 (Zn) } ×7
$(Al_xGa_{1-x})_{0.52}In_{0.48}P$	4.2	0.30	*p*-5E17 (Zn)
$(Al_xGa_{1-x})_{0.52}In_{0.48}P$	9.6	0.70	*p*-5E17 (Zn)
$(Al_xGa_{1-x})_{0.52}In_{0.48}P$	15	0.30	*p*-5E17 (Zn)
$(Al_xGa_{1-x})_{0.52}In_{0.48}P$	15	0.70	*p*-5E17 (Zn)
$(Al_xGa_{1-x})_{0.52}In_{0.48}P$	90	0.30	Wave guide
$Ga_xIn_{1-x}P$	6.8	≈0.41	Quantum well
$(Al_xGa_{1-x})_{0.52}In_{0.48}P$	90	0.30	Wave guide
$(Al_xGa_{1-x})_{0.52}In_{0.48}P$	94.5	0.51	*n*-5E17 (Si)
$(Al_xGa_{1-x})_{0.52}In_{0.48}P$	1000	0.70	*n*-5E17 (Si)
$Ga_xIn_{1-x}P$	10	0.52	*n*-5E17 (Si)
GaAs	332.5		*n*-2E18 (Si)
GaAs substrate			

Table 3: MQB2

Layer	Thickness (nm)	x	Doping
GaAs	400		*p*-2E19 (Zn)
$Ga_xIn_{1-x}P$	10	0.52	*p*-2E18 (Zn)
$(Al_xGa_{1-x})_{0.52}In_{0.48}P$	500	0.70	*p*-5E17 (Zn)
$(Al_xGa_{1-x})_{0.52}In_{0.48}P$	500	0.40	*p*-5E17 (Zn)
$(Al_xGa_{1-x})_{0.52}In_{0.48}P$	900	0.70	*p*-5E17 (Zn)
$(Al_xGa_{1-x})_{0.52}In_{0.48}P$	4.5	0.30	*p*-5E17 (Zn)
$(Al_xGa_{1-x})_{0.52}In_{0.48}P$ ×6	4.2 ×6	0.70 ×6	*p*-5E17 (Zn) ×6
$(Al_xGa_{1-x})_{0.52}In_{0.48}P$	4.2	0.30	*p*-5E17 (Zn)
$(Al_xGa_{1-x})_{0.52}In_{0.48}P$	9.6	0.70	*p*-5E17 (Zn)
$(Al_xGa_{1-x})_{0.52}In_{0.48}P$	15	0.30	*p*-5E17 (Zn)
$(Al_xGa_{1-x})_{0.52}In_{0.48}P$	15	0.70	*p*-5E17 (Zn)
$(Al_xGa_{1-x})_{0.52}In_{0.48}P$	90	0.30	Wave guide
$Ga_xIn_{1-x}P$	6.8	≈0.41	Quantum well
$(Al_xGa_{1-x})_{0.52}In_{0.48}P$	90	0.30	Wave guide
$(Al_xGa_{1-x})_{0.52}In_{0.48}P$	94.5	0.51	*n*-5E17 (Si)
$(Al_xGa_{1-x})_{0.52}In_{0.48}P$	1000	0.70	*n*-5E17 (Si)
$Ga_xIn_{1-x}P$	10	0.52	*n*-2E18 (Si)
GaAs	332.5		*n*-2E18 (Si)
GaAs substrate			

Appendix 11.3: Gaussian curve fitting - Vertical transverse optical cross-section of operating Control QW laser.

Below is the Gaussian equation and parameters evaluated in curve fitting the vertical transverse cross-sections of the control QW device analysed in Figure 8.9 of Chapter 8. Curve fitting was performed using the software *Origin Pro 7.0.*

Below threshold: 1.78V; 27mA

Model: Gauss

Equation: y = y0 + (A/(w*sqrt(PI/2)))*exp(-2*((x-xc)/w)^2)

Weighting: y No weighting

Chi^2/DoF = 8.8085

R^2 = 0.96015

y0 = 1.79836 ± 0.33017

xc = 758.22592 ± 2.66332

w = 364.45772 ± 6.73338

A = 18847.18789 ± 398.95624

Above threshold: 2.06V; 92mA

Model: Gauss

Equation: y = y0 + (A/(w*sqrt(PI/2)))*exp(-2*((x-xc)/w)^2)

Weighting: y No weighting

Chi^2/DoF = 42.31822

R^2 = 0.9941

y0 = 9.2867 ± 0.74002

xc = 758.50121 ± 1.02225

w = 373.47278 ± 2.61816

A = 111645.37488 ± 905.17469